

FACILITY FORM 602

N65-35611	N65-376
(ACCESSION NUMBER)	(THRU)
270	1
(PAGES)	(CODE)
CR 64951	30
(NASA CR OR TMX OR AD NUMBER)	(CATEGORY)
N69-18999-18987	

CONFERENCE CONFERENCE

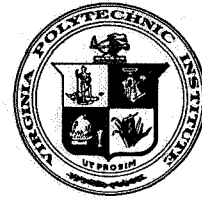
THE ROLE OF SIMULATION IN SPACE TECHNOLOGY PART C

Cover design by David J. E. Greene and John G. Wisnosky of the VPI College of
Architecture.

(Background—courtesy NASA, Langley Research Center)

CASE FILE
COPY

VIRGINIA POLYTECHNIC INSTITUTE



ENGINEERING EXTENSION SERIES CIRCULAR No. 4
(In four parts: A,B,C,D)

PART C

PROCEEDINGS OF THE CONFERENCE ON

The Role of Simulation in Space Technology

AUGUST 17-21, 1964

Supported by grants from the National Aeronautics and Space Administration
and the National Science Foundation; assisted in planning and presentation
by the NASA Langley Research Center.

TABLE OF CONTENTS

PART C

REAL-TIME DYNAMIC SIMULATION

Computers for Simulation of Space Vehicle Systems - R. M. Howe	XII
Discussion of Existing and Planned Simulators for Space Research - A. W. Vogeley	XIII
Visual and Motion Simulation Techniques - John Lott Brown	XIV
Dynamic Simulators for Tests of Space Vehicle Attitude Control Systems - G. Allan Smith	XV

STRUCTURAL DYNAMICS

Introduction to the Session on Structural Dynamics - I. E. Garrick	XVI
Principles and Practices for Simulation of Structural Dynamics of Space Vehicles	XVII
Models for Orbiting Effects of Ground Winds on Space Vehicles Erected on the Launch Pad - Wilmer H. Reed, III	XVIII
Simulation of Structural Dynamics of Space Vehicles During Launch - H. L. Runyan	XIX

165-152

COMPUTERS FOR SIMULATION OF SPACE VEHICLE SYSTEMS

by

R. M. Howe

The University of Michigan

1. Introduction

The importance of simulation in the design and testing of space vehicle systems is self evident. Simulation also plays a vital role in the training of both astronauts and ground crews. It may even form a vital part of the mechanization of on-board displays. One of the most important parts of any space-system simulator is the computer which calculates the simulated performance of the vehicle. In previous years the simulation of aircraft and missiles in six degrees of freedom has posed challenging computational problems. These problems become even more severe in the simulation of space vehicles, since the dynamic range of problem variables becomes much larger and the flight times become much longer. For example, simulation of the full Apollo mission requires accurate computation of vehicle trajectories over the earth-moon distance, more than 10^9 feet, for times of many hours or even days. Yet the same computer is required to simulate docking maneuvers with resolution of better than one foot, as well as reentry maneuvers where vehicle pitching and yawing frequencies up to several cps and higher are encountered. In fact, accurate simulation of jet-reaction attitude control systems, including precise computation of fuel usage, may require computer time resolution in the millisecond region.

Although the above example is a severe one, it illustrates the type of problems that may face the simulator designer in choosing the appropriate computer system for the task. The purpose of this paper is to outline some of the performance considerations of analog and digital computers which are important in space-vehicle simulation. The choice of axis systems such that computer performance requirements will be less severe will also be described, along with some typical computer results.

In considering the simulation of space vehicles there is a very wide range of problem types which one encounters. We have already mentioned a full-mission Apollo simulation in real time, which might be used for mission studies or actual astronaut training. On the other hand one might be interested in simulating just the rotational degrees of freedom of one stage of a space-vehicle booster system as part of an autopilot-design study. Such a simulation need not be in real time unless actual flight hardware is substituted for parts of the computer as the design progresses. Or repetitive simulation of space-vehicle reentry trajectories at speeds thousands of times faster than real time may be required to implement a predictor display, or to mechanize a computation of the optimum reentry trajectory. Most of the discussion that follows will concentrate on the computational requirements for the six-degree-of-freedom full mission type of simulation, since other simulation tasks are usually part of this overall, larger task.

2. Scope of the Full-Mission Simulation. Analog, Hybrid, or Digital Computation

In a simulation that involves lunar or planetary missions accurate trajectory computation requires that a high-precision digital computer be

used. This is because of the enormous range in force magnitudes which act on the vehicle, and because analog computers have precision limited to the order of 0.01 percent of full scale. In fact, care must be taken in a digital simulation of such trajectories to make certain that roundoff and truncation errors do not generate unacceptably large errors. For example, in Figure 1 are shown the results of a study performed by the Link Division of General Precision, Inc., where a highly eccentric earth-satellite orbit with apogee equal approximately to the earth-moon distance has been computed using a fourth-order Runge-Kutta integration formula. The abscissa is essentially proportional to the vehicle distance from the earth, with check point 60 representing lunar distance. Hence, except for the lack of inclusion of the lunar gravity, the results are representative of an Apollo lunar trajectory. The ordinate is position error, which builds up to 30,000 feet using a 24 bit word length (single precision). This would be unacceptably large in many cases. On the other hand, using double precision reduces the error to less than 2000 feet, an acceptable number. In many cases simulation of space-vehicle trajectories may have to be accomplished using two simultaneous integrations, one at low iteration rate using double precision and a second at high iteration rate using single precision. The second integration provides trajectory information at high enough rates to be used to drive visual displays, but gets updated at the end of each computational cycle of the first integration.

Although the space-vehicle trajectory may require digital solution, one may wish to solve the rotational equations on an analog computer. This is because the accuracy requirements of the rotational equations are much less severe, but at the same time the frequency components are much higher.

Although current digital computers are capable of solving both rotational and translational equations in real time, the initial programming of the equations is extremely expensive as compared with an analog computer. Also, one may wish to solve the equations faster than real time in order to avoid long solution times in engineering studies, in which case an analog computer must be used. Figures 2 and 3 show block diagrams of the equations which might be solved on the analog and digital portions, respectively, of such a simulator. They also illustrate the complexity of the equations which must be solved in such a six-degree-of-freedom simulation. When both analog and digital computers are combined in such a simulation, we have a hybrid computer, which requires analog-to-digital converters and digital-to-analog converters for communication back and forth between the machine elements. Actually, an all-digital simulation requires such converters to serve as input-output devices, in any case. Although hybrid computers offer an obviously efficient solution to the six-degree-of-freedom space-vehicle simulation problem, programming the computers and interface equipment is by no means a trivial problem. For this reason, it is probably well to avoid hybrid simulations of this type unless there is a sizeable economic advantage or unless it is required because of performance considerations.

One of the computational areas where the digital computer has a sizeable advantage over the analog is in generation of multivariable functions. For example, suppose that the rotational equations of motion are to be solved on the analog computer, except that the digital computer is to be used to calculate the aerodynamic pitching moment, since it is a complicated function of Mach number M , altitude h , and angle of attack α . A block diagram of the pitch loop is shown in Figure A, where the pitch acceleration $\ddot{\theta}$ is computed in analog voltage form by dividing the total pitching moment

$M_a + M_c$ by the pitching inertia I_{yy} . $\ddot{\theta}$ is then integrated twice to obtain an analog voltage θ representing the vehicle attitude. The flight-path angle γ is subtracted from this to compute the angle of attack α , which is then converted to digital form and fed, along with Mach number and altitude, into a digital computer which calculates the aerodynamic pitching moment M_a . This is in turn converted back to analog form and added to the voltage representing the jet-reaction pitching moment M_c , thus closing the computational loop.

Let us now consider the effect of the finite calculation time T required by the digital computer to calculate the pitching moment M_a . To simplify the analysis we will assume that the flight-path angle γ remains constant, as well as the Mach number M and the altitude h . Furthermore, for these constant values let us make the assumption that the aerodynamic pitching moment M_a is approximately a linear function of α . Then the computer loop as shown behaves as a mass-spring system with a natural frequency which we shall denote by ω_p . This is just the approximate transient frequency of the vehicle pitching dynamics under these flight conditions.

By means of the method of Z-transforms, such as is used in analyzing sampled data systems, it can be shown that the computing loop in Figure 4 has a transient frequency ω and damping ratio ζ (fraction of critical damping) given approximately by¹

$$\omega = \omega_p \left(1 - \frac{\gamma}{12} \omega_p^2 T^2 \right),$$

$$\zeta = -\frac{3}{4} \omega_p T, \quad T < \frac{1}{\omega_p} \quad (2.1)$$

¹ Howe, R. M., Error Analysis of Combined Analog-Digital Computer Systems, Information and Control Engineering Program, The University of Michigan, Ann Arbor, Michigan, May, 1964.

Here ω_p is the ideal oscillatory frequency. Ideally, the damping ratio $\zeta = 0.7$ is the digital cycle time ($1/T$ is the number of computations of M_a per second). The effect of the digital computer cycle time T is second order on the frequency, but is first order on the damping. The computer loop as shown will have a transient which exhibits a fractional growth in amplitude per cycle equal to $-2\pi\zeta$. A more complete simulation of the pitch system would include a slight amount of aerodynamic damping (moment proportional to $\dot{\theta}$), but in any event the damping-ratio error will be approximately that given in Eq. (2.1). For example, if ω_p is 10 radians per second, the digital cycle time T must be in 1 millisecond to have a damping-ratio error less than 1 percent.

The accuracy of the computing loop in Figure 4 can be improved remarkably by updating the angle of attack into the A-D converter by the sum of the time-delay exhibited by the digital computer (t seconds) and the D-A converter ($0.5 T$ seconds on the average, assuming a zero-order hold). Noting that $\dot{\alpha} = \dot{\theta}$ ($\dot{\gamma}$ is negligible), we feed $\alpha + 1.5\dot{\theta}T$ into the A-D converter. Under these conditions one can show that the frequency ω and damping ratio ζ are given by²

$$\begin{aligned}\omega &= \omega_p \left(1 + \frac{13}{24} \omega_p^2 T^2 \right), \\ \zeta &= -\omega_p^4 T^4, \quad T < < \frac{1}{\omega_p}\end{aligned}\quad (2.2)$$

Here the damping ratio error is fourth-order in T , representing an enormous improvement over the result in Eq. (2.1), where we failed to update the analog input to the A-D converter.

Analyses similar to the above can be applied to all-digital computation

² Howe, R. M., op. cit.

of second-order computing loops, where the error in frequency and damping using various numerical integration schemes is determined as a function of iteration period T . Although actual three and six-degree-of-freedom flight equations are much more complicated, those portions of the problem with the highest frequency outputs usually behave approximately like the loop in Figure 4. Thus the simplified analysis as presented here yields valuable insight into the computational speeds required to obtain given accuracy.

Most pure analog elements, such as summing amplifiers, integrating amplifiers, coefficient potentiometers, function-generators, etc., have dynamic behavior in the problem-frequency range which approximates that of a first-order linear system, i.e., with a transfer operator of the form $K(1 + \tau_p)^{-1}$, where τ is the equivalent time constant.³ For typical state-of-the-art analog computer components τ is the order of magnitude of 1 microsecond. In implementing computing loops similar to Figure 4 using analog components exclusively, one can show that the damping-ratio error is approximately given by

$$\zeta \approx \frac{\omega_p}{2} \sum_{i=1}^N \tau_i \quad (2.3)$$

where the τ_i represent, respectively, the time constant of each of the N analog elements around the loop. A typical value for $\sum \tau_i$ would be 10^{-5} seconds, in which case ω_p values up to 2000 radians per second (320 cycles per second) could be handled with less than one percent damping error. For many problems this means that the solution can be run at much faster speeds than real time.

³ Howe, R. M. Design Fundamentals of Analog Computer Components, Chapter 2, D. Van Nostrand, 1961.

3. Axis Systems for Computation of Space and Reentry Trajectories

In writing the translational equations of motion to be solved by the computer, either analog or digital, the forces, including inertial, are normally summed along each of three axes and the resulting accelerations are integrated twice to obtain velocity and position coordinates. The importance of the choice of this axis system is readily illustrated by comparing trajectory computation with the accelerations and velocities referred to flight path axes and conventional body axes. For a near-circular satellite the velocity along the x flight-path axis is relatively constant, and velocity components along the y and z axes are zero by definition. The velocity along the flight path can be computed as a small difference from circular-orbit velocity. If, however, the equations of motion are solved in body axes and the vehicle tumbles, then the components of velocity along the x, y, and z body axes may be either positive or negative and the magnitude of any component may be as great as the total vehicle velocity. Therefore, each velocity component must be scaled for at least twice the maximum flight-path velocity. Furthermore, each velocity component must be capable of changing from maximum positive to maximum negative in the time it takes for half a body revolution. The equivalent artificial acceleration due to the rotating axes can be many times as large as the net gravitational and inertial acceleration acting on the body; hence the true acceleration might be masked by errors in computing accelerations along the body axes. Using the same computer, the flight-path axis computation will obviously be much more accurate than the body-axis computation.

It has been common practice to express the trajectory equations of motion directly in a rectangular cartesian inertial frame with origin at

the center of the earth. In such a coordinate system, it is apparent that the x, y, and z distances must be scaled to range through at least twice the apogee radius from the center of the earth, the x, y, and z velocity components must be scaled to range through at least twice the orbital velocity, and the x, y, and z acceleration components must be scaled to range through at least twice the gravitational acceleration. Since a velocity error of more than a few feet per second cannot be tolerated, it is obvious that great computational accuracy is required to avoid unacceptable error build-up over the integration period of hours or even days, when such unfavorable scaling is used. The classical method of obtaining good scaling of the computation is to write the equations of motion in terms of the elements of the osculating orbit. This "method of variation of parameters" has several serious drawbacks for real time simulation. The equations are more complicated than the usual Newtons' Laws equations. There are a number of bothersome singularities in them, and the results of the computation are obtained in terms of orbit elements, rather than conventional length or angle coordinates, hence require further processing if one wishes to display a trajectory.

A basic objective in selection of axes for the translational equations, then, is to choose the axes to obtain some of the scaling benefits of the method of variation of parameters but to retain direct computation of position coordinates for display purposes. The selection of the reference frame in which the equations of motion are to be expressed requires a compromise between good scaling, simplicity of the equations and convenience of use of the computed results. For best scaling, it is apparent that the reference direction should be aligned with the velocity vector, \vec{V}_p . The equations of motion are somewhat simpler, however, if the reference direction is aligned with the horizontal component of the velocity vector. For orbits of small

eccentricity there is little difference in scaling between the two systems of equations, so the latter reference frame, called the H-frame, has proven to be preferable.⁴

The H-frame is defined as a rectangular cartesian coordinate system, x_h, y_h, z_h with origin at the vehicle center of gravity. The x_h axis is normal to the radius from the center of the earth and points forward in the plane of the motion. The y_h axis is horizontal and normal to the plane of the motion. The z_h axis is along the radius from the center of the earth, positive downward.

Considering the components of the acceleration with respect to inertial space along the x_h, y_h, z_h directions, we obtain the following equations of motion for a vehicle of mass m , velocity components U_h, V_h, W_h ($V_h = 0$ by definition) and external forces X_h, Y_h, Z_h :⁴

$$\dot{U}_h - \frac{U_h W_h}{r} = \frac{X_h}{m} \quad (3.1)$$

$$r \dot{U}_h = \frac{Y_h}{m} \quad (3.2)$$

$$\dot{W}_h = -\ddot{r} = \frac{U_h^2}{r} - \frac{g_0 r_0^2}{r^2} + \frac{Z_h}{m} \quad (3.3)$$

In these equations r is the radial distance from the center of gravitational attraction, g_0 is the gravity acceleration at a nominal distance r_0 , and r_h is the z_h or radial component of H-frame angular velocity.

Note that Eqs. (3.1) and (3.3) can be solved for the in-plane motion

⁴ Fogarty, L. E., and Howe, R. M., "Flight Simulation of Orbital and Reentry Vehicles" - IRE Transactions on Electronic Computer Vol. EC-11, Aug. 1962.

independently of Eq. (3.2). Eq. (3.1) can be rewritten as

$$r\dot{U}_h + \dot{r}U_h = \frac{rX_h}{m}$$

which can be integrated directly and solved for U_h . Thus

$$U_h = \frac{1}{r} \left[\int_0^t \frac{rX_h}{m} dt + r(0) U_h(0) \right] \quad (3.4)$$

In the absence of external force X_h , Eq. (3.4) allows the horizontal velocity U_h to be solved directly as an algebraic function of radial distance r . Thus an open-ended integration of \dot{U}_h to obtain U_h , as would be computed from Eq. (3.4), is avoided and much higher computational accuracy results. The time duration over which sizeable non central-force field external forces X_h exist is relatively short (e.g., thrusting and reentry) and the open-ended integration in Eq. (3.4) gives no problem. Actually, Eq. (3.4) is just the statement of conservation of angular momentum.

A further scaling advantage is obtained by writing Eqs. (3.3) and (3.4) in terms of the variation δr in radial distance from the fixed mean radius r_0 and the variation δU_h in horizontal velocity component from the circular orbit velocity U_{h_0} for radius r_0 ($U_{h_0} = \sqrt{g_0 r_0}$). Thus we let

$$r = r_0 + \delta r \text{ and } U_h = \sqrt{g_0 r_0} + \delta U_h \quad (3.5)$$

Rewriting Eq. (3.3) in terms of δr and δU_h , we obtain

$$\delta \ddot{r} = \frac{2\sqrt{g_0 r_0} \delta U_h + (\delta U_h)^2}{(r_0 + \delta r)^2} - \frac{Z_h}{m} \quad (3.6)$$

For near circular satellite orbits the net radial acceleration $\delta \ddot{r}$ is the small difference between gravity acceleration $g_0 r_0^2 / r^2$ and centrifugal acceleration U_h^2 / r . The first term on the right side of Eq. (3.6) represents this difference directly and hence allows much more favorable computer scaling. In fact, Eqs. (3.4) and (3.6) can be solved with satisfactory accuracy using an analog computer, whereas equations based on more conventional coordinate systems are completely unsuitable for analog solution.

Consider, for example, a low eccentricity orbit with the analog computer scaled to allow a range in δr of ± 80 statute miles. We assume a pure central force gravity field with no other external forces.⁵ Several typical analog solutions starting with the vehicle at perigee are shown in Figure 5. For the case where the initial perigee altitude is at 16 miles the first apogee is within 200 feet of the correct value of 146.5 miles and the second perigee is within 200 feet of the initial value, indicating orbit closure to that accuracy.

Also shown is a case representing, ideally, injection into a circular orbit. The computer solution, blown up by a factor of 200, is shown in the figure and indicates that the altitude holds to within 200 feet of the initial value over one orbital distance. The results in Figure 5 were computed at 100 times real time. Comparable results were obtained in real time and at 10 times real time. In the computer circuit used for these recordings the horizontal velocity deviation δU_h was represented to allow a full-scale

⁵ Fogarty, L. E., and Howe, R. M., op. cit.

excursion of $\pm U_{h0}$ (corresponding to full circular-orbit velocity) even though the actual range in δU_h in the solution shown in Figure 5 is a small fraction of this. Similarly, W_h was scaled to a maximum of $\pm U_{h0}/5$ even though the actual range for the near-circular orbits shown in much smaller. This was to allow for utilization of the same scaling in the computation of ascent and reentry trajectories. Despite this unfavorable scaling for the near circular orbit case, the results using the H-frame coordinates appear to be quite favorable. The H-frame has proven to be extremely advantageous for digital computation, too.

In the above example the angular momentum integral was used to compute horizontal velocity directly, as indicated in Eq. (3.4). One can utilize conservation of energy as a constraint, too.⁶ In this scheme the total energy, potential and kinetic, as determined from the position and velocity coordinates, is subtracted from the known total energy as computed from the initial energy plus the time integral of the energy rate of change due to external forces. This difference defines the energy error ϵ . A term proportional to $\epsilon \dot{r}$ is then added to the right side of Eq. (3.6) to drive $\delta \ddot{r}$ in such a direction as to make $\epsilon = 0$.

The effectiveness of the use of energy constraint is illustrated by considering the analog solution of a highly-eccentric satellite orbit. Dimensionless radius $\rho = r/r_0$ is shown as a function of dimensionless time τ in Figure 6, where the starting perigee = $0.12r_0$ and the resulting apogee should be $1.88r_0$. In this case the initial horizontal velocity $U_h = 3.96U_{h0}$ which should yield a minimum horizontal velocity at apogee of $0.252U_{h0}$. The analog computer exhibited the periodic solution shown in Figure 6 with a

⁶ Fogarty, L. E., and Howe, R. M. Axis Systems for Analog and Digital Computation of Space and Reentry Trajectories, Application Report, Applied Dynamics, Inc., Ann Arbor, Michigan, September, 1963

measured apogee of $\rho = 1.877$ compared with the ideal value of 1.880 and a horizontal velocity at apogee equal to $0.256U_{h0}$ instead of the ideal value of $0.252U_{h0}$. Both results agree with the corresponding theoretical values to the order of 0.1 percent of full scale, which is reasonable considering that the required multiplications were carried out using quarter-square multipliers with accuracies of approximately 0.05 percent.

Figure 7 shows a number of cycles with the energy-correction term removed from the circuit. The resulting solution decays slowly with time. After some 75 orbits the energy correction was repatched to the \ddot{r} integrator, with the result that the solution returns within one cycle to its correct amplitude.

As a final example of space-vehicle trajectories, consider the simulation in three dimensions of a lifting reentry vehicle. The problem was set up on an analog computer using the H-frame equations as described earlier. The three dimensional equations were solved for a number of different bank-angles, ϕ for fixed ballistic coefficient values, and for fixed lift-to-drag ratios L/D . A typical recording of altitude versus downrange distance is shown in Figure 8. Figure 9 shows a plot of altitude L versus longitude λ for a nominal equatorial trajectory, and a number of additional trajectories, each with a different fixed bank angle.⁷ Although these computer runs were made using an x-y plotter (approximately 800 times real time) the problem was also solved in repetitive operation at 80,000 times real time and the different values of bank angle were set for each trajectory using a sample-hold circuit driven by a low frequency sawtooth wave. The result, when displayed as latitude L versus longitude λ on the face of a cathode-ray oscilloscope, appears as a

⁷ Fogarty, L. E., and Howe, R. M., Op. Cit.

more-or-less continuous picture similar to Figure 9. If the L/D ratio is now varied slowly, one can sweep out very quickly the footprint of possible landing points for the lifting reentry vehicle.

It should be noted that solution of lifting reentry trajectories at these high speeds requires analog computing components of considerable bandwidth, since the trajectory oscillations near the end of the reentry have a frequency of approximately 1 kilocycle.

4. Summary

We have seen that the simulation of space-vehicle systems poses sizable computer problems, depending on the scope of the particular simulation being undertaken. Many simulation problems, including some real-time problems, are amenable to all-digital solution. Other simulation problems are more suitable for all analog mechanization. There is a sizable class of problems which is best solved on hybrid computer systems, although the programming complexity in such a mechanization should not be overlooked. Whatever type of computer system is used, it is important to choose appropriate axis systems in writing equations of motion so that required computer precision and speed is minimized. Long term future trends in space-vehicle simulation will probably see digital computers used more for real-time simulation of computer problems, whereas analog computers will be used for faster-than-real-time problems, such as trajectory optimization studies and predictor displays. Combined analog-digital systems will probably be used less for real-time simulation but very much more for optimization and other design studies, where the speed of the analog and the precision and function-storage capability of the digital can be combined to advantage.

-XII-16-

Single Precision Error Vs. Double Precision Error
(Runge-Kutta Fourth Order)

Step Size 107 Seconds

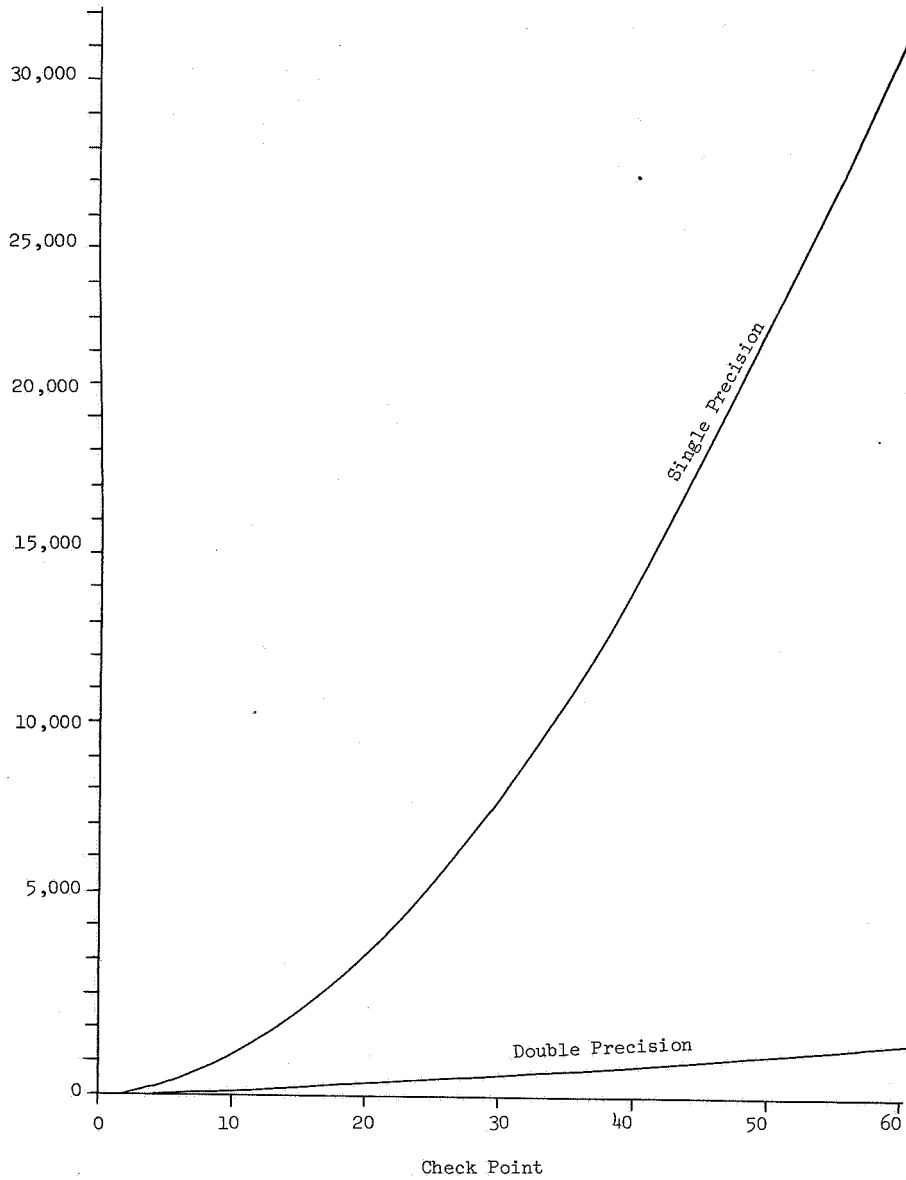


Figure 1. Single precision versus double precision error in computing an earth-moon trajectory

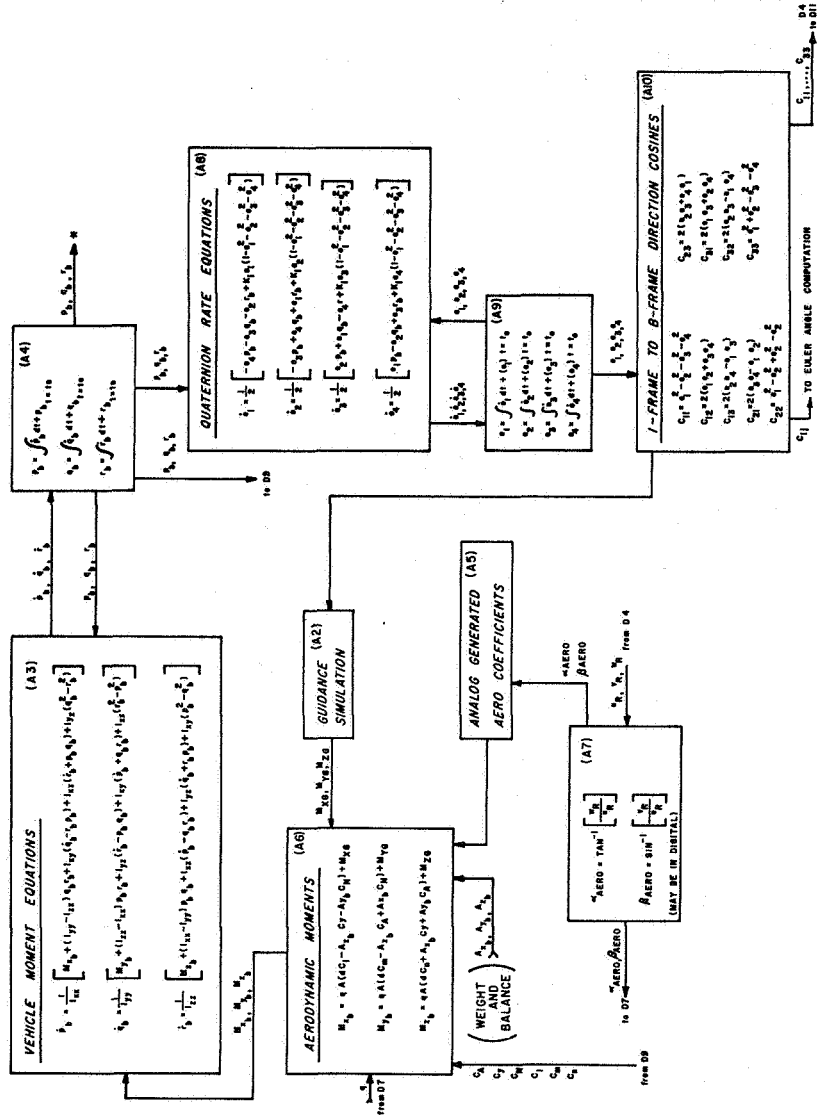


Figure 2. Equations to be solved on the analog computer for a hybrid six-degree-of-freedom space vehicle simulation.

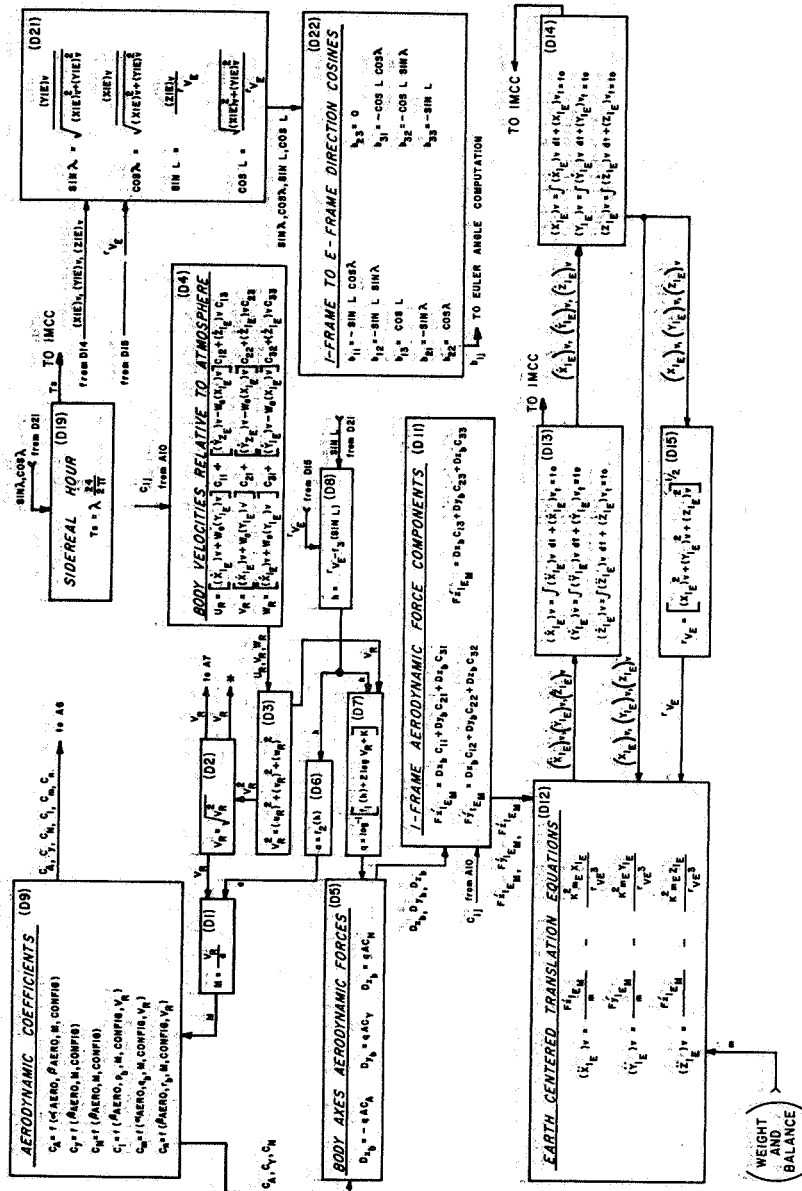


Figure 3. Equations to be solved on the digital computer for a hybrid, six-degree of freedom simulation.

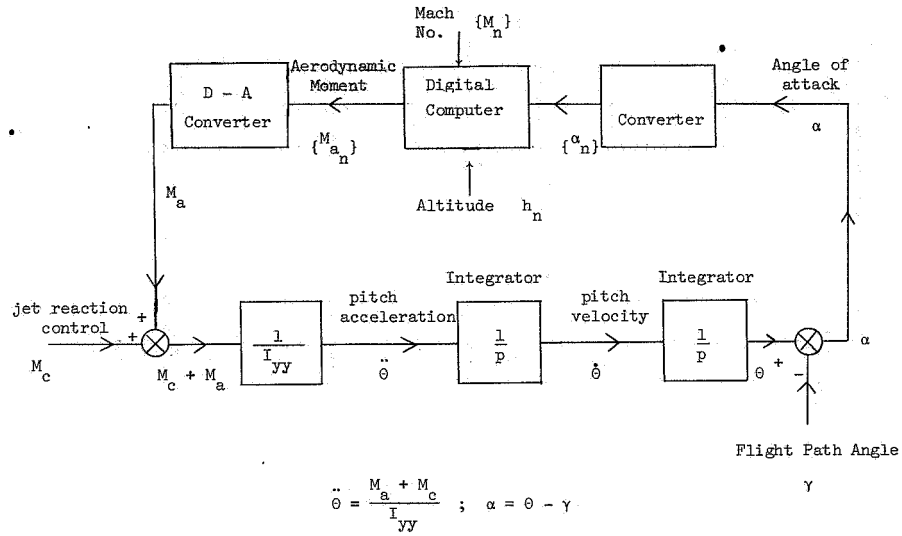


Figure 4. Block diagram of hybrid computing loop for calculating pitch angle θ .

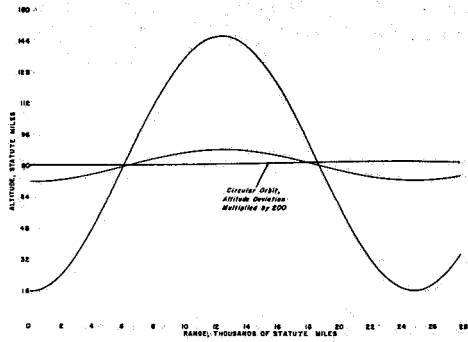


Figure 5. Analog solutions for low-eccentricity orbits.

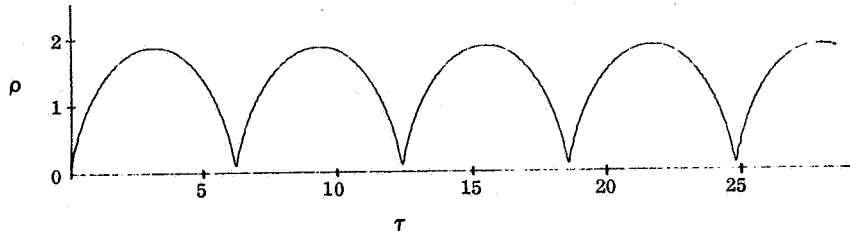


Figure 6. Typical solution for a highly-eccentric orbit.

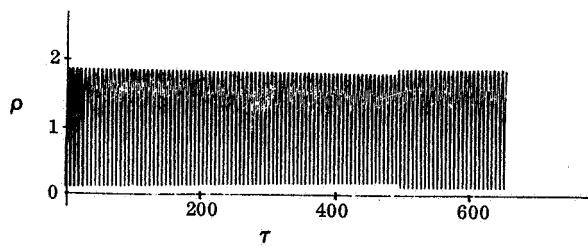


Figure 7. Periodic solution with no energy constraint initially. Energy constraint is added after about 75 cycles.

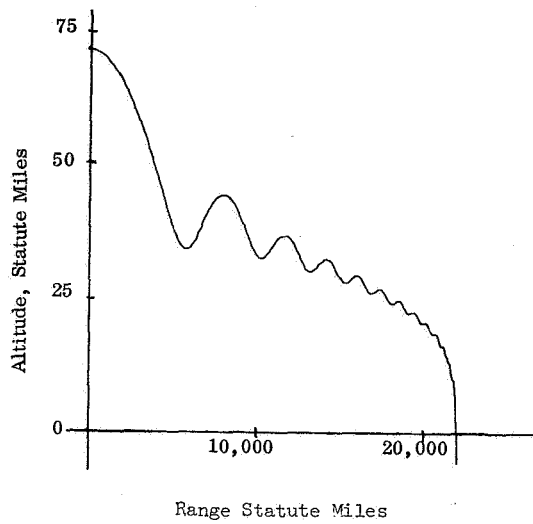


Figure 8. Typical reentry profile, L/D = 2.0

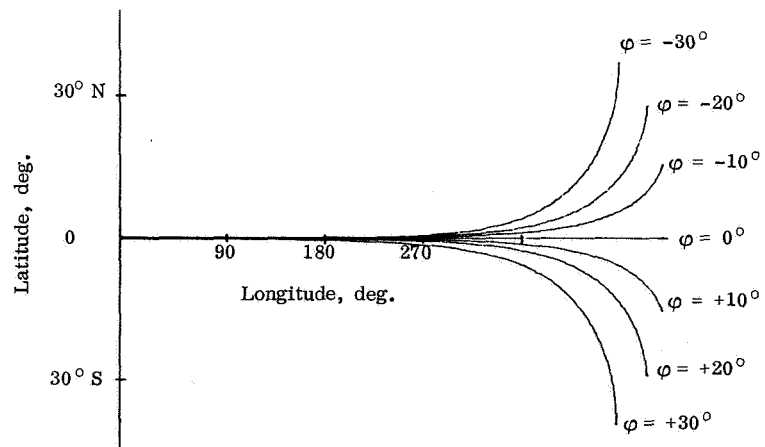
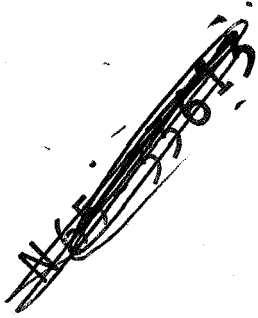


Figure 9. Typical impact footprint, L/D = 2.0



DISCUSSION OF EXISTING AND PLANNED SIMULATORS FOR SPACE RESEARCH

by

A. W. Vogeley

NASA - Langley Research Center

SUMMARY

Man is an essential element in many of our space programs. In exploring the unknown only man can observe the unpredictable or react intelligently to the unexpected. Not only do we need man in space as an explorer and observer but we also need his capabilities in the management and control of our missions in order to improve their reliability and chances of success. To take full advantage of man's unique attributes we must study his capabilities, define them, and then using this information design our space systems so that he becomes an integral part of the mission. These objectives are accomplished through the use of manned flight simulators.

This paper discusses a variety of manned flight simulations that are particularly applicable to space research. Most of the simulators described are in operation, but are relatively new. Some of the simulators are still under construction or in the planning stage. A few of the simulators are nonexistent.

- that is, although the research problems have been defined no satisfactory methods for adequately simulating the problems have been found. The facilities described have been selected either because they present new and novel methods for simulating some of the peculiar aspects of the space environment or because they contain unique construction or operational features that may have application to other simulation facilities.

BASIC SIMULATOR COMPONENTS

Manned flight simulators are designed to study the human problems of how to manage and control our aircraft or space vehicles. In these facilities we try to simulate realistically those features of the environment which affect man's senses. These sensory inputs - what a pilot sees, feels, or hears - are used in flight simulators as sources of information by the pilot and govern his decisions and actions. Other inputs - environmental stresses - which normally have little information content and therefore do not have an immediate impact on pilot performance can, under certain circumstances, have an important effect and must then be included in a meaningful simulation. For this reason, some flight simulators must include these stresses and examples of these will be presented. On the other hand, manned simulators which are primarily concerned with the physiological effects of these stressful inputs are not the main subject of this paper.

The interrelationships of the various elements which may be required in a flight simulator are shown in figure 1, prepared by Mr. John Dusterberry of the NASA Ames Research Center. As this figure shows, the main objective of a flight simulator, regardless of what elements are included in or omitted from

the main "box", is to study pilot performance in the accomplishment of any given task. To accomplish this task the pilot must operate his vehicle through his control system. The pilot cannot, however, operate blindly. He needs information in order to make his decisions and to observe the consequences of his actions. The pilot may obtain this information through his instruments, from his view of the outside world, or from motion cues. Finally, as shown, the pilot's "basic" capability or efficiency may be changed, either abruptly or gradually, as a result of the effects upon him of environmental stresses.

These are the basic components, or physical characteristics - present in varying degree - in all flight simulators. How these components are mixed and used determines the success or failure of simulation research.

THE ART OF FLIGHT SIMULATION

Research simulation is much more an engineering art than it is a science. An important ingredient for successful research simulation is timeliness. This is achieved primarily through foresight in anticipating and then defining problem areas, inventiveness and ingenuity in the rapid development of new simulation techniques, and in the efficient conduct of the research program. The value of the results is determined in part by the proper choice of the simulation hardware which is used, but mainly by the proper qualification of the conclusions which are obtained. These conclusions to be valid and worthwhile must combine both quantitative results and, of greater importance, qualitative results in the form of pilot opinion. In addition the conclusions often reflect the inputs from other disciplines such as from psychologists, physiologists, control systems engineers, etc. Because of the importance of these qualitative aspects, much of the value of simulation

research is determined by experience. This experience must not only be individual in nature but must be experience of the group because of the interdisciplinary aspects of simulation work. This group experience is evident by close cooperation and coordination and by a clear understanding by all personnel of the problems involved in the research work.

In many respects successful research simulation is analogous to successful production of a Broadway play or a Hollywood movie. Referring back to figure 1 we can visualize the flight simulator as being analogous to the theater itself and the research personnel to the production company. It is the task of the production company to translate the author's (research scientist's) story (task) into a performance which the public or program office will buy. It is the responsibility of the director (project engineer) to mold all of the elements in his production to achieve the maximum result. He will call upon his set designers to provide the visual displays. He will ask his special effects men to create unusual effects such as simulated lunar gravity or weightlessness. He will use script writers to prepare his research and computer programs and he will employ prop men and technicians to provide the other facilities necessary. He will combine these facilities in varying degree depending upon the specific story he is directing. He will use a capable crew and a competent supporting cast headed by an experienced and talented "star." During rehearsals both the director and the "star" will be their own severest critics. They will continuously assess and improve the performance to try to get the most out of what they have available.

I do not want to continue this analogy much further except to say that experienced direction and a talented cast can produce an excellent performance with limited facilities. On the other hand, the best story and the best facilities cannot produce a good performance under poor direction or inexperienced

acting. One common mistake made in simulation research is to use engineers with some flight experience as test subjects rather than to use experienced experimental research test pilots. It is not sufficient to simply perform in the simulation. It is necessary to bring experience and training to bear so that the performance can be interpreted and valid conclusions can be reached which properly take into account the limitations that are always present in any simulation equipment.

Just as the theater has developed a course of action in producing plays, research simulation has also evolved an efficient procedure which is illustrated in figure 2. This figure diagrams the research simulation process only at the task level. It should be realized that this same process may be carried back to the mission phase level and, in some instances, even back to the entire mission level. The process starts at the upper left with the selection of a research task or problem. The problem is examined and in this process may be broken down into subtasks, as shown. After each subtask has been defined, a choice of the most appropriate simulation facilities available is made. In some instances it is necessary to study a problem with more than one simulator. After the simulator has been selected the research program is conducted and both quantitative and qualitative results are obtained. These results are weighed and combined to form preliminary conclusions. These preliminary conclusions, in general, require that adjustments or changes be made to the basic simulation hardware or to the research program or even to the task definition. When this cycle has been repeated sufficiently so that everyone is satisfied with the conclusions, these are issued as research results. Sometimes, as shown, these conclusions combine the results of separate simulations which may have been necessary. These research results are used as inputs to the system design. Often these inputs are found to be incompatible

with the inputs that have been obtained by simulations of other tasks or phases of the mission. In this event compromises and changes have to be made which form another loop that starts the research process over again. This cycle, in turn, may be repeated several times until an integrated system design is evolved. When this point is reached this particular research program is essentially completed. At some later date validation, hopefully, of the simulation results is obtained when the actual mission is accomplished. The flight information which is eventually obtained provides valuable background information for future simulations and is an important input to the experience which is necessary for the successful conduct of research simulation. Actual flight results provide the only valid information upon which to base changes in the simulation techniques that will improve the quality of future simulations.

TYPES OF SIMULATORS

Because each research problem generates its own peculiar simulation requirements, many kinds and varieties of simulators have been developed. Because of this great variety a number of attempts have been made to classify simulators. Although a certain amount of order has been established, these efforts have not been completely successful because, to completely describe the various simulators, it is generally found necessary to establish about as many classifications as there are simulators. However, a number of major categories have been proposed and some of the more commonly used descriptive terms are listed in figure 3. I shall not go into a detailed discussion of the pros and cons of these various types because a number of excellent papers have been published which discuss various types of simulators and the advantages

and disadvantages of one kind with respect to another. Rather I would like to confine my discussion of simulator types to a few general remarks.

Most research simulators are ground-based, fixed-base, special-purpose simulators. These simulators are represented in figure 1 by the small interior "box." They generally consist of a simple chair and controls, a few essential flight instruments, and control system and vehicle dynamics generated by an analog computer. Such simulators are readily set up, operated, and maintained. They are extremely valuable for a preliminary "look" at problems. System parameters and initial test conditions can be readily varied through the analog computer, making it possible to study both normal operations and also a great variety of emergency situations. The results from these simulations, however, must be properly qualified. The simplicity of the setup, the lack of motion cues, or the absence of external visual cues may be extremely important with regard to the interpretation of the results and must always be kept in mind. When properly used, the great flexibility of these simulators makes them very valuable for research work.

Developmental simulators for a specific vehicle often start out as simulators of the kind I have just described. However, as the development proceeds other tasks and instruments are added, and also the analog computer is gradually replaced by actual hardware components. While these simulators start with the flexibility of a research simulator their evolutionary process gradually eliminates this flexibility. On the other hand, the simulator becomes more and more an exact replica of the vehicle that is under development. Most developmental simulators reach the end of their useful life when the vehicle finally goes into production and all of the hardware kinks have been eliminated. A shining exception to this situation exists in the case of the X-15 developmental simulator. This simulator is being used daily at the Flight Research Center as a training aid for the research pilots to prepare them for upcoming

research flights.

Procedural and full-mission simulators also duplicate, down to the smallest detail, the characteristics and problems of an actual vehicle. This duplication is primarily with respect to the pilot or crew. Unlike the developmental simulator it generally does not contain actual hardware components but simulates the operational characteristics of the hardware by means of a very detailed computer setup. These simulators do not go through an evolutionary process such as in the case of developmental simulators. In general, these simulators are built toward the end of the research and development program when most of the details of the system have been finalized. These simulators are also extremely inflexible in terms of research use, since it is generally difficult to make major or rapid changes to vehicle or mission characteristics. However, flexibility of a sort is provided which allows a great variety of emergency situations to be simulated. The sole purpose of these simulators is to provide pilots and crews with training and experience in the detailed operation of the vehicle system.

Many research problems require that motion cues be provided to the pilot. When this is done we have, of course, arrived at moving-base simulators. A common example of a moving-base simulator is the well-known piloted centrifuge. Also in many instances it is extremely important to study the influence of out-the-window, external visual displays. Use of external visual information by the pilot and crew is becoming of great importance in space research. It is recognized that for long-duration missions complete reliance cannot always be placed on instrument indications. The great complexity and high sophistication of the electronics that are required to provide the instrumentation bring up problems of reliability. As a consequence, great effort is being put into the development of simplified guidance and control techniques, using sources of

information such as motion or visual cues which are independent of the electronic equipment, as replacement or backup procedures in order to increase mission reliability. There are many techniques available for providing motion and visual cues but I will not describe them here since this subject is discussed in a separate paper in this conference.

When several part-task simulations are combined we tend toward the development of whole-task simulators. Whole-task simulators are often required in research in order to study the compatibility problems between tasks that may in actual missions take place either in quick succession or even in parallel.

Since research problems often require either whole-task simulation, motion cues, or visual cues in an infinite variety of possible combinations it is sometimes proposed to build general-purpose simulators so as to achieve the adaptability and flexibility that are so highly desirable in research. General-purpose simulators, in the limit, try to provide all of the facilities that are diagrammed in figure 1. While in principle general-purpose simulators would seem to be attractive, they do suffer from two major faults. In the first place, since they are conceived for general purposes they are not designed with a specific problem or objective in view. As a result they often are not able to handle any specific problem with the fidelity that is perhaps necessary and obtainable with a special-purpose simulator. Secondly, since most research problems do not require the simultaneous use of all of the capabilities of a general-purpose simulator, a general-purpose simulator operates almost all the time at less than maximum efficiency. For these reasons, few general-purpose simulators have been built. Generally, it is more desirable to have a few well-chosen, small facilities available. Most simulators, therefore, are originally constructed for specific, special purposes. This is not to say that special-purpose simulators have limited utility.

It is invariably the case that today's special-purpose simulator, designed and built to study today's special problem, becomes tomorrow's special-purpose simulator for tomorrow's problem through generally minor modifications. Few instances are known where special-purpose simulators have lost their usefulness and had to be abandoned.

An overwhelming percentage of research simulators are ground based. In certain situations, however, ground-based simulators can never provide the fidelity required. These situations generally are concerned with problems of landing and touchdown. These problems are best handled by flight-test simulators. Ground-based simulators, no matter how sophisticated they may become in providing visual or motion cues, will probably never be able to realize the degree of realism and be able to generate the motivation that is required to obtain adequate answers in these situations. This can be obtained only by putting the pilots in a true flight environment.

It would seem to be a simple matter to distinguish between ground-based and flight-test simulators. However, later on I shall describe a simulator which is rather difficult to classify as one or the other. I mention this now only, in concluding this short discussion of various types of simulators, because further discussion of the subject is best handled by a discussion of various problem areas and then describing the simulators that are being used and are best suited to study of these problems.

MANNED-SPACE-MISSION PHASES

The major phases of a typical manned space mission are shown in figure 4. Each mission begins with an earth launch, followed by the establishment of an earth orbit. After establishment of earth orbit, orbital operations take place.

These operations may consist of nothing more than final checkout before injection into an interplanetary trajectory. In our more ambitious follow-on missions, however, these operations may involve rendezvous, docking, orbital assembly, extra-vehicular activities, etc. The midcourse and return portions of interplanetary flights will require from days to perhaps months of operations involving relatively little activity. Activity will be restricted primarily to navigation, onboard maintenance, and perhaps onboard simulations in order to maintain proficiency in accomplishing end-point maneuvers. When the planetary objective is reached, the mission phases involved may include orbit establishment, letdown and landing, surface operations, launch, rendezvous and docking, and, finally, injection into a return trajectory. Upon return the phases which terminate the mission include reentry, landing, and touchdown. Each of these various phases have their own special problems and requirements; and for this reason special-purpose simulators are used to study these problems.

EARTH LAUNCH AND REENTRY

Earth launch and reentry are characterized by a gradual build up in longitudinal acceleration. In launch the acceleration may reach as high as 6g or 8g, and in reentry the acceleration level may approach 12g to 16g. In the case of launch this longitudinal acceleration profile may be repeated two or three times at each system stage. Lateral and angular accelerations will also be present and these may reach significant magnitudes and frequencies. Although to date all earth launches have been under automatic control, there is growing interest in the development of manual-control techniques. Manual control of large conventional boosters may offer benefits in reliability and

also in safety when emergency situations arise. Manual control may also assume great importance when we consider maneuverable and recoverable boosters.

One type of simulator which has been used extensively in studying launch and reentry problems is the human centrifuge. An example of this type of simulator which has been used effectively is the Ames five-degree-of-freedom simulator shown in figure 5. Although the g-level obtainable is somewhat restricted (6g at full speed) this level has been adequate for many situations. High angular accelerations are available (18 radians per second per second in roll, 6 in pitch, and 12 in yaw) and are adequate to duplicate most vehicle performance. The Ames centrifuge is unique in that gimbal motions are powered by chain-belt drives attached to sprockets mounted to the motor shaft and moving around the rubber-based gimbal rings. One of these drives is shown in figure 6. This type of drive eliminates gear weight, noise, and backlash and allows for the use of a high-speed low-weight motor. Another novel feature is that the centrifuge arm is driven by an endless steel cable wrapped around the outside of the track and picked up and laid down by pulleys mounted on the arm. This drive is shown in figure 7. The advantage of this type of drive is that it avoids the cost of large gears or high-torque electrical motors. On the other hand, the track noise has been somewhat of a problem since it furnishes an unwanted cue to the pilot which informs him of the application of a side force before he feels the force itself. Efforts are being made to reduce this track noise to lower levels. These centrifuges are very worthwhile in the development of cockpit layouts, controllers, and pilot restraint systems so that the pilot can perform adequately under these acceleration conditions. When this equipment is properly designed it has generally been found that adequate pilot performance can be maintained under practical mission conditions.

Centrifuges are furthermore often useful in uncovering unusual problems. One recent launch simulation, for example, showed that a particular structural frequency was such as to make it impossible for the pilot to read his instruments.

RENDEZVOUS

Visual rendezvous may start as far as 200 miles from the target and terminates as the target acquires some size and detail. One simple, economical simulator which was assembled 4 years ago to study visual rendezvous problems is shown in figure 8. This facility is the Langley inflatable planetarium. This planetarium is nothing more than a surplus Air Force inflatable radar dome. Although the interior is dark and unpainted, this surface has been found to be satisfactory since it is required only to be able to see a star field, a point light (probably flashing) for the target, and perhaps an horizon for gross orientation. When the pilot is dark-adapted, these visual features are clearly discernible. This type of projection surface, however, would not be adequate for the simulation of approach or landing where more detail must be displayed. A typical hardware arrangement used in visual-rendezvous studies is shown in figure 9, which shows a setup made for studying Gemini/Agna problems. The mock-up Gemini half-cockpit can be seen and behind it the equipment for generating the visual displays. This equipment consists of a star-field projector, a target projector, and an horizon projector. These are mounted on a surplus Nike-Ajax radar drive, modified by the addition of a third axis. We have, incidentally, found this radar drive to be readily adaptable to analog simulation work and it is being used not only here but in a number of other simulations at Langley. A closeup view of a typical star-field projector is shown in figure 10.

The projector operates on a concept developed by Spitz. It consists of a point-light source reflecting off a centrally located highly reflective sphere which directs the light outward through the many holes representing the stars. The size of the holes is varied to vary star magnitude. The star images are brought to a focus on the inside of the planetarium by lenses glued to the surface of the projector. Simple geometric relationships such as the size of the projector and the diameter of the projection sphere govern the focal length required for these lenses. Although this type of projector does not have the precision required for the study of navigation problems it is very adequate for pilot control problems such as rendezvous where the star field is primarily used as an attitude reference.

DOCKING

Docking operations are considered to start when the pilot first can discern vehicle target size and aspect and terminate, of course, when soft contact is made. One unusual docking simulator that has been in operation at Langley for the past year is shown in figure 11. This Rendezvous Docking Simulator employs full-scale mock-ups of spacecraft cockpits mounted in gimbals. This facility is unique in that the entire gimbal assembly is supported by a cable system attached to an overhead crane. The unique cable arrangement effectively rigidizes the system and avoids pendulous motion so that correct linear motions can be commanded. A novel lightweight hydraulic-pneumatic counter-balance system is used to support the gimbal assembly. This permits the use of a relatively small vertical-drive motor which has only to overcome the inertia of the hanging system. The facility enables simulation of the docking operation from a distance of 200 feet to actual contact with the target. A full-scale mock-up

of the target vehicle is suspended near one end of the track. An Agena target used in recent studies is shown in figure 12. On this we have mounted the actual Agena docking mechanism and also various types of visual aids. We have been able to devise visual aids which have made it possible to accomplish nighttime docking with as much success as daytime docking. Many of the astronauts have flown this simulator in support of the Gemini studies and they, without exception, appreciated the realism of the visual scene. The simulator has also been used in the development of pilot techniques to handle certain jet malfunctions in order that aborts could be avoided. In these situations large attitude changes are sometimes necessary and the false motion cues that were generated due to earth gravity were somewhat objectionable; however, the pilots were readily able to overlook these false motion cues in favor of the visual realism.

Another docking simulator which uses closed-circuit television techniques is also in operation at Langley and is shown in figure 13. In this Visual Docking Simulator a small-scale model of the target vehicle having three degrees of freedom is mounted in front of the television camera. The model translates along the camera axis and rotates in response to the pilot's control inputs and the analog computer. The image of the target is transmitted by the TV system to a two-axis mirror above the pilot's head and is projected in correct size on the inside of a 20-foot-diameter spherical screen. Through the added action of this mirror system all six degrees of freedom are simulated. The pilot and crew are seated in a full-scale mock-up of the Gemini cockpit. The small scale of the target model and the loss in resolution through the TV system made the visual realism of this simulator considerably poorer than the realism that was achieved in the Rendezvous Docking Simulator. On the other hand, this simulator did not introduce any false motion cues. This simulator

also has a much larger operating volume than does the other docking simulator. Therefore it is particularly useful in study of such problems as in-close inspection of uncooperative targets, for example. For docking studies the lack of three-dimensionality inherent in these closed-circuit TV systems or other projection-type systems is a distinct handicap. This handicap is reflected in the fact that more training on this simulator was required to reach the same proficiency in docking than with the Rendezvous Docking Simulator.

The Visual Docking Simulator had an extremely wide field of view. Other simulators have been constructed to study docking problems which used small-size viewing screens with CCTV or image-generation systems of the type shown in figure 14. This type of docking simulation, with restricted field of view, places unnecessary restrictions on the pilot since he has to provide more attitude control than necessary in order simply to keep the target in view. Because of this restriction he requires more fuel than necessary and the results of studies with this type of equipment may, in this respect, be misleading.

ONBOARD SIMULATORS

The small field of view available from these types of display systems may be a restriction that will have to be accepted for onboard simulators. Onboard simulators are considered to be necessary for long-duration missions in order to maintain pilot proficiency for the accomplishment of intricate maneuvers either at the mission objective or upon return. The limitations that may have to be accepted for onboard simulators must be carefully evaluated and, if possible, new techniques for overcoming these limitations may have to be devised.

ORBITAL OPERATIONS

Orbital operations, insofar as pilot or crew are concerned, include such activities as extra-vehicular locomotion, orbital assembly, and astronaut retrieval in the event that malfunctions occur. Extra-vehicular locomotion problems are now being studied through the use of in-flight simulators wherein airplanes fly zero-g trajectories as shown in figure 15. At the present time this technique is the only one that we have available which permits six-degree-of-freedom maneuvering. It is severely restrictive, however, in that the period of weightlessness is limited to something less than one-half minute. The initial high-acceleration pull-up and the necessity for securing the test equipment and test subjects in order to withstand the final pull-out are also complicating factors. Perhaps the most serious limitations in this technique are due to the Coriolis forces that cannot be eliminated and to the fact that the reference frame of the experiment is continually shifting because of the airplane pilot's maneuvers in attempting to hold the zero-g trajectory. A better simulation technique to study these types of problems would be highly desirable.

Extra-vehicular locomotion will probably always be accomplished with the astronaut tethered to his vehicle by a safety cable. Should some emergency occur it will be necessary to retrieve the astronaut through this cable. The problem of astronaut retrieval is not simple, as shown in figure 16. If the astronaut is only a few thousand feet from his vehicle and has only a slight lateral velocity with respect to his vehicle when the malfunction occurs conservation of angular momentum during the reel-in process results in very unsatisfactory conditions on contact. In order to avoid these problems much more sophisticated concepts than simple reel-in are required. Unlike the extra

vehicular locomotion problem which is three dimensional the retrieval problem can probably be reduced to two dimensions. In this respect, then, the development of simulators to study this problem may be simpler. It may be possible, for example, to develop small ground-effects machines that can simulate the problem. One type of tethering simulator, on a small scale, is shown in figure 17 as proposed in a recent study contract to Langley on the retrieval problem. A preliminary setup of this type of simulator has been built at Langley and this approach appears feasible.

Orbital assembly may require that astronauts move large masses either through their own efforts or with the assistance of self-contained, readily attachable propulsion modules (small space tugs) which they directly or remotely control. Techniques for realistically simulating these situations are nonexistent. This simulation problem appears even more difficult than the extra-vehicular locomotion problem

LUNAR ORBIT, LANDING, APPROACH, AND TAKE-OFF OPERATIONS

The guidance and control systems for tasks to be accomplished in the vicinity of the moon should be as simple and reliable as possible. Although a number of part-task simulators have been used to study various aspects of lunar operations, it is necessary to have some facility that can study the whole-task problem in order to arrive at an optimum integrated system. For this purpose there is under construction at Langley a new facility called LOLA, which stands for Lunar Orbit Landing and Approach Simulator. This simulator is shown schematically in figure 18 and consists of a pilot's capsule, a closed-circuit TV complex, and models of the lunar surface. There are four models of different scale which permit altitude coverage from 200 miles to 200 feet above

the lunar surface. The models include a 20-foot-diameter sphere, two spherical segments, and one flat section. The models are arranged so that only two camera transport mechanisms and two closed-circuit TV systems are needed to view the four models. A photograph of LOLA under construction is shown in figure 19. The heart of LOLA will be the optical pickup. The system which is currently scheduled for installation is shown schematically in figure 20. The lunar surface is viewed through a single wide-angle 220° lens. This single view is then operated on electronically to provide the various vehicle motions. Midway through the system the single scene is projected on a television screen and viewed by four pickup cameras. These four pickup cameras then, in turn, project their separate views through the four portholes of the space vehicle so that the view from each porthole will correspond to the view that the pilot will see.

Simulators somewhat similar to LOLA are being used or are under construction in industry. A view of what the pilot might see in this type of simulator is shown in figure 21, which pictures the Boeing simulator. This figure, incidentally, also illustrates one limitation of this general class of visual display system. This limitation is the loss in detail and resolution as the model is closely approached. While simulators of this type will be extremely valuable in studying problems where close maneuvering is not required (such as in orbital operations and the initial phases of landing), the lack of detail and the absence of three-dimensional effects preclude the effective use of these facilities for the final landing and touchdown situations. These problems can be studied most effectively through actual flight-test simulators.

Sometimes used in another simulation technique which attacks the problem in a different way from LOLA. Shown in figure 22 is a view of the Ryan simulator. This simulator makes use of a point-light-source projection technique.

As can be seen, the large transparency is hung above the pilot's head. This transparency is driven through a computer in response to the pilot's control inputs so that the scene shifts properly. The scene is projected in front of the pilot on a spherical screen by a point-light source shining through the transparency. This simulator has been used very effectively in the study of helicopter and VTOL problems and could equally well be used in the study of space vehicle problems. It is, however, similar to the other simulators just discussed in being affected by the loss of detail as the scene is closely approached. For this reason this type of simulator is generally used primarily for the initial landing and maneuvering phases and not for actual close-contact problems.

LUNAR SURFACE OPERATIONS

When the astronauts land on the moon they will be in an unfamiliar environment involving, particularly, a gravitational field only one-sixth as strong as on earth. A novel method of simulating lunar gravity has been developed and used at Langley to study the problems of how to walk, run, or jump on the moon. The Lunar Walking Simulator is shown in figure 23. As you can see, the subject is supported by a puppet-type suspension system at the end of a long pendulum. A floor is provided at the proper angle so that one-sixth of the subject's weight is supported by the floor with the remainder being supported by the suspension system. This simulator allows almost complete freedom in vertical translation and pitch and is considered to be a very realistic simulation of the lunar walking problem. For this problem this simulator suffers only slightly from the restrictions in lateral movement it puts on the test subject. This is not considered a strong disadvantage for ordinary walking problems

since most of the motions do, in fact, occur in the vertical plane. However, this simulation technique would be severely restrictive if applied to the study of the extra-vehicular locomotion problem, for example, because in this situation complete six degrees of freedom are rather necessary. This technique, in effect, automatically introduces a two-axis attitude stabilization system into the problem. The technique could, however, be used in preliminary studies of extra-vehicular locomotion where, for example, it might be assumed that one axis of the attitude control system on the astronaut maneuvering unit may have failed.

ROTATING SPACE-STATION OPERATIONS

The simulation technique just described can be applied to the study of locomotion in a rotating space station. A rotating space-station simulator concept is shown in figure 24. As may be seen the test subject is hung in the sling support and suspension so that he is initially in a zero-g condition. Then the entire suspension system and the space station are rotated so that artificial gravity is supplied through centrifugal force.

LUNAR LANDING

Ground-based simulators are not very satisfactory for studying the problems associated with the final phases of landing and for this reason it is preferable to go to some sort of flight-test simulator. One research facility designed to study the final phases of lunar landing is now in the checkout phase at Langley. This Lunar Landing Research Facility is shown in figure 25. Because of its large size it is difficult to get a good picture of this facility so an artist's conception is presented. The facility is an overhead crane structure

about 250 feet tall and 400 feet long. The crane system supports five-sixths of the vehicle's weight through servo-driven vertical cables. The remaining one-sixth of the vehicle weight pulls the vehicle downward simulating the lunar gravitational force. During actual flights the overhead crane system is slaved to keep the cable near vertical at all times. A gimbal system on the vehicle permits angular freedom for pitch, roll, and yaw. The facility is capable of testing vehicles up to 20,000 pounds. A research vehicle, weighing 10,500 pounds fully loaded, has been constructed and is shown in figure 26. This vehicle is provided with a large degree of flexibility in cockpit positions, instrumentation, and control parameters. It has main engines of 6,000 pounds thrust throttleable down to 600 pounds and attitude jets. This facility will be able to study the problems of the final 200 feet of lunar landing and the problems of maneuvering about in close proximity to the lunar surface. It will not, however, be able to study the important problems of transition from the letdown operation to the final touchdown phase. With regard to type of simulator, this facility may be described as five-sixth ground-based and one-sixth flight-test. It will be subject to the same vicissitudes of weather conditions as flight-test vehicles and also it must be designed with safety precautions to counter the hazards that exist in all types of flight research.

Another simulator for studying the lunar landing problem is in the final assembly and checkout stage at the NASA Flight Research Center. This simulator is shown in figure 27. The vehicle is being built by Bell Aerosystems and contains a gimbaled jet engine which provides an upward force along the gravity vector that equals five-sixths of the vehicle's earth weight. Rocket engines are used to decelerate the vehicle, provide stability and damping, and for maneuvering. This simulator will be extremely valuable for investigating

problems associated with the final three to four thousand feet of the lunar landing operation. This will take the operation through the very critical transition phase from final approach to actual soft letdown to the lunar surface. As is the case with every flight-test simulator, this vehicle suffers from a certain amount of inflexibility in that it is difficult to make configuration changes. It is also, of course, subject to the usual hazards of flight-test research and to the extraneous factors of wind and weather conditions which do not exist on the moon.

EARTH LANDING

The problem of studying earth landings, particularly with some of the rather unconventional configurations that are now being proposed makes the use of flight-test simulators necessary. Lightweight glide vehicles of the type shown in figure 28 have proved extremely valuable in studying some of the problems that arise in landing these unusual space vehicles. These types of simulators have proved to be low cost and have required a relatively short time to put into operation. This technique of building manned flying models of space vehicles for study under actual flight conditions is now being extended, and somewhat more sophisticated vehicles are being built. Several are now under construction by the Northrop Corporation. They will be launched from a B-52 at high subsonic speeds. Installation of small rocket engines in order to drive them to supersonic speeds is also being considered. These vehicles are being built at a cost which compares very favorably with the more complex ground-based simulators and will undoubtedly do a better job of simulation.

WHOLE MISSIONS

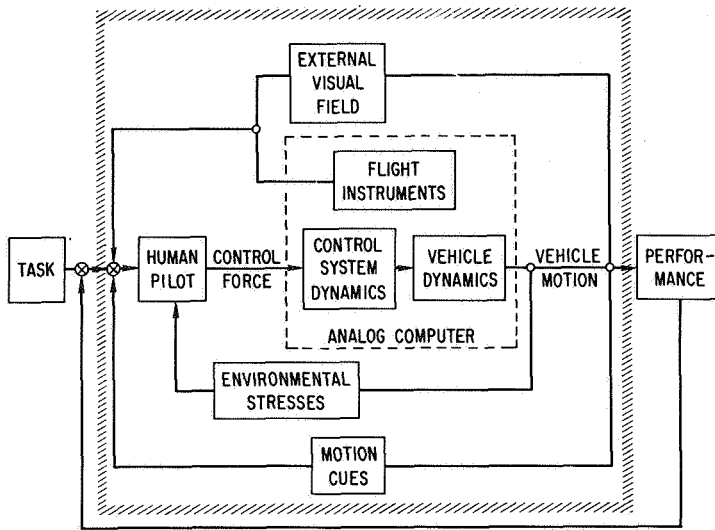
One type of whole-mission simulator is being planned by the Ames Research Center and is called the Space Flight Guidance Research Facility. This is a research simulator designed to study the whole-mission problems taking into account many of the physiological factors that may be of importance. As such it is being designed primarily as a centrifuge. A photograph of the model of the centrifuge is shown in figure 29. The centrifuge will provide the capability of simulating the acceleration conditions during launch and reentry. During midcourse operations the centrifuge will be brought to rest next to an adjacent facility which will allow the crew to perform midcourse navigation and control tasks under realistic visual conditions. The unique feature of this facility will be that the gimballed three-man cab will be provided with life-support equipment so that long-duration missions can be simulated in real time. As a research facility this simulator will be provided with a great deal of flexibility through the capabilities of the centrifuge, the life support system, the navigation and guidance equipment, and the associated computer complex.

Another type of whole- or full-mission simulator is shown as an artist's concept in figure 30. This simulator, designed primarily for astronaut training purposes, is being constructed at the Manned Spacecraft Center in Houston. As you can see, this Apollo Mission Simulator will contain a complex of visual display systems to provide realistic out-the-window views for the various phases of the mission. The Apollo systems and equipment will be simulated with the aid of a large complex of computing equipment to provide a realistic operation environment to the crew. As is characteristic of these types of full-mission simulators no attempt will be made to give the pilot any motion cues.

This type of full-mission simulator, or procedures trainer, has proven very valuable. In the case of the Mercury program, the Procedures Trainer was very effective in training the astronauts to handle both normal and the emergency situations which, as everyone knows, did arise.

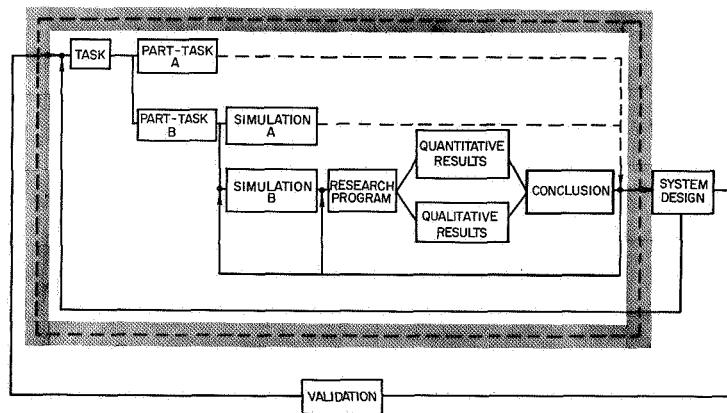
CONCLUDING REMARKS

Flight simulation in space research is assuming a more important role than it had in aeronautical research. In our space programs every effort has to be made to solve all of the possible problems before first flight. The space program does not have the opportunity to conduct developmental flight testing for hours and hours before the final vehicle goes into service use. The only way this intensive development can be carried out is through the use of simulation. As I have tried to show, our flight simulators come in all shapes and sizes due to the great variety of our space problems. Some of these facilities must be highly sophisticated. Well-conceived facilities and well-directed simulation programs are required to provide timely answers to the many new problems peculiar to space-flight missions.



NASA

Figure 1.- Piloted flight simulator.



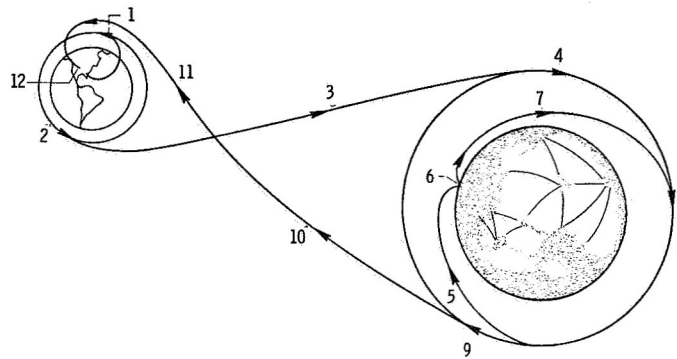
NASA

Figure 2.- Research simulation process.

GROUND-BASED	FLIGHT TEST
FIXED-BASE	MOVING BASE
PART TASK	WHOLE TASK
SPECIAL PURPOSE	GENERAL PURPOSE
RESEARCH	PROCEDURAL
DEVELOPMENTAL	FULL MISSION

NASA

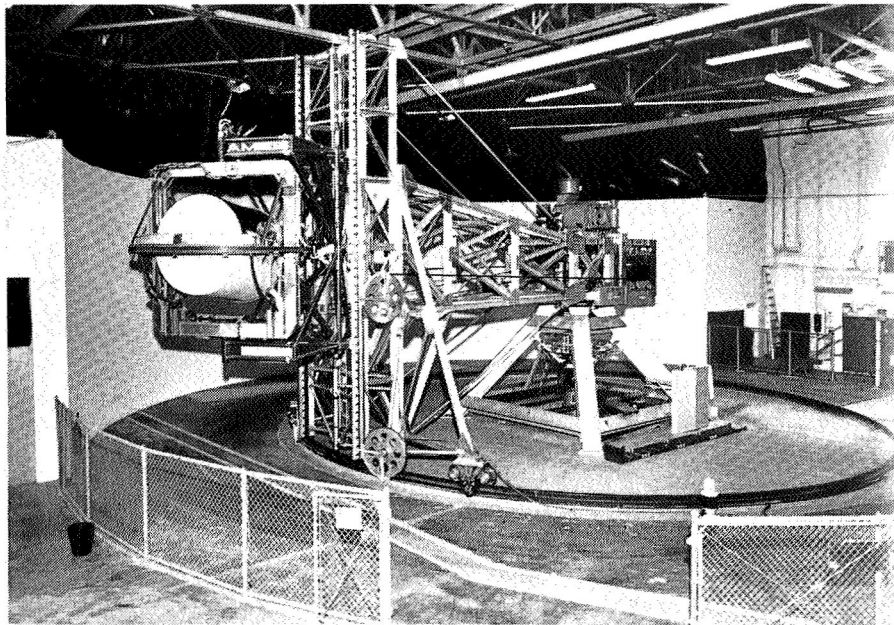
Figure 3.- Types of simulators.



- | | |
|------------------------|-----------------------------|
| 1. EARTH LAUNCH | 7. LAUNCH |
| 2. ORBIT OPERATIONS | 8. RENDEZVOUS AND DOCKING |
| 3. MIDCOURSE | 9. TRANSFER ORBIT INJECTION |
| 4. ORBIT ESTABLISHMENT | 10. RETURN |
| 5. LANDING | 11. EARTH REENTRY |
| 6. SURFACE OPERATIONS | 12. LANDING AND TOUCHDOWN |

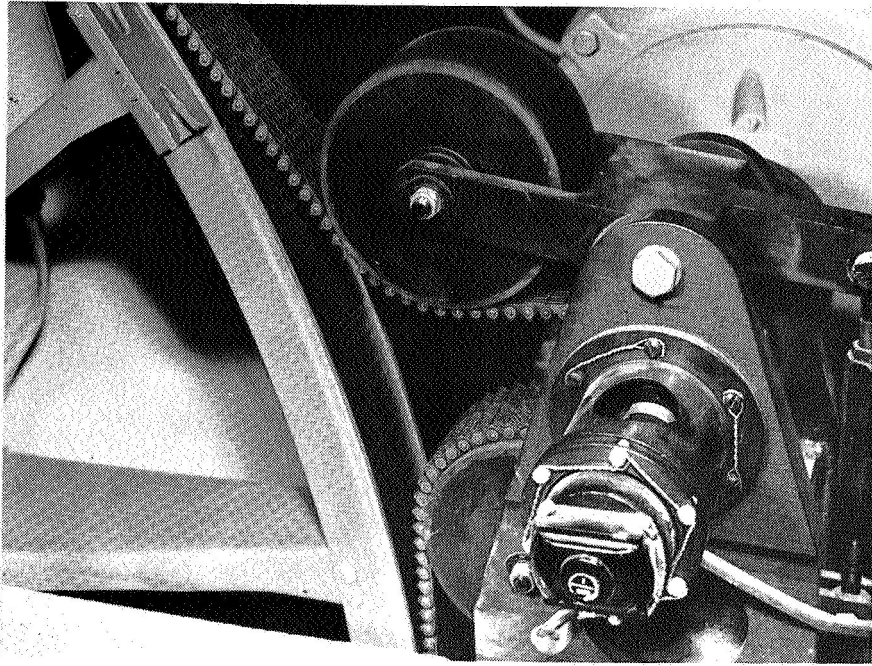
NASA

Figure 4.- Manned space-mission phases.



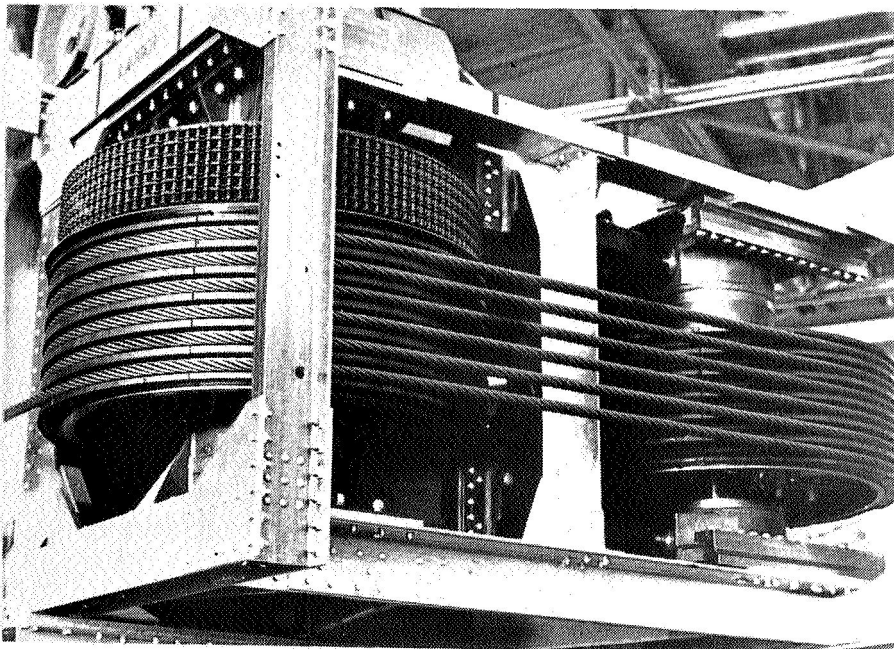
NASA

Figure 5.- Ames five degree of freedom simulator.



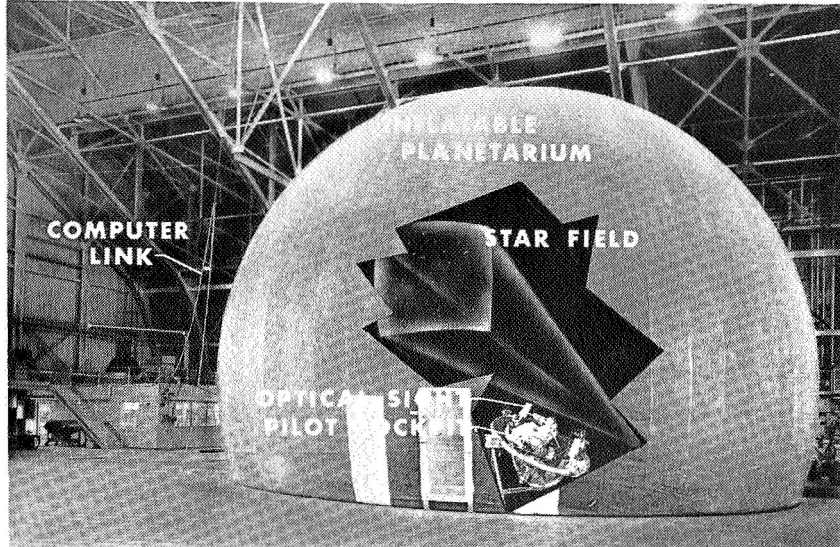
NASA

Figure 6.- Silent chain belt drive.



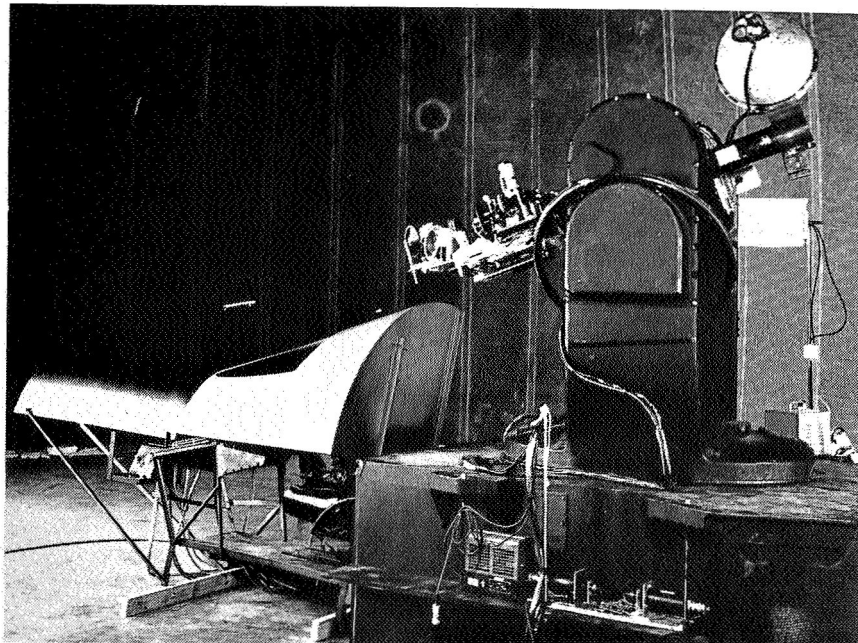
NASA

Figure 7.- Cable drive.



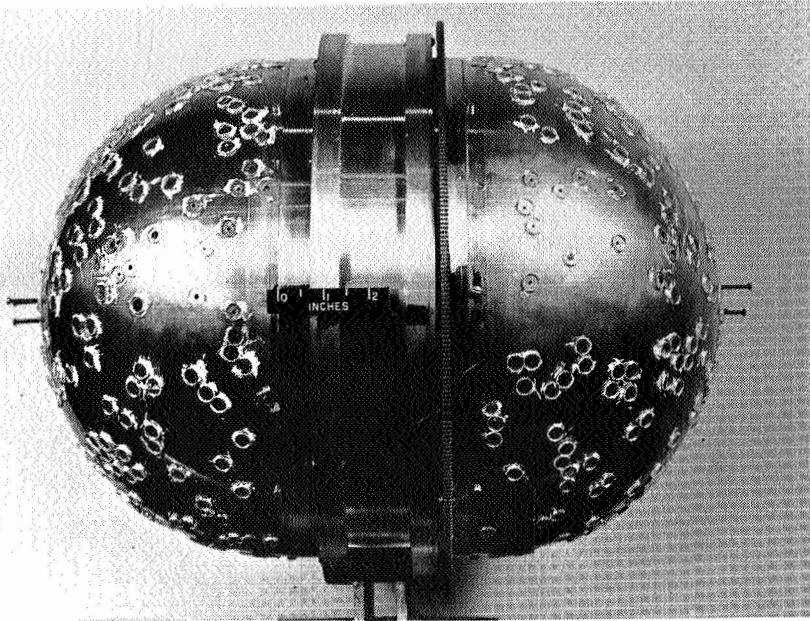
NASA

Figure 8.- Visual Rendezvous Simulation.



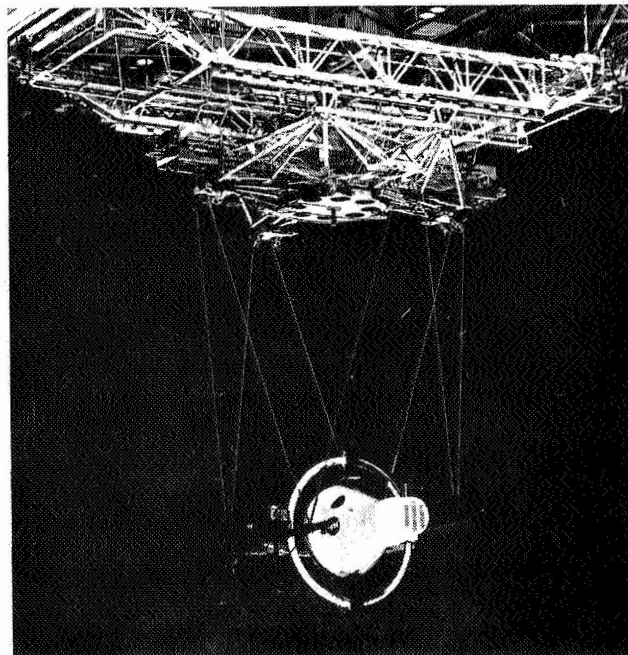
NASA

Figure 9.- Visual rendezvous equipment.



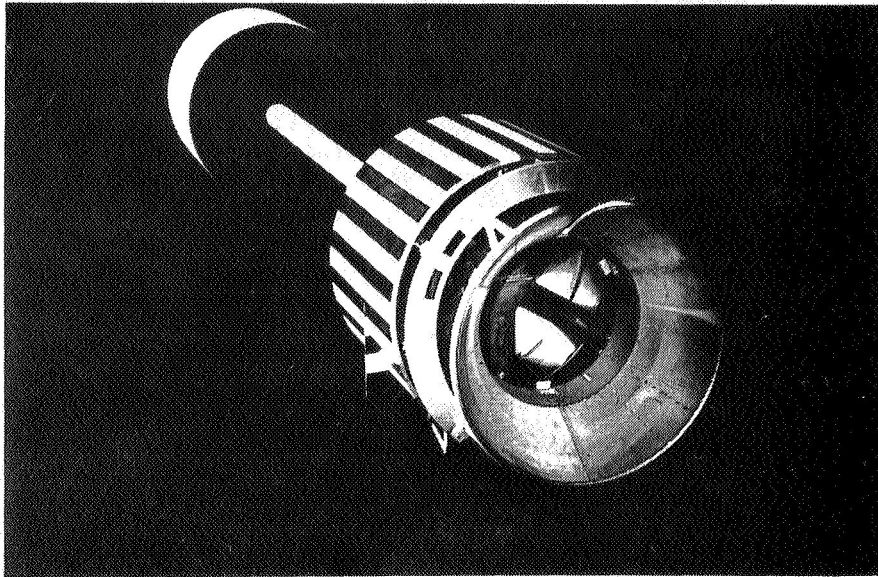
NASA

Figure 10.- Star projector.



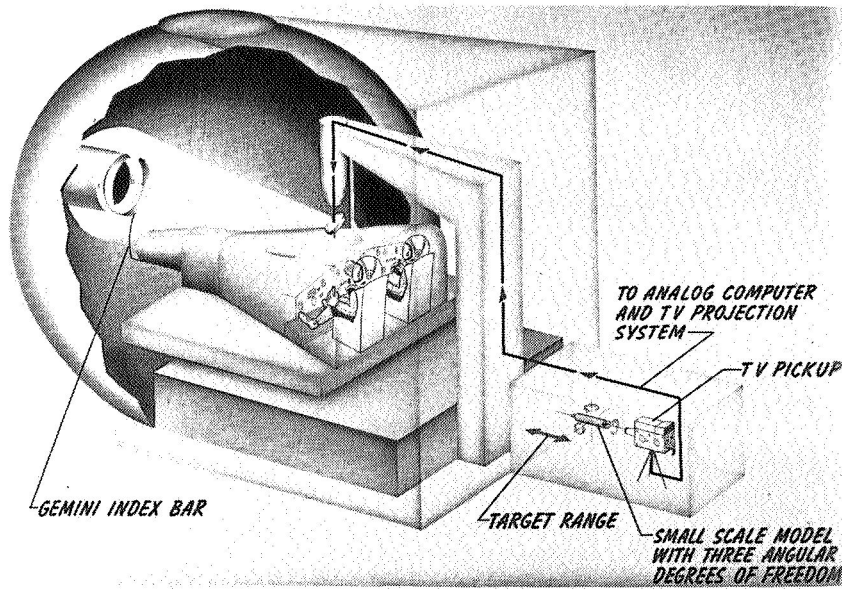
NASA

Figure 11.- Rendezvous docking simulator.



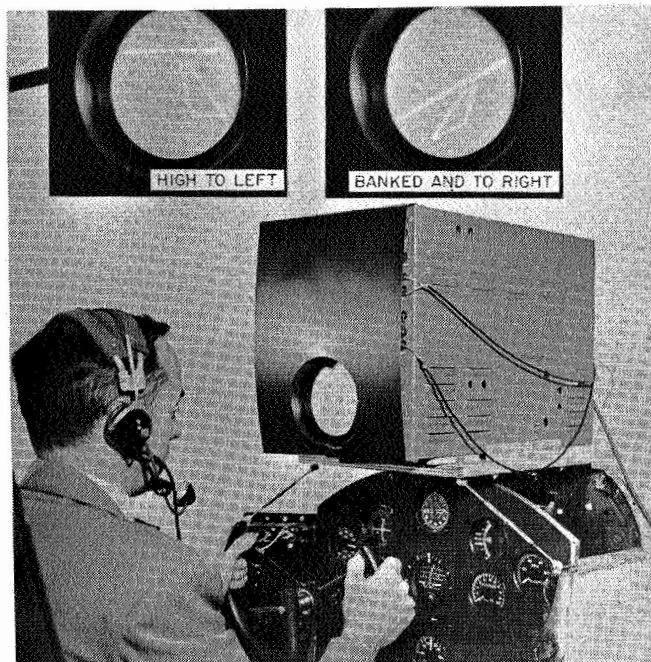
NASA

Figure 12.- Docking target.



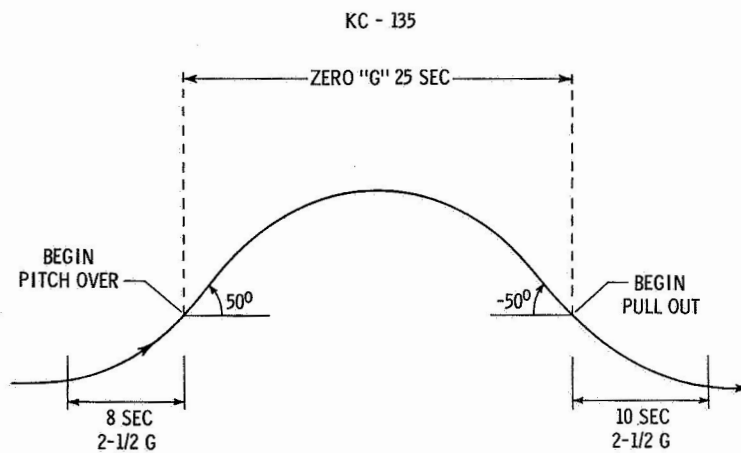
NASA

Figure 13.- Visual docking simulator.



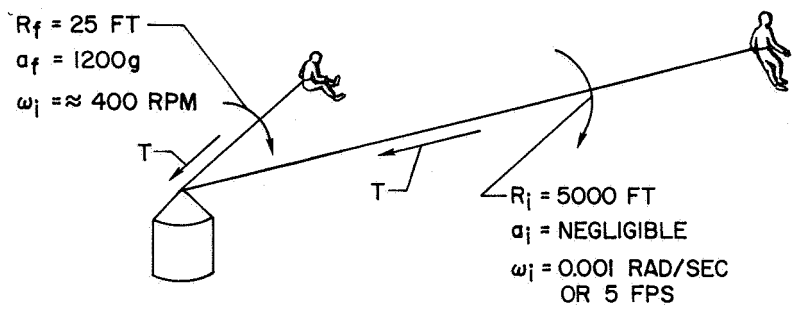
NASA

Figure 14.- Image generator.



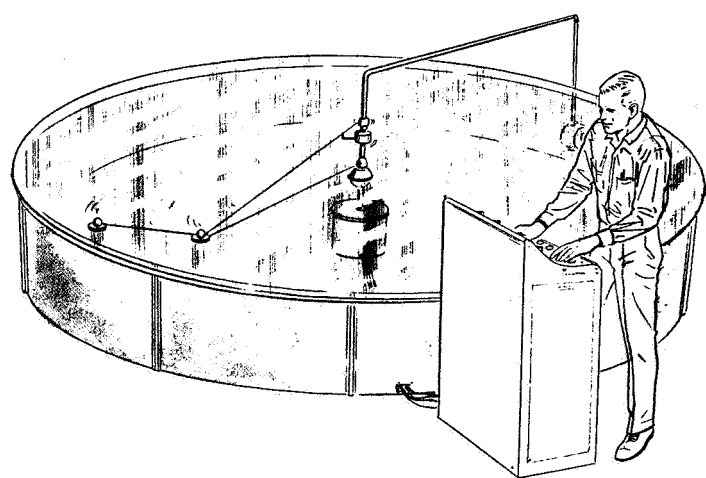
NASA

Figure 15.- Zero-"G" trajectory.



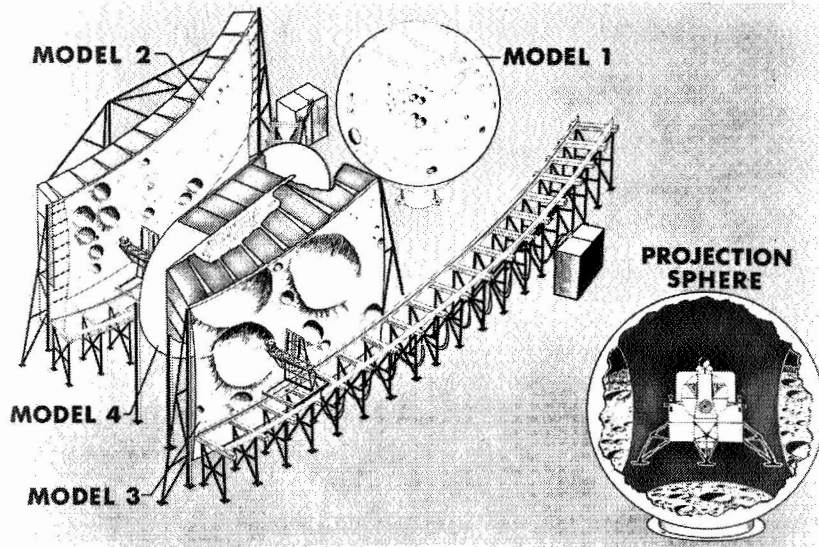
NASA

Figure 16.- Astronaut retrieval.



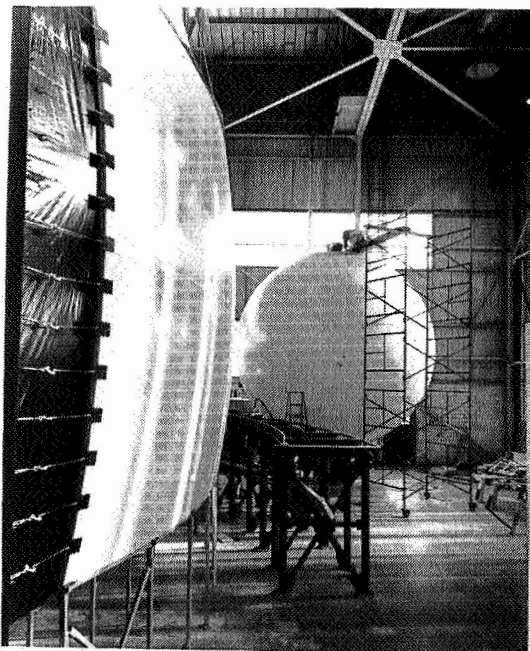
NASA

Figure 17.- Scale model controlled tethering simulator.



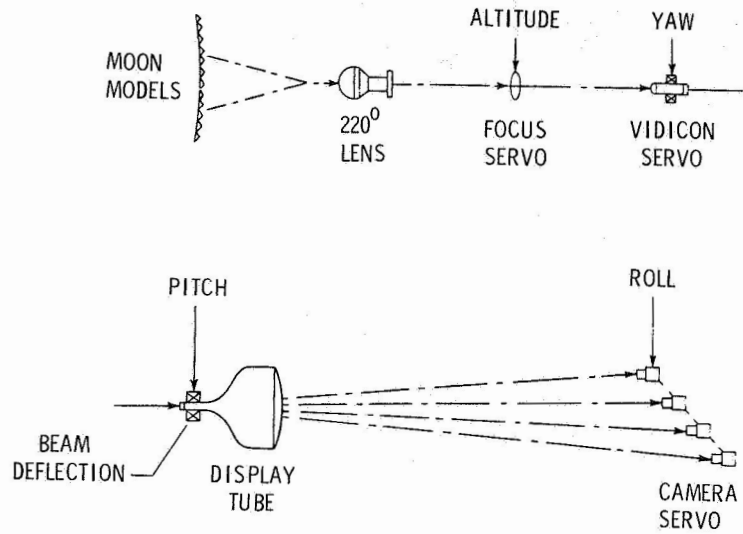
NASA

Figure 18.- Lunar orbit landing approach.



NASA

Figure 19.- LOLA construction.



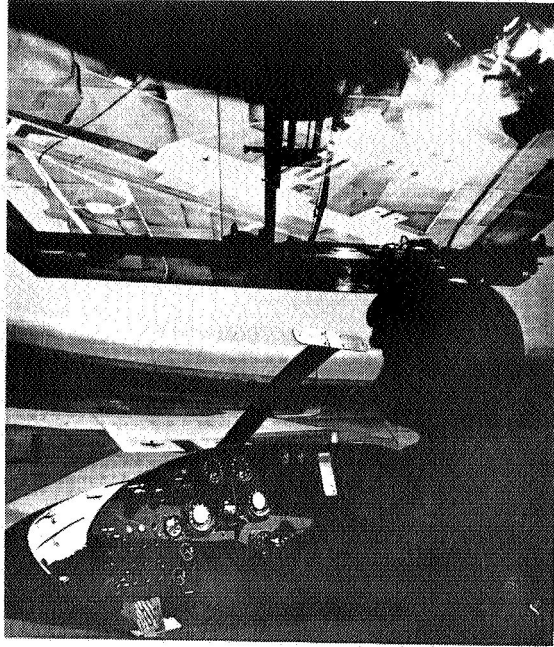
NASA

Figure 20.- LOLA optical pickup.



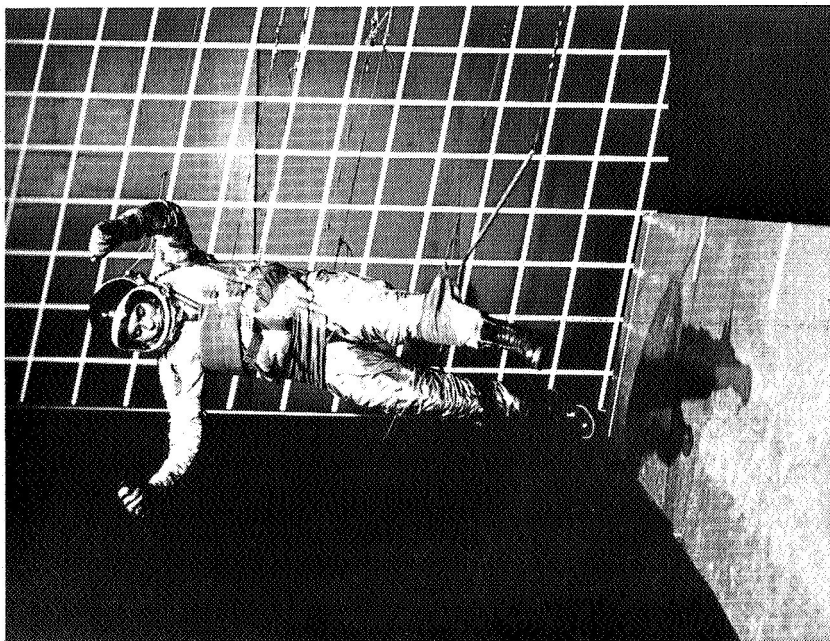
NASA

Figure 21.- Pilot's view.



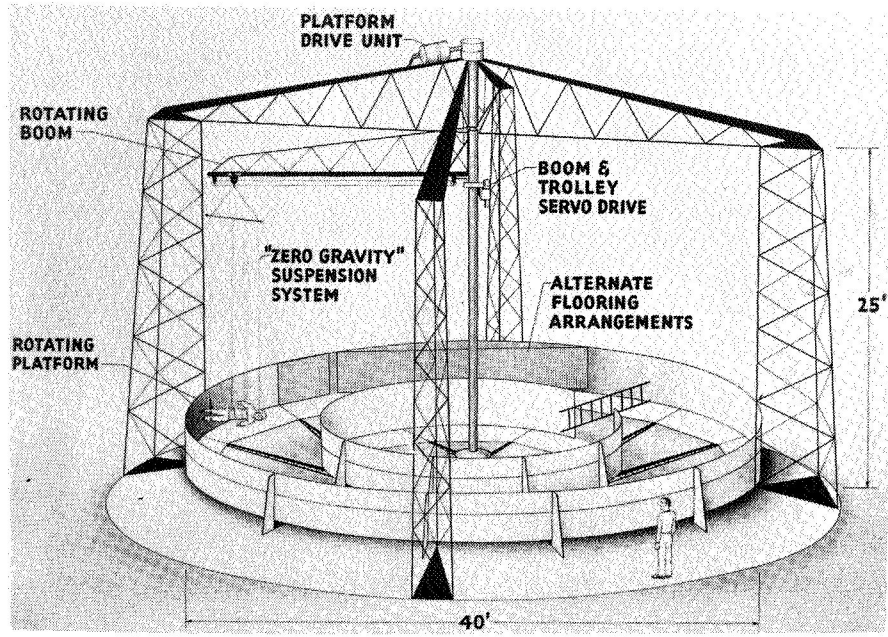
NASA

Figure 22.- Ryan simulator.



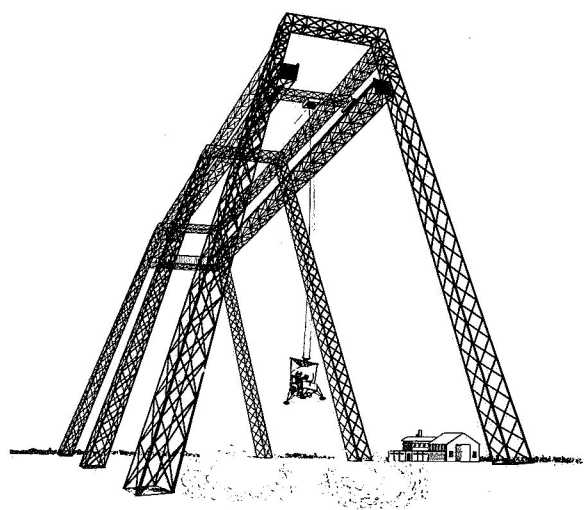
NASA

Figure 23.- Lunar walking simulator.



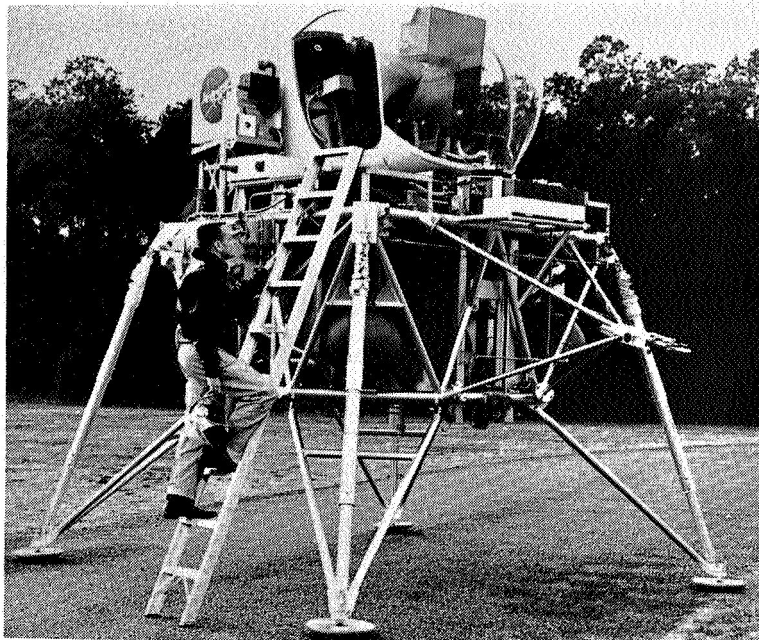
NASA

Figure 24.- Rotating space station simulator.



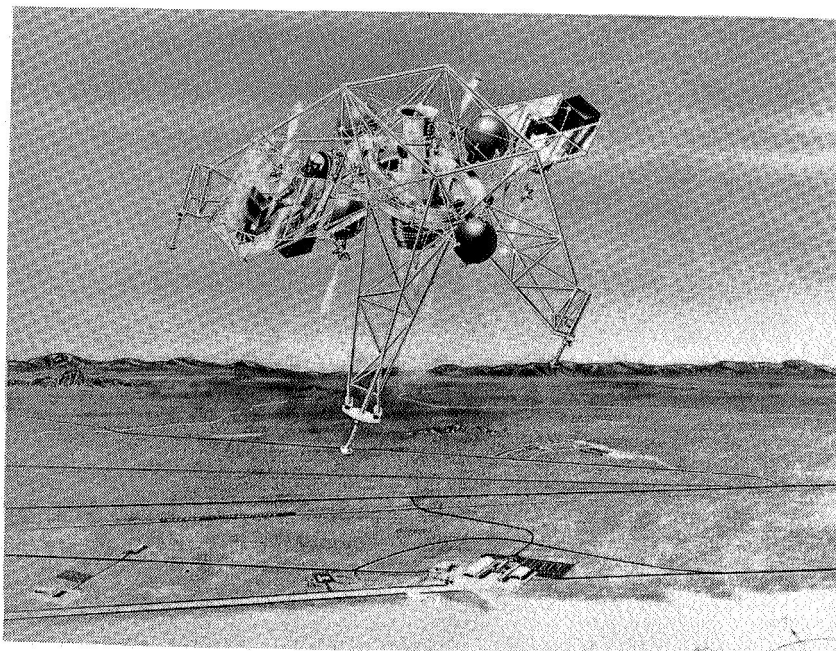
NASA

Figure 25.- Langley lunar landing research facility.



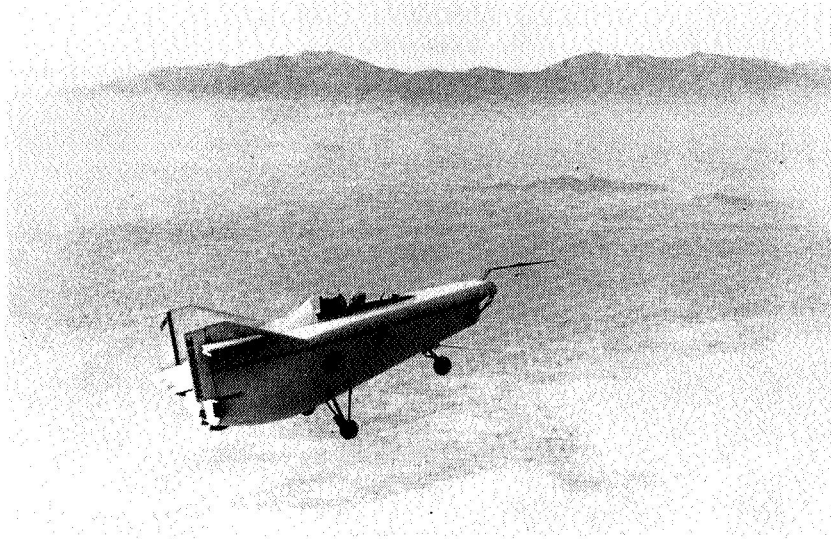
NASA

Figure 26.- Research lunar lander.



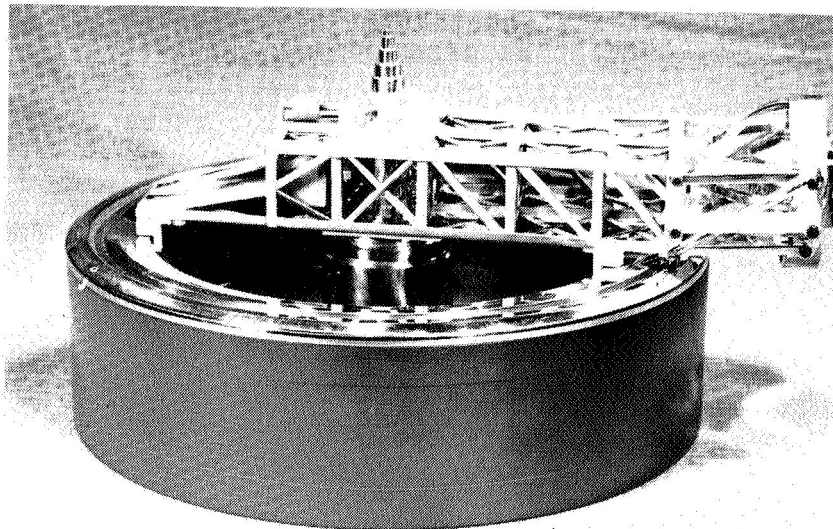
NASA

Figure 27.- Lunar landing research vehicle.



NASA

Figure 28.- Lightweight M-2.



NASA

Figure 29.- Ames space flight guidance simulator.

APOLLO MISSION SIMULATOR
LINK PHOTO

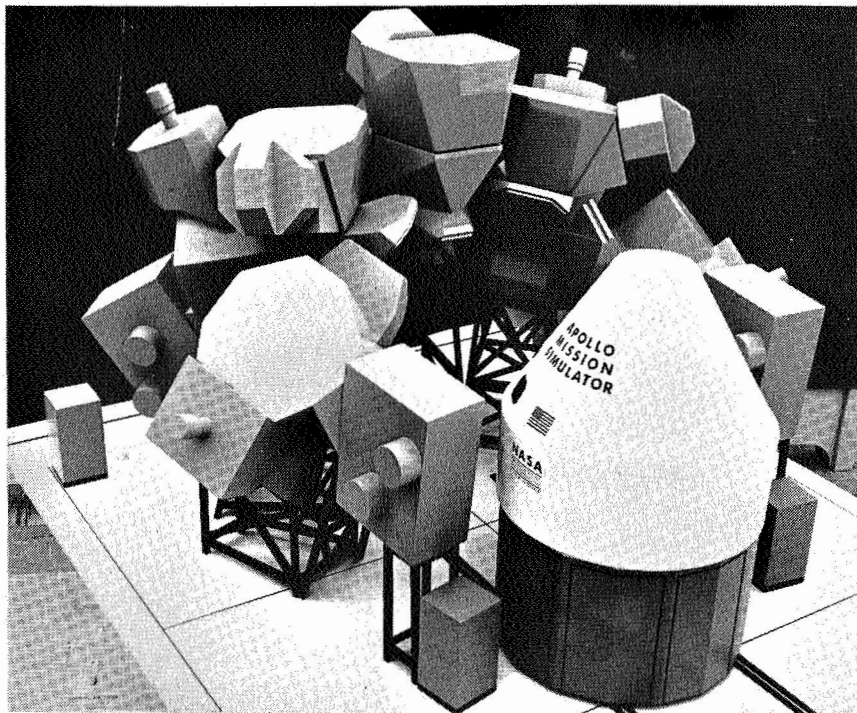
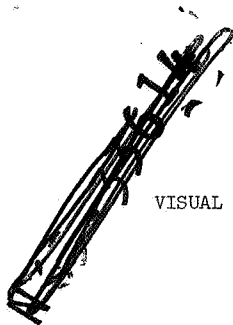


Figure 30.- Apollo mission simulator.

NASA



VISUAL AND MOTION SIMULATION TECHNIQUES

by

John Lott Brown

University of Pennsylvania

INTRODUCTION

It is impossible in the time available for this presentation to provide more than superficial coverage of the subjects of vision and motion simulation techniques as these have been applied in space flight research. Fortunately, the excellent presentation by Vogeley on the existing and planned simulators for space research in the NASA program reduces the need for any extensive treatment of the application of techniques which provide for a complete visual simulation. I will therefore discuss problems of visual simulation in more general terms and treat fundamental characteristics of the visual system which are relevant to successful simulation techniques rather than discussing specific applications of these techniques. It may then be useful to consider the way in which sensory information is integrated and processed in our attempt to realize from it a knowledge of the physical world. This will provide an introduction to the discussion of motion and clarify the reasons for including motion cues in simulators.

VISUAL SIMULATION

There are a variety of visual capabilities which will be important in space flight (5). Some of these need not be considered in relation to continuous task simulators, however. Our primary concern is with simulators which provide a basis for testing man's performance in a continuous task situation such as the control of a moving vehicle. We will not discuss the important problems of visual search, detection, and recognition. Visual tasks which are of concern to us are those of the discrimination of size, distance, and relative motion (20, 22, 32).

Visual Size Discrimination

Typically, the discrimination of size of an object is based either on a knowledge of the physical sizes of objects around it in the visual world, or else on a knowledge of its distance from the observer. It is extremely difficult to make accurate judgments of size in the absence of such cues.

Distance Judgments

The judgment of distance is based on a number of cues (20, 22). An important one is that of linear perspective. This refers to the gradual decrease in the visual angle subtended by elements in the visual world as they are located further and further away from the observer. It may relate to the texture of the terrain or, to cite a familiar example, the apparent separation of railroad tracks as they recede toward the horizon. This kind of cue is of far greater importance to one who is living on an apparently flat, extended surface than it would be to someone living in

relatively empty three-dimensional space without a continuous distribution of objects and terrain from his immediate location out to the location of an object whose distance he desires to judge.

Another important cue is that of interposition. Stated simply, this refers to the fact that an object whose outline or surface is interrupted by another object will be judged further away than the interrupting object. The interposed object is obviously the nearer object.

At surface of the earth, atmospheric haze provides an important cue for the judgment of distance. The reduction by haze in clarity of object detail and the reduction in the range of color seen reflected from an object provides cues as to the object's distance. Another important cue is that of monocular movement parallax. This refers to the fact that when an observer is himself moving he will see relative motion in the visual world between nearby objects and objects more remotely located. The nearby object will appear to be moving in a direction opposite to his own motion. Telephone poles seen from a train window relative to the distant horizon afford a familiar example.

Unfortunately, all of these cues require either a distribution of objects in depth from the observer, familiarity with the object, or other conditions which are found on the earth's surface. Many situations in space flight may be devoid of all of these cues. Judgment involving other space vehicles may be among the most difficult, but even judgments of surfaces will be difficult when they are normal to the line of sight, and especially when they are unfamiliar. Recent photographs of the surface of the moon show a remarkable continuity in the nature of its appearance from a distance of thousands of miles down to a distance of thousands of feet. Apparently the size of moon craters varies over a continuous

range from extremely large to extremely small. This renders it difficult to make judgments of distance or size on the basis of visual angles subtended by details of the surface. A careful examination of the surface presented in Figure 1 is of little help in assessing its distance. As soon as a familiar object is included however, as in Figure 2, the judgment of distance and size is a simple matter.

There is an important cue to distance which does not depend upon object familiarity. This is the cue provided by the fact that the two eyes of a binocular observer are located at different points in space and hence see the world from slightly different perspectives (22). Thus an object with some extent in depth may be seen as three dimensional as long as this cue is operating, or two objects at different depths can be correctly discriminated in relation to which is closer and which is further away with no knowledge of their relative size. It has been demonstrated that deviations from the stimulation of precisely corresponding points on the two retinas of less than 30 seconds of arc can be discriminated as representing differences in depth. Rays of light from an object in space at an infinite distance will be parallel on entering the two eyes. One can calculate the distance at which rays of light from an object will deviate by an angle of 30 seconds of arc or more on entering two eyes separated by the normal interpupillary distance of 65 mm. The distance is approximately 500 yards. Thus objects at 500 yards or less should be seen as closer than much more distant objects purely on this basis of binocular stereoscopic vision and independent of their size or shape. The value of such a cue should not be discounted for certain phases of a space mission.

Movement Discrimination

The relative movement of objects in the visual world is discriminated in terms of changing visual angle (10, 11, 12, 21). For objects which are moving in a frontal plane relative to the observer, angular rate is assessed in relation to the changing visual angle between the moving object and some fixed reference point. In the absence of any stable reference point, such a judgment may be extremely difficult. The approach or recession of an object of finite size is inferred from changes in the visual angle subtended by its breadth. A large amount of basic research has been conducted on the minimum thresholds for detection of angular change in the visual world (10, 12). These thresholds will provide a basis for the estimation of boundaries within which visual motion may play an important role in simulation.

SENSORY INTEGRATION

Most individuals would agree that their perception of the visual world is put together on the basis of information derived from the various senses. They would also agree that it is not necessary to make any conscious effort to perform this integration but rather that it occurs quite unconsciously. They might be disturbed at the notion that information derived from various individual sensory channels cannot always be consciously separated and identified in relation to its source, however. There is evidence that the integration of various sensory inputs depends upon experience and requires considerable learning (28). On the other hand, there is also evidence that it may be difficult or impossible to separate information provided by one sensory channel from information provided by

another. A recent experiment provides an example of this (29). If a man is seated in a chair and views a vertical line of light directly in front of him, he can recognize its orientation and make corrections when it is deviated from the vertical. If his chair and the vertical line are both tilted away from the vertical he is able to correct the line orientation back close to the true vertical. The basis for his correction must depend upon information which he receives from the deviation of his own body orientation from vertical. One source of such information is the imbalance in tension of the musculature on the sides of the neck which maintains the head in an erect position. If now, an observer is seated erect while wearing a helmet which can be weighted on one side, his visual perception may be distorted by this off-balance load on the neck muscles even though he is perfectly aware that he has not been deviated from an upright position. Differences in tension in the sternocleidomastoid muscles on the two sides were measured electromyographically for various amounts of body tilt. The same differences in tension were then created by off-balance loading, and a truly vertical line was judged to tilt in amounts comparable to the amount of body tilt which corresponded to the differential tension. Thus, in a restricted visual situation where only a single illuminated line could be seen, muscle tension had an important influence on visual perception.

Changes in the resultant acceleration force on a man induced by motion on a centrifuge are perceived via tactual and other cues. In this kind of a situation the orientation of the entire environment seems to change (23). The apparent change in orientation of the environment cannot be eliminated even by the most sophisticated conscious analysis on the part of the observer of the forces at work.

Much more elaborate gyrations of the visual world result from movements or rotations of the head which are not along or about an axis about which the body is being rotated (24). Forces induced by head movement during rotation of the body result in stimulation of the vestibular mechanisms of the inner ear. Vestibular stimulation may have a profound effect on visual perceptions (25).

It is clear that the senses cannot be regarded as independent in their function and even conscious effort may not be sufficient to separate out information provided by one sense modality from that provided by another (18). This situation has posed a serious problem for modern aviation, particularly with respect to vestibular function. The vestibular mechanism is useful and appropriate for a man residing on the earth's surface, but its outputs are quite inappropriate in many of the angular motion situations encountered by aviators (1). This is attested by the tremendous difference in accident rate between IFR and VFR conditions. In order to fly instruments, a pilot must learn to discount all of his senses save vision, and visual information is presented to him in a highly artificial manner. Oftentimes false perceptions which result from vestibular stimulation may override the information obtained from instruments and accidents are the result. It has been estimated that more than 80% of aircraft accidents which are not a direct result of equipment failure are the result of illusions or false perceptions. It is conceivable that these problems may be even more serious in certain aspects of space flight.

VALUE OF MOTION SIMULATION

In the preceding section we have discussed problems which result from

false perceptions induced by movement. An extension of this discussion provides a justification for adding motion to a simulator which is not often heard. If the motions of flight may give rise to false perceptions, then in their absence a pilot might be expected to perform better than in the real life situation. Thus if motion is added, a more pessimistic but more realistic assessment of pilot performance may result. Unfortunately, in any laboratory simulation the simulation of motion will necessarily be so limited that its use can never be justified on these grounds. Only in the variable-stability aircraft simulator discussed earlier by Westbrook can a reasonably accurate simulation of motion qualities of a vehicle be achieved. This is a highly specialized type of simulation, however, and far superior to the laboratory simulations with which we are concerned here.

The most frequently heard justification for the addition of motion cues is that they afford an increase in realism. When this justification is applied to situations in which motions are not extreme it must be examined very carefully. There is very little satisfactory evidence to validate the assumption that the addition of motion cues in a laboratory simulator actually increases realism. In an earlier discussion the speaker referred to the importance of subjective opinion in assessing simulations. The subjective opinions of experienced pilots are indeed most important (15), but they alone are not enough. Another speaker referred to a simulation situation which was so realistic that in an emergency, a crew man injured his head in an effort to escape through a dummy hatch. This kind of an anecdote certainly implies some validation of the realism of the situation, but it is hardly a sufficient basis for assessing the real value of the simulator. The value of a simulator must be measured in terms of how well

it improves our ability to predict the way a pilot will do his job in the situation which is being simulated.

There are some situations in which the best judgment dictates that motion be added even though its importance is not subject to immediate validation. These situations include all those where motion characteristics are extreme. An excellent example is the X-15 research rocket aircraft (14). The design characteristics of this vehicle were such that fairly extreme conditions of linear acceleration were anticipated during reentry from high altitude missions. In the event of damper failure these accelerations and the conditions of motion were expected to be even more extreme and in a range where the maintainance of control by a pilot was in serious doubt. For this reason, some simulation of linear acceleration profiles was considered imperative prior to actual flight testing of the X-15, even though it was recognized that in certain respects these motion simulations would be inaccurate.

TECHNIQUES OF MOTION SIMULATION

Motion may be characterized in relation to three orthogonal axes of angular motion and three orthogonal components of linear motion. It is possible to duplicate all six degrees of freedom of motion of a maneuvering vehicle precisely only by utilization of the same motion and the same amount of three dimensional space. This is obviously impossible within the confines of a laboratory. Techniques of motion simulation in the laboratory are therefore usually based upon an incomplete simulation in which certain of the six components are neglected (i.e. permitted to assume whatever values are required for a precise simulation of the other

components with the available equipment), or an attempt is made to include only those motion characteristics which can be detected by a human pilot.

Angular Components

In conventional flight, the angular components of motion are probably most important. In those instances where they may not be, a justification for considering them rather than linear components can be made on practical grounds. Realistic simulation of linear components of motion with respect to acceleration is possible only with some sort of centrifuge device if the required space is to be limited to even a fairly large laboratory. In most motion simulators therefore, the concern is with angular motions, specifically with angular acceleration.

Detection of angular motion. The most important of the sensory mechanisms for the detection of angular motions is the semicircular canal system of the vestibular apparatus (19). This is illustrated in Figure 3. On each side of the head there are three canals in mutually perpendicular planes, with a lateral canal inclined upward in the front at an angle of approximately 30° from the horizontal, and a superior canal and a posterior canal the planes of which are each at an angle of approximately 45° to a median plane through the head and tilted backward at approximately 30° from the vertical such that they are each perpendicular to the lateral plane. Thus the lateral canals on each side are approximately in the same plane and the superior canal on one side is in a plane parallel to the plane of the posterior canal on the opposite side. Each canal contains a fluid which moves relative to the canal as a result of rotational inertia during angular acceleration. Relative movement of the fluid within the

canal causes deflection of a structure called the crista within an enlargement in the canal. This is illustrated in Figure 4. The bending of hair cells of the crista gives rise to sensory stimulation. The compound output of sensory activity from all six semicircular canals is uniquely determined by the orientation and magnitude of angular acceleration.

There is, of course, a threshold for the detection of angular acceleration. This will vary with the method of testing and other circumstances, but will fall somewhere between $0.2^\circ/\text{sec}$ and $2^\circ/\text{sec}^2$ (30, 31). The latency of detection of an angular acceleration will also vary with the level of acceleration (16). This is illustrated in Figure 5. From a knowledge of these thresholds, it should be possible to introduce angular acceleration in a simulation only for those circumstances where angular acceleration in real vehicle motion is above threshold. At all other times angular motions in the reverse direction may be introduced at accelerations below threshold in order to return the simulator structure to some neutral position. This procedure is called the "washout" technique. Its application (17) is illustrated for a roll maneuver in Figure 6. In the upper graph, roll angle (ϕ) is illustrated as a function of time. The first and second derivatives of ϕ are illustrated in the succeeding graphs. Solid lines in each graph represent the value for an aircraft. Dotted lines illustrate the way in which the derivatives of ϕ can be approximated even though the actual value of ϕ at the end of the maneuver is the same as the initial value.

By considering the angular terms which describe a typical vehicle maneuver and relating these to the thresholds for angular motion of the human pilot, it should be possible to determine the minimum necessary space in which angular acceleration could be simulated realistically in a laboratory. The procedure would require the use of motion introduced

at sub-threshold levels of angular acceleration to return to neutral or median positions whenever maneuvers did not demand the application of supra-threshold accelerations away from the neutral position. If threshold values for the detection of angular accelerations based on laboratory studies are employed, the result of such an analysis will be unduly pessimistic in terms of the predicted space requirements. The thresholds of laboratory investigations are far lower than those which would be appropriate for a complex situation in which a subject is bombarded with many other distracting cues. Nonetheless, an analysis of available data might prove of great utility.

Any large scale effort to apply motion simulations according to these general procedures should include some kind of validation program. There is always the possibility that the addition of artificial motion cues may render the results of simulator studies less valuable for prediction than would have been the case had no motion cues been added.

Linear Components

Linear acceleration components which affect a pilot are illustrated in Figure 7. These are named in terms of the orientation of their line of action with respect to the long axis of the human body (13). Direction is considered to be that in which the man will tend to move against his restraint, rather than the direction of action of the accelerating force. Positive g refers to the component which tends to "pull the pilot down into his seat". This component of linear acceleration interferes with the circulation of blood toward the head. It is therefore of considerable physiological significance. Negative acceleration acts in the opposite direction and aids the flow of blood to the head. Its effects are even

more serious than those of positive acceleration because it can cause cerebral hemorrhaging. The effects of transverse fore-and-aft, and transverse lateral accelerations are not as serious if a pilot is given adequate support and restraint.

Some of the maneuvers which induce various forms of acceleration are illustrated in Figure 8.

Centrifuge Simulation

Laboratory simulation of linear acceleration components can only be accomplished with the aid of a centrifuge device. The largest of these which is currently available is the navy centrifuge at the Aviation Medical Acceleration Laboratory at Johnsville, Pennsylvania (17). This is illustrated in Figure 9. In recent months the arm of this device has been replaced and a new and larger gondola mounted in a two gimbal system has been located at its end. The radius is 50 feet and the device is capable of accelerating at an angular rate which produces a centripetal force on objects located within the gondola of greater than 40 g in less than 10 seconds. By rotation of the gondola about its two independent gimbal axes it is possible to vary the orientation of the resultant acceleration force with respect to a subject within the gondola to conform to variations in the orientation of the resultant linear acceleration force in any desired motion pattern. The outer gimbal quadrant gear and the 360° circumferential gear of the gimbal system are illustrated in Figure 10.

The resultant acceleration force in a rectangular coordinate system of three dimensions is calculated in accordance with equation 1.

$$A = (a_x^2 + a_y^2 + a_z^2)^{1/2} \quad (1)$$

The resultant acceleration force on a man in a centrifuge gondola reflects components due to the earth's gravitational field, the angular velocity of the arm, and any tangential acceleration forces which result from variation in the angular rotation rate. The calculation of this resultant acceleration is illustrated by equation 2.

$$A = (g^2 + \omega^4 L^2 + \dot{\omega}^2 L^2)^{1/2} \quad (2)$$

If appropriate gimbal motions can be calculated in order to obtain a proper time history of orientation of the resultant force, then any linear acceleration time history within the capability of the centrifuge can be described in terms of equation 2 and the appropriate values of outer and inner gimbal position as a function of time.

Catapult launching. A very simple simulation (7) is illustrated in Figure 11. The outer gimbal was so positioned that the gondola and the pilot in his seat faced in the direction of rotation. At the instant the arm was started, the largest acceleration component produced by the arm was the tangential component forcing him back into his seat. As angular velocity increased the centripetal force increased and the gondola was rotated toward the center of rotation of the arm. Rotation was continued in such a way that the resultant acceleration from the tangential component and the centripetal component was always oriented from chest to back through the pilot. In this fashion it was possible to impose a linear acceleration component on a pilot similar in its orientation and magnitude to that encountered in a catapult launching. Unfortunately, the temporal response characteristics of the centrifuge system are far too slow to achieve the abrupt onset of acceleration which is characteristic of a

catapult launching. Nevertheless, the technique is illustrative.

The X-15. The aforementioned simulation of the X-15 research aircraft was accomplished on the navy centrifuge. A cockpit simulation was installed within the gondola. A photograph of the instrument panel used in this simulation is illustrated in Figure 12. All of the important flight instruments were operative and their indications changed in a manner appropriate to the mission under simulation (2, 8). Some justification of the importance of this simulation may be obtained by an examination of the acceleration time history of positive g predicted for a situation during a reentry with air brakes closed and failure of the pitch damper. This is illustrated in Figure 13 by the dotted line. There is a relatively high frequency oscillation of acceleration between 4 and 8 1/2 g's. This is a range in which unconsciousness is induced in many subjects. It was therefore considered extremely important to determine whether a representative sample of test pilots could continue to perform any effective control of the vehicle during exposure to accelerations of this kind. The best that could be achieved on the centrifuge is illustrated by the solid line in Figure 13. The reduced amplitude of oscillation is a result of the frequency characteristics of the centrifuge system itself. In spite of the fact that these accelerations are not as severe as those predicted from the vehicle design, the possibility of demonstrating that a pilot could withstand them and continue to control his vehicle was of some importance. The accomplishment of this demonstration added considerably to the confidence of all concerned with the X-15 program.

Satellite launching. Another situation in which extreme acceleration

forces were a matter of concern was that of the launching of a multi-stage orbital vehicle (3). An acceleration time history which is representative for such a vehicle is illustrated in Figure 14 by solid lines. The centrifuge simulation is shown by the dotted line. It is clear that the centrifuge provides a reasonable approximation of the linear acceleration time history. It is limited for two important reasons. In the first place, it is not possible with a centrifuge rotating in a horizontal plane to introduce any motion component which will offset the earth's gravitational field. Thus all resultant accelerations will include the component of gravity and it will not be possible to reduce the resultant acceleration force below 1 g at any time. This limitation is illustrated after the third stage in the Figure 14. Another important limitation is the fact that to change the acceleration component due to angular rotation of the arm requires the introduction of a tangential component of acceleration. If any attempt is made to change angular rate abruptly the magnitude of the tangential term will be prohibitively great. Changes must therefore be made gradually. This is illustrated in Figure 14 by the reduction of acceleration at a finite rate at the end of each stage.

Results of centrifuge studies. Several specific findings of importance were derived from simulator studies on the navy centrifuge. In the case of the X-15, it was found that the scanning pattern required for adequate control of the vehicle was difficult with the instrument panel layout first used (8). This difficulty might not have been considered significant had the pilot not had to contend with the high linear acceleration forces.

In the case of the orbital vehicle, a side arm controller was found by

four test pilots to be loaded inappropriately during the simulated exit accelerations (3). The loading of this controller had been selected as optimum by these same test pilots in a static simulator. Both the loading and the balance were improved following centrifuge simulator studies.

Another important finding from this experiment was the fact that pilots can and must learn to cope with acceleration forces (3). This is illustrated in Figure 15. Pilots' scores on a tracking task are illustrated in terms of integrated error in pitch control as a function of trial blocks. It is evident that performance improves markedly from the first through the last trial block. Three of the pilots had had extensive training in the tracking task in a static simulator prior to exposure to acceleration. Interspersed with determinations of tracking performance under acceleration, trials with the centrifuge stationary were given in order to provide a reference level of performance. The three pilots who had had prior static training showed a high level of proficiency and little or no further improvement during the course of these stationary control tests. On the other hand, the pilot who had received no prior static training did just as poorly during the stationary tests as under acceleration, but his performance under acceleration was comparable to that of the other three pilots. In this situation, training in a tracking task under stationary conditions apparently resulted in no improvement of the same tracking task under acceleration. The task was like a completely different one when acceleration was added.

Closed-loop operation. In the situations that have been considered thus far, the motion of the centrifuge was preprogrammed and the control manipulations of the subject had no direct effect on the acceleration to

which he was exposed. In actual practice one can expect an interaction between acceleration effects and the pilot's control manipulations. Each will influence the other. These situations have been studied on the navy centrifuge with a simulation technique which is illustrated in Figure 16. In this case, vehicle dynamics are simulated on an analog computer (17, 26). A pilot's control manipulations are fed to the analog computer, which then calculates vehicle motion. This is converted to appropriate terms for the control of the centrifuge. These are fed back to the centrifuge drive system and result in motions which produce a linear acceleration time history on the pilot appropriate for his control manipulations. At the same time, the instrument display presents information appropriate to the maneuvers being performed. This kind of a simulation is limited by the frequency response characteristics of the arm itself and of the outer and inner gimbal systems. The main arm provides the primary limitation and outer and inner gimbal responses must therefore be delayed in order to maintain synchrony among all three systems. This delay can be compensated by taking advantage of delay which is characteristic of the aircraft system and including centrifuge delays within this delay time in the computer system.

The closed loop simulation techniques has been employed in a variety of programs (4). Subjective impressions of its value vary considerably with the nature of the program. For the simulation of conventional aircraft maneuvers, pilots are uniformly agreed that the simulation is poor. It must be remembered that only the linear acceleration components can be accurately simulated with this device. Only highly approximate simulations of angular effects are possible. In some cases, in order to maintain the proper orientation of a resultant linear acceleration force it is necessary

to introduce an angular rotation in the opposite sense from that which would occur during an aircraft maneuver. This is disconcerting to a pilot who is highly dependent in his control manipulations on the sensory feedback from motion cues, whether he is willing to admit it or not.

Fortunately, the effect of angular accelerations on a pilot appears to diminish as the magnitude of linear acceleration is increased. Therefore, in situations such as the X-15 where high amplitude linear accelerations were encountered, and in orbital vehicles where high linear accelerations and relatively low angular accelerations are encountered, the centrifuge simulation is extremely valuable.

A tracking experiment. The effects of centrifuge motions on the performance of a tracking task (6) were studied with a cockpit simulation like that illustrated in Figure 17. A tracking task command signal was presented on an oscilloscope mounted over the panel. It was the pilot's task to maneuver his aircraft so that a target spot was maintained centered on the scope. Results of this experiment are illustrated in Figure 18 in terms of cumulative error scores for vertical tracking, horizontal tracking, and flight coordination. The solid black bars illustrate performance with the centrifuge stationary. The cross-hatched bars illustrate performance with the centrifuge in motion. It is clear that performance in the vertical tracking task is poorer with the centrifuge in motion than under control conditions. On the other hand flight coordination is far superior with the centrifuge in motion than under control conditions. The reason for this is clear: if the centrifuge is in motion the pilot is given constant reminders of imperfect flight coordination in the form of jostling which may reach unpleasant proportions. It is therefore more important

to him to control this dimension than it is in a stationary situation. The degradation of his performance with the centrifuge in motion can probably be attributed to the distraction afforded by the requirement that he pay more attention to flight coordination.

A validation experiment. I have expressed concern for the requirement that simulators be subjected to validation. An effort has been made to do this with the Johnsville centrifuge relative to its possible use for the simulation of conventional aircraft (9). The TV2 cockpit interior illustrated at the bottom in Figure 19 was duplicated within the centrifuge gondola as illustrated at the top of the figure. A tracking task signal was recorded on magnetic tape in terms of both pitch and roll commands as illustrated in the top two traces of Figure 20. Errors in following these commands were recorded and are illustrated in Figure 20 in the third and fourth traces from the top. The control surface deflection angles for both ailerons and elevators are illustrated in the bottom two traces of the figure.

Six subjects were employed in the experiment, and all six flew the aircraft, a static simulation of the aircraft and two centrifuge simulations. The two centrifuge simulations consisted of one which represented the linear acceleration components as accurately as possible and another which included angular accelerations in the correct sense at the initiation of each maneuver with some loss on the fidelity of linear components. This was accomplished by means of a high-pass filter in the gimbal system.

Results in terms of integrated error for the control of the roll dimension are illustrated in Figure 21. There is a striking similarity

in the profile of performance of the three test pilots in the four different experimental conditions. The performance of the navy pilot is similar but somewhat different, and the performance of the two non-pilots is even more different. One of the non-pilots who had had extensive centrifuge experience performed best on the centrifuge but proved poorest in performance of the task in the aircraft. The pilots all had their poorest performance on the centrifuge and best in the aircraft. These results suggest that there may be negative transfer of training between a centrifuge and an aircraft. Training in one may tend to degrade performance in the other. The reasons for this, if it is true, may be based precisely on those angular motions which are sensed by a pilot in an aircraft and which influence his control manipulations even though he may be unaware of the fact. For a subject trained on the centrifuge the angular terms are quite different, and if they feel natural to him it is to be expected that an aircraft will seem unnatural and strange.

This discussion has been based on integrated error scores. Another kind of data analysis which leads to somewhat different interpretations of the same experiment (33) is illustrated in Figures 22 and 23. In Figure 22, an autocorrelation of the pilot's performance in control of roll has been calculated for each of the four conditions of the experiment. The form of the autocorrelation function depends on the frequency components of the control motions. It is clear that the form of the autocorrelation function is more nearly similar for the centrifuge simulations and the aircraft than it is for the static simulation and the aircraft. It is most like the aircraft in the centrifuge simulation which included angular acceleration terms. The form of these autocorrelation functions shows that the subject employed a higher frequency response function for

his control manipulations in the static situation than he did on the centrifuge. His frequency response was lower when angular terms were included than for the linear acceleration simulation, and still lower in the aircraft. In terms of results presented in Figure 22, performance in the aircraft could best be predicted from the centrifuge simulation with angular motion terms added. An elaboration of these results which supports the same conclusion is presented in Figure 23. Here, power spectral density, calculated from the autocorrelation function, is presented as a function of frequency. Power is increasingly restricted to the lower frequency domain with a transition from static simulation to centrifuge I (pure linear), centrifuge II (some angular), and finally the aircraft. Pilots become less likely to employ abrupt control manipulations the higher the penalty for a mishap.

Psychological Stress

The psychological importance of centrifuge simulations of the kind described for the X-15 and for orbital vehicles has been justified by the comments of pilots of the X-15 and the Mercury astronauts. All of these individuals felt that exposure to accelerations in flight was far less disturbing than it would have been had no prior experience under laboratory conditions been available. The centrifuge helps test pilots of these experimental vehicles to get over at least some of the psychological hurdles which otherwise would have to be taken in the first test flight. Evidence that a ride on the centrifuge may itself induce some anxiety (7) is illustrated in Figure 24. Heart rate in these graphs is presented as a function of acceleration level. It is clear that in the case of the dotted line there is an increase in heart rate with acceleration.

The important consideration in this case is the fact that these heart rates were measured prior to exposure and immediately after the subjects learned what acceleration level they were about to be subjected to. If one can assume that an elevation of heart rate is an index of anxiety, then it is clear that the anticipation of acceleration exposure can induce anxiety. This may be of real value. The inability to induce the fears which will attend an actual test in a laboratory simulation of the test represents a serious weakness in most simulator programs.

BIBLIOGRAPHY

1. Bonner, R. H. Spatial disorientation. Review 7-63, USAF School of Aerospace Medicine, Brooks Air Force Base, Texas, August, 1963.
2. Brown, J. L. Tracking performance during simulated exit and reentry flights of the X-15 research aircraft. Report No. NADC-MA-5801, U. S. Naval Air Devel. Center, January, 1958.
3. Brown, J. L. Pilot performance during centrifuge simulation of the boost accelerations of the Dyna Soar orbital vehicle exit flight. Report TED-ADC-RS 7019, U. S. Naval Air Devel. Center, April, 1959.
4. Brown, J. L. Acceleration and motor performance. Human Factors, 1960, 2, 175-185.
5. Brown, J. L. Sensory and perceptual problems in space flight. Ch. 7 in Physiological problems in space exploration, ed. by J. D. Hardy. Springfield: C. C. Thomas, 1964.
6. Brown, J. L. and Collins, C. C. Air-to-air tracking during closed-loop centrifuge operation. J. Aviat. Med., 1958, 29, 794-804.
7. Brown, J. L., Ellis, W. H. B., Webb, M. G. and Gray, R. F. The effect of simulated catapult launching on pilot performance. Report No. NADC-MA-5719, U. S. Naval Air Development Center, December, 1957.
8. Brown, J. L. and Hudson, E. M. Instruments and controls to be used in the X-15 research aircraft. Report, TED-ADC-1406 (NM II 02 12.4) U. S. Naval Air Devel. Center, December, 1957.
9. Brown, J. L., Kuehnel, H., Nicholson, F. T. and Futterweit, A. Comparison of tracking performance in the TV-2 aircraft and the ACL computer/AMAL human centrifuge simulation of this aircraft. Rept. No. NADC-MA-6016, U. S. Naval Air Devel. Center, 1960.
10. Brown, R. H. Velocity discrimination and the intensity-time relation. J. Opt. Soc. Amer., 1955, 45, 189-192.
11. Brown, R. H. Influence of stimulus luminance upon the upper speed threshold for the visual discrimination of movement. J. Opt. Soc. Amer., 1958, 48, 125-128.
12. Brown, R. H. Visual sensitivity to differences in velocity. Psych. Bull., 1961, 58, 89-103.
13. Clark, C. C., Hardy, J. D. and Crosbie, R. Terminology. In Human Acceleration Studies, National Academy of Sciences, National Research Council Publication 913, 1961

14. Clark, C. C. and Woodling, C. H. Centrifuge simulation of the X-15 research aircraft. Report No. NADC-MA-5916, U. S. Naval Air Development Center, December, 1959.
15. Cooper, G. E. Understanding and interpreting pilot opinion. Aeronautical Engineering Review, 1957, 16, 47-52.
16. Crampton, G. H. Vestibular physiology and related parameters in orbital flight. Symposium on possible uses of earth satellites for life sciences experiments. Natl. Acad. of Sci., Amer. Inst. of Biol. Sci., and Nat. Sci. Fdn. May, 1958.
17. Fischer, C. F. and Nicholson, F. T. Acceleration simulations on the human centrifuge. In Symposium on Space Medicine Electronics. The Franklin Inst., pp. 32-51, May 18, 1959.
18. French, J. D. The reticular formation. Ch. 52, Section 1: Neurophysiology, Vol. II, Handbook of Physiology, Washington: American Physiological Society, 1960.
19. Gernandt, R. E. Vestibular mechanisms. Ch. 22, Section I: Neurophysiology, Vol. 1. Handbook of Physiology, Washington: American Physiology Society, 1959.
20. Gibson, J. J. The perception of the visual world. New York: Houghton-Mifflin, 1950.
21. Goldstein, A. G. Judgments of visual velocity as a function of length of observation time. J. Exp. Psychol., 1957, 54, 457-461.
22. Graham, C. H. Visual perception. Ch. 23 in Handbook of experimental psychology. ed. by S. S. Stevens. New York: Wiley, 1951.
23. Graybiel, A. Oculogravic illusion. A. M. A. Arch. Ophthal., 1952, 48, 605-615.
24. Graybiel, A. and Hupp, D. The oculogyral illusion. J. Aviat. Med., 1946, 17, 3-27.
25. Guedry, F. E., Collins, W. E., and Sheffey, P. Perceptual and oculomotor reactions to interacting visual and vestibular stimulation. Report No. 463, U. S. Army Medical Research Laboratory, March 15, 1961.
26. Hardy, J. D. and Clark, C. C. The development of dynamic flight simulation. Aero Space Eng., 1959, 18, 48.
27. Hardy, M. Observations on the innervation of the macula sacculi in man. Anat. Rec., 1934, 59, 403-418.
28. Hebb, D. O. The organization of behavior. New York: Wiley, 1949.

29. Klein, S. J. Wapner, S., Shaw, W. A., Cohen, M. M., and Werner, H. The relationship between muscle action potentials (MAP) and the perception of verticality. Amer. Psychol., 1964, 19, 562.
30. MacCorquodale, K. and Iverson, L. Effects of angular acceleration and centrifugal force on non-visual space orientation during flight. Report No. 14, School of Aviation Medicine, U.S. Naval Air Station, Pensacola, July 13, 1946.
31. McFarland, R. A. Human factors in air transport design. New York: McGraw-Hill, 1946.
32. Teuber, H. L. Perception. Ch. 65, Section 1: Neurophysiology, Vol. III. Handbook of Physiology. Washington: American Physiological Society, 1960.
33. Tremblay, H. G., Brown, J. L. and Futterweit, A. Application of harmonic analysis in a study of tracking performance in the TV-2 aircraft and in centrifuge and stationary simulations of that aircraft. Rept. No. NADC-AC-6406, U. S. Naval Air Devel. Center, March, 1964.
34. Wersall, J. Studies on the structure and innervation of the sensory epithelium of the crista ampullares in the guinea pig. Acta Oto-laryng. Suppl. 126, 1956, 1.

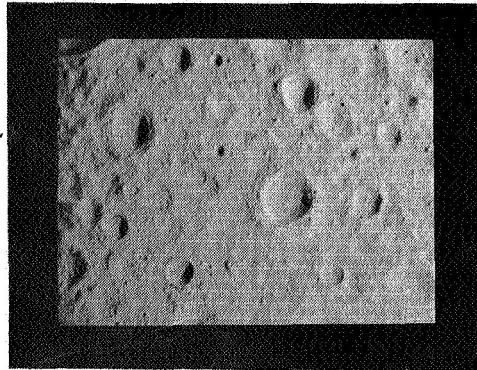


Figure 1: An unfamiliar surface which illustrates the difficulty of size and distance judgments.

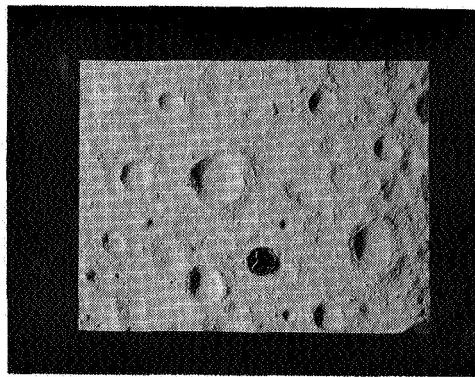


Figure 2: Judgment is influenced by the presence of a familiar object.

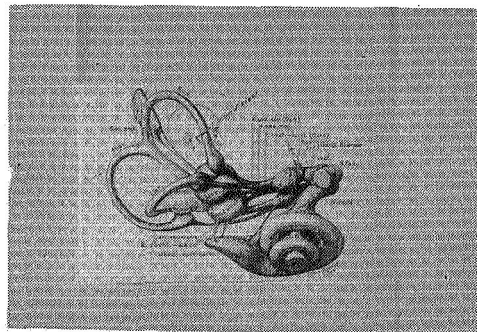


Figure 3: The human labyrinth: semicircular canals, utricle and saccule, cochlea (Hardy, 1935).

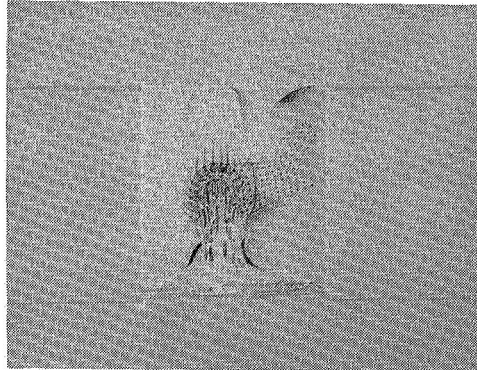


Figure 4: The crista of the semicircular canal (Wersall, 1956).

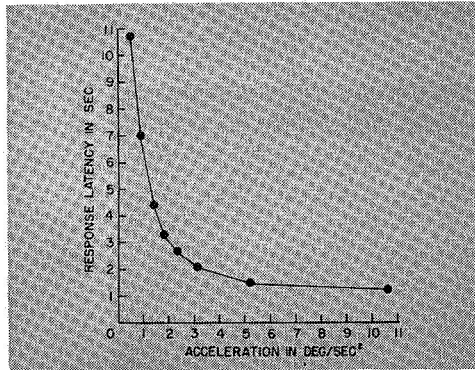


Figure 5: Latency of response to rotation as a function of angular acceleration (Crampton, 1958).

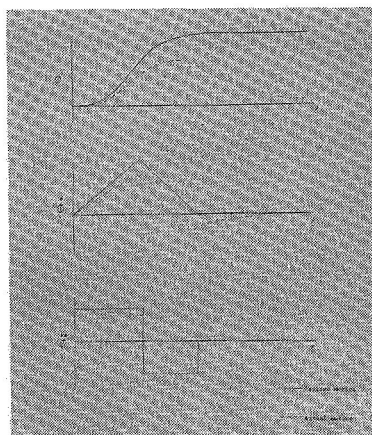


Figure 6: Roll angle and roll angle derivatives which demonstrate the "washout" technique. Solid lines represent values for an aircraft maneuver; dashed lines represent values employed in a simulator (Fischer and Nicholson, 1959).

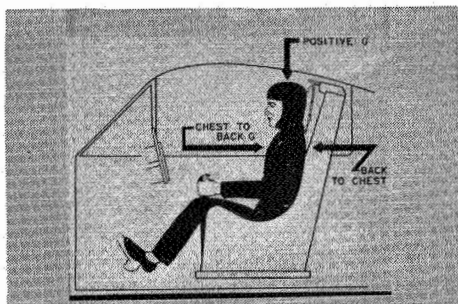


Figure 7: Components of linear acceleration which act on a pilot in the median plane.

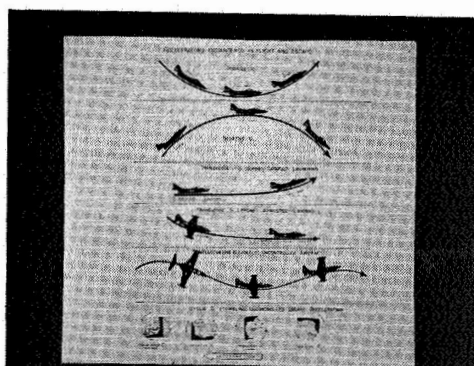


Figure 8: Aircraft maneuvers and the types of acceleration to which they subject the pilot.

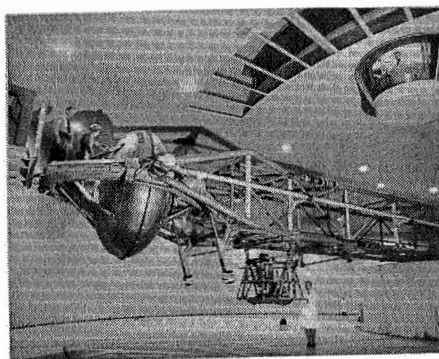


Figure 9: The navy centrifuge at Johnsville, Pennsylvania.

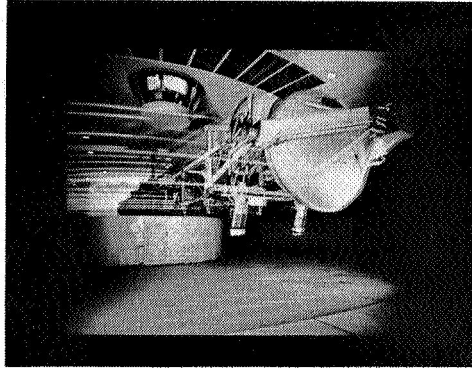


Figure 10: Illustration of the gearing of the gondola gimbal drives.

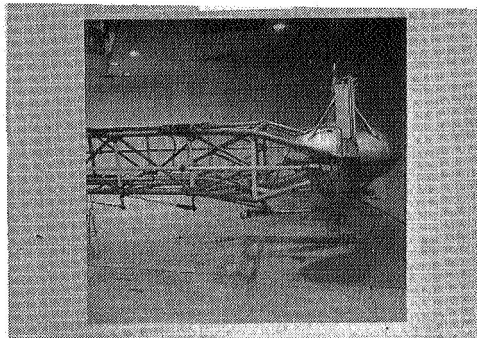


Figure 11: Centrifuge gondola positioning for simulation of a catapult launching.

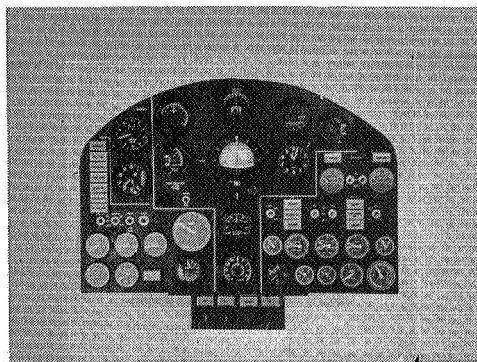


Figure 12: The instrument panel employed on an X-15 simulation.

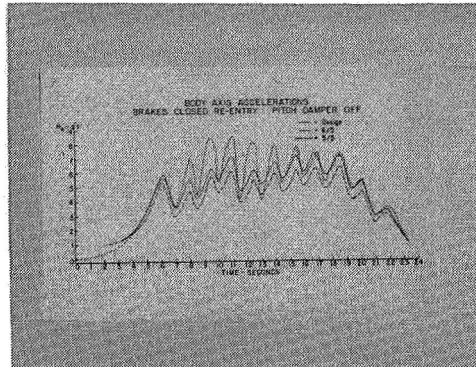


Figure 13: A computed positive acceleration time history for X-15 reentry (dotted line) and two approximations of this time history by the navy centrifuge.

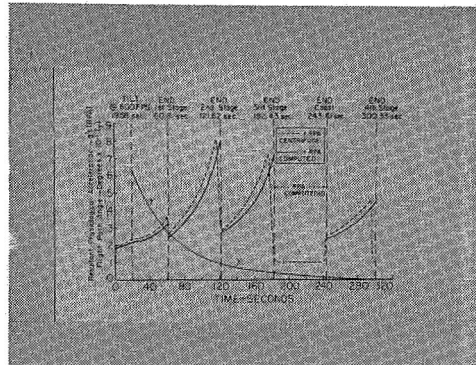


Figure 14:

An acceleration time history for launch of a 4-stage orbital vehicle. Solid lines represent actual value; dashed lines represent centrifuge simulation. Flight path angle is also shown.

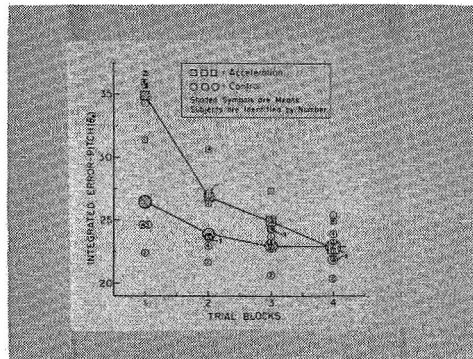


Figure 15: Integrated error scores on successive blocks of trials for performance of a tracking task during simulation of the launching of a 4-stage orbital vehicle. Squares represent data obtained during exposure to acceleration; circles represent data obtained with the centrifuge stationary.

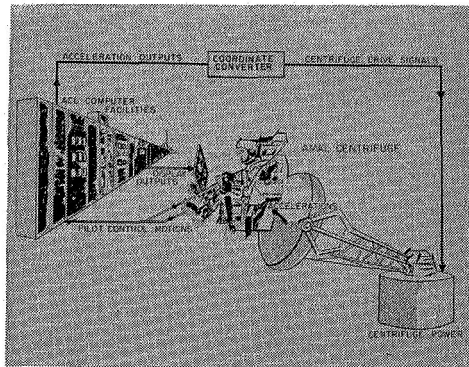


Figure 16: Schematic illustration of closed-loop computer control of the navy centrifuge.

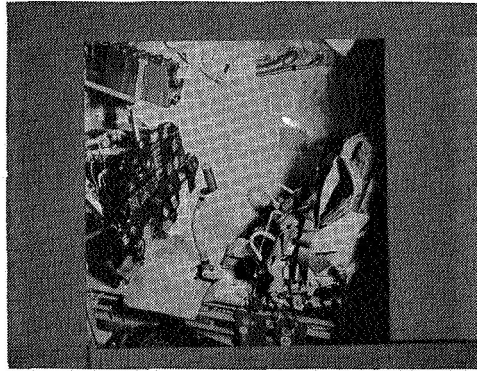


Figure 17: A cockpit simulation in the centrifuge gondola.

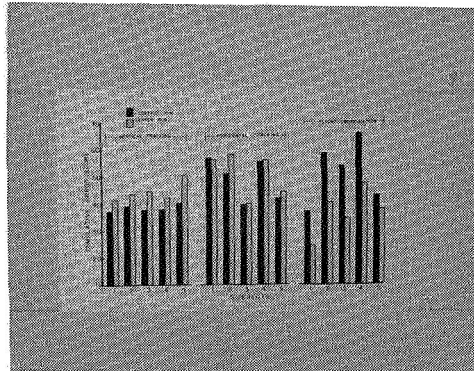


Figure 18:

Integrated error scores for performance of a tracking task during closed-loop centrifuge control and with the centrifuge stationary. Note the improvement in flight coordination and the degradation of vertical tracking during closed-loop control.

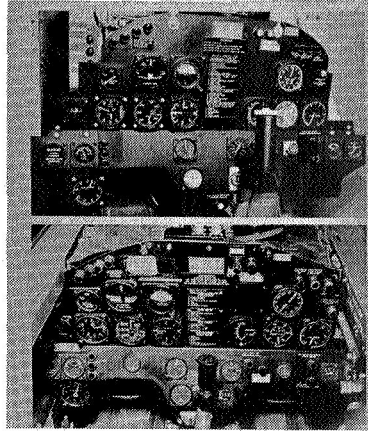


Figure 19: Instrument panel for a TV-2 aircraft simulation at the top and photograph of the actual panel at the bottom.

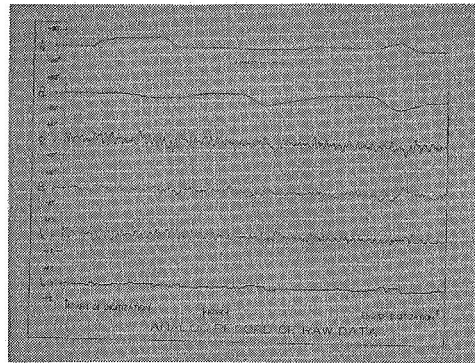


Figure 20: Analog record of raw data in a study of the validity of centrifuge simulations of the TV-2 aircraft.

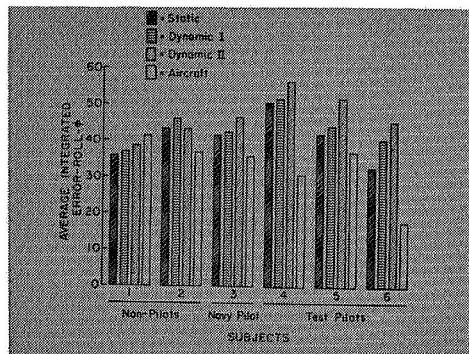


Figure 21: Integrated error scores for roll control in the TV-2 study.

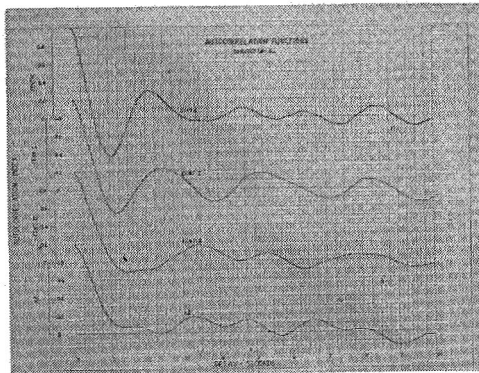


Figure 22: Autocorrelation index functions for roll control in the TV-2 study

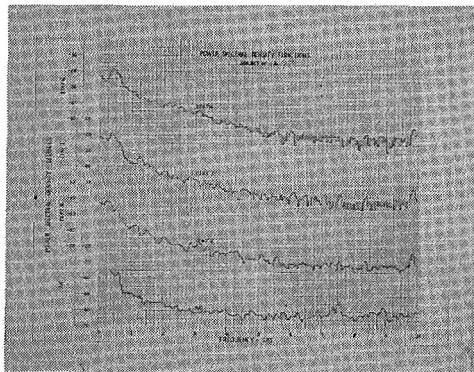


Figure 23: Power spectral density functions for roll control in the TV-2 study.

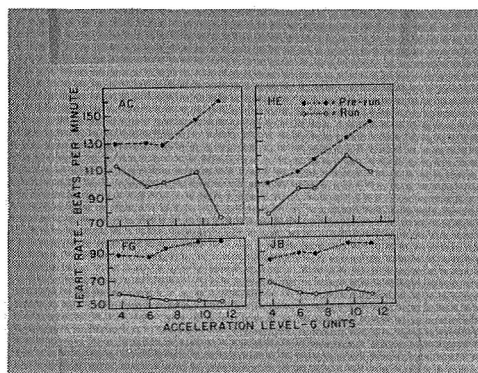
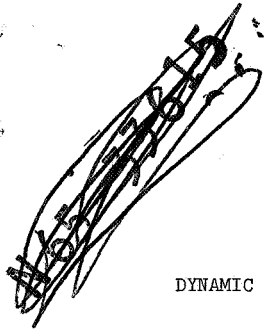


Figure 24: Subject heart rate as a function of acceleration. Dashed lines represent heart rate after the subject was told what acceleration would be, but before the run started. Solid lines represent heart rate during the run.



DYNAMIC SIMULATORS FOR TEST OF SPACE VEHICLE
ATTITUDE CONTROL SYSTEMS

by

G. Allan Smith

NASA - Langley Research Center

INTRODUCTION

Both manned and unmanned spacecraft are designed to carry out a variety of missions in support of NASA programs for the exploration and exploitation of space. The great majority of these spacecraft require some sort of attitude control in order to carry out their assigned mission. The scientific spacecraft utilize radio to transmit their data back to earth so it is necessary to point an antenna. Many satellites depend upon panels of solar cells to supply power and hence the satellite must be oriented so that the panels receive maximum solar radiation. The nature of certain scientific experiments requires that instruments maintain a specified orientation, in the case of one of the largest and most complex satellites, the orbiting astronomical observatory (OAO), the entire spacecraft must be precisely pointed at a star in order to observe it with the large telescope rigidly

mounted to the vehicle. Spacecraft designed for lunar or planetary missions will be required to make trajectory corrections in route so the thrust vector must be properly oriented. A precise thrust vector orientation must also be achieved in order to go into orbit around the moon, or a planet, or to re-enter the earth's atmosphere from orbit.

There are four primary factors that determine the performance of a spacecraft attitude control system. They are:

- (a) Spacecraft inertia
- (b) External torques (solar pressure, gravity gradient, micrometeorites)
- (c) Applied torque (from controller)
- (d) Attitude sensors

In the development of a control system these factors must be considered during the analytical formulation, and they are likewise important for dynamic system simulation which has come to play an essential role in the verification and refinement of performance when actual components are employed.

Two important and unique features of the space environment especially pertinent to attitude control systems are the cancellation of gravity effects by the trajectory acceleration, and the virtual absence of frictional resisting torques due to the near vacuum environment. These features can be accounted for during analytic investigation and computer simulations, but present a problem for simulation studies that involve physical equipment. No method of simulating zero gravity is available in the laboratory although gravity effects can be minimized in a dynamic simulation to the extent that the center of rotation can be made to coincide with the center of gravity. The most satisfactory way to simulate the low friction aspect of the space environment is by the use of the airbearing supported test platform, and the remainder of this paper will deal with the design and use of airbearing platforms for space vehicle attitude control system studies and tests. It

will be shown that the airbearing platform provides a mounting of extremely low friction with wide orientation capability. It does not duplicate the zero gravity effect, but it can permit sensitive balance to bring the center of gravity very close to the center of rotation and hence minimize pendulous effects. Essentially, the airbearing platform permits an accurate representation of spacecraft inertia and realistic use of the actual vehicle attitude control torque sources and sensors.

THE AIRBEARING PLATFORM

Figure 1 is a picture of an airbearing supported platform constructed at NASA Ames Research Center in 1959. It may appear very simple compared to the present state of the art as exemplified by several large and complex facilities in the aerospace industry, but it illustrates most of the fundamental advantages and problems of airbearing tables. The table is supported by a 5-inch-diameter spherical aluminum bearing which has a cylindrical neck to which the frame of the platform is bolted. The bearing seat is a matching hemisphere of epoxy resin cast into a metal cup that rests upon a four-legged support to the floor. The raised center construction puts the center of rotation about three inches above the working platform to minimize the need for extra balance weights to maintain the platform in pendulous balance as attitude control equipment is added to the platform. A major effort is made to keep the table center of rotation and center of gravity coincident so that gravity effects will be avoided. In fact, a fundamental and ubiquitous problem in the use of airbearing platforms is to avoid torques due to gravity unbalance. The use of stiffened rib construction in this platform is an attempt to prevent platform flexure with changes in pitch and roll. Such flexure is termed an

anisoelectric effect and considerable theoretical and design effort is expended to minimize the resultant gravity torque in the most precise facilities. The platform in Figure 1 supports an optical sensor to provide an electrical error signal as the platform attempts to drift from a desired orientation. This error signal actuates the inertia wheels which develop a torque to maintain the desired platform attitude. It will be noted that these wheels are in a plastic enclosure to assure that they provide torque only by their inertial effect and not by friction against the air.

Figure 2 is a photograph of a similar platform in operation with a more elaborate control system. The entire platform is enclosed beneath a hood to avoid thermal air currents in the laboratory that can cause serious interference torques, a manifold is also installed around the spherical bearing to pump off the air used for support, a number of small wires are brought from the base to the table around the airbearing. This causes a slight interference torque but permits operational flexibility by providing electrical power and instrumentation connections to the laboratory bench. Two two-axis star trackers are mounted on the table to give control signals in all three axes. Three torquers are used, each of which utilizes a pair of control moment gyros (Ref. 1). This equipment was used to investigate dynamic performance when the table was displaced through small angles from the reference light sources - about 1/2 degree. It was necessary to tape all wires to the table as slight shifts with table attitude changes caused unbalanced effects. This equipment was able to maintain its reference attitude within about one second of arc in all three axes.

IMPORTANT CONSIDERATIONS IN AIRBEARING TABLE DESIGN AND OPERATION

The foregoing pictures and descriptions of specific test platforms will

serve to introduce the subject of design problem areas which is the primary concern of this paper.

Design problems arise because it is desirable from a research standpoint (and the airbearing platform is essentially a research tool) to provide maximum convenience in the operation of the platform and at the same time to maintain all interfering disturbance torques at a very low level to simulate their absence in space. The most important operational flexibility requirements include the ability to substitute various pieces of equipment on the the platform quickly; the ability to supply electrical power to equipment on the table; the ability to measure the instantaneous attitude of the table; the ability to utilize a variety of platform torque sources including inertia wheels, control moment gyros, magnetic field torquers and gas reaction jets; and the ability to use various tracking devices such as star trackers, planet trackers, sun trackers, horizon scanners and inertial sensors.

The most straightforward way to carry out equipment modifications on an airbearing platform by simple interchange of components would introduce significant unbalance torques. A major design effort is therefore expended in providing the required operational flexibility by means that keep the interfering torques at an acceptable level. In general, the replacement of a piece of equipment will cause a shift of the platform center of gravity away from the center of rotation and the resulting unbalance torque due to gravity will be balanced out by shifting adjustable weights on the platform.

In order to judge how serious various disturbing torques are, the following is an estimate of disturbance torques that will act upon an actual satellite in orbit. One of the largest NASA scientific satellites that will require very precise attitude control will be the Orbiting Astronomical Observatory. As shown in Figure 3, it will approximate a cylinder 6 feet in

diameter and 10 feet long. It will weigh 3600 pounds and have a maximum moment of inertia of 1450 slug feet squared. While in orbit at 500 miles, it will experience gravity gradient torque of 600 dyne cm, radiation torque of 150 dyne cm, aerodynamic drag torque of 150 dyne cm, and magnetic torque of 600 dyne cm. The control system must be designed to cope with these torques in space as well as to change satellite attitude on command. It would be desirable if the interfering torques acting on a ground based airbearing facility used to simulate the control system operation could be kept below these values. This level of disturbance torque is however quite low and very difficult to obtain in a ground based environment. It will be recalled that the dyne cm is an extremely small unit of torque; an ounce inch is 70,615 dyne cm, and a foot pound is 13,558,200 dyne cm.

PLATFORM DISTURBANCE TORQUES

The disturbance torques acting on an airbearing table have been categorized into the four groups of Figure 4. These torques will be considered in sequence.

The first group depends upon the construction of the airbearing platform itself. The first five platform torques in the first group are basically due to gravity acting on a shift of the center of mass from the center of rotation. They are minimized by construction of a platform that is very rigid and made from materials that do not deform as the platform attitude is changed, or as temperature changes. Solenoid valves used to release jet thrust or relays used to cage gyros will cause impulsive torques, and unbalance torques as the solenoid element shifts position.

The second group of torques arise in the support. The airbearing itself

contributes aerodynamic turbine torques if the airflow is not precisely symmetrical. Exhaust air impingement on the platform due to imperfect scavenging of the bearing also produces a torque.

The environmental torques of the third group are particularly troublesome. An aerodynamic damping torque will arise as the platform moves through the air. Some large industrial facilities have placed the entire table in a vacuum chamber to eliminate this torque. One of the most serious torques is due to the effect of stray air currents acting on the platform. It may not be convenient to place the platform in a vacuum chamber, but work to any reasonable degree of precision requires that the platform be located within some sort of shielding enclosure. An effort should be made to construct the table from nonmagnetic materials. Some current research platforms are placed between three pairs of large Helmholtz coils which can neutralize the earth's field. Vibration effects are minimized by mounting the airbearing support pedestal on an isolated seismic block.

The fourth group of torques in Figure 4 depends upon the particular scheme used to mechanize the control system being tested. Unbalance torques due to unsymmetrical depletion of tanks as compressed gas is used for reaction thrust can be appreciable. Even carefully balanced pairs of compressed gas tanks with a common manifold are still troublesome as they expand under pressure and shift slightly. Mass unbalance torques within batteries as they discharge are so difficult to compensate that research investigations frequently utilize laboratory electrical power supplies with very flexible leads dropped into the center of the platform. For research purposes the requirements for frequent modification of equipment are so important that some sort of automatic or semi-automatic balance system is needed. A simple arrangement of three weights that can be motor driven linearly along mutually perpendicular directions can be

controlled by an operator observing table motion or can be slaved to sensitive rate gyros or linear accelerometers to achieve rebalance after any change of platform load.

PLATFORM BALANCE CALCULATIONS

Figure 5 illustrates an unbalance with the platform horizontal because the center of gravity is displaced horizontally and vertically by distances x and y from the center of rotation. When the platform rotates through an angle θ from its horizontal position the torque due to gravity is

$$T = -Mgx \cos \theta - Mgy \sin \theta \quad (1)$$

If the platform is allowed to oscillate as a pendulum through a very small angle, the period will be

$$T = 2\pi \sqrt{\frac{I}{MgL}} \quad (2)$$

(for very small unbalance, the moment of inertia I measured about the center of rotation is very close to I measured about the center of gravity). The period can be used to compute the distance L between the center of rotation and center of gravity. Practical measurements of unbalance involve instrumentation techniques that will be discussed later, but if it is assumed that platform angles and external applied forces can be measured to great enough precision, then certain simple calculations can help greatly in the actual task of balancing a platform.

The horizontal shift of the center of gravity can be determined by measuring the externally applied torques T_1 and T_2 required to maintain the platform at equal and opposite angles θ and $-\theta$. Applying equation (1) with applied torque equal to minus gravity unbalance torque

$$T_1 = Mgx \cos \theta + Mgy \sin \theta \quad (3)$$

$$T_2 = Mgx \cos \theta - Mgy \sin \theta \quad (4)$$

$$x = \frac{T_1 + T_2}{2Mg \cos \theta} \quad (5)$$

$$y = \frac{T_1 - T_2}{2Mg \sin \theta} \quad (6)$$

For example, in simulating a spacecraft as large as the Orbiting Astronomical Observatory with a weight of 1600 kilograms and a 2000 kilogram meter squared moment of inertia, a horizontal center of gravity displacement of one hundredth of a cm would produce a gravity unbalance torque of

$$T = -Mgx = 1600 \times 10^3 \times 980 \times 10^{-2} = 15.7 \times 10^6 \text{ dyne cm}$$

For another example, a center of rotation - center of gravity shift of a hundredth centimeter would produce a pendulous period of

$$T = 2\pi \sqrt{\frac{I}{MgL}} = 2\pi \sqrt{\frac{2000}{1600 \times 9.8 \times 10^{-4}}} = 224 \text{ sec}$$

Anisoelastic effects are due to deformations of the platform that change

as the platform angle with respect to gravity changes. Figure 6 shows these effects. The top left figure shows an undeformed platform as it would appear in the absence of gravity. The top right figure shows a deflection due to the effect of gravity acting on the mass of the table which is assumed to be concentrated in two blocks which each exert a torque $MgL/2$ to bend the table. Each block is deflected downward a distance d_o . It is assumed that the platform center of gravity and center of rotation coincide in this normal gravity loaded position. The bottom figure shows how the platform begins to straighten out as it tips. The torques causing platform deflection are reduced from $MgL/2$ to $(MgL/2) \cos \theta$.

Since the deflection is small and varies from a maximum (d_o) for the platform level at $\theta = 0$ to zero when the platform is vertical $\theta = 90^\circ$ it is a reasonable approximation to assume that the deflection varies proportionally to the torque and at any tilt angle θ would be $d = d_o \cos \theta$. The distance by which the center of gravity rises above the center of rotation perpendicular to the platform as the platform tilts, is

$$e = d_o - d = d_o(1 - \cos \theta)$$

At any tilt angle θ this center of gravity shift causes a disturbance torque

$$Mge \sin \theta = Mgd_o(1 - \cos \theta) \sin \theta = Mgd_o(\sin \theta - 1/2 \sin 2\theta)$$

It is interesting to note that the disturbance torque due to anisoelectricity has components proportional to both θ and 2θ . A numerical example for the platform values considered previously with a maximum bending deflection of $d_o = 0.01$ cm shows an unbalance torque at 20° of

$$T = 1600 \times 10^3 \times 980 \times 10^{-2} \left(0.34202 - \frac{0.64279}{2} \right)$$

$$= 318,000 \text{ dyne cm}$$

Another interesting disturbance torque that can act upon a platform is due to gravity gradient. The force of gravity falls off inversely as the square of the distance from the center of the earth. A simplified analysis would consider that at a reference level it would be $g_o = G/R^2$ where R is the radius of the earth at the reference. At an altitude h above the reference level it would be $g = G/(R+h)^2$. In Figure 7 the table is tipped through an angle θ so the vertical displacement between the two concentrated centers of mass is $h = 2L \sin \theta$. If the torque due to the lower mass at the reference altitude is $(M/2)g_o L \cos \theta$, that due to the upper mass is $-(M/2)gL \cos \theta$ so the net torque is

$$T = \frac{ML}{2} \cos \theta [g_o - g]$$

$$= \frac{ML}{2} \cos \theta \left[\frac{G}{R^2} - \frac{G}{R^2 \left(1 + \frac{h}{R}\right)^2} \right] = \frac{ML}{2} \cos \theta \left[\frac{G}{R^2} \frac{2h}{R} \right]$$

if terms in h^2 are dropped. Inserting the expressions for h and g the next torque due to gravity gradient is then

$$T = 2M_{g_o} L^2 \frac{\cos \theta \sin \theta}{R} = \frac{M_{g_o} L^2 \sin 2\theta}{R}$$

It is interesting to note that this is a function of twice the tilt angle in a fashion similar to anisoelectric torque. For the previous example with two

800 kilogram concentrated weights one meter apart at a tilt angle of 30° and
R = 6371 km

$$T = \frac{1600 \times 10^3 \times 980 \times 50^2 \times 0.866}{6371 \times 10^5} = 5340 \text{ dyne cm}$$

This simplified analysis neglects the fact that the radii from the center of the earth to the two concentrated masses are not strictly parallel. A more rigorous derivation (Ref. 2) would reveal that the gravity unbalance torque is increased 50% by this effect from

$$\frac{M}{g_o} \frac{L^2 \sin 2\theta}{R} \text{ to } \frac{3}{2} \frac{M}{g_o} \frac{L^2 \sin 2\theta}{R}$$

OPERATIONAL AIRBEARING PLATFORMS

The next few figures will illustrate some currently operational platforms that have been used to investigate a variety of satellite attitude control systems. They will give an idea of the designs used by different groups and indicate some of the possible refinements that have been employed.

a. Jet Propulsion Laboratory

Figure 8 is a photograph of a platform developed by the Jet Propulsion Laboratory. This platform represents the second generation of airbearing equipment developed at JPL and incorporates several interesting features. The platform is made very stiff by the use of heavy metal plates in a webbed construction so unbalance torques due to platform deformation are kept below 10 gram cm. Stainless steel construction is used to minimize magnetic torques from the earth's field. The platform weighs 800 pounds before mounting any

experimental equipment. A 30-channel telemetry system is utilized instead of any wires between the platform and the laboratory. Sealed nickel cadmium batteries are used for power on the platform. They contribute less than 5 gram cm torque for a 90° platform tip. An automatic balance system drives weights along three axes in response to sensitive rate gyro signals to achieve static balance before testing. The bearing is a 10-inch-diameter beryllium ball spherical to within ± 30 micro inches. The bearing pad is 5 inches across and has two concentric circles of air jets, one circle 1-1/2 inches in diameter has ten jets. The other circle 3.6 inches in diameter has 23 jets. The pad mounting assembly provides a nylon ring as a support for the ball and table at times when there is no air pressure applied. The bearing pad itself is so constructed that it rises as a piston with air pressure. About 140 psi air supply is required to float the table. An attitude control system mounted on the table has included gyros, sun sensors, canopus sensor and control jets. Figure 9 shows the offset pedestal which allows the platform to tip past 90°. Figure 10 shows how the entire pedestal can be motor-driven to swing out of the way to allow maximum tip in any direction.

b. Ames Research Center

Figure 11 is a sketch of an airbearing supported man-carrying platform used at Ames Research Center of NASA to evaluate twin gyros as an attitude control torque source (Ref. 1). Star trackers with a resolution of 2 arc seconds were used as attitude sensors. The passenger was constrained to a movement while manipulating a theodolite as a planet tracker. The control system was able to maintain the platform attitude to within 5 arc seconds. Figure 12 is a photograph of this platform. Compressed air was used to unload the twin gyro controllers; motor-driven balance weights along three axes were used for static balance. The platform weighed 1800 kilograms and was

supported on a 24-cm stainless steel ball in an epoxy resin seat by about 300 psi air through a single hole in the bottom of the bearing seat.

c. Langley Research Center

Figure 13 is a photograph of an airbearing supported platform used at the Langley Research Center of NASA to investigate a wobble damper for a spinning satellite (Ref.3). The platform is supported by a 6-inch-diameter stainless steel ball in an epoxy resin seat. Air at 20 psi is admitted through a 0.09-inch-diameter hole in the bottom of the seat. After this platform is spun up to about 20 rpm by the motor mounted on the overhanging beam, the beam is swung out of the way to allow the platform ± 20 degrees of freedom to tip about a horizontal axis.

Figure 14 is a photograph of another airbearing platform that was used at the Langley Research Center to test a satellite attitude control system using both inertia wheels and a large bar magnet (Ref. 4). This table was supported by a 3-inch-diameter brass ball in an aluminum seat. Air at 15 psi was admitted through 12 holes located around the cup. Power was connected to the platform through small-coiled wires suspended above the center of the table.

d. Marshall Space Flight Center

Figure 15 is a photograph of an early airbearing table constructed by the Marshall Space Flight Center of NASA. The offset support permits $\pm 120^\circ$ attitude change in roll and pitch and unlimited freedom in yaw (Ref. 5). The bearing is a 10-inch-diameter ball manufactured to a tolerance of 50 millionths of an inch. Air is admitted to the bearing cup through tiny holes arranged in two concentric circles and is vented both at the edge and at the center of the cup. The platform is balanced by first applying a brake to the ball to keep the table stationary, and then measuring table motion when the brake is released. Balance weights are then adjusted to minimize the motion. Two rather clever

devices are employed for fine balance. Steel strips are attached to the platform by nylon mounting pads whose large temperature coefficient causes a shift in the center of gravity of the steel strips to compensate for temperature effects on the table as a whole; also three pairs of cantilever springs with weights attached can be used to compensate for anisoelastic torques by generating a torque which to a first approximation varies with the sine of twice the deflection angle of the platform. No external connections are made to this table, dry cell batteries are used on the platform, and information from the control system is telemetered out.

Figure 16 illustrates a second generation platform recently installed at Marshall Space Flight Center. This platform is a highly symmetrical disc-shaped body and offers extreme rigidity and large moments of inertia with minimum mass. The platform is built of nonmagnetic material (aluminum) and is specially treated to prevent warping. The bearing consists of an aluminum sphere and cup. To balance the simulator it is temporarily constrained to rotate about a single axis by means of a small auxiliary spherical airbearing which can be attached to the platform at any of three locations which represent three orthogonal axes about which balance is to be achieved. Acceleration is then measured about the axis of freedom in order to compute the unbalance torque. A recent communication from Marshall made the following comments about this platform:

At Marshall the major problem encountered while attempting to employ the simulator for control system studies has been that of achieving and maintaining balance at any angular position. The sources of unbalance that exist in general and current methods of overcoming them are tabulated below:

1. Torque caused by platform deformation which results from:
 - a. Heating by radiation from external reference sources such as sun, star or earth simulators.

- b. Heating by radiation and conduction from onboard instrumentation.
(No completely satisfactory solution for a and b.)
 - c. Changes in the ambient temperature of the room.
(Solved by very accurate control of room temperature.)
 - d. Gravity anisoelasticity torques. (Solved by cantilever spring mass compensators.)
2. Airbearing or "turbine" torques.
3. Torques due to nonsphericity of the bearing. (Both 2 and 3 solved by holding airbearing manufacturing tolerances to the minimum allowed by the state of the art - ten millionths of an inch.)
4. Torques caused by air currents which result from:
- a. Room air conditioning system.
 - b. Convection currents from hot equipment in the room or onboard the simulator. (A complete solution would require operation in a vacuum chamber. A close fitting enclosure and shut-down of room air conditioning and ventilation will help.)
5. Torques caused by shift of the center of mass of onboard batteries.
(No satisfactory solution. It has been determined that the mass shift is a function of angular position, time in the angular position, and discharge rate.)
6. Torques caused by shift of mass of onboard instrumentation.
- a. Relay armatures. (Solved by use of solid state switching or employment of balanced armature relays.)
 - b. Deformation of wiring harnesses and components. (Solved by constructing rigid containers with securely attached components and solidly anchored to the platform. All wiring harnesses are potted and anchored.)

7. Torques caused by shift of the composite mass of the simulator due to depletion of an onboard propellant supply - compressed gas.
(Solved by making the center of mass of the propellant cavities coincident with the center of rotation of the platform.)
8. Torques caused by gravity gradient. (Solved by use of the anisotropy compensators since it is a function of twice the tilt angle of the platform.)
9. Torques caused by the earth's magnetic field. (Solved by using 3 pairs of Helmholtz coils to cancel the earth's field.)

e. United Aircraft Corporation

There are several large and complex airbearing installations in industry. Three of these, those at United Aircraft, Grumman, and General Electric, will be described to fill out the picture of existing research facilities.

Figure 17 is a picture of the airbearing facility at United Aircraft Corporate Systems Center, Farmington, Connecticut. This platform is distinguished by a very accurate attitude measurement system. The 5-foot-diameter table is surrounded by a three-axis following gimbal system which utilizes autocollimator signals to track the airbearing platform without any physical contact. Angular pickoffs on the gimbal axes then provide attitude data for the platform to within a few seconds of arc. The platform is supported on a 16-inch-diameter airbearing. The sphericity of the ball is within approximately 100 micro inches; it has a surface finish of 5 micro inches. The bearing is supported with dry nitrogen at 250 psi and about 12 cubic feet per minute. With a full load of 8000 pounds on the platform the clearance between the bearing and its seat is about 0.001 inch. There are no external wires connected to the table. All instrumentation power is supplied from onboard batteries and data is telemetered from the table. Ventilation air flow through the laboratory is

is kept to a minimum, controlled to within $\pm 3^\circ$ F in temperature and filtered of dust particles larger than 0.3 micron diameter.

f. Grumman Aircraft Engineering Corporation

Figure 18 is a pictorial representation of the airbearing facility at Grumman Aircraft Engineering Corporation, Bethpage, New York (Ref.6). The platform is enclosed in a chamber that can be evacuated to 0.75 millimeters of mercury to effectively eliminate air current effects which are a very troublesome source of extraneous torques. Three pairs of Helmholtz coils 14 feet in diameter surround the platform to first neutralize the earth's magnetic field and then simulate on a dynamically programmed basis the magnitude and direction of the changing field at satellite altitude during a simulated orbit. For star tracking studies five collimators, 5 inches in diameter, are located within the chamber. They can represent stars from -1.0 to +6.0 magnitude. Each provides a star whose angular subtense is less than eight arc seconds with a parallax error less than five arc seconds. The entire chamber is mounted on a 110-ton concrete seismic foundation.

g. General Electric Company

Figure 19 is a photograph of one of the airbearing installations at the General Electric Company, Space Technology Center, Valley Forge, Pennsylvania (Ref.7). The photograph shows an engineering mock up of the orbiting astronomical observatory mounted on a 10-inch-diameter stainless steel ball. The photograph was taken during the fine balance of the platform and small catenary chains connected from the platform to supporting posts can be seen. This is part of their "chain-o-matic" procedure for balance. This procedure utilizes the chains to apply a proportional restoring torque to the platform so that the oscillation period is shortened by an order of magnitude. This allows much more rapid adjustment of weights for fine balance. Balance shifts due to

temperature changes have been overcome by maintaining full electrical power to the test platform on a continuous 24-hour-a-day basis.

Another development platform at General Electric has interesting features. Attitude is read out to a few seconds of arc by a small three-axis following gimbal system built around the bearing support beneath the platform. Mounted on this gimbal system are magnetic torques that can apply precisely measured torques to the platform at any attitude. In conjunction with the precision attitude measuring system this permits the kind of torque and angle measurements discussed in the section on platform balance calculations. An additional feature of this platform is the use of a ball support with a 1/2-inch-diameter hole drilled clear through so that air from the bearing support can be transferred to the platform for use in air jet attitude control systems without the unbalance that can occur as onboard tanks are depleted.

CONCLUSIONS

It seems apparent that the technology of airbearing platforms has moved swiftly from a simple qualitative research tool some five or six years ago, to a complex and potentially quite precise quantitative instrument for investigation of a wide variety of attitude control research problems and performance verification studies. In order to overcome the numerically small but theoretically important extraneous platform torques due to gravity unbalance, and externally applied forces, it appears necessary to construct rather elaborate facilities. The possibility of quite precise quantitative numerical data is presented by such features as: isolation in a vacuum chamber and construction of a following gimbal system for attitude readout with its additional use for applying calibration torques to the platform and providing a virtually disturbance free means for connecting electrical wires to the platform.

REFERENCES

1. Havill, Jerry R., and Ratcliff, Jack W.: A Twin-Gyro Attitude Control System for Space Vehicles. NASA TN D-2419, Aug. 1964.
2. Debra, Dan: Vectors and Dyadics, the Natural Tools of Space Vehicle Mechanics. Presented at American Astronautical Society Meeting held in San Francisco, Calif., Aug. 1, 1961.
3. Adams, James J.: Simulator Study of an Active Control System for a Spinning Body. NASA TN D-1515, Dec. 1962.
4. Adams, James, J., and Howell, W. E.: Simulator Study of a Satellite Attitude Control System Using Inertia Wheels and a Magnet. NASA TN D-1969, Oct. 1963.
5. Haeussermann, Walter, and Kennel, Hans: Satellite Motion Simulator. Published in the ARS December 1960 edition of Astronautics, Vol. 5, no. 12.
6. Imgram, D. A., Muench, W. K., and Rabb, L.: Dynamic Testing of the OAO Stabilization and Control Subsystem. AIAA Paper no. 63-176. AIAA Summer Meeting, Los Angeles, Calif., June 1963.
7. Bachofer, B. T., and Seaman, L. T.: Air-Bearing Dynamic Testing - One Arc Second Accuracy. AIAA Paper no. 64-205, 1st AIAA Annual Meeting, Washington, D. C., June 29 - July 2, 1964.

**EARLY AIR BEARING PLATFORM
AMES RESEARCH CENTER - 1959**

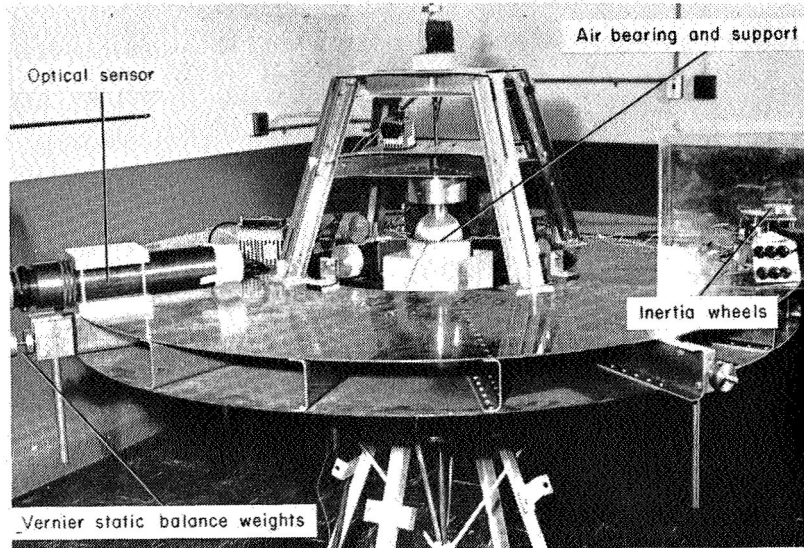


Figure 1

**PLATFORM WITH TWIN GYRO ATTITUDE CONTROL
SYSTEM**

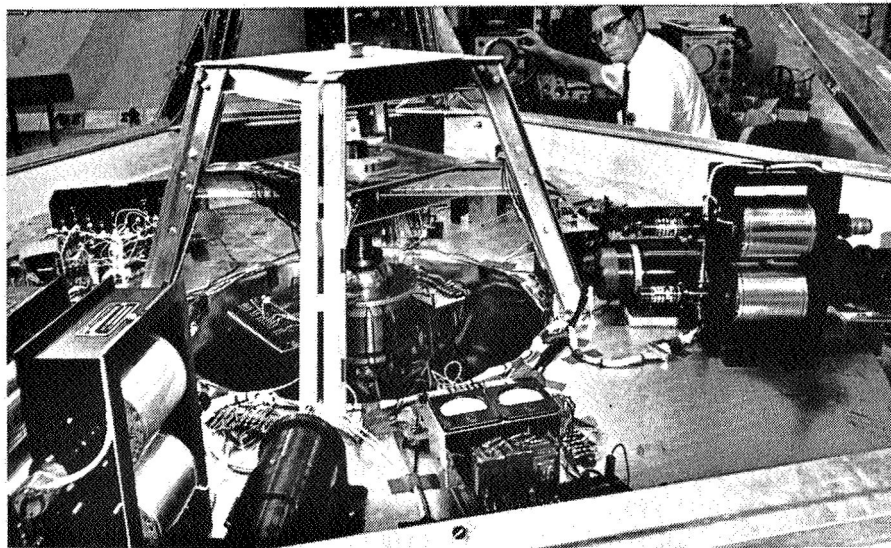


Figure 2

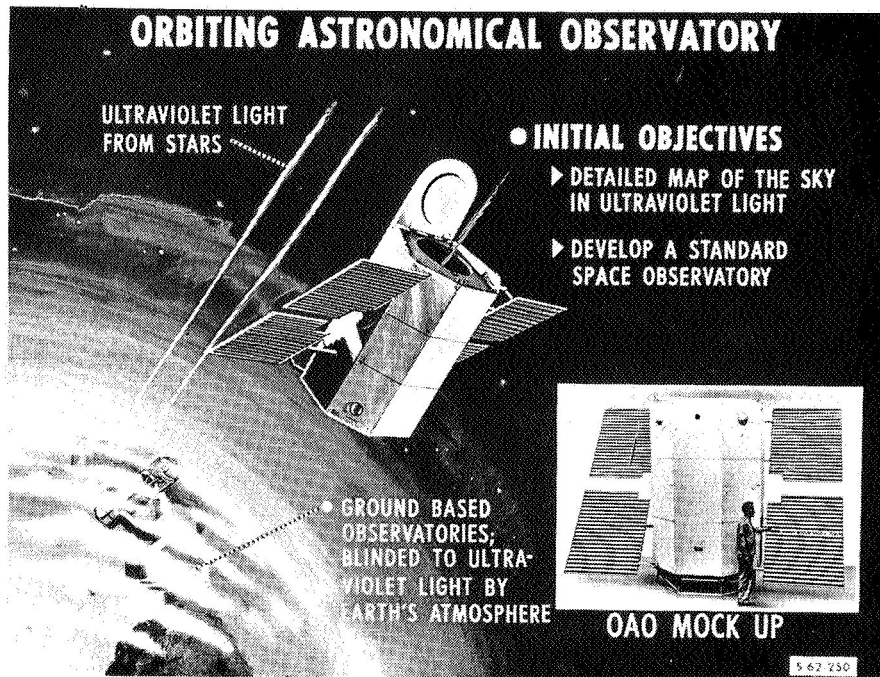
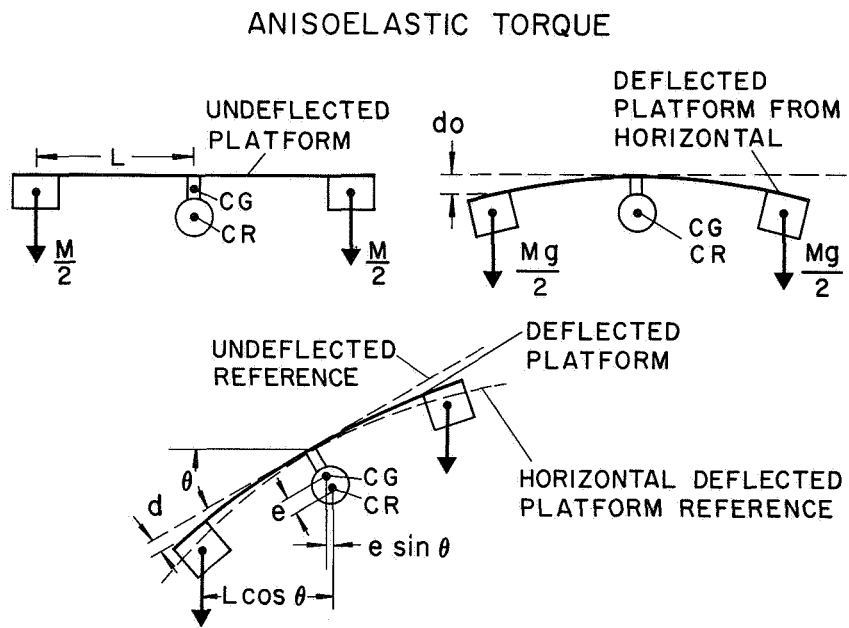
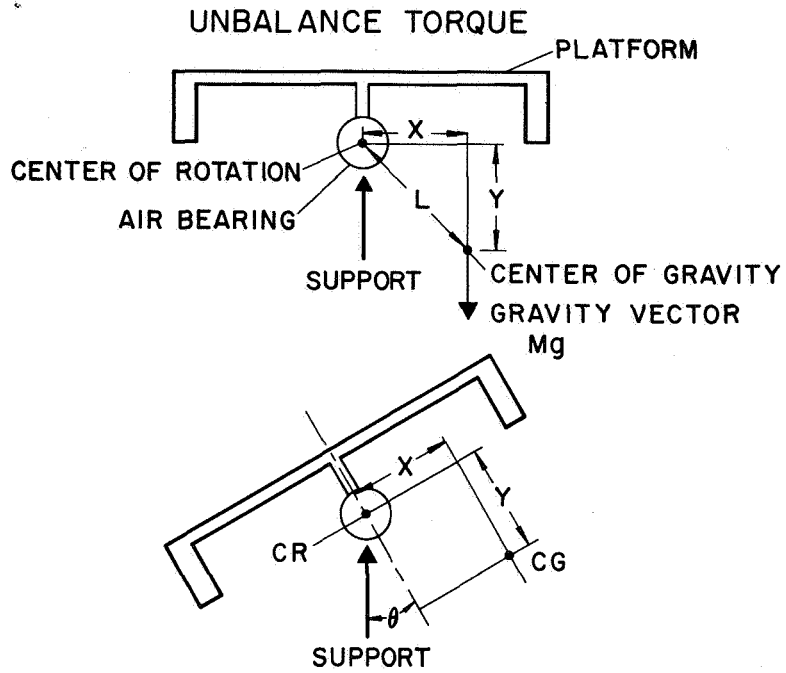


Figure 3

DISTURBING TORQUES ON AN AIR-BEARING PLATFORM

- | | |
|---|--|
| <p>I TORQUES ARISING FROM PLATFORM</p> <ul style="list-style-type: none"> STATIC UNBALANCE DYNAMIC UNBALANCE ANISOELASTICITY MATERIAL INSTABILITY STRESS-TEMPERATURE-HUMIDITY-EVAPORATION GRAVITY GRADIENT EQUIPMENT MOTION SOLENOIDS-RELAYS | <p>III TORQUES FROM ENVIRONMENT</p> <ul style="list-style-type: none"> AIR DAMPING AIR CURRENTS MAGNETIC FIELDS VIBRATION RADIATION PRESSURE |
| <p>II TORQUES FROM BEARING</p> <ul style="list-style-type: none"> AERODYNAMIC TURBINE EFFECT EXHAUST AIR IMPINGEMENT | <p>IV TORQUES FROM TEST SYSTEM</p> <ul style="list-style-type: none"> ELECTRICAL WIRES TO BASE MASS SHIFT IN BEARINGS AND LOOSE FITS BATTERY DISCHARGE REACTION JET SUPPLY DISCHARGE REPLACEMENT OF COMPONENTS |

Figure 4



GRAVITY GRADIENT TORQUE

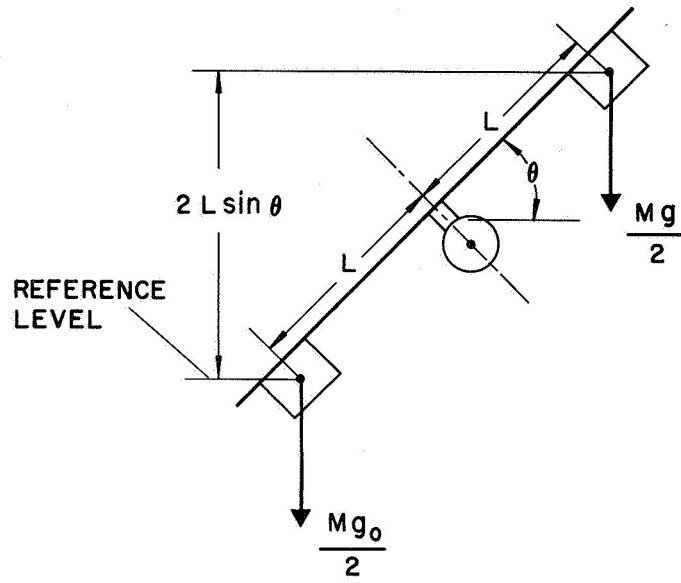
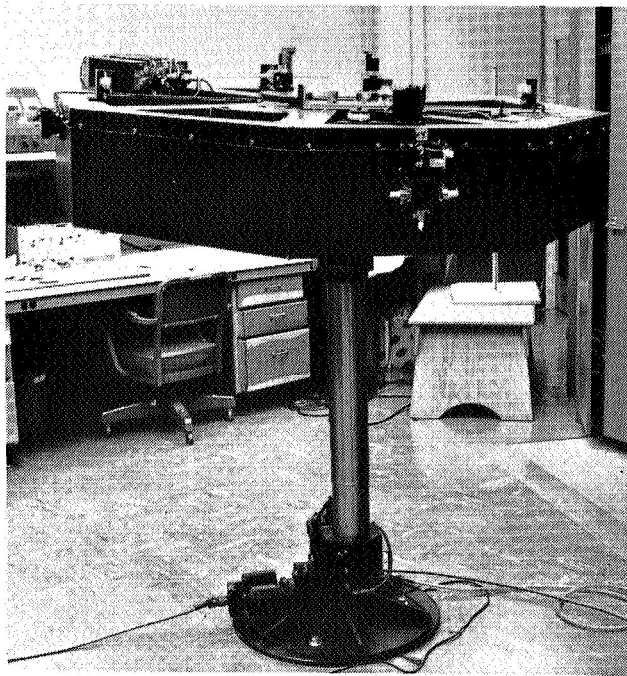
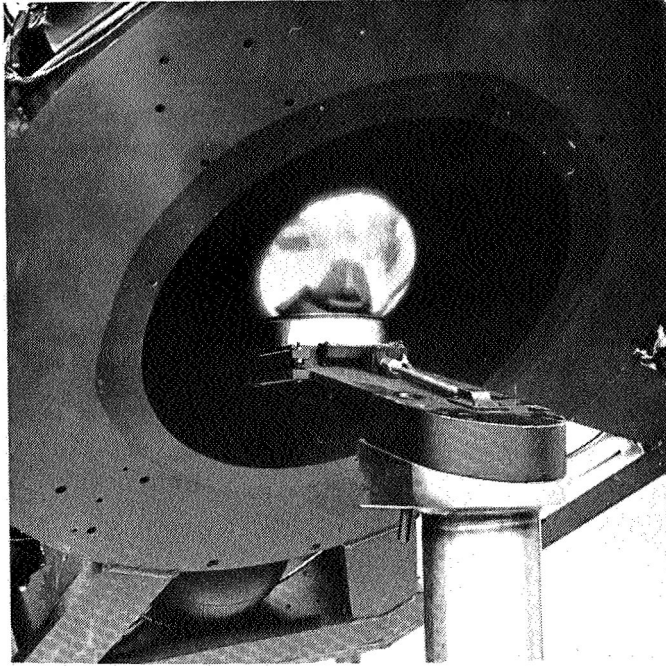


Figure 7



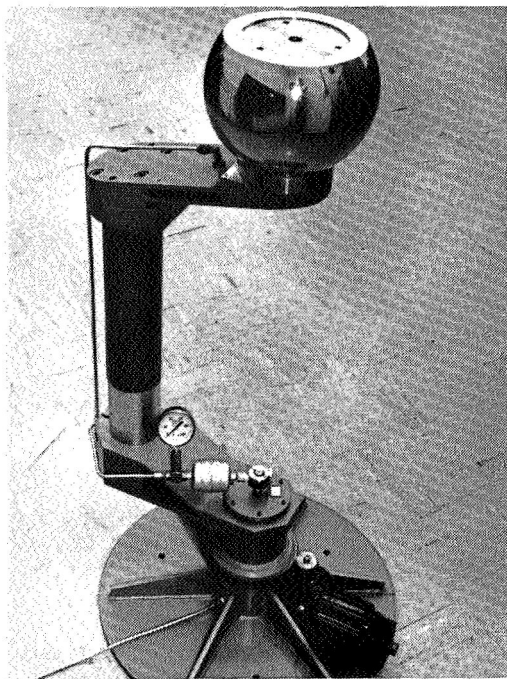
JPL
AIR BEARING
PLATFORM

Figure 8



JPL
ECCENTRIC
BEARING

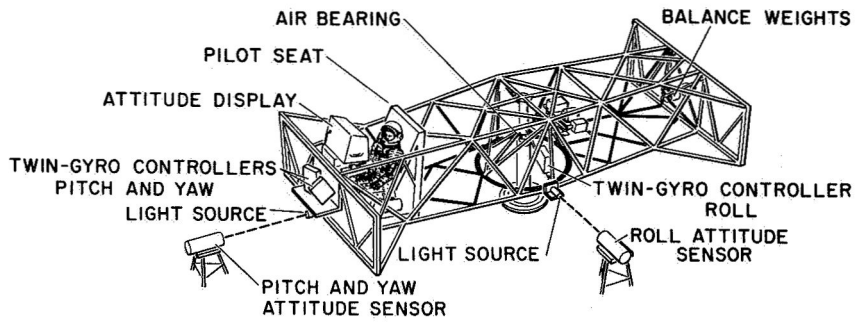
Figure 9



JPL
PEDESTAL

Figure 10

SCHEMATIC VIEW OF SPACE VEHICLE ATTITUDE SIMULATOR



LENGTH	730 cm	ROLL MOMENT OF INERTIA	$8 \times 10^9 \text{ gm-cm}^2$
WIDTH	365 cm	PITCH MOMENT OF INERTIA	$9 \times 10^{10} \text{ gm-cm}^2$
HEIGHT	125 cm	YAW MOMENT OF INERTIA	$1 \times 10^{11} \text{ gm-cm}^2$
WEIGHT	1800 kg		

Figure 11

SPACE VEHICLE ATTITUDE SIMULATOR

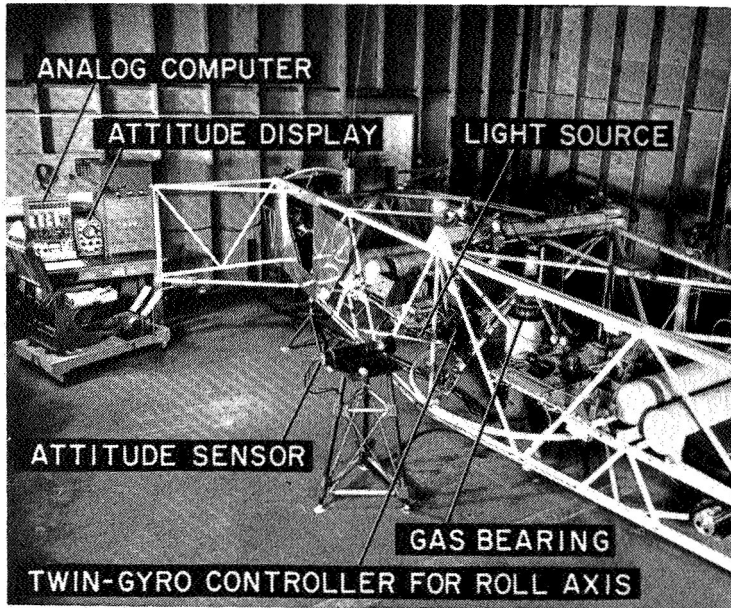
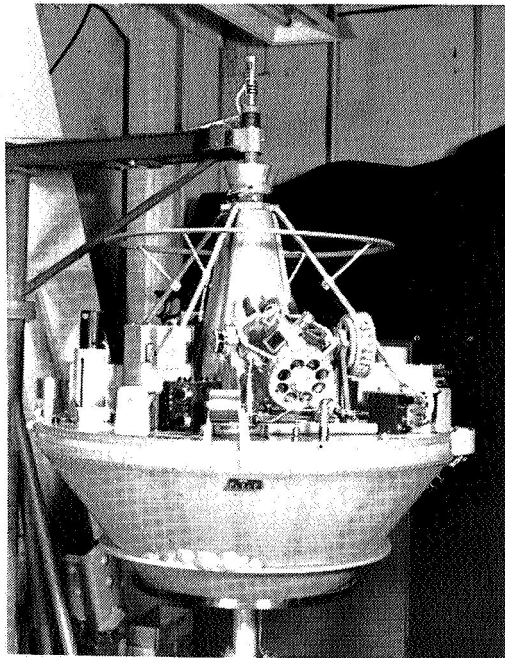


Figure 12



**LANGLEY
RESEARCH CENTER
SPINNING SATELLITE
SIMULATOR**

Figure 13

LANGLEY PLATFORM WITH MAGNETIC TORQUER

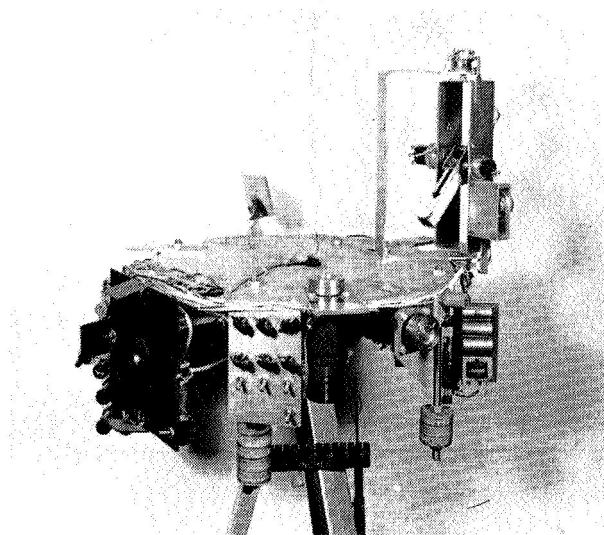
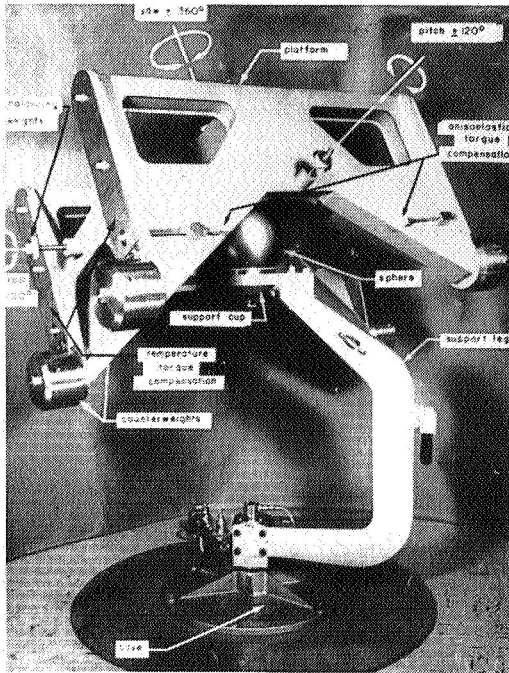


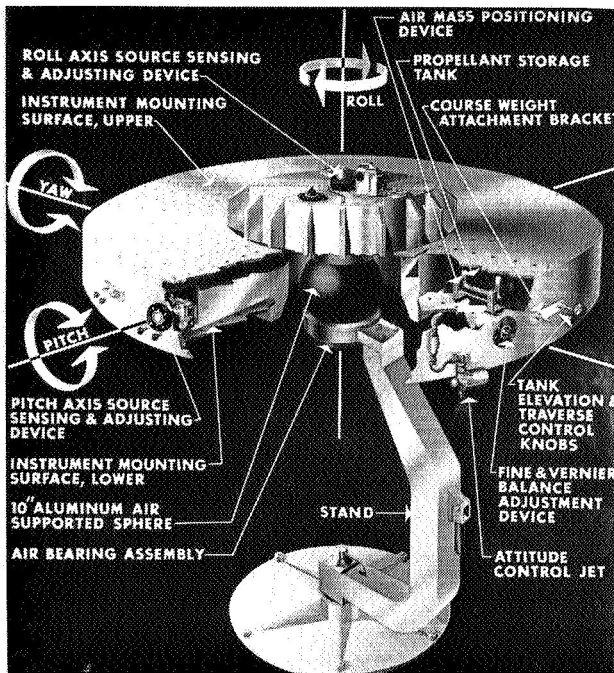
Figure 14



**MARSHALL
SPACE FLIGHT CENTER
PLATFORM**

ABOUT 1960

Figure 15



**MARSHALL SPACE
FLIGHT CENTER
PLATFORM**

SECOND GENERATION

Figure 16

AIR-BEARING TEST FACILITY WITH FOLLOWING GIMBAL
UNITED AIRCRAFT CORP.

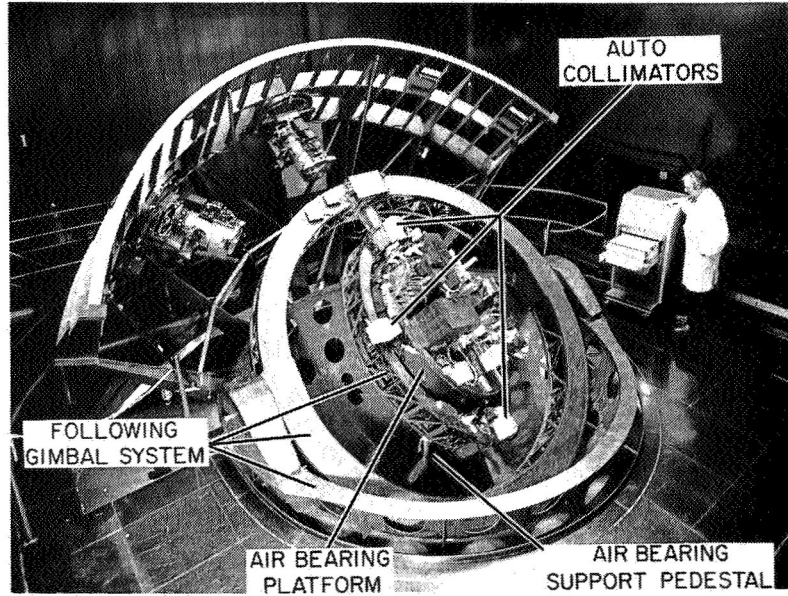
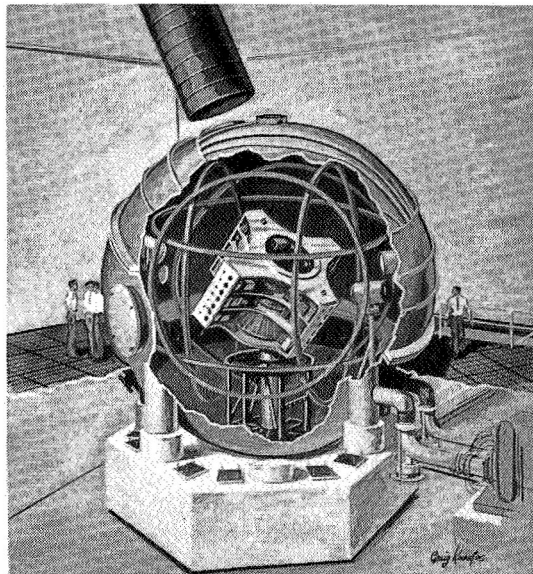


Figure 17

AIR-BEARING TEST FACILITY WITH VACUUM CHAMBER
GRUMMAN AIRCRAFT ENGINEERING CORP.



AIR-BEARING TEST FACILITY
GENERAL ELECTRIC CO.

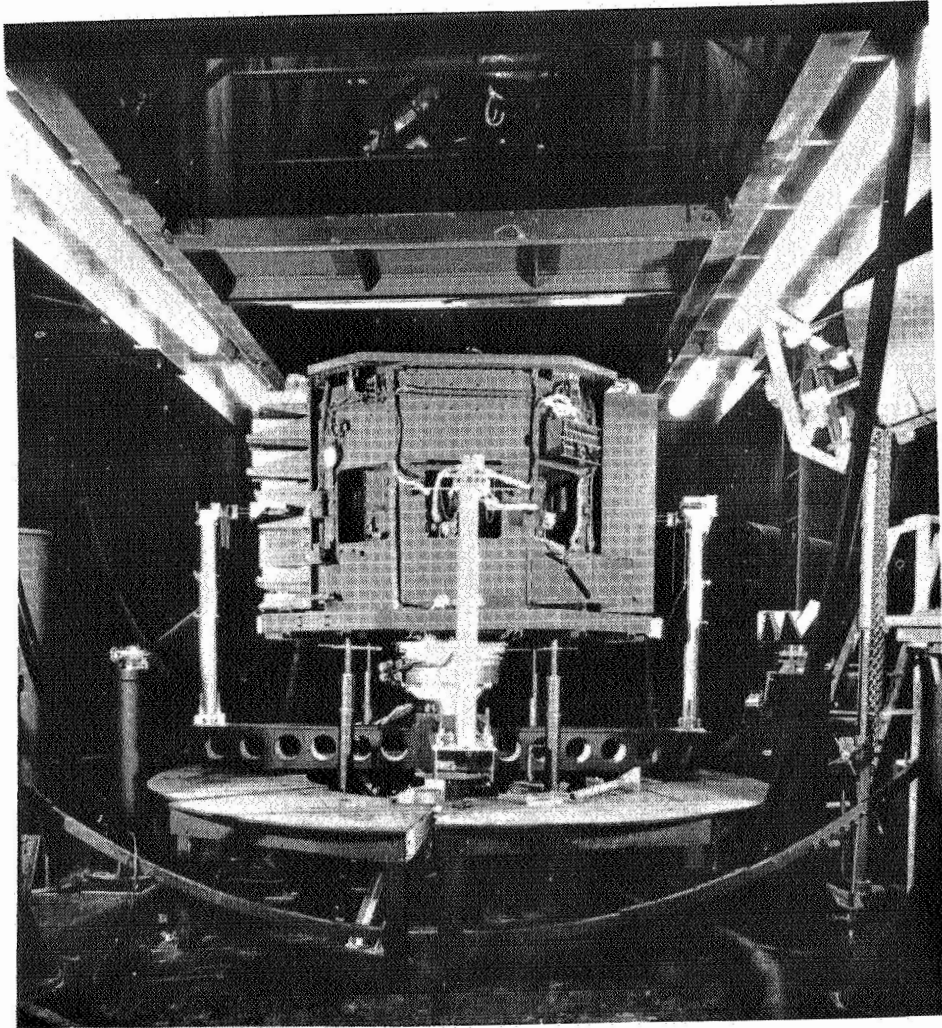


Figure 19

N 65-33516

Introduction to the Session on Structural Dynamics

by

I. E. Garrick

National Aeronautics and Space Administration

It is my privilege to act as chairman for this Session on Structural Dynamics. I wish to give a special welcome to the 15 professors who were at the Langley Research Center in the American Society for Engineering Education program. The full session topic could appropriately read, "The Role of Simulation in Structural Dynamics for Space Technology;" still more precisely, we could use the word "similitude" for the word "simulation." "Simulation" is a word with many connotations. It could mean pretending to be what you are not, for example, the protective coloration assumed by some animals in nature; or it could stand for the act of piloting a space vehicle without leaving the ground. In the use of the word in structural dynamics, we may mean to describe the role of a similar or dynamically scaled model, or even the parameters of governing equations of a mathematical model. A mathematical idealization of a physical situation always contains a degree of simulation. The art of a mathematical model lies in the simplest model that yet simulates. In fact, for Nature herself, the word "simulation" has the two distinct

meanings: as, for example, protective color in animals or insects; or the meaning as given in D'Arcy Thompson's classic book, "On Growth and Form," in which famous scaling laws applying to large and small species in natural evolution are so clearly described.

All three of the talks for this morning's session are being given by my colleagues from Langley, and these talks, as well as the fourth talk to be given by Mr. Bozajian this afternoon, all deal with space vehicles, launch vehicles, and payloads, on the ground and in space. As you may know or realize on brief reflection, the major cost of our national space programs is in the hardware, in the vehicle itself, and its payload; thus, the major problems, moneywise, are in the engineering technology rather than in pure science. Space science, however, cannot be pursued without a suitable technological base. Distinguished scientists have frequently planned their scientific experiments well, but in many early space attempts have completely overlooked factors of the environments in which these experiments are placed. The role of simulation in space technology is thus very much like an insurance premium, and its main objectives are to reduce costs and ensure reliability of the final products. Many factors need to be considered in the realm of simulation of similitude: structural dynamics; physical phenomena; governing mathematical equations; parameters, dimensional and non-dimensional; the natural environments as well as induced environments; material properties. Although very much remains to be done, progress has already been made, as our speakers will disclose.

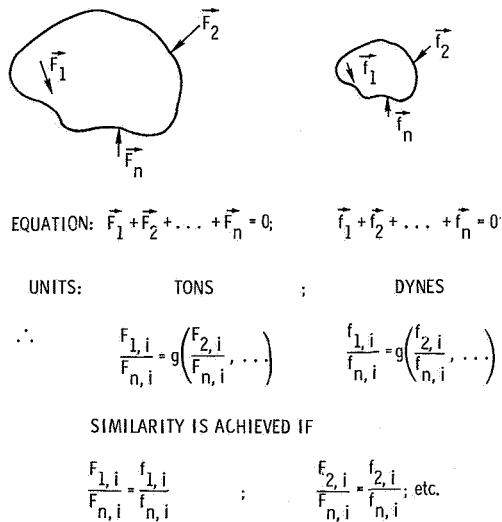
	ENVIRONMENT		
	ACTUAL	APPROX.	SIMULATED
STRUCTURE			
FULL SCALE			
ACTUAL FLIGHT	X		
BOILER-PLATE FLIGHT		X	
GROUND TESTS			X
COMPONENTS			X
DYNAMIC MODEL			
REPLICA			X
DYNAMICALLY SIMILAR			X
COMPONENTS			X

NASA

Figure 1.- Approaches to experimental analysis of space vehicles.

1. ON THE BASIS OF PAST EXPERIENCE WITH RELATED PROBLEMS
2. DERIVATION AND NONDIMENSIONALIZATION OF GOVERNING EQUATIONS
3. FORMATION OF RATIOS OF DIMENSIONALLY SIMILAR QUANTITIES WHICH GOVERN SYSTEM RESPONSE
4. APPLICATION OF THE PRINCIPLES OF DIMENSIONAL ANALYSIS

Figure 2.- Techniques for obtaining pertinent dimensionless ratios.



NASA

Figure 3.- Derivation of dimensionless ratios by nondimensionalization of governing equations.

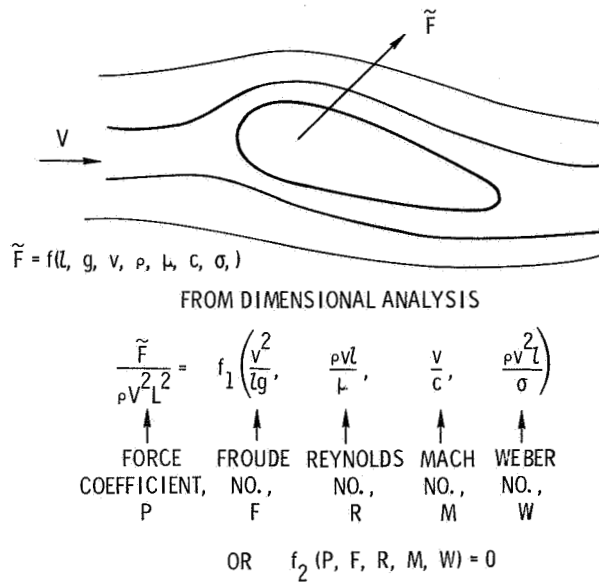


Figure 4.- Example of a complete set of dimensionless ratios for an assumed set of pertinent variables.

NASA

- GEOMETRIC:
CORRESPONDING LENGTHS ARE PROPORTIONAL OR
CORRESPONDING ANGLES ARE EQUAL
- KINEMATIC:
CORRESPONDING CHANGES IN GEOMETRIC SHAPE
OR POSITION OCCUR AT TIMES WHICH ARE
PROPORTIONAL
- DYNAMIC:
CORRESPONDING FORCES ON CORRESPONDING
ELEMENTS OF MASS PRODUCE INTERNAL AND
EXTERNAL MOTIONS WHICH ARE GEOMETRICALLY
AND KINEMATICALLY SIMILAR

NASA

Figure 5.- Definition of various types of similarity.

● SCALE FACTORS

LENGTH: $l_f = \bar{\lambda} l_m$

TIME: $t_f = \bar{\tau} t_m$

MASS: $m_f = \bar{\mu} m_m$

TEMPERATURE: $\theta_f = \bar{\theta} \theta_m$

● RELATIONSHIP OF SCALE FACTORS FOR SIMILARITY

GEOMETRIC: $\frac{l_f}{l_m} = \bar{\lambda}$

KINEMATIC: $\frac{l_f}{l_m} = c_1 \frac{t_f}{t_m}$ OR $\bar{\lambda} = c_1 \bar{\tau}$

$\therefore v_f = (\bar{\lambda}/\bar{\tau}) v_m$ and $a_f = (\bar{\lambda}/\bar{\tau}^2) a_m$

DYNAMIC: $\frac{F_{1f}}{F_{1m}} = \frac{F_{2f}}{F_{2m}} = \frac{F_{if}}{F_{im}} = \dots = \frac{m_f a_f}{m_m a_m} = \bar{\mu} \left(\frac{\bar{\lambda}}{\bar{\tau}^2} \right)$

NASA

Figure 6.- Inherent relationships for various types of similarity.

PREFLIGHT

SHOCK AND VIBRATION DURING HANDLING AND SHIPPING

GROUND WIND LOADS

ENGINE IGNITION SHOCKS

INFLIGHT

PULSATIONS OF ENGINE THRUST

TURBINE AND PUMP INPUTS

ROCKET ENGINE ACOUSTIC PRESSURES

FUEL SLOSHING FORCES

CONTROL FORCES

GUST, WIND SHEAR, AND FLOW SEPARATION PRESSURES

BOUNDARY LAYER NOISE

HIGH STEADY-STATE ACCELERATIONS

STAGE SEPARATION SHOCKS

LANDING

MANEUVER LOADS

TOUCHDOWN SHOCKS

NASA

Figure 7.- Sources of excitation of space vehicle structures.

TYPE	OBJECTIVE	DATA OBTAINED	USE OF DATA
STRUCTURAL DYNAMICS	STRUCTURAL CHARACTERISTICS	NATURAL FREQUENCIES MODE SHAPES DAMPING STRUCTURAL IMPEDANCE FORCED RESPONSE	STRUCTURAL INPUTS FOR SYSTEMS ANALYSIS
AERODYNAMIC	AERODYNAMIC FORCES AND MOMENTS	PRESSURE DISTRIBUTIONS FORCES AND MOMENTS STABILITY DERIVATIVES FLOW CHARACTERISTICS	AERODYNAMIC INPUTS FOR SYSTEMS ANALYSIS
AEROELASTIC	AEROELASTIC RESPONSE	BUFFETING PRESSURES DIVERGENCE FLUTTER AERODYNAMIC DERIVATIVES	INDICATE LOADS AND STABILITY BOUNDARIES OF FULL-SCALE VEHICLES
PROPELLANT-DYNAMICS	PROPELLANT CHARACTERISTICS	NATURAL FREQUENCIES MODE SHAPES DAMPING FORCES ON TANKS	PROPELLANT INPUTS FOR SYSTEMS ANALYSIS
LANDING DYNAMICS	LOADS AND STABILITY DURING LANDING	LANDING LOADS STABILITY DURING LANDING ON VARIOUS SURFACES	INDICATE LOADS AND STABILITY BOUNDARIES OF FULL-SCALE VEHICLES

NASA

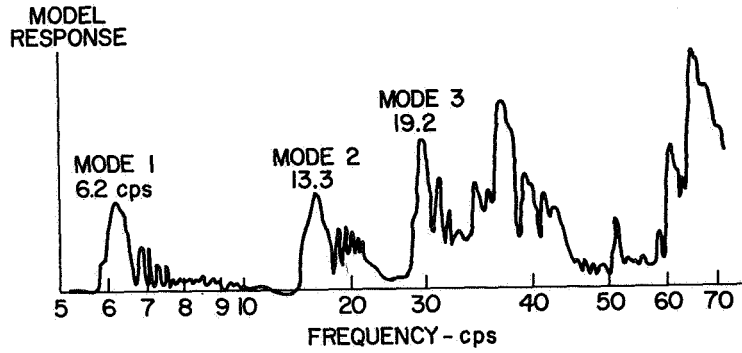
Figure 8.- Various types of dynamic models used in space vehicle systems analyses.

FULL SCALE		DYNAMIC MODELS		
	VEHICLE	SCALE (PERCENT)	PURPOSE	
MONOCOQUE	SCOUT	15.0	GROUND WINDS	
	JUPITER	20.0	GROUND WINDS	
	TITAN-GEMINI	7.5	GROUND WINDS	
	TITAN III CORE	20.0	STRUCTURAL DYNAMICS	
	SATURN V	16.3	STRUCTURAL DYNAMICS	
	SATURN V	10.0	STRUCTURAL DYNAMICS	
	SATURN V	3.0	GROUND WINDS	
CLUSTER	SATURN V	2.5	STRUCTURAL DYNAMICS	
	TITAN III	7.5	GROUND WINDS	
	SAI BLOCK I	20	STRUCTURAL DYNAMICS	
	SAI BLOCK I	7.5	GROUND WINDS	
	SAI BLOCK II	7.0	GROUND WINDS	
	SAI BLOCK II	8.0	BUFFETING	
	SATURN IB	5.5	GROUND WINDS	

NASA

Figure 9.- Dynamic models of launch vehicle configurations under study at the Langley Research Center.

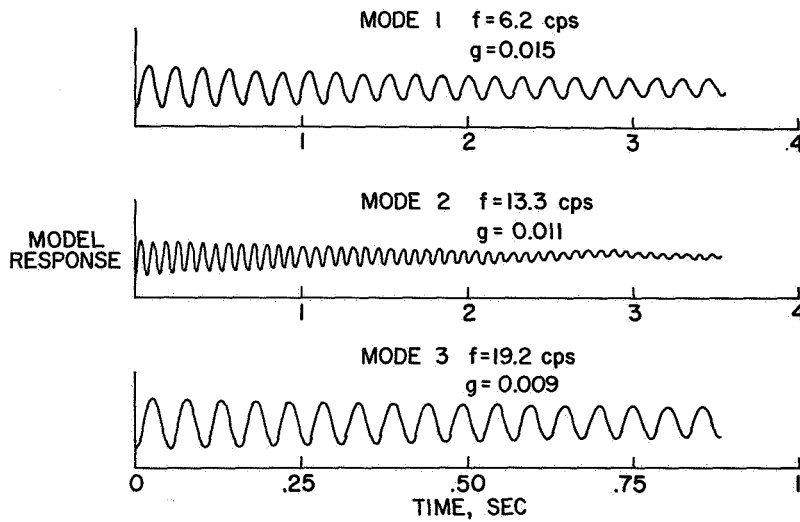
ACCELEROMETER ON PAYLOAD,
RESPONSE IN YAW DIRECTION



NASA

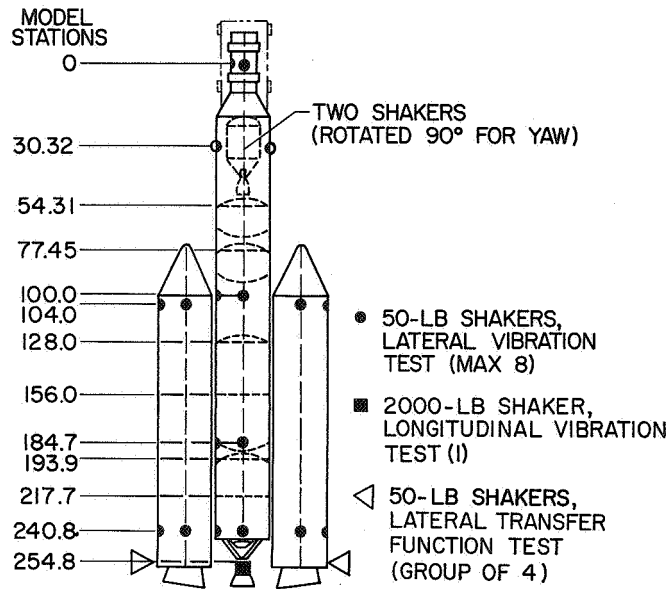
Figure 10.- Typical sample of response data from 1/5-scale structural dynamics model of Titan III.

ACCELEROMETER ON PAYLOAD,
RESPONSE IN YAW DIRECTION



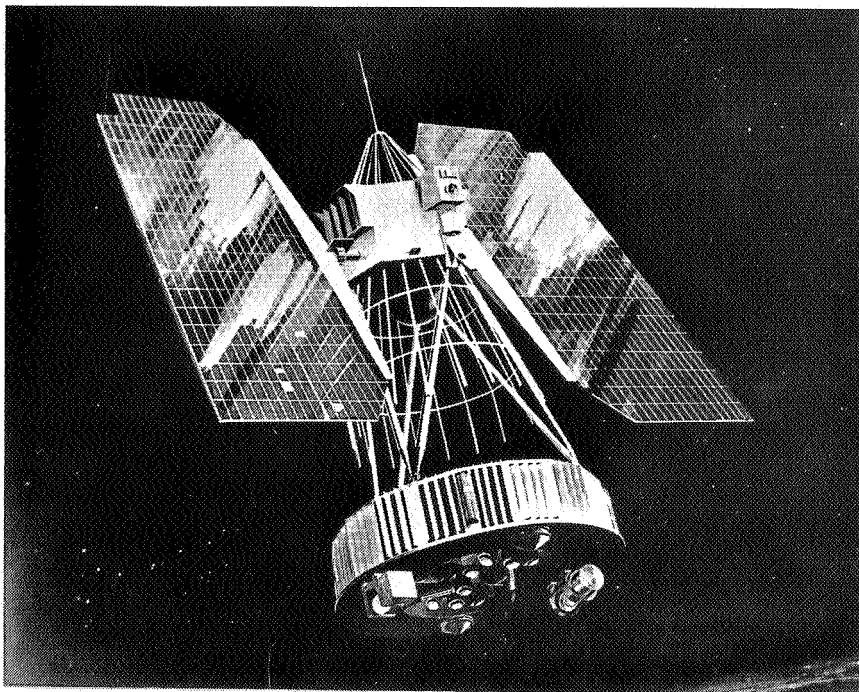
NASA

Figure 11.- Damping of 1/5-scale structural dynamics model of Titan III.



NASA

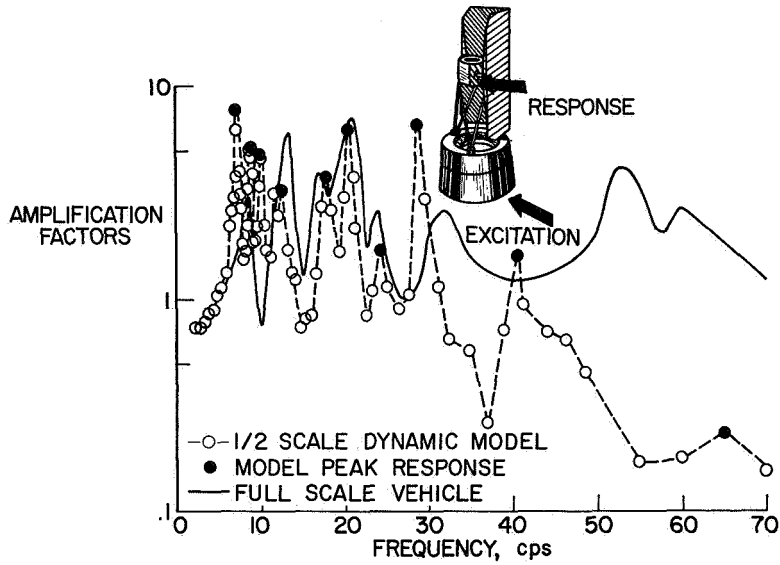
Figure 12.- Sketch of 1/5-scale structural dynamics model of Titan III.



NASA

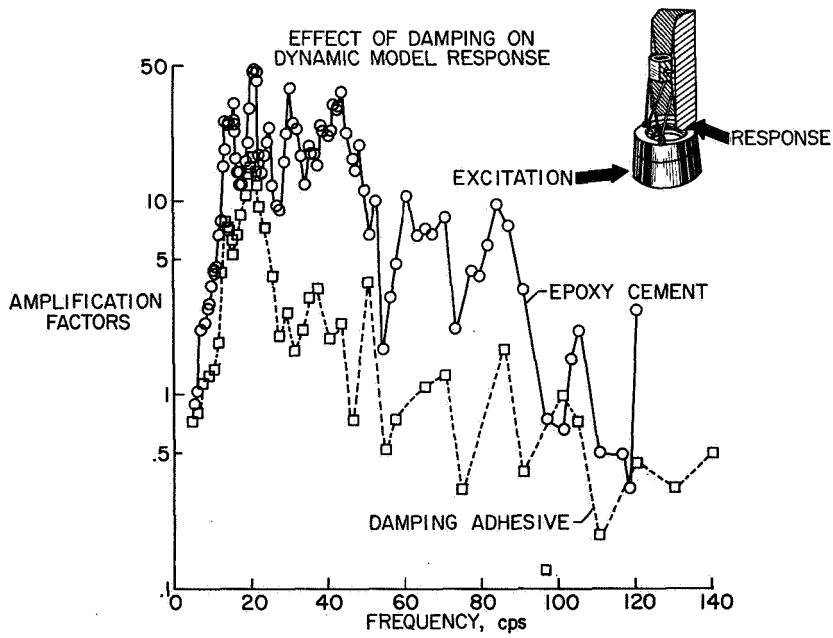
Figure 13.- Nimbus - Polar Orbiting Weather Satellite.

COMPARISON OF MODEL AND FULL SCALE RESPONSES



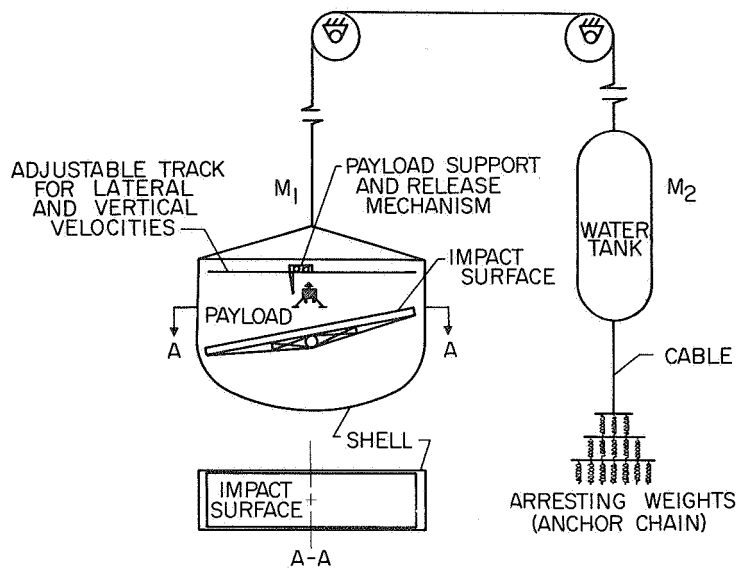
NASA

Figure 14.- Comparison of responses at the base of control section on 1/2-scale model and full-scale spacecraft. Excitation along pitch axis. Model frequencies divided by 2.



NASA

Figure 15.- Effect of solar panel damping on dynamic amplification as a function of excitation frequency.



NASA

Figure 16.- Impact simulator for lunar and planetary gravitational fields.

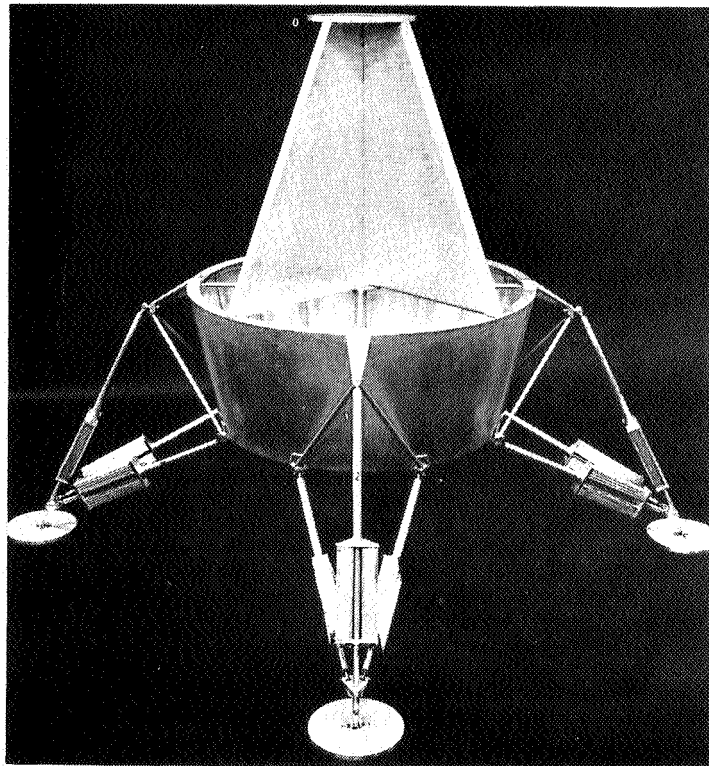
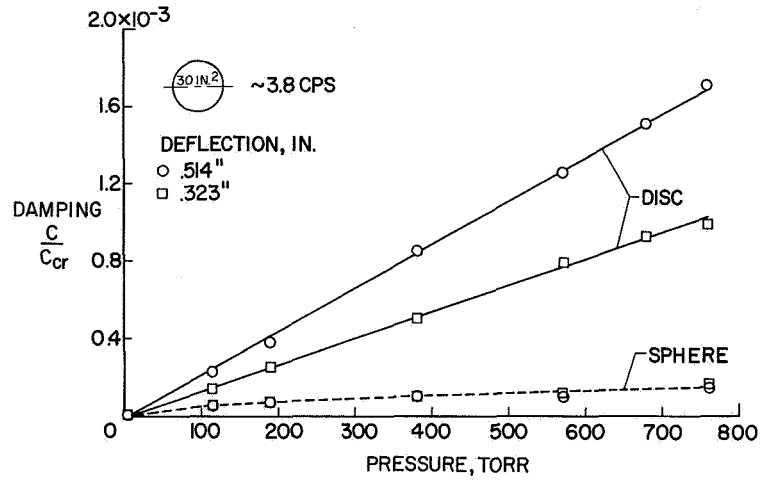
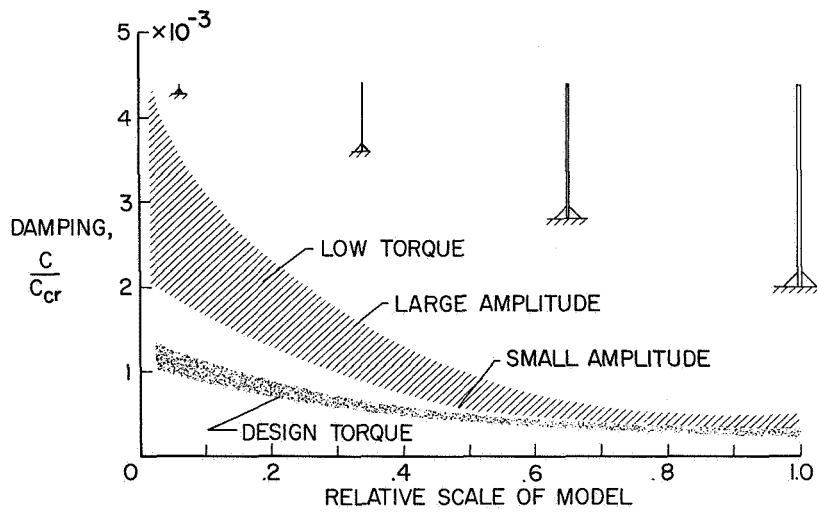


Figure 17.- 1/6-scale dynamic model of lunar landing spacecraft.



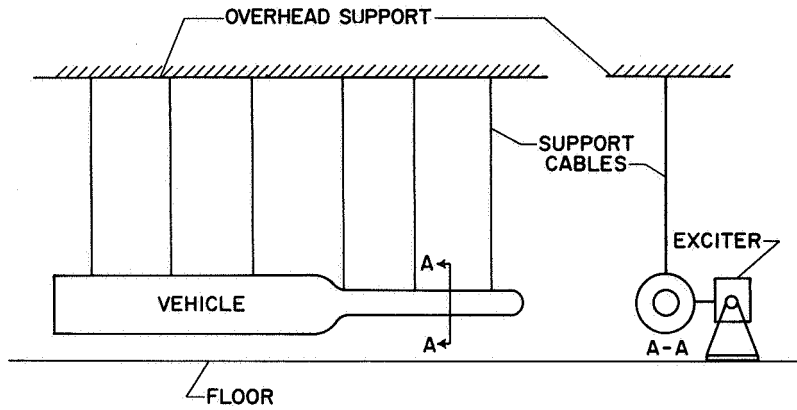
NASA

Figure 18.- Effect of atmospheric pressure and amplitude of oscillation on aerodynamic damping of plates and spheres.



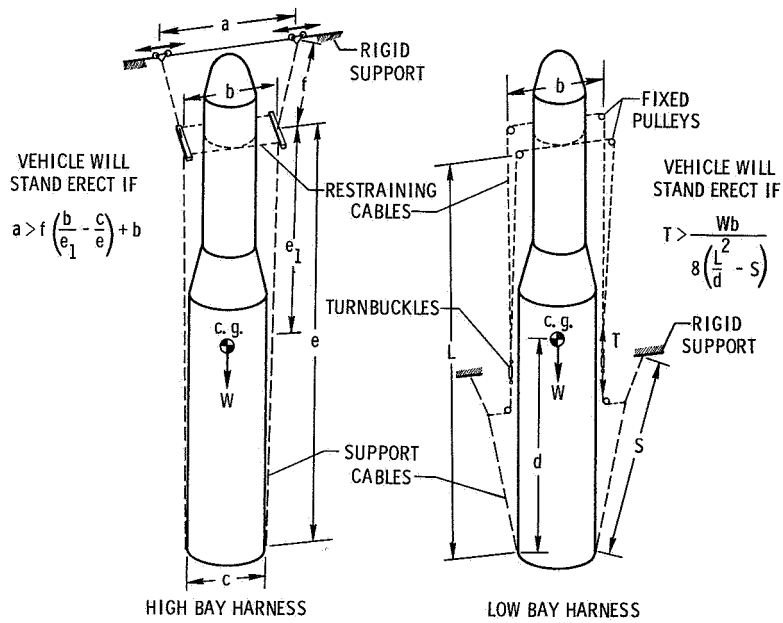
NASA

Figure 19.- Effect of model scale on damping.



NASA

Figure 20.- Horizontal support systems for launch vehicles.



NASA

Figure 21.- Vertical support systems for launch vehicles.

N65-33617

PRINCIPLES AND PRACTICES FOR SIMULATION OF
STRUCTURAL DYNAMICS OF SPACE VEHICLES

by

George W. Brooks

NASA - Langley Research Center

ABSTRACT

33617

The paper discusses the philosophy and principles for the selection and design of dynamic models for analysis of structural dynamics of space vehicles. Subjects treated include similitude, model scaling, applications of modeling to launch vehicles and spacecraft, and considerations relative to damping and model support systems. An appendix is included which summarizes the various dimensionless ratios used in aerospace flight.

INTRODUCTION

author

From practical considerations we begin with the situation that we have a structure which is designed to place some useful payload into space. Typical examples include both clustered and nonclustered configurations with either

liquid- or solid-propellant systems. During the performance of this task, the structure is subjected to an environment or combination of environments, which induces external and/or internal responses of the structure. For example, wind loads create external motions of these structures and induce internal stresses in the structural elements. As engineers we have both a professional interest and responsibility, peculiar to our own field of endeavor, to maximize the efficiency and reliability of the structures which we employ. Although our principal interest at this conference and the content of this paper are principally devoted to space vehicle systems, the reader will recognize that the general philosophy and much of the basic content are generally applicable to structures associated with other engineering disciplines.

In order to design efficient space vehicle structures we must have adequate means for predicting the characteristics of the structure, the environment and loads to which it is subjected, and its response. If the structures were simple and the environment and loads well defined in a spatial and temporal sense, adequate solutions could be obtained by straightforward analytical procedures. Unfortunately it is usually difficult and often impossible either to define the structure or the forcing function with necessary finesse to assure high confidence in calculated response, and hence it becomes necessary to rely on experimental programs to generate the information desired for solution of immediate problems and to guide the formulation of analytical procedures for future analyses of similar systems. Furthermore, since the principal objective of our research programs is to continually advance the state of the art, we cannot anticipate a situation where the structural systems and environments of interest are sufficiently well defined that interesting problems can be adequately

formulated and solved solely on the basis of theoretical analysis. Consequently, our interest in and reliance on properly planned experimental programs as an adjunct to theoretical developments is more likely to wax than wane in the foreseeable future.

As outlined in figure 1, experimental programs may be conceived which employ the following: (a) full-scale structures and the actual environment; (b) modified full-scale structure and a similar environment; or (c) replica or dynamically similar model structures and simulated environments. Relative to the structural dynamics of space vehicles, the aforementioned approaches may be briefly characterized by the following considerations.

The experimental study of exact full-scale structures and their reaction to the exact environment essentially means that we employ whatever theoretical and experimental knowledge and experience we have to design and build what we think we want, fly several vehicles, and see what happens. If the vehicles perform as desired, we consider ourselves fortunate and are in business. If the performance is deficient during the flight of early vehicles, later vehicles are modified to correct these deficiencies and the program is continued to completion. For smaller, comparatively simple, inexpensive space vehicle systems, and for those which are not man rated, experience tells us that this is a good approach. Thor-Delta is a good example.

Ground vibration tests of full-scale launch vehicles or flight tests of launch vehicles with boilerplate payloads are representative of the second category. In the first case the spatial and temporal distributions of vibratory loads are simulated by acoustic pressure fields or multipoint shaker load. In the second case, internal coupling of structural elements and the coupling of the structure with the environment are somewhat compromised; however, the results of flight programs for Mercury, Gemini, and Apollo

substantiate their value. The sheer size and complexity of the systems and hardware involved postulate that such programs are both complex and expensive.

The study of replica or dynamically similar model structures and their response to simulated environments is the subject of primary concern in this paper. By a replica model, we essentially mean that we keep the same materials, the same type of construction, and essentially build a miniature of the flight article. If we have a good understanding of the structure and are primarily interested in basic phenomena and the magnitudes of events such as natural frequencies and nodal locations, it is usually possible to economize on manufacturing and test procedures and costs by use of a model which is dynamically similar. Such techniques have been successfully employed in the aircraft industry for many years and will be discussed to some extent in the present paper.

The fact that dynamic models have been used with excellent results in the study of structural dynamic problems in aircraft may, in itself, be sufficient justification for their use in space vehicles since the basic problems and structural characteristics are substantially similar. However the tremendous size, complexity, and cost of space vehicle systems indicate that construction, testing, and modification of full-scale hardware pose problems of a higher order of magnitude and further emphasize the need for effective dynamic model programs either as a sole or companion source of experimental data.

SIMILARITY AND MODEL SCALING

Fundamentals of Similarity

In general terminology, a model structure is similar to a full-scale structure in at least some respect. The extent of this similarity may vary widely. It depends on the nature of the problem under study, the types of structure involved, and to a large extent, on the feasibility of close simulation of the full-scale structure and the environment which induces some type of internal or external response of the structure.

Granting that dynamic models are of some value in the study of the structural dynamics of space vehicles, the basic question then arises: How do we design and construct the model and its environment to simulate the full-scale response of interest and obtain the needed response data?

Many technical reports and textbooks have been written with the intent of answering this question, and although the scope of this paper does not permit a detailed discussion of the answer, an attempt will be made to outline the basic principles.

To begin, we recognize that the response of any physical system is governed by a set of equations, usually differential, which are based on principles of conservation of one or more quantities. Conservation of mass, conservation of energy, and conservation of momentum are typical examples. Newton's second law, stated in the manner of d'Alembert, that $F - ma = 0$ is a very simple but typical example. Bernoulli's equation for the pressure along a streamline in an incompressible flow is another example. In some cases, where the system of structure and environment and their mutual interactions are well known, the equations which govern the response can be derived, and certain classes of these may be solved. If the governing equations can be derived and solved, the physical system is converted to a mathematical analog and the need for a dynamic model or physical analog diminishes or disappears. Thus we are primarily interested in systems for which we cannot write the governing

equations, cannot solve them, or cannot interpret the analytical solutions adequately in terms of physical responses which describe the behavior of the system.

Even if the governing equations cannot be written conceptually, they still exist and we know from the principles of dimensional homogeneity that the dimensions of every term of any given governing equation must necessarily be the same. For example, every term of a force equation is a force and every term of a moment equation is a moment, etc.

Since the dimension of each term of a governing equation is identical, the ratio of any two terms is dimensionless. Thus, conceptually, all governing equations for any physical system may be made dimensionless, and every term then becomes a dimensionless ratio. The solutions of the governing equations are then independent of the dimensions of the system. Complete similarity is then achieved if all significant dimensionless ratios (a complete set) are included and corresponding dimensionless ratios pertinent to the problem have the same value for both the model and full-scale systems where the system includes both the structure and the environment.

The next task for achieving similarity is the determination of the dimensionless ratios which are pertinent to the problem at hand. During the decades which have followed since Professor Osborne Reynolds critical analysis of the importance of simulating significant dimensionless ratios in experimental research, many such ratios (frequently referred to as parameters or numbers) have been derived which pertain to one or more regimes of aerospace flight. The more important of these have been assembled by Norman Land of the Langley Research Center and are compiled in the appendix for reference. Four possible ways of obtaining these ratios are outlined in figure 2 and briefly described as follows:

- (1) Select the parameters which are significant on the basis of past experience. For example, past experience indicates that the forces and moments on a rigid wing at subsonic speeds are dependent on the Reynolds number and if model and full-scale tests are run at the same Reynolds number, full-scale forces and moments may be determined from model test results.
- (2) Write the governing equations of motion and nondimensionalize them. As illustrated in figure 3, the dimensionless parameters are readily obtained if the governing equations can be written, but for most of the problems of real interest, this may not be possible.
- (3) Form ratios of dimensionally similar quantities which govern the system response. Reynolds number is obtained and defined, for example, as the ratio of the fluid inertia forces to the fluid viscous forces.
- (4) Derive the dimensionless parameters by application of the principles of dimensional analysis. Since the techniques involved here are widely known and published, further discussion of dimensional analysis is not believed to be necessary.

The reader will recognize from the foregoing discussion that the successful application of dynamic model techniques to the study of any class of problems requires a substantial knowledge of the structure, the environment, and a fair assessment of what the response will be. We must know what variables, forces, moments, etc., are important, and we must have some recognition of why and how a given variable influences the response. If insignificant variables are introduced, they complicate the problem, and if important variables are omitted, the results may be completely erroneous and useless. Consequently, dynamic model design and testing are perhaps as much an art as a science and the scaling of dynamic models usually involves selection of the important dimensionless ratios by application of several or all of the four aforementioned techniques, as will be borne out by specific examples given in subsequent sections of the paper.

The dimensionless ratios or dimensionless products of interest are independent of each other in the sense that no one of the ratios is a product of powers of the others. A sufficient condition that each ratio be

independent is the condition that each ratio contain at least one variable which is contained in no other ratio. The set of all possible independent dimensionless ratios which can occur for a given problem is then complete. As an example, figure 4 shows the complete set of independent dimensionless ratios for the force on a body in a fluid under the assumption that the force is dependent on the length of the body, gravity, and the velocity, density, viscosity, speed of sound, and surface tension of the fluid.

Finally the question arises as to the number of dimensionless ratios which occur in the study of a given problem. To answer this question, we must first define the nature of the physical quantities which we use for our standard of measurement and thus designate as fundamental, i.e., will we use mass, length, and time or force, length, and time. Mass, length, and time are dimensionally independent in the sense that their magnitude can be determined by only one specific type of measurement. On the other hand, force is not dimensionally independent because it can be determined by measuring mass, length, and time, or mass and acceleration. If the fundamental physical quantities are dimensionally independent and r in number, and if the problem involves a total of n physical quantities, then, as shown in reference 1, the number of independent dimensionless ratios will be $n - r$. In any event the number of independent dimensionless ratios in the complete set will be equal to the number of variables minus the rank of their dimensional matrix.

Let us consider two examples involving the forces on a body in an inviscid, compressible flow where, in the first case, the fundamental quantities are dimensionally independent and, in the second case, they are dimensionally dependent.

Case I

	\tilde{F}	V	l	ρ	c	g
M	1	0	0	1	0	0
L	1	1	1	-3	1	1
T	-2	-1	0	0	-1	-2

Since there are 6 variables involved and the rank of the matrix is 3, there will be three dimensionless products in the complete set. These will be the Force coefficient, Mach number, and Froude number.

Case II

	\tilde{F}	V	l	ρ	c	g
F	1	0	0	1	0	0
L	0	1	1	-4	1	1
T	0	-1	0	2	-1	-2

Though the matrix is different, the rank is still 3 and the comments pertaining to case I are pertinent.

Types of Similarity

With respect to structural dynamics of space vehicles, the types of similarity of primary interest are geometric similarity, kinematic similarity, and dynamic similarity. The definition of each of these types of similarity is given in figure 5 and the relationships which exist between the independent quantities (length, mass, and time) are given in figure 6 where the subscripts f and m are used to denote corresponding full-scale and model quantities, respectively.

In addition to geometric, kinematic, and dynamic similarity, in some instances there is a need for thermal similarity. However, the introduction of thermal effects may be treated as a separate problem, and is not of prime importance to the discussion on structural dynamics presented herein. The subject of thermal similarity is discussed in some detail in references 2, 3, and 4.

DERIVATION OF SCALE FACTORS FOR STRUCTURAL
DYNAMICS MODELS
Launch-Vehicle Structures

In the scaling of launch-vehicle structures for lateral or longitudinal structural dynamics, only dynamic similarity is of principal concern. Kinematic similarity is automatically assured if dynamic similarity is achieved. Since the tests of such models do not, in general, involve aerodynamic flows, geometric similarity enters only in a gross sense.

Lateral dynamics. The lateral dynamics of a liquid-propellant launch vehicle involve the longitudinal distributions of four principal types of forces; namely:

Structural stiffness

$$\frac{\partial^2}{\partial z^2} \left(EI \frac{\partial^2 u}{\partial z^2} \right)$$

Structural inertia

$$m \frac{\partial^2 u}{\partial t^2}$$

Fluid stiffness

$$\bar{m} a$$

Fluid inertia

$$\bar{m} \frac{\partial^2 u}{\partial t^2}$$

where

- EI flexural rigidity of structure
- u structural bending displacements, or lateral fluid displacements
- m mass per unit length of vehicle (includes structural mass plus propellant mass which moves with the structure)
- \bar{m} mass of propellant per unit length of vehicle which moves as a separate degree of freedom and participates in fuel sloshing
- a absolute acceleration of vehicle (includes acceleration of gravity plus acceleration of vehicle relative to a fixed coordinate system)

If the distributed values of the ratios of these forces are the same on the model and full-scale vehicles, dynamic and kinematic similarity are assured.

If the fluid stiffness forces are neglected, and l is a characteristic length, the fluid mass may be considered as additive to the structural masses, and

$$\left[\frac{EI/l^3}{(m + \bar{m})l} \right]_f = \left[\frac{EI/l^3}{(m + \bar{m})l} \right]_m \quad (1)$$

or

$$\omega_m^2 = \omega_f^2 \frac{\left[\frac{EI}{(m + \bar{m})l^4} \right]_m}{\left[\frac{EI}{(m + \bar{m})l^4} \right]_f}$$

On the other hand, if the fluid stiffness is felt to be important from the standpoint of the coupling of fluid and structural masses, then the structural and fluid frequencies are related as follows:

$$\omega_{m,s}^2 = \omega_{f,s}^2 \frac{(EI)_m m_f l_f^4}{(EI)_f m_m l_m^4} \quad (3)$$

$$\omega_{m,p}^2 = \omega_{f,p}^2 \frac{a_m l_f}{a_f l_m} \quad (4)$$

and since the structural and fluid frequencies should bear the same ratios on model and full-scale vehicles,

$$\frac{(EI)_m m_f l_f^3}{(EI)_f m_m l_m^3} = \frac{a_m}{a_f} \quad (5)$$

For a replica model, the quantity on the left is equal to $\bar{\lambda}$ and the conditions for similarity are satisfied only if the acceleration field for the model tests is increased by a factor of $\bar{\lambda}$. However, similarity can also be achieved by any combination of reduction in stiffness or increase in mass of the model such that the product reduces the left-hand side of equation (5) by $\bar{\lambda}$.

Longitudinal dynamics. The procedure here is the same as for lateral dynamics. The forces are:

Structural stiffness

$$\frac{\partial}{\partial z} \left(EA \frac{\partial w}{\partial z} \right) \quad (6)$$

Structural inertia

$$m \frac{\partial^2 w}{\partial t^2} \quad (7)$$

Fluid stiffness

$$\bar{m} a \quad (8)$$

Fluid inertia

$$\bar{m} \frac{\partial^2 w}{\partial t^2} \quad (9)$$

where

EA extensional rigidity of structure

w structural extensional displacements, or longitudinal fluid displacements

Again if the distributed values of the ratios of these forces are the same for the model and full-scale structures, the conditions for dynamic similarity are satisfied. The scale factors which evolve are the same as those for lateral dynamics.

Tank pressures. In the case of liquid-propellant launch vehicles, a condition for similarity is that the stresses induced by internal ullage pressure bear the same ratio to the dynamic stresses for the model and prototype. It can be readily shown that this condition is satisfied if the model and full-scale ullage pressures are equal either for a replica model or for a model designed to maintain full-scale ratios of structural frequencies to fluid frequencies.

Spacecraft Structures

In the design of orbiting spacecraft structures, it is only necessary to maintain the full-scale distributions of mass and stiffness throughout. This condition assures proper simulation of mode shapes and the model to full-scale frequency ratio is readily calculated from simple beam, plate, or mass-spring considerations.

However, if the spacecraft is to land, its toppling stability during

landing is dependent on the gravitational field. The condition for simulation then requires that the ratio of the inertia forces to the gravity forces be invariant or that

$$\frac{\omega_m^2 l_m}{\omega_f^2 l_f} = \frac{g_m}{g_f} \quad (10)$$

where g is the acceleration due to gravity.

If the model is a replica model, $(\omega_m^2/\omega_f^2) = \bar{\lambda}^2$ and since $(l_m/l_f) = \bar{\lambda}^{-1}$, simulation of the dynamics during landing requires that $(g_m/g_f) = \bar{\lambda}$. Thus, to model a lunar landing spacecraft for tests on earth, $(g_m/g_f) = \bar{\lambda} = 6$. If the scale is larger, the model must be distorted or the gravitational field has to be reduced by testing in a simulator.

APPLICATIONS OF DYNAMIC MODELS

General Remarks

For practical reasons, dynamic model studies of space vehicles seldom involve a complete simulation of the composite environment-structure system. Instead, such studies are usually problem oriented in that one or more dynamic models is designed to study a specific or limited group of related problems. The logic of this approach has several justifications among which are those discussed in the following sections.

Multiplicity of Environmental Conditions

From a dynamics viewpoint, the environment of space vehicles may be defined as the composite of conditions which induce, or limit dynamic motions of the structure. Those conditions which induce motions, commonly referred

to as the sources of excitation, are of fundamental importance and will be discussed first.

Figure 7 lists the primary sources of excitation of space vehicle structures. Even a cursory glance at the figure will indicate to the reader the difficulty of a realistic simulation of these sources of excitation on any given dynamic model in a realistic test setup. Yet, each of the inputs has posed severe problems for one or more vehicles, and most vehicles are encumbered by the majority of the inputs. As indicated by the figure, induced responses of the structure become of concern during the manufacturing and shipping stage, persist through ignition, lift-off, flight, stage separation, and in the case of the Apollo vehicle, pose a significant problem during landing.

During flight through the atmosphere, the sources of excitation are highly transient due to the structure of the atmospheric wind profiles, the dissipation of launch-vehicle fuel, the changes in characteristic flows about the vehicle from subsonic to transonic to supersonic, and the changes in vehicle structure due to separation of spent stages. As a consequence of these highly transient and variable conditions, the spatial and temporal distributions of the sources of excitation are only approximately known and hence any one of the environmental effects can only be approximately simulated. Of significance also is the fact that, during the flight phase, nearly all of the inputs are superimposed, leading to a condition commonly referred to as "combined environments."

The principal phenomenon of importance relative to the limiting of dynamic motions is damping, and from a structural dynamics viewpoint, the principal concern relative to environmental effects is that the thermal and vacuum environments of space, acting separately or collectively, may

tend to reduce the damping of composite structures to the very low levels associated with the hysteretic dissipation of energy in the structural materials themselves. Some comments pertinent to this problem are presented in a separate section on damping.

Various Types of Dynamic Models

In view of the difficulty of subjecting a single dynamic model to the space vehicle environment and interpreting the full-scale response by scaling up the dynamic model results, the general approach at present is to use a combination of models to generate structural, aerodynamic, and propellant inputs which are integrated into analytical programs for prediction of overall vehicle responses. The types of models used to accomplish these objectives, and the nature of the data obtained are given in figure 8. In some instances, such as for aeroelastic and landing dynamics studies the model results may be scaled to directly indicate full-scale vehicle responses. In addition, special purpose models for studying various phenomena and problem areas are widely used as in the case of aircraft. Models to study control-surface loads, propellant baffle dampers, and the response of panels to acoustic pressures are typical of these.

To date, the application of models to the study of space vehicle dynamics has been primarily focused on the launch-vehicle characteristics with the spacecraft represented as a concentrated mass, or appropriate aerodynamic shape. Figure 9 shows some such models utilized in various studies, current or in the past, by the Langley Research Center. Details of the model design characteristics, research objectives, and test results are presented in comparison papers at this symposium by Reed and Runyan. As shown by the figure, the models represent both monocoque and cluster

launch-vehicle configurations, and are used to study problems involving structural dynamics, ground winds, and buffeting.

Typical Examples of the Use of Structural Dynamics Models

Launch vehicles - Titan III. Typical samples of the data obtained from tests of structural dynamics models of launch vehicles are shown in figure 10 and 11. These data were derived from early tests of a 1/5-scale model of Titan III, the vehicle shown in figure 12.

Figure 10 shows the acceleration of a simulated 45,000-pound payload in the yaw direction (the longitudinal plane containing the solids) for a simulated flight condition wherein one-half of the mass of the strapped-on solids is spent. Resonance conditions, exemplified by peak response levels, are shown and the first three natural modes are identified. Although the exact structural deformations involved have not yet been clearly identified the figure also shows the existence of strong resonances at higher frequencies.

An interesting observation from figure 10 is the fact that the response levels at resonance increase with frequency which indicates that, since the magnitudes of the force inputs are held essentially constant, the damping of the structure-fuel system decreases with frequency. This trend is substantiated by the logarithmic decay presented in figure 11 which show that the damping of the third natural mode is only 60 percent as high as for the first natural mode and about 80 percent as high as for the second natural mode.

The data presented in figures 10 and 11 represent only a small sample of the data being generated on this model. The Langley Research Center, is working in cooperation with the Air Force and Martin-Denver (who designed,

built, and is jointly testing the model) to measure the structural dynamics characteristics for the full range of payloads, inputs, and propellant loadings. The test program involves the use of multiple shakers and includes analysis of both the core and core-plus-solids configurations. It is hoped that the model test results will provide the necessary checks and modifications to the theory so that the full-scale responses can be analyzed with confidence without the need for extensive dynamic testing of the full-scale hardware.

Orbiting spacecraft - Nimbus. As previously mentioned, the use of dynamic models to study the experimental aspects of the structural dynamics of space vehicles has been focused on launch vehicles. The reason for this is that the great majority of spacecraft in the past have been small enough to permit a full-scale dynamic mockup to be readily constructed and tested, or they have been sufficiently compact that the structure could be adequately restrained from highly undesirable dynamic responses. Ranger and Tiros, respectively, are good examples.

As spacecraft become larger, more flexible, and more expensive, an increased need for dynamic model tests will no doubt arise. As an example the Nimbus spacecraft, a future polar orbiting weather satellite shown in figure 13, exhibited complex high-amplitude dynamic responses during early qualification tests wherein the solar panels were folded to simulate the launch configuration. A review of the early test results suggested the need for a simple, inexpensive, dynamic model program to establish:

- (1) The characteristic motions of the vehicle as a function of frequency including natural frequencies, mode shapes, and forced response;
- (2) The relative merits of hard vs. soft mounting systems for attaching the spacecraft to the launch vehicle; and

(3) The effectiveness of localized and distributed damping on the frequency response.

Sketches of the model and two samples of the test results, selected from reference 5, are shown in figures 14 and 15. The scale chosen was 1/2, and as shown in figure 14, the model afforded a reasonable simulation of the dynamics of the full-scale structure over the lower frequency range as desired. The model was constructed of standard tubing and plates with mixed welded and riveted construction. In lieu of honeycomb sandwich solar panels, the model panels were constructed by laminating two thin sheets of aluminum to a sheet of balsa. Two sets of panels were constructed. In one set the bonding agent used to laminate the panels was an epoxy resin (a hard-setting glue) and in the other set the bonding agent was a visco-elastic damping adhesive. Figure 15 shows that the use of the damping adhesive effectively reduced the amplification factor (the ratio of output to input accelerations) by nearly an order of magnitude over the frequency range of primary interest. Other tests also demonstrated the effectiveness of isolation techniques, and all test results were of substantial aid in the definition of the contributions of the various components of the structure to the overall vehicle motions.

Landing spacecraft - Apollo LEM. A substantial research effort is currently directed to the analysis of the landing dynamics of space vehicles designed to land on extraterrestrial surfaces such as the moon. This research includes both theoretical and experimental studies, and is oriented to establish both the tipover stability during the landing process and the loads and motions generated in the landing gear during the impact process.

Among the more important variables for such problems is the gravitational constant. As shown in a previous section of the paper, free-fall

drop tests of a vehicle on the earth's surface will not simulate landing of the same vehicle on the moon even though the velocity conditions and the surface materials at the point of touchdown are the same. The necessary experimental test results can be obtained by testing full-scale structures or large dynamic models in some type of lunar gravitational simulators, or by testing 1/6-scale dynamic models.

Gravitational simulators may be of several types such as the inclined plane, a counter force system which supports 5/6 of the weight of the vehicle, or a simulator which permits impacts for the velocity and surface conditions desired onto a surface which is accelerating downward relative to the earth. A simulator of the latter type is discussed in reference 6 and shown in figure 16. For simulation of full-scale lunar landing vehicles, the impact surface would accelerate downward relative to earth at 5/6g and the ratio of the counter mass M_2 to the simulator mass M_1 would be such that $M_1 \approx 11M_2$.

An example of a 1/6-scale dynamic model for simulating lunar landing dynamics is shown in figure 17. The basic structure of the model is designed to readily permit variations in spacecraft mass and moments of inertia by appropriate distribution of added masses to the basic structure. Landing-gear configurations can also be varied in number and structural details. The configuration shown has four tripod gears with each member of the tripod having honeycomb shock absorbers to permit dissipation of the impact energy with minimum rebound. Other gear configurations are also under study. In addition to generating basic information on landing dynamics of lunar spacecraft, the model parameters are selected so as to include values pertinent to the Apollo LEM vehicle.

DAMPING

General Remarks

The damping of launch-vehicle and spacecraft structures is among the more critical factors in the control of their response to the many types of inputs. Since the peak amplitudes of forced responses are essentially inversely proportional to damping, and since the rate of exponential decay of free oscillations is directly proportional to damping, it is necessary to know the inherent damping of the structure in all cases to predict its response. As a general rule, the higher the inherent damping the better, and a great deal of effort has been expended in recent years on the development of viscoelastic films, tapes, sandwiches, etc., to achieve higher damping.

From the viewpoint of simulation, damping is among the more difficult quantities to scale. Several types of damping are of concern including aerodynamic damping and structural damping. Some discussion of each of these as they pertain to dynamic modeling is presented in the following paragraphs.

Aerodynamic Damping

Since the primary vibrations of launch vehicles and spacecraft occur during flight, the density of the air which surrounds the structural components of the vehicles during conditions of peak response is usually lower than ambient conditions at the earth's surface. Yet for convenience, it is highly desirable to be able to conduct tests of structural dynamic models under atmospheric conditions. Thus the question of the effect of air density on the aerodynamic damping of the vibrations of space vehicles and

their components arises. In addition to the density effect, the question of size or area of the components also exists. In an effort to determine the effects of these and other variables on the damping of structures for space vehicle applications, a study of the damping of typical components was recently conducted at the Langley Research Center. The study consisted of measuring the damping of various sizes of circular and rectangular panels, spheres, and cylinders at air pressures ranging from atmospheric down to 4×10^{-2} torr. The test components were mounted on the ends of cantilever beams of different frequencies and the damping was determined by measuring the logarithmic decay of the free vibrations of the beam-component systems. Typical samples of the results are shown in figure 18, where the ratio of the damping to the critical damping is plotted as a function of the pressure of the surrounding air medium for a panel and sphere for two amplitudes of oscillation. For the case shown, the cross-sectional area was 30 square inches and the frequency of oscillation was 3.8 cycles per second. The results show that the aerodynamic contribution to the damping of the panel, obtained by subtracting out the damping at 4×10^{-2} torr, is proportional to the amplitude of oscillation and the density of the test medium. The results also show that the damping of the sphere is essentially proportional to density, but independent of amplitude. Other tests involving cylinders showed the same characteristic variations as for spheres. In summary the results of the studies to date show that the damping for panels varies as follows:

$$\delta = 22 \frac{\rho x A^{4/3}}{m}$$

where

- δ damping coefficient, $2\pi c/c_{cr}$
 ρ density of the test medium, slugs/ft³
 X amplitude of oscillation, ft
 A area of the panel, ft²
 m effective mass of the panel-beam system, slugs

Thus it appears that the increase in damping due to testing panel-type structures in atmosphere as opposed to the low-pressure space environment is directly proportional to the pressure ratios and can be readily accounted for. The same is true for spheres and cylinders. On the other hand, the results show that the damping ratio for a model of a panel structure tested in atmosphere is substantially less because of the smaller area than it would be for a full-scale structure tested under similar conditions. The damping factor for spheres and cylinders, however, are independent of size and the scaling problem is rather straightforward. The essence of these remarks also points up the fact that the low-amplification factors measured for tests of spacecraft having large solar panel arrays may be due to high aerodynamic damping - a condition that will not exist during flight in low-density regimes.

Structural Damping

In addition to the aerodynamic damping which may dissipate the motion of a structure, all structures possess an internal dissipation mechanism usually referred to as structural damping. For purposes of this paper, structural damping is defined as the composite of those effects which involve hysteretic dissipation within the crystals of the structural materials and the damping associated with the deformation of the structure at its joints.

It has long been expected that the damping of small composite structures representative of aerospace usage would have higher structural damping than larger structures constructed of the same materials by the same techniques. In other words, is the structural damping coefficient of a replica dynamic model inherently higher than that for the full-scale structure? In an attempt to answer this question, the Langley Research Center constructed four aluminum beams with cantilever supports and tested them. The beams had a rectangular cross section with a width-to-thickness ratio of 6 to 1, and a length-to-width ratio of 10. The largest beam was 5 feet long. The cantilever support for each beam consisted of two machined angle blocks designed so that the stresses in the support were consistent with the stresses in the beam. The relative scale of the models and the results of the damping tests are shown in figure 19. The beams were mounted to a massive steel and concrete backstop and every precaution was taken to assure that the mounting and test conditions were consistent.

During the tests, the clamping pressure of the beam supports was controlled by varying the torque applied to the bolts and for a comparative test condition, the clamping pressure for all beams was the same. The damping was measured for both a low torque condition (representative of a semitight fit) and a design torque condition. For each torque condition, the damping was also measured for a range of amplitudes.

The results of the tests show that the damping coefficient decreases as the clamping pressure, joint tightness, or torque is increased, and increases as the amplitude of the vibration is increased. But perhaps of greater importance from the standpoint of dynamic modeling of structures is the fact that the structural damping increased by a factor of 2 as the scale was reduced by a factor of about 18 for design torque conditions and by a

factor of 4 for low torque conditions. Yet every attempt was made to assure that each beam was a replica model of the other three. On the basis of these results, it would appear highly likely that the structural damping of a realistically sized dynamic model of a launch vehicle might differ substantially from that of the full-scale structure. Furthermore, the results also emphasize the importance of maintaining close control over joint tightness and integrity during model construction.

Another factor of concern relative to the structural damping of spacecraft is the probability that long exposure to space vacuum conditions may outgas the adsorbed gases from the mating surfaces at structural joints and permit them to vacuum weld. In this event the structural damping of the assembled structure would approach the inherent damping of the materials - a reduction of one or more orders of magnitude. A conservative approach in this case would be to use welded joints in the construction of dynamic models to assure that the amplification factors for the full-scale structure do not exceed those of the model insofar as structural damping is concerned.

MODEL SUPPORT SYSTEMS

Launch Vehicles

In essentially all cases of interest, the boundary conditions for launch vehicles are essentially free-free, and an equivalent support system must be used during dynamic model tests to assure that the natural frequencies, mode shapes, structural damping, and dynamic response of the model represent those which occur on the full-scale vehicle under flight conditions. The fundamental criteria is one of frequency separation. If the frequency of the support system can be made sufficiently low compared to the natural frequency

of the lowest frequency natural mode of interest, say by a factor of 3 octaves, the effect of the support system on the structural characteristics of the model can usually be neglected.

If the structure of the vehicle is such that it may be handled as a unit and can be oriented horizontally, the better approach is usually to support it as shown in figure 20. In this type of support system, the effect of the support is secondary, and if, in the excitation of the natural modes of the structure, the supports are located at the nodal points, their effect on the structure is negligible. It is usually desirable to mount the exciter near an anti-node to maximize the response of the structure in the mode of interest. However, if the response of the vehicle indicates coupling of other modes, such coupling can be minimized by mounting the exciter at a node point of the mode producing the undesired coupling effect.

In general, the support cables should be made of elastic shock cord but the results of many tests of small solid-propellant rocket vehicles at the Langley Research Center indicate that steel cables can be used successfully if properly adjusted. In most cases, a two-point support is adequate for such vehicles, the location of these supports being adjusted to coincide with nodal points of the mode being excited.

In some cases, particularly those involving vehicles containing liquid propellants and thin pressurized shells, it is necessary to orient the vehicle vertically to properly simulate the effects of the earth's gravitational field on the dynamics of the vehicle-propellant system. Robert W. Herr of the Langley Research Center has studied this problem, reference 7, and has developed two unique and very effective support systems which are shown in figure 21. Both of these systems closely duplicate the

free-free boundary conditions for such vehicles.

The first of these vertical support systems is referred to as a high-bay harness. The weight of the vehicle is carried by two support cables which are attached to the bottom of the vehicle and to the overhead support structure. Stability is achieved by two horizontal restraining cables tied between the support cables and the periphery of the vehicle at some point, e.g., above the vehicle's center of gravity. This support system has essentially two degrees of freedom in the plane normal to the cables - translation as a pendulum and pitching. In terms of the dimensions shown on the figure, the stiffness, and thus the frequency, of the pitching mode can be controlled by separation of the points where the support cables fasten to the rigid support structure. The vehicle will stand erect if

$$a > f \left(\frac{b}{e_1} - \frac{c}{e} \right) + b$$

and the frequency of the pitching mode will approach zero as

$$a \rightarrow f \left(\frac{b}{e_1} - \frac{c}{e} \right) + b$$

This support system was used successfully on the 1/5-scale SAL-Block I, and the 1/40-scale SATURN V dynamic models studied at the Langley Research Center.

In some instances involving the tests of very large dynamic models or full-scale launch-vehicle structures, it may be difficult to provide an overhead rigid support structure as necessary for the high-bay harness. In such cases, the low-bay harness, though slightly more complicated is

preferable and is being used for the structural dynamics studies of the full-scale Thor-Agena launch vehicle to be conducted at Langley in the near future. As was the case for the high-bay harness, the weight of the vehicle is carried by two support cables. However, in this case the support cables may be much shorter than the length of the vehicle. The vehicle is held erect by controlling the tensions in the restraining cables by means of turnbuckles, and the condition for neutral stability, and hence, zero frequency in pitch, is

$$T = \frac{Wb}{8\left(\frac{L^2}{d} - S\right)}$$

Although it is still necessary to have some support structure near the top of the vehicle, this structure can be relatively light since it need support only a small fraction of the weight of the vehicle.

Spacecraft

Since the majority of spacecraft are small relative to the size of launch vehicles, the support of spacecraft models for dynamic studies can be accomplished with comparative ease. Since spacecraft are usually mounted to the launch vehicles in semirigid fashion, the in-flight support system is closely representative of fixed-free boundary conditions. Hence the general procedure is to rigidly fasten the spacecraft to the exciter for tests along the longitudinal or flight axis, and to attach the spacecraft to a slippery table for excitation of lateral modes and frequencies. It is important to recognize, however, that the impedance of the support system, whether it be the exciter or slippery table, will differ from that of the launch vehicle, and proper consideration of this fact should be exercised

during interpretation of the response data obtained during vibration tests of spacecraft or spacecraft models.

CONCLUDING REMARKS

During recent years, dynamic models have been used to good advantage for solution of some of the problems related to structural dynamics of space vehicles. Because of the size, complexity, and cost of the structures and the variable environments which constitute the structural loads, it appears that current trends which involve the construction and testing of specialized models for analysis of structural characteristics, and responses to ground winds, wind shear, buffeting, and fuel sloshing loads will continue in the foreseeable future. Much additional work is necessary to understand the effects of the highly transient nature of structural properties and loading conditions, and to establish appropriate modeling techniques for their simulation and analysis. Particular attention is needed in the areas of simulation of the coupling of propellant systems with the structure to avoid instabilities such as the POGO oscillations.

As pointed out in the paper, careful attention must be given to proper simulation of both aerodynamic and structural damping in model design and testing.

Proper support of launch-vehicle models to simulate free-flight conditions during tests is important, and methods are presented in the paper which have proven to be adequate and simple.

In several areas of concern such as fuel sloshing and lunar landing, gravity is an important variable. Some of the techniques which may be employed to simulate gravity effects are discussed.

APPENDIX

DIMENSIONLESS RATIOS

The dimensionless ratios which pertain to fluid and flight dynamics are summarized in the following table. The variables which are combined to form the various ratios are defined in the symbols, which are presented at the end of this appendix. Insofar as possible, pertinent references are given which relate to their derivation and use.

SYMBOLS FOR DIMENSIONLESS RATIOS

Symbols and definition	(l, m, t, T, Q dimension	Frequently used dimension
a sonic speed	l/t	ft/sec
B magnetic induction field	m/Qt	
b semichord	l	ft
c_p specific heat at constant pressure . . .	l^2/t^2T	Btu/lb-°R
c_v specific heat at constant volume	l^2/t^2T	Btu/lb-°R
D coefficient of self-diffusivity	l^2/t	
E_1 energy	$m l^2/t^2$	ft-lb
E_2 modulus of elasticity in tension	$m/l t^2$	lb/in. ²
F force	$m l/t^2$	lb
G_1 modulus of elasticity in torsion	$m/l t^2$	lb/in. ²
g gravitational acceleration	l/t^2	ft/sec ²
h heat transfer/area/time/temperature . .	m/t^3T	Btu/ft ² /sec/°R
k Thermal conductivity	$m l/t^3T$	Btu/hr-ft-°R
l reference length	l	ft
L length of mean free path, $\frac{16}{5} \frac{\mu_1}{\rho \sqrt{2\pi RT}}$. .	l	ft
m unit of mass	m	lb-sec ² /ft
\dot{m} mass flow rate	m/t	slugs/sec
\dot{m}_1 mass flow rate	m/t	lb-sec/ft
p local static pressure	$m/l t^2$	lb/ft ²
p_c critical or vapor pressure	$m/l t^2$	lb/ft ²
Q unit of electric charge of flux	Q	coulombs
Q_1 heat added at constant pressure	$m l^2/t^2$	Btu

Symbol and definition	($l, m, t,$ T, Q) dimension	Frequently used dimension
q dynamic pressure	m/lt^2	lb/ft ²
R universal gas constant	l^2/t^2T	
r radius	l	ft
T temperature	T	°R
t time	t	sec
V speed	l/t	ft/sec
V_a Alfven wave speed, $\sqrt{\frac{B^2}{\mu_2 \rho}}$	l/t	ft/sec
β coefficient of thermal expansion	$1/T$	in./in.-°R
μ_1 coefficient of viscosity, abs	m/lt	lb-sec/ft ²
μ_2 magnetic permeability	Q^2/ml	
ρ mass density	m/l^3	lb-sec ² /ft ⁴
σ_1 coefficient of surface tension	m/t^2	dynes/cm
σ_2 electrical conductivity	Q^2t/ml^3	ft ³ /ohm
σ_3 structural density	m/l^3	lb-sec ² /ft ⁴
ω frequency	$1/t$	rad/sec
ω_α torsional frequency	$1/t$	rad/sec

REFERENCES

1. Langharr, Henry L.: Dimensional Analysis and Theory of Models. John Wiley & Sons, Inc., 1951, Chapter 3.
2. Katzoff, S.: Similitude in Thermal Models of Spacecraft. NASA TN D-1631, 1963.
3. O'Sullivan, William J., Jr., Theory of Aircraft Structural Models Subject to Aerodynamic Heating and External Loads. NACA TN 4115, 1957.
4. Molyneux, W. G.: Scale Models for Thermo-Aeroelastic Research. C. P. 579, British A.R.C., 1962.
5. Carden, Huey D., and Herr, Robert W.: Vibration Studies on a Simplified 1/2-Scale Model of the Nimbus Spacecraft. Thirty-third Symposium on Shock, Vibration, and Associated Environments. Washington, D. C., December 3-5, 1963.
6. Brooks, George W.: Techniques for Simulation and Analysis of Shock and Vibration Environments of Space Flight Systems. ASME Shock and Vibration Colloquium, New York. Nov. 27, 1962, edited by Will J. Worley.
7. Herr, Robert W., and Carden, Huey D.: Support Systems and Excitation Techniques for Dynamic Models of Space Vehicle Structures. Symposium on Aeroelastic and Dynamic Modeling Technology, AIA RTD-TDR-63-4197, Part 1. Dayton, Ohio, September 23-25, 1963, pp. 249-277.
8. Streeter, Victor L.: Handbook of Fluid Dynamics. McGraw-Hill Book Co., Inc., New York, First ed., 1961.
9. von Karman, Theodore: Fundamental Equations in Aerothermochemistry. From Selected Combustion Problems, II. Butterworth's Scientific Publications, London, 1956.
10. Neihouse, Anshal I., and Pepoon, Philip: Dynamic Similitude Between a Model and a Full-Scale Body for Model Investigation at a Full-Scale Mach Number. NACA TN 2062, 1950.
11. Ipsen, D. C.: Units, Dimensions, and Dimensionless Numbers. McGraw-Hill Book Co., Inc., New York, 1960, Chapter 12.
12. Alfrey, Turner, Jr.: Mechanical Behavior of High Polymers. Interscience Publishers, Inc., New York, 1948.
13. Kreith, Frank: Principles of Heat Transfer. Int. Textbook Co. (Scranton, Pa.), c.1958.
14. Bisplinghoff, R. L., Ashley, H., and Halfman, R. L.: Aeroelasticity. Addison-Wesley Publishing Co., Inc., Cambridge, Mass., 1955, p. 561.

15. Timoshenko, S., and Goodier, J. N.: Theory of Elasticity. McGraw-Hill Book Co., Inc., New York, Second Ed., 1951, p. 9.
16. Harris, Cyril M.: Handbook of Noise Control. McGraw-Hill Book Co., Inc., 1957, Chapter 33, p. 18.
17. Eide, Donald G.: Preliminary Analysis of Variation of Pitch Motion of a Vehicle in a Space Environment Due to Fuel Sloshing in a Rectangular Tank. NASA TN D-2336, 1964.
18. Frueh, Frank J.: A Flutter Design Parameter to Supplement the Regier Number. AIAA Jour., Vol. 2, no. 7, July 1964.
19. Harris, G., and Head, A. L., Jr.: Flutter Criteria for Preliminary Design. Engineering Report 2-53450/3R467. Chance Vought Corp., A Division of Ling-Temco Vought, Inc., Dallas 22, Texas, September 1963. (CONFIDENTIAL)

DIMENSIONLESS RATIOS

Name	Symbol	Associated variables	Meaning	Application or comments	Reference
Blot	B_L	h_l/h_b	$\frac{\text{Heat transferred to fluid}}{\text{Heat transferred through body}}$	Compares external thermal resistance to internal	13
Bond		$\rho^2 g / \sigma_1$	Gravity/Surface tension	Capillary flow, sloshing equals $1/F \times W$	17
Cauchy	C	v^2/a^2	Inertia/Fluid elastic	Compressible flow equals M^2	8
Cavitation	σ	$(p - p_c)/q$	A pressure coefficient	Hydrofoils, liquid nozzles, and pumps	8
Dam Kohler's 1st	Dam 1	t/W_{chem} or $t_{transl.}/t_{chem}$	Transit time / $\left\{ \begin{array}{l} \text{Relaxation} \\ \text{Reaction} \end{array} \right\}$ time	Real-gas effects	9
Dam Kohler's 2nd	Dam 2	$Q_1/c_p \rho_1 m$	Heat content after reaction / Heat content before reaction	Real-gas effects	9
Structural damping coefficient	\bar{g}		A measure of energy dissipated during vibration due to structural friction	Free, forced, and self-excited vibrations of structures	14
Euler	E	$p/\rho v^2$	Pressure/Inertia	Pressure distributions	8
Force coefficient	C_F or C_R	$2F/\rho v^2 l^2$	Fluid force/Dynamic pressure \times Area	Immersed moving bodies	8
Fourier	F_o	$kt/\rho c_p l^2$	Heat conducted/Heat capacity	Temperature-time problems	13
Froude	F_r	v^2/gl	Inertia/Gravity	Surface ships, airplane flight path, structural sag	10, 8
Grsetz		mc_p/kl	Heat transported by fluid motion / Heat transported by molecular motion	Laminar convective heat transfer in pipe equals Constant $\times P_e$	11
Grashof	G	$\beta(\Delta T)g^2 \rho^2/\mu_1^2$	Inertia \times Buoyant / (Viscous) 2	Free thermal convection equals $\beta(\Delta T) \times R_e^2/F_r$	11, 2
Hartmann	H	$B l \sigma_1^2/\mu_1^{1/2}$	Magnetic/Viscous	Flow of viscous magnetic fluid	8
Knudsen	K	l/L	Reference length/Mean free path	Free molecule flow equals $1.28\sqrt{M/R}$	8
Lewis	L_e	$D_e \rho/k$	A fluid property	Equals F_r/S_c	9

DIMENSIONLESS RATIOS - Concluded

Name	Symbol	Associated variables	Meaning	Application or comments	Reference
Mach	M	V/a	Inertia/Fluid elastic	Compressible flows	8
Magnetic Mach	M _m	V/V _a	Flow speed/Alven wave speed	Magnetic compressibility	8
Magnetic Reynolds	R _m	V/a ₀ μ/2	Motion induced field/applied field	Fluid field interaction	8
Nusselt	Nu	h/k	Heat transferred to fluid Heat transferred through fluid	Convective heat transfer	11, 2
Peclet	Pe	c _p ρVl/k	Heat transported by fluid flow Heat transported by molecular motion	Compressible flow equals R x Pr	11
Poisson	μ	(E ₂ /E ₁) - 1	Lateral contraction Longitudinal extension	Elasticity	15
Froude	Fr	c _p μ/k	A fluid property	Equals 2/5 monatomic, 3/4 diatomic, 2-1.0 polyatomic	2
Regier	R _r	bo ₀ μ ^{1/2} /a	Measure of torsional stiffness required for neutral flutter stability	Flutter index for subsonic speeds	18, 19
Reynolds	Re	ρVl/μ ₁	Inertia/Viscous	Skin friction, boundary layers, sedimentation	8
Schmidt	S _c	μ ₁ /Dp	A fluid property	Equals 0.7 to 0.74 real gases	10
Sherwood	S _h	S _c Nu/Pr	Mass transfer by diffusion	Mass transfer in gases	15
Specific-heat ratio	γ	c _p /c _v	A gas property	Ideal isentropic gas flow equals 1.67 monatomic, 1.4 diatomic	8
Stanton		h/ρc _p V	Heat transferred to fluid Heat transported by fluid flow	Conductive heat transfer	11
Strouhal	St	ωa/V	Vibration Shed vortex	Flutter, wind-induced oscillation	16
Viscoelastic	G ₁ /ωμ ₁		Elastic shear/Viscous shear	Dynamics of plastics and "thick" liquids	12
Weber	W	ρV ² /σ ₁	Inertia/surface tension	Ripple surface waves, capillary flow	11
Nuclear explosion	λ	r/(E ₁ ^{1/2} /σ) ² e/5	Growth parameter	Spherical wave instant energy added at center	8
Magnetic-Dynamic	N	σ ₁ ² /ρV ²	Magnetic/Dynamic pressures	Magnetic fluid flow	8
Mass ratio	μ ₃	σ ₃ /ρ or m ^{1/2} /ρ ^{1/2}	Structural mass/Fluid mass	Flutter, airplane stability	4
		E ₂ /ρV ²	Structural stiffness/Aero. force	Aero. deflections	4
		σ ₂ g/E ₂	Structural weight/Stiffness	Sag due to weight	4

MODELS FOR OBTAINING EFFECTS OF GROUND WINDS ON
SPACE VEHICLES ERECTED ON THE LAUNCH PAD

by

Wilmer H. Reed, III

NASA - Langley Research Center

ABSTRACT

~~22678~~ over

The paper describes how, through simulation with physical and mathematical models, the effects of ground winds on erected launch vehicles are being studied at the NASA, Langley Research Center. Experimental programs include both aeroelastically scaled models in wind tunnels and full-scale vehicles in natural winds. With the aid of a mathematical model having nonlinear aerodynamic damping, insight is gained which helps explain why in some instances the response at supercritical Reynolds numbers is a result of random forced excitation while in other instances is characterized by a self-excited periodic motion.

Consideration is also given to the response of erected vehicles to atmospheric turbulence. It is shown that at the fundamental cantilever frequency of Saturn V class vehicles the gust velocities along the vehicle

are essentially uncorrelated for separation distances greater than a few vehicle diameters. Calculations indicate that the response is significantly reduced when these spatial correlations of gusts are taken into account.

Author

INTRODUCTION

This paper will concern a search for new solutions to an old problem; namely, the effect of wind loads on flexible bluff bodies. For years civil engineers have grappled with the problem in the design of such structures as smoke stacks, suspension bridges, and tall masts. (See, for example, refs. 1 through 4). I should point that included in these studies are contributions by the Director of this Conference, Professor Maher, who has conducted extensive wind-tunnel tests of suspension bridge section models. (See, for example, ref. 2.)

Starting with Goldman's investigation of ground-wind loads for the Vanguard in 1957 (ref.5), some form of wind-tunnel tests relating to this problem has been a part of the development program for practically every launch vehicle. Examples of such studies on specific vehicles are to be found in references 6 through 9, and other more general studies of vortex shedding from cylindrical bodies are given in references 10 through 13. We find further evidence of the extent of effort presently being expended in this area by noting that at the annual AIAA Conference on Structures and Materials held at Palm Springs, California in April of this year, five out of a total of seventeen papers in sessions on structural dynamics concerned the subject of vortex shedding from bodies of revolution. Despite this extensive research, there remain many important

questions to be answered, especially in the high Reynolds number range.

With the aid of figure 1 let us identify the primary ingredients of the problem at hand. This schematic diagram shows a launch vehicle on a flexible support structure standing beside an umbilical tower. A steady wind imposes both static and dynamic loads on the vehicle. The static loads act primarily in the direction of the mean wind and the dynamic loads, which are associated with vortices shed from the vehicle, are largest in the direction perpendicular to the wind. These dynamic loads, which may result from either a random forced response or a periodic self-excited response, are frequently several times greater than the static drag loads. The adjacent tower structure and its turbulent wake may also have an influence on wind loads. These wind loads create problems in structural strength, guidance alignment, and clearance between adjacent structures.

The purpose of this paper will be to discuss recent studies in the area of ground-wind loads being conducted at the Langley Research Center. In particular, we will consider four items: wind-tunnel models and test techniques, self-excited response, effects of atmospheric turbulence, and full-scale programs.

WIND-TUNNEL MODELS AND TEST TECHNIQUES

Aeroelastic Models

The aerodynamic forces associated with ground-wind loads on erected launch vehicles are a result of flow separation from bluff bodies. Since such loads are critically dependent on Reynolds number, efforts are made to duplicate full-scale Reynolds numbers in the wind tunnel. Also, because of the sensitivity of flow separation to minor surface protuberances, such as conduits or surface roughness conditions, careful attention must be given to the simulation of detailed geometric features. If steady-state loads were the only consideration, a rigid model having the same geometric features and Reynolds numbers as the prototype would be adequate for predicting ground-wind loads. Unfortunately, launch vehicles are not rigid and usually the predominant aerodynamic loads are not steady. Therefore, the structural dynamic properties of the vehicle, that is, mass, frequency, and damping, also become important considerations in model scaling. Experience has shown that the predominant dynamic response of launch vehicles to wind-induced loads is essentially that of the first mode alone. The significant additional nondimensional parameters to be matched in the wind tunnel are then the reduced frequency based on the fundamental frequency of the vehicle $\omega_1 D/U$, the structural damping, and a mass ratio involving generalized mass of the fundamental mode to the mass of air displaced by the vehicle.

A model which simulates both aerodynamic and structural dynamic parameters is referred to as an "aeroelastic" model. Wind-tunnel tests of such models are believed to provide the most direct and reliable means of predicting the response of launch vehicles to a steady wind. (See, for

example, refs. 14 and 15).

Shown in figure 2 are some aeroelastic models of specific vehicles which have been used in ground-wind-load studies in the Langley 16-foot transonic dynamics tunnel during the past 4 years. Notice that in most instances the vehicle models are tested in the presence of simulated umbilical towers or service structure. These towers are usually scaled only with regard to over-all geometry. The exception is the erector tower for the Titan-Gemini which had scaled frequencies. The models - vehicle and tower structures - are installed on a remotely controlled turntable so as to permit response measurements to be taken from any wind direction.

By using a freon test medium, which has a kinematic viscosity of about one-fifth that of air, Reynolds number simulation can be approximately achieved for all of the vehicles shown except for the Saturn V. For this model, which is 3 percent of full-scale size, the Reynolds number in the wind tunnel was one-third of the full-scale value.

Even when Reynolds number is matched, however, there are differences in the flow in wind tunnels as compared with that in the natural atmosphere. In the wind tunnel the flow is approximately uniform and steady; in the atmosphere near the ground the mean wind varies with height and is gusty. An approximate means of taking into account wind variations with height is to relate the wind-tunnel velocity to a calculated "equivalent" velocity which produces the same steady-state base-bending moment as does the actual wind profile. A reasonable approximation of natural wind profiles has been simulated in wind tunnels by use of a transverse grid of various sized rods. (See refs. 16 and 17.) A pilot study is presently underway at Langley to determine the feasibility of applying these techniques in ground-wind load studies.

Modeling criteria for simulating atmospheric turbulence in wind tunnels have also been successfully applied in reference 18. These scaling laws, however, are not compatible with those used in the scaling of aeroelastic models. Some further consideration of the scaling of natural turbulence in wind tunnels will be given in a later section of this paper.

Response Measurements

The principal response measurements in these studies are the static and dynamic bending moments in two planes at the base of the model, and corresponding accelerations at the nose. Although time histories of the quantities are recorded, the most useful readout system employed in a two-axis oscilloscope and camera. As illustrated in figure 3, the outputs of X and Y bending-moment strain gages are fed to the X and Y axes of the scope and the sensitivities of the two channels are made equal. A time-exposure photograph of the oscillograph screen produces a roughly elliptical pattern which defines the envelope of the maximum bending-moment oscillations encountered during the data sampling period; typically, the model encounters between 2,000 and 3,000 cycles of oscillation during this period, which, in terms of the full-scale vehicle, is equivalent to wind exposure times of the order of 1 hour. The vector from the wind-off point to the center of the elliptical pattern represents the static moment, and the longest vector which can be drawn from the wind-off point to the tangent on the ellipse is the maximum resultant moment. Note that information on the correlation between the two-moment time histories is displayed with this type of data presentation. It has been found that the probability of the lateral and dragwise bending moments reaching maximum values at the same time is very low.

Damping Devices

Structural damping has been found to be one of the key parameters which governs the susceptibility of a vehicle to wind-induced oscillations. It is very difficult, however to control damping in a model as accurately as other parameters. A viscous damper, shown in figure 4, has been developed which permits precise regulation of the damping in a model. The device works on the principle of the classical Lanchester damper. It consists of a series of lead slugs (auxiliary masses) that are free to slide on concave trays inside of a cylinder filled with viscous oil. As the cylinder vibrates in a horizontal plane, the oil moves relative to the slugs, thereby causing energy to be dissipated. The damping can be varied by changing the number of slugs or the viscosity of the oil. Figure 5 shows the increase in damping in the 0.03-scale Saturn V model obtained with eight 72-gram slugs in the damper.

Various damping devices have been used or proposed as means of alleviating wind-induced oscillations of smoke stacks. Usually the dampers are connected to the structure by means of guy wires (ref. 3 and 4). Since guy wire supports are often not feasible in launch vehicle applications, it is of interest to consider the use of auxiliary mass dampers, which requires no external connections, as a possible method for reducing wind-induced loads on full-scale vehicles. Such devices presumably could be attached to the vehicle during high wind conditions and then be removed prior to launch.

Theoretical performance characteristics of an auxiliary mass damper are shown in figure 6 as a three-dimensional surface. It is assumed that an auxiliary mass m is connected to the vehicle structure through a spring k_d and dashpot c , as indicated schematically in the figure. The

vehicle structure is represented mathematically as a single-degree-of freedom oscillator having a generalized mass M and natural frequency ω_1 . The case shown is for $m/M = 0.05$. The vertical axis in the figure is the damping ratio ζ_1 associated with the vehicle mode; this was determined from the real part of one root of the characteristic equation for the coupled system. Plotted on the other axes are ω_d/ω_1 , the ratio of uncoupled frequencies, and $c/2m\omega_1$, a nondimensional viscous damping parameter. This figure simply illustrates a well-known result from the theory of vibration absorbers (see, for example, ref. 19) that when the auxiliary mass is "tuned" to the natural frequency of the system to which it is attached, and $c/2m\omega_1$ is near an optimum value, large energy dissipation can be achieved. The previously discussed Lanchester type damper is represented by the curve for $\omega_d/\omega_1 = 0$. Note that this damper has optimum performance at $c/2m\omega_1 = 0.5$. The wind-tunnel research applications where precise control of damping in aeroelastic models is desired, the fact that ζ_1 is relatively insensitive to variations in $c/2m\omega_1$ becomes an attractive feature; however, in full-scale applications, where weight of the auxiliary mass may be an important consideration, tuned dampers offer more than an order of magnitude improvement in performance.

SELF-EXCITED RESPONSE

Various and conflicting theories have been advanced regarding unsteady aerodynamic forces associated with vortex shedding from circular cylinders. In the supercritical Reynolds number range - the range of primary interest for the present problem - experimental data indicate that in some instances these forces are random and insensitive to motion of the structure (Fung,

ref. 10) and in other instances periodic and strongly dependent on motion (Buel, et al., ref. 12 and Den Hartog, ref. 3). This section of the paper will be devoted to consideration of these apparent differences. In particular, a simple mathematical model, involving nonlinear aerodynamic damping, is presented which has behavior consistent with both of the above-mentioned phenomena.

Experimental Results

In recent wind-tunnel tests at Langley involving Saturn I-B and Saturn V ground-wind load models violent self-excited oscillations were encountered. These oscillations occurred at Reynolds numbers as high as 4×10^6 based on the model's maximum diameter. On both models the instability appeared at reduced frequencies, based on the maximum diameter, in the neighborhood of 0.2 which happens to be the Strouhal number of the Karman vortex street at subcritical Reynolds number.¹ Similar self-excited response phenomena have been observed on large, lightly damped, steel smokestacks and the solution has been to add damping (ref. 3) or attach aerodynamic spoilers to the structure (ref. 20).

Now it might be argued that these high response conditions observed at a particular wind velocity could be in the nature of a forced resonant oscillation rather than an instability. Data presented in figure 7, however,

¹ It should be noted that for these models the peak response appears to be a result of vortex shedding from the lower stages at a Strouhal number of 0.2. Response characteristics were relatively insensitive to changes in nose shape or surface roughness conditions; for other vehicles configurations, nose shape and roughness may be the dominant factor affecting response. (See ref. 12.)

serve to disprove this argument. These data were obtained on the 0.03-scale Saturn V model. The figure shows the variation of dynamic bending-moment response with velocity for three values of structural damping. First, note that for the smallest damping of $\zeta = 0.004$, the response peaks sharply at a reduced velocity of approximately 4.5. The sample time history shown for the peak response point is a nearly constant amplitude sine wave at the fundamental model frequency. When the damping is increased from 0.004 to 0.008 the sharp spike is eliminated and the response time history is characterized by a random-amplitude constant-frequency motion typical of the response of a lightly damped system to a random-forcing function. This complete change in character of the response time histories as damping increases suggests that at a certain critical velocity the structural damping of the system is a controlling factor which determines whether the dynamic response is a result of self-excited or externally forced motions. In either case it is apparent that structural damping of the model is an important parameter to be simulated. Furthermore, the commonly used scaling laws (ref. 21) based on the response of systems to random or periodic forcing functions, without consideration of motion-dependent aerodynamic forces, would be inapplicable for these cases of self-excited response. Similar results are shown in reference 12.

Conceptual Model of Self-Excited Response

Let us now attempt to interpret the mechanism producing these observed dynamic instabilities. Scruton, in reference 22, has made extensive wind-tunnel studies of industrial structures such as smokestacks and towers, and has reported similar instabilities which he attributes to a nonlinear aerodynamic damping that becomes negative at a particular wind velocity. Scruton's results were obtained at subcritical Reynolds numbers; however, his findings

appear to be applicable to the present studies where Reynolds number varies from 1 to 6 million.

A launch vehicle structure and the aerodynamic loads associated with vortex shedding are represented conceptually by the block diagram pictured in figure 8. Let $F_S(t)$ be the aerodynamic forcing function which is independent of vehicle motion and $F_D(t)$ to a nonlinear aerodynamic damping force which depends on the vehicle motion. In the equations of motion, also given in figure 8, the left-hand side describes dynamics of the structure in terms of a natural frequency and damping ratio and the right-hand side expresses the aerodynamic forces in terms of a lateral force coefficient $C_L(t)$ and damping coefficient C_x . For the present purpose it will be assumed that $C_L(t)$ is a random function of time. Depending on the relative magnitudes of the structural and the aerodynamic damping coefficients, the response $x(t)$ of the structure in the direction perpendicular to the wind can take on either of the two forms indicated in the figure. When the damping is predominantly structural, the response will be the characteristic random-amplitude constant-frequency motion typical of a lightly damped system driven by a random forcing function. With aerodynamic damping present in a nonlinear form such as measured by Scruton, the possibility exists for self-excited motions indicated in the figure by the constant amplitude sinusoidal response. A representative plot of the variation of C_x with reduced frequency (see fig. 9) shows that over a narrow range of fD/U near 0.20, the aerodynamic damping has a destabilizing influence which depends strongly on the amplitude of motion. At this critical value of reduced frequency the destabilizing effect becomes smaller as the amplitude of motion increases. Thus, an energy balance is eventually established between the energy input by negative aerodynamic damping and the energy absorbed by positive

structural damping. This leads to a limit-cycle oscillation whose amplitude is inversely proportional to structural damping as shown in plot on right side of figure 9.

Analog Computer Studies

Further insight into the behavior of the nonlinear mathematical model presented in figures 8 and 9 may be gained from analog computer solutions. For this purpose the equation in figure 9 has been programmed on an analog computer in the manner shown in figure 10. The random lateral forcing function $C_L(t)$ was obtained by passing the output of a Gaussian white-noise generator through a first-order low-pass filter. The filter time constant was adjusted to make the power spectrum of $C_L(t)$ approximate closely the spectrum for fixed cylinders presented by Fung in figure 11 of reference 10. Output of the noise generator was adjusted such that the root-mean-square of C_L matched Fung's measured value of 0.12. As an approximation to Scruton's results in reference 22, the nonlinear damping coefficient was assumed to be inversely proportional to a running average of the absolute value of response.

The results are shown in figure 11 as a plot of maximum response observed during a computer run against damping of the structure. The plot on the left of the figure represents the system response with the motion-dependent aerodynamic force set equal to zero. This response varies inversely as $\sqrt{\zeta}$ which is the relationship predicted for lightly damped systems acted on by a random forcing function. (See ref. 21.) According to Scruton's data this is representative of conditions when the natural frequency of the system is not in the vicinity of the Strouhal frequency. The right-hand side of the figure shows corresponding results when the natural frequency and the Strouhal frequency have approximately the same

values, say, $f_n D/U \approx 0.2$. Note the similarities in these analog time histories and the bending-moment time histories shown in figure 7 for the Saturn V model.

The apparent inconsistencies between Fung's observation (ref. 10) - aerodynamic forces on cylinders are random and essentially independent of body motions - and the self-excited response observed for both wind-tunnel models and smokestacks might then be reconciled as follows: In Fung's investigation, the cylinder motion was limited to reduce frequencies below 0.12; Scruton (ref. 22) and the present wind-tunnel studies indicate that motion dependent forces, in the form of negative aerodynamic damping occur in a narrow range of reduced frequencies near the Strouhal number of 0.2. In order to shed further light on these and related questions, a generalized research study on two-dimensional cylinders will be conducted in the Langley transonic dynamics tunnel up to Reynolds number of 20×10^6 . The Martin Company, George C. Marshall Space Flight Center, and Langley Research Center will be joint participants in this program.

RESPONSE TO TURBULENCE

Comparison of Wind-Tunnel and Atmospheric Turbulence

Unlike the uniform profile of steady wind in a wind tunnel, atmospheric winds near the ground are typically as illustrated in figure 12. The profile patterns shown represent instantaneous distributions of horizontal wind that may occur as a field of turbulence is blown past an erected vehicle. The dashed line in the figure represents the mean wind averaged over, say, a 1-minute period; the little arrows represent more rapid wind fluctuations of wind components in the direction of the mean flow. As indicated in the figure, these unsteady wind components vary randomly in both time and space. Since

these winds produce random loadings on the structure, power spectral techniques appear to offer the most fruitful method of analysis and will be the approach discussed in the present paper.

Before considering some mathematical techniques for predicting the response of launch vehicles to ground wind turbulence, let us first discuss the possibility of simulating such turbulence in a wind tunnel. Consider the question: To what extent would the turbulence structure representative of wind tunnels need to be modified in order to simulate "atmospheric" turbulence in wind-tunnel testing of aeroelastically scaled models? Figure 13 will serve to answer this question. The figure shows typical plots of the power spectrum of wind-tunnel turbulence and atmospheric turbulence near the ground. The curves are plotted against the familiar frequency scaling parameter fD/U . Turbulence, whether it be in the earth's boundary layer or in a wind tunnel, can be characterized by a mean eddy size or "scale" length L , and the rms intensity of fluctuation components relative to the mean wind velocity, $\sqrt{u^2}/U$. For atmospheric winds near the ground, the scale of turbulence is of the order of the over-all length of Saturn V vehicle, or 10 vehicle diameters. In wind tunnels a typical value of L might be 1/10 the diameter of a ground-wind-loads model. Also, the intensity of turbulence is an order of magnitude different for the two cases, being, say, 20 percent of the mean wind for the atmosphere as compared with 1 or 2 percent for wind tunnels. In summary, the figure indicates that over the frequency range of interest in the present problem, typical values of the scale and intensity of turbulence in wind tunnels and in the atmosphere are vastly different; therefore, study of the effects of gust loads associated with atmospheric turbulence in wind tunnels must await the development of new techniques for the generation and control of wind-tunnel turbulence.

Basic Power Spectral Relationships

In absence of suitable wind-tunnel techniques for studying the response of vehicles to atmospheric turbulence, we must work either with mathematical models or actual structures exposed to natural winds. Both of these approaches are being pursued at NASA-Langley. This section of the paper will concern an analytical approach to the problem.

Power spectral techniques have proved to be powerful tools for analyzing the response of systems to random inputs. Such techniques for aircraft gust-load prediction have been under development for more than a decade and offer an excellent foundation on which to formulate the present problem. Of particular value is the paper by Houbolt, Steiner, and Pratt (ref. 23) which presents an exhaustive review and extension of power spectral techniques in relation to the response of airplanes to atmospheric turbulence. A basic equation for the power spectrum of a linear system acted upon by multiple random inputs is presented in references 23 and 24 wherein the structure is assumed to be divided into an arbitrary number of segmented areas with a random forcing function acting at the center of each segment.

$$\begin{aligned} \phi_r(\omega) = & \phi_{11} H_1 H_1^* + \phi_{22} H_2 H_2^* + \phi_{33} H_3 H_3^* + \dots \\ & + 2R_e(\phi_{12} H_1^* H_2 + \phi_{13} H_1^* H_3 + \dots \phi_{23} H_2^* H_3 + \dots) \end{aligned} \quad (1)$$

where

$\phi_r(\omega)$ power spectrum of a response variable r which may denote base bending moment, tip deflection, etc.

ϕ_{ij} cross spectrum of turbulence velocities at i^{th} and j^{th} points on the structure

H_i frequency response function which gives the response due to
a unit sinusoidal gust component velocity acting at the
segment of surface area associated with the i^{th} point

$H_i^*(\omega) = H_i(-\omega)$ complex conjugate of H_i

Re denotes the real part

In its general form this equation indicates that a considerable amount of information regarding the spectral description of turbulence is required in order to define the response spectrum. Specifically, the power spectrum of horizontal components of turbulence must be specified as a function of frequency at each of n points on the structure together with the cross spectra between all combinations of pairs of the velocity components. Since such information is rarely available in the form required, various simplifying assumptions must be made in order to obtain numerical solutions to equation (1). The most frequently made assumptions are that the gust velocities are in phase at every point on the structure and that the turbulence field is homogeneous; that is,

$$\phi_{11} = \phi_{12} = \phi_{13} \cdots \phi_{1n} \quad (2)$$

With these assumptions, equation (1) reduces to the following simple form

$$\phi_r(\omega) = |H|^2 \phi_{11} \quad (3)$$

where

$H = H_1 + H_2 + \dots + H_n$ frequency response function for a sinusoidal gust uniformly distributed over the vehicle length

ϕ_{11} power spectrum of gust components

Bohne, in reference 25, utilizes this equation in analyzing the response of launch vehicles to ground-wind turbulence. Various empirical expressions

for the power spectrum of turbulence, derived from data obtained from wind towers and airplanes, are available for use in such calculations. (See, for example, refs. 23, 26, 27, and 28.)

An obvious shortcoming of the assumption of perfect correlation of gusts along the length is that dynamic response in the fundamental mode is likely to be grossly overestimated, especially if gust wave lengths corresponding to the fundamental structural frequency are small in comparison with the vehicle length. A more rational assumption would be to account for correlation of gust velocities on the basis that atmospheric turbulence is locally homogeneous and isotropic; that is, its statistical properties in a given volume of air are the same at all points and are independent of rotations of the reference axes. In an analysis of response of line-like structures to gusty winds, Davenport (ref. 29) makes similar assumptions and justifies them on the basis of experimental evidence. Under these conditions the cross spectra depend only on the separation distance between points and are independent of height above the ground. The following relations then apply

$$\begin{aligned}\phi_{11} &= \phi_{22} = \phi_{33} = \dots \phi_{nn} \\ \phi_{12} &= \phi_{23} = \phi_{34} = \dots \phi_{n,n+1} \\ \phi_{13} &= \phi_{24} = \phi_{35} = \dots \phi_{n,n+2}\end{aligned}\quad (4)$$

and equation (1) becomes

$$\begin{aligned}\phi_r(\omega) &= \phi_{11} \left\{ H_1 H_1^* + H_2 H_2^* + \dots + 2\text{Re} \left[\frac{\phi_{12}}{\phi_{11}} (H_1^* H_2 + H_2^* H_3 + \dots) \right. \right. \\ &\quad \left. \left. + \frac{\phi_{13}}{\phi_{11}} (H_1^* H_3 + H_2^* H_4 + \dots) + \frac{\phi_{1n}}{\phi_{11}} (H_1^* H_n + H_2^* H_{n+1} + \dots) \right] \right\} \quad (5)\end{aligned}$$

Cross Spectra of Turbulence

In order to calculate the response spectrum on the basis of equation (5) the cross-spectra functions must first be specified. These functions are derived in appendix A from theoretical considerations which employ Taylor's hypothesis (i.e., fixed patterns of turbulence are transported at the mean wind velocity) together with the assumption that over the height intervals of interest the turbulence is homogeneous and isotropic. Results from the theory are plotted in figure 16. Also shown in figure 15(a) are experimental data obtained by Singer (ref. 30) from a 400-foot tower in wooded country at the Brookhaven Laboratory and by Davenport (ref. 29) on a 500-foot mast in open grassland. It is encouraging to note that the experimental data from both of these sites are in reasonable agreement and that the theoretical curve falls within the scatter of the data.

Probably the most significant feature of figure 15 is that for vertical separation distances greater than about 0.3 of u component wavelengths or 0.5 of v component wavelengths the gusts are essentially uncorrelated. For example, in a 60-knot wind at a frequency corresponding to the Saturn V fundamental cantilever frequency ($f = 0.5$ cps), correlation of u gust components is negligible for separation distances greater than two maximum-vehicle diameters.

The ordinate in figure 15, defined as the square root of the coherency function, represents the modulus of the complex cross spectra which consists of a real (copower) part and an imaginary (quadpower) part. It should be pointed out that in the theoretical cross spectra the quadpower is zero whereas in the experimental cross spectra a small quadrature component was measured. These quadrature components are due in part to shear flow in the wind profile and also probably lags in the wind sensors.

Applications

In appendix B the frequency response functions indicated in equation (5) are derived in terms of natural vibration modes of a structure. The response spectrum for a two-dimensional gust input is then expressed as a product between the response spectrum for one-dimensional gusts and a so-called "attenuation" factor which accounts for the two-dimensionality of turbulence. For example, the spectrum of response in the x direction due to u gust components is (see eq. (B-15a))

$$\phi_x(k) = T_{un}(k) \phi_{x,\text{uniform}}(k)$$

where the subscript n refers to the mode number and $T_{un}(k)$ is the attenuation factor given by equation (B-16) in appendix B. Examination of this matrix equation indicates that $T_{un}(k)$ is dependent on such factors as vehicle geometry, mode shape, wind profile shape, and the cross spectra of turbulence between points along the vehicle.

In order to present some specific results the gust attenuation factor $T_{un}(k) = \phi_x / \phi_{x,\text{uniform}}$ was evaluated for a Saturn V class vehicle in a cantilevered unfueled condition. The Saturn V has a maximum diameter of 33 feet and is about 350 feet tall. Natural frequencies of the first two cantilevered modes were assumed to be 0.48 cps and 1.85 cps. The steady wind profile shape considered followed a 1/5 power law variation with height as suggested in reference 31.

Results of these calculations are presented in figure 16. Note that for reduced frequencies fD/U greater than about 0.1 attenuation due to two-dimensional effects is approximately twice as great for the first mode as it is for the second mode. A physical explanation of this result can be gained by recognizing that in the first mode a 180° phase shift for gusts on opposite

sides of the node line has a load amplifying effect. Similar results are noted in reference 24.

Although gust correlation effects tend to attenuate the first mode to a much greater extent than the second mode, the absolute response is, nevertheless, predominantly that of the first mode. This result is associated with the rapid decrease in turbulent energy with increasing frequency.

An interesting feature to be noted is that the curves in figure 16 are independent of the scale of turbulence. This is a consequence of the assumption made in appendix A that the gust wavelengths of interest are equal to or less than the scale of turbulence.

Power spectra of first-mode response to u and v gust components are presented in figure 17 for 1-D and 2-D turbulence. The response deflection has been made nondimensional by dividing it by the static deflection associated with the mean wind speed. In these calculations it has been assumed that the wind speed is the 99.9 percent probable maximum at Cape Kennedy (ref.31) which is 43.4 knots at the 240-foot height. The velocity at this height is the effective wind velocity U_e which, if distributed uniformly over the vehicle, would produce the same static dragwise base bending moment as does the assumed wind profile. The mean square turbulence was assumed to be $\bar{u}^2 = \bar{v}^2 = 0.03 U_e^2$. And finally, the form of the power spectra for u and v was assumed to be given by equation (B-14) with $L = 10D_0 = 330$ ft at all heights.

Note in the figure that at the lower frequencies, corresponding to long wavelengths, the 1-D and 2-D response curves are almost identical. In the vicinity of the first-mode natural frequency, however, the effects of 2-D turbulence are indeed significant. From areas under the spectra curves the variance of response for 1-D gusts are approximately twice that of the 2-D gusts.

FULL-SCALE STUDIES

In previous sections of the paper we have discussed ways in which the response of launch vehicles to ground-wind loads can be simulated by means of models - both physical and mathematical. Whether or not these models are the intended analogs of their full-scale counterparts must be judged on the basis of comparisons between appropriate model and full-scale data. Although considerable effort has been devoted to wind-tunnel studies of aeroelastic ground-wind models, there is little in the way of full-scale data available for correlation with similar model data.

Jupiter and Thor Vehicles

In order to fill this gap the Langley Research Center is engaged in two programs aimed at obtaining ground-wind response data on full-scale vehicles. The first of these programs involves use of a Jupiter and a Thor vehicle which have been acquired as surplus property. These vehicles are to be used solely for ground-wind-load studies over a 1-year period at Wallops Island. Vehicle response, in the form of bending moments and accelerations, will be measured together with the wind inputs at two heights near each vehicle. In addition, other wind measurements will also be obtained from five elevations on a 250-foot tower located about 1/4 mile from the vehicle site. Special fast-response anemometers similar to the prototype shown in figure 18 (ref. 32) will be used. These instruments have flat response to frequencies several times greater than the fundamental vehicle frequencies. Vehicle response and wind input data will be automatically recorded on magnetic tape at regular intervals, or whenever the wind exceeds a preselected value.

The previously mentioned wind-tunnel tests of a 20-percent scale Jupiter model indicated that small strake-type spoilers placed on the nose had a pronounced load alleviation effect. These results are shown in figure 19 as a plot of the maximum resultant bending moment against wind speed. One of our first objectives in the full-scale program, then, will be to determine if spoilers are in fact as effective as predicted in the wind-tunnel studies.

Titan-Gemini

The second full-scale ground wind response program has been established for the Titan-Gemini at Cape Kennedy. This program is being conducted by Martin-Baltimore under contract with the Air Force and Manned Spacecraft Center. It will be closely followed by the Langley Research Center while, in addition to having conducted wind-tunnel studies of the vehicle and erector system, is providing the previously mentioned fast-response anemometers for the wind-measurement phase of the program. The bending-moment response of the vehicle will be read out from load cells which are a part of the launch pad hold-down structure. For each vehicle there will be two opportunities to obtain response data when the vehicle is not sheltered by the erector tower; these are during a fuel loading checkout and immediately prior to launch.

Although the system is not yet fully operational, some bending-moment response data were obtained by the Martin Company just prior to launch of the first Titan-Gemini vehicle. These data are presented in figure 20 together with wind-tunnel results and theoretical predictions of response due to turbulence. The only source of wind data available at the time of these measurements was a propeller-type anemometer mounted a few feet above the blockhouse and read out visually on a meter. Therefore, precise values

for the mean wind and the intensity of turbulence at the vehicle are not known; the intensity of turbulence assumed in these calculations was $\sqrt{u^2}/U = \sqrt{v^2}/U = 0.2$. Although there appears to be reasonable agreement indicated between these full-scale measurements and the predictions based on wind-tunnel data and assumed turbulence conditions, quantitative comparisons should not be attempted until the more precise measurements of the wind are available.

CONCLUDING REMARKS

This paper concerns the role simulation plays in prediction of effects of ground winds on space vehicles erected on the launch pad. It is shown that with present techniques, both wind-tunnel and mathematical models are required in order to predict the response of vehicles to gusty winds. By means of a conceptual representation, which involves a random forcing function and nonlinear aerodynamic damping, new insight is gained into the mechanism of self-excited response which has been observed at supercritical as well as subcritical Reynolds numbers. In consideration of the response to ground-wind turbulence, it is indicated that the spatial correlation of gusts along the vehicle length can have significant effects. Finally, it is hoped that by correlation of response measurements now being obtained on full-scale vehicles with those predicted from models the adequacy of existing simulation techniques can be better established.

SYMBOLS

a_n, b_n	generalized coordinates for the nth modal functions in the x and y directions, respectively
C_L	lateral force coefficient
$C_{\dot{x}}$	aerodynamic damping coefficient
c	viscous damping coefficient
D	diameter
D_0	vehicle maximum diameter
$f(r), g(r)$	nondimensional correlation functions of velocity components parallel and perpendicular, respectively, to a line r between two points in the field of turbulence
f	frequency, cps
$F_S(t)$	random forcing function due to vortex shedding from a fixed cylinder
$F_D(t)$	aerodynamic damping force
H_i	frequency response functions relating response to a unit sinusoidal input force at station i on the structure
$H_n^{(1)}(i\alpha)$	Bessel function of the third kind
k	reduced frequency ($k = \omega D_0 / U_0$), or spring constant
$K_n(\alpha)$	Bessel function of the second kind for imaginary argument
l	vehicle over-all length
L	scale of turbulence (see eq. (A-8))
m	auxiliary damper mass or mass per unit length
M_n	generalized mass of the nth natural mode
$M_{x, y}$	bending moment about axis indicated by subscript
p_i, q_i	orthogonal components of gust velocity at a point i

$Q_{x,n}, Q_{y,n}$	generalized forces for the nth mode in x and y directions, respectively
r	correlation distance
R_e	real part of a complex quantity
$R_{ij}(\tau)$	cross correlation of horizontal gust components at point i and j on a vertical line
S_{n1}, S_{n2}, S_{n3}	integrals defined in appendix B
s	nondimensional time ($s = U_0 t / D_0$)
t, τ , T	time
T_{un}, T_{vn}	attenuation of response spectra in nth mode due to spatial correlation of u and v gusts (see eq. B-15))
u, v	horizontal components of turbulence in direction parallel and perpendicular, respectively, to the mean wind
u_0, v_0	amplitude of sinusoidal u and v gusts
U, U_0	mean wind velocity, subscript 0 denotes reference value
U_e	equivalent uniform wind velocity
$W(z)$	function defined in equation (B-4)
x, y	deflection response or horizontal axes
x_{st}	static deflection associated with mean wind
x_n, y_n	deflections of nth natural mode of vehicle relative to the tip deflection
z	axial distance along vehicle
$\alpha = \frac{\Delta z}{L} \sqrt{1 + v^2}$	
γ	normalized cross spectra of gusts (see eqs. (A-15) and (A-17))
δ	see equation (B-3)
c	distance between segmented areas

ζ	viscous damping ratio relative to critical damping
ξ_n, η_n	Nondimensional response functions $\left(\xi_n = \frac{x_n}{D_0}, \eta_n = \frac{y_n}{D_0} \right)$
κ_n	density ratio parameter $\left(\kappa_n = \frac{\rho L D_0^2}{M_n} \right)$
κ	constant in figure 9 $\left(\kappa = \frac{\rho U^2 D}{2m} \right)$
λ	nondimensional time delay $\left(\lambda = \frac{U\tau}{L} \right)$
ν	reduced frequency based on L , $\left(\nu = \frac{\omega L}{U} \right)$
ρ	density of air or wind-tunnel test medium
σ	nondimensional separation distance $\left(\sigma = \frac{\Delta z}{L} \right)$ or standard deviation of a random variable
$\Phi_{ij}(\omega)$	power spectra or cross spectra of a random variable
ω	circular frequency

Notation:

A dot ($\dot{}$) denotes differentiation with respect to time

A prime (\prime) denotes differentiation with respect to s

A bar ($\bar{}$) denotes average value

An asterisk ($*$) denotes conjugate of a complex quantity

Vertical bars $||$ denote modulus of a complex quantity

[] row matrix

[] square matrix

{ } column matrix

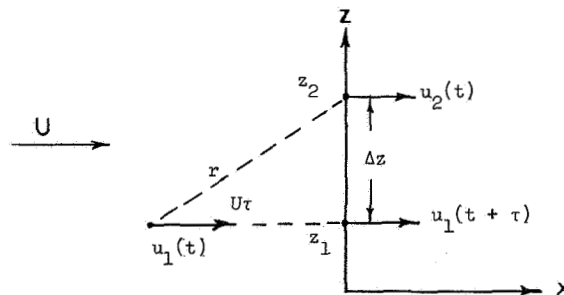
APPENDIX A
DERIVATION OF CROSS SPECTRA OF VERTICALLY SEPARATED
COMPONENTS OF TURBULENCE

Consider the horizontal components of turbulence along a fixed vertical line representing the center line of an erected vehicle. In accordance with Taylor's hypothesis it will be assumed that turbulence can be treated as a space pattern of velocities which are transported at a mean horizontal velocity U . In addition, the turbulence is assumed to be homogeneous and locally isotropic. With these assumptions the correlation of velocities between two points depends only on the distance between the points so that a simple relationship exists between space correlations and time correlations.

The method of analysis to follow may be considered an extension of the cross spectra of vertical gust derived by Houbolt (ref. 24) in connection with two-dimensional gust loads on aircraft.

Cross Spectra of $u(t)$

Consider the u component of turbulence at two points a distance Δz apart on the vertical z axis (see sketch a).

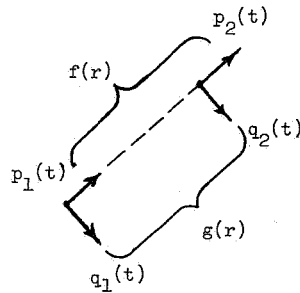


Sketch a.

The quantity of interest is the cross correlation between $u_1(t + \tau)$ and $u_2(t)$ from which the cross spectra can be derived. The cross correlation function, defined as

$$R_{12}(\tau) = \lim_{T \rightarrow \infty} \frac{1}{T} \int_0^T u_1(t)u_2(t + \tau)dt \quad (A-1)$$

can be expressed in terms of the one-dimensional correlation function of the turbulence field. The two such functions required are $f(r)$ and $g(r)$ which denote the correlation of velocity components parallel and transverse, respectively, to a line r between two points in the field. (See sketch b.)



Consider the situation at time t . The velocity at point z_2 in sketch a is $u_2(t)$. Upstream of point z_1 a distance Ur is the velocity $u_1(t)$ which will arrive at z_1 τ seconds later. These components, $u_1(t + \tau)$ and $u_2(t)$, can be expressed in terms of components parallel and perpendicular to the line $r = \sqrt{(\Delta z)^2 + (Ur)^2}$ at time t . Thus

$$\begin{aligned} u_1(t + \tau) &= p_1(t) \cos \theta + q_1(t) \sin \theta \\ u_2(t) &= p_2(t) \cos \theta + q_2(t) \sin \theta \end{aligned} \quad (A-2)$$

where

$$\sin \theta = \frac{\Delta z}{\sqrt{(\Delta z)^2 + U^2 \tau^2}} ; \quad \cos \theta = \frac{U\tau}{\sqrt{(\Delta z)^2 + U^2 \tau^2}}$$

Substitution of equation (A-2) into equation (A-1) yields

$$R_{12}(\tau) = u^2 [f(r) \cos^2 \theta + g(r) \sin^2 \theta] \quad (A-3)$$

where $f(r)$ is the correlation of velocities p_1 and p_2 in the direction of r and $g(r)$ is the correlation of velocities q_1 and q_2 in the direction normal to r . These correlations are defined as

Longitudinal:

$$f(r) = \frac{R_{p_{12}}(r)}{R_{p_{11}}(0)} = \frac{\overline{p_1 p_2}}{\overline{p_1^2}} \quad (A-4)$$

Transverse:

$$g(r) = \frac{R_{q_{12}}(r)}{R_{q_{11}}(0)} = \frac{\overline{q_1 q_2}}{\overline{q_1^2}}$$

Also, in deriving equation (A-3) use has been made of the following relations which result from the assumption of isotropic turbulence

$$\overline{p_1^2} = \overline{q_1^2} = \overline{u^2}$$

and

$$\overline{p_1 q_1} = \overline{p_2 q_2} = 0 \quad (A-5)$$

The cross spectrum of the $u_1 u_2$ components of turbulence is defined as the Fourier transforms of the cross-correlation function given by equation (A-3)

$$\phi_{12}(\omega) = \frac{1}{\pi} \int_{-\infty}^{\infty} R_{12}(\tau) e^{-i\omega\tau} dt \quad (A-6)$$

Thus in order to derive a specific analytical expression for the cross spectrum it is necessary to assume a specific form of $f(r)$ and $g(r)$ in equation (A-3). For this purpose the simple exponential correlation functions which closely follows the form of isotropic turbulence observed in wind tunnels will be used. (See refs. 33 and 34.) These functions are

$$\left. \begin{aligned} f(r) &= e^{-|r|/L} \\ g(r) &= \left[1 - \frac{|r|}{2L} \right] e^{-|r|/L} \end{aligned} \right\} \quad (A-7)$$

where L is the so-called integral - scale of turbulence defined as

$$L = \int_0^{\infty} f(r) dr \quad (A-8)$$

Substitution of equations (A-7) into equation (A-3) gives

$$R_{12}(\tau) = \frac{\overline{u^2}}{(\Delta z)^2 + U^2 \tau^2} \left[U^2 \tau^2 e^{-\frac{\sqrt{(\Delta z)^2 + U^2 \tau^2}}{L}} + (\Delta z)^2 \left(1 - \frac{\sqrt{(\Delta z)^2 + U^2 \tau^2}}{2L} \right) e^{-\frac{\sqrt{(\Delta z)^2 + U^2 \tau^2}}{L}} \right] \quad (A-9)$$

Now let $\sigma = \Delta z/L$

$\lambda = U\tau/L$

Then

$$R_{12}(\lambda) = \overline{u^2} \left(1 - \frac{\sigma^2}{2\sqrt{\sigma^2 + \lambda^2}} \right) e^{-\sqrt{\sigma^2 + \lambda^2}} \quad (\text{A-10})$$

and the cross spectra of turbulence then follows from equation (A-6)

$$\left. \begin{aligned} \phi_{u_{12}}(\omega) &= \frac{\overline{u^2 L}}{\pi U} \int_{-\infty}^{\infty} \left(1 - \frac{\sigma^2}{2\sqrt{\sigma^2 + \lambda^2}} \right) e^{-\sqrt{\sigma^2 + \lambda^2}} e^{-i\omega\tau} d\tau \\ \text{or} \\ \phi_{u_{12}}(\nu) &= \frac{\overline{u^2}}{\pi} \int_{-\infty}^{\infty} \left(1 - \frac{\sigma^2}{2\sqrt{\sigma^2 + \lambda^2}} \right) e^{-\sqrt{\sigma^2 + \lambda^2}} e^{-i\omega\lambda} d\lambda \end{aligned} \right\} (\text{A-11})$$

where $\nu = \omega L/U$. Integration of this equation produces the following expression for cross spectrum

$$\left. \begin{aligned} \phi_{u_{12}}(\nu) &= \frac{2\overline{u^2}\sigma^2}{\pi} \left[\frac{1}{\alpha} K_1(\alpha) - \frac{1}{2} K_0(\alpha) \right] \\ &= \frac{\overline{u^2}\sigma^2}{2} \left[-\frac{2}{\alpha} H_1^{(1)}(i\alpha) - iH_0^{(1)}(i\alpha) \right] \end{aligned} \right\} (\text{A-12})$$

where

$$\alpha = \sigma \sqrt{1 + \nu^2}$$

and

$K_n(\alpha)$ the Bessel function of the second kind for imaginary argument,

$H_n^{(1)}(i\alpha)$ the Bessel function of the third kind

Equation (A-12) is a real quantity indicating that the derived cross spectrum has a zero quadrature component.

As the separation distance Δz approaches zero, the cross spectrum (eq. (A-12)) reduces to the power spectrum of the u component of turbulence which, for $f(r) = e^{-r/L}$, is simply

$$\phi_{u_{11}}(\nu) = \frac{\overline{2u^2}}{\pi} \frac{1}{1 + \nu^2} \quad (A-13)$$

It is convenient in response calculations to express the cross spectrum in the following normalized form

$$\gamma_{u_{12}} = \frac{\phi_{u_{12}}}{\phi_{u_{11}}} \quad (A-14)$$

Equations (A-12) and (A-13) substituted into equation (A-14) give

$$\gamma_{u_{12}} = \frac{\pi}{4} \alpha \left[-2H_1^{(1)}(i\alpha) - \alpha H_0^{(1)}(i\alpha) \right] \quad (A-15)$$

An important simplification results when it is recognized that the wavelengths for frequencies of primary interest are in general less than the scale of turbulence; that is $2\pi(U)/\omega < L$. The parameter α in equation (A-15) then reduces to a single nondimensional parameter

$$\alpha = \frac{\Delta z}{L} \sqrt{1 + \frac{\omega L}{U}}^2$$
$$\approx \frac{\omega \Delta z}{U} \quad \text{for} \quad \frac{\omega L}{U} \gg 1.0 \quad (A-16)$$

Therefore

$$Y_{u_{12}} \approx \frac{\pi}{4} \left(\frac{\omega \Delta z}{U} \right) \left[-2H_1^{(1)} \left(i \frac{\Delta z \omega}{U} \right) - \frac{\omega \Delta z}{U} H_0^{(1)} \left(i \frac{\omega \Delta z}{U} \right) \right] \quad (A-17)$$

The absolute value of equation (A-17) is shown plotted in figure 15(a), together with experimental data obtained by Singer in reference 30 and Davenport in reference 29.

Cross Spectra of $v(t)$

The equation for the cross spectra of horizontal transverse v components of turbulence is identical to Houbolt's expression for the vertical w components presented in reference 24. This expression is

$$\phi_{v_{12}}(v) = \frac{u^2}{2} \left\{ \frac{-\sigma^2}{1+v^2} \left[iH_0^{(1)}(i\alpha) \right] + \frac{\sigma(1+3v^2)}{(1+v^2)^{3/2}} \left[-H_1^{(1)}(i\alpha) \right] \right\} \quad (A-18)$$

In the limit for $\Delta z = \sigma = 0$, this equation reduces to the power spectrum for transverse components of turbulence which, for $g(r)$ as given in equation (A-7), is

$$\phi_{v_{11}}(v) = \frac{u^2}{\pi} \frac{1+3v^2}{(1+v^2)^2} \quad (A-19)$$

Therefore

$$Y_{v_{12}} = \frac{\phi_{v_{12}}}{\phi_{v_{11}}} = \frac{\pi}{2} \left\{ \frac{-\alpha^2}{1+3v^2} \left[iH_0^{(1)}(i\alpha) \right] - \alpha \left[H_1^{(1)}(i\alpha) \right] \right\} \quad (A-20)$$

Again, it can be stated that for the frequency range of interest in the present study ($v \gg 1.0$) equation (A-20) is essentially a function of $\omega \Delta z/U$ alone and can be written

$$\gamma_{v_{12}} \approx -\frac{\pi}{2} \frac{\omega \Delta z}{U} H_1^{(1)} \left(i \frac{\Delta z \omega}{U} \right) \quad (A-21)$$

Equation (A-21) is found to be an excellent approximation to equation (A-20) for wavelengths equal to or less than $2L$.

A plot of equation (A-21) as a function of $f \Delta z/U$ is shown in figure 15(b), where f is frequency in cycles per second.

In order to obtain somewhat simpler analytical expressions for use in response calculations, the cross spectra defined by equations (A-15) and (A-21) have been approximated by damped cosine functions. On the basis of a least-squares-fit, the following empirical equations were obtained.

$$\left. \begin{aligned} \gamma_{u_{12}} &= e^{-4.4(f \Delta z)/U} \cos \frac{4\pi}{3} \left(\frac{f \Delta z}{U} \right) \\ \text{and } \gamma_{v_{12}} &= e^{-3.2(f \Delta z)/U} \cos \frac{\pi}{2} \left(\frac{f \Delta z}{U} \right) \end{aligned} \right\} \quad (A-22)$$

APPENDIX B

DERIVATION OF GUST RESPONSE EQUATIONS

Frequency Response Functions

Two sets of frequency response functions will be derived. One set relates the response of the vehicle in the x direction to a sinusoidal $u(t)$ gust input and the other relates response in the y direction to a sinusoidal $v(t)$ gust input. The following assumptions are made:

- a. The vehicle is structurally and aerodynamically symmetrical about its z axis which is vertical.
- b. Wind forces on the vehicle are proportional to the local diameter such that the assumptions of two-dimensional strip theory are applicable.
- c. Wind forces are quasi-static (proportional to the instantaneous dynamic pressure) and act in the direction of flow relative to the vehicle.
- d. The unsteady components of wind are small in relation to the mean wind speed.
- e. Coupling between natural structural modes can be neglected.

First, consider the deflection response of a vehicle in the direction of the mean wind. Let the x component of deflection be expressed in terms of natural modes of the structure

$$x(z,t) = a_1(t)x_1(z) + a_2(t)x_2(z) + \dots \quad (B-1)$$

where $x_n(z)$ is the n th natural mode shape and $a_n(t)$ is a generalized coordinate determined from solution of the differential equation

$$\ddot{a}_n + 2\zeta_n \omega_n \dot{a}_n + \omega_n^2 a_n = \frac{Q_{x,n}}{M_n} \quad (B-2)$$

In equation (B-2) ζ_n is the equivalent viscous structural damping relative to critical damping, ω_n the natural frequency, M_n the generalized mass, and $Q_{x,n}$ the generalized force - each for nth mode of vibration.

Assume that a gust velocity $u(t)$ acts over an element of length ϵ centered over station z_1 on the structure. The generalized force in equation (B-2) then becomes

$$Q_{x,n} = \int_0^L \frac{1}{2} \rho C_D D \left[U - \dot{a}_n x_n + u(t) \delta(z, z_1) \right]^2 x_n dz \quad (B-3)$$

where $\delta(z, z_1)$ is a function which has the following properties

$$\delta(z, z_1) = 1 \quad \text{when} \quad (z_1 - \frac{\epsilon}{2}) \leq z \leq (z_1 + \frac{\epsilon}{2})$$

$$= 0 \quad \text{elsewhere}$$

With the assumption that the air density ρ is constant and the mean wind U is large compared with u and \dot{a}_n , equation (B-3) can be written

$$Q_{x,n} = \frac{1}{2} \rho U_0^2 D_0 \int \left[S_{1n} - 2 \frac{\dot{a}_n}{U_0} S_{2n} + 2 \frac{\epsilon}{L} W(z_1) \frac{u(z_1, t)}{U_0} \right] \quad (B-4)$$

where

$$W_n(z) = \frac{D(z)}{D_0} \frac{U(z)}{U_0} x_n(z) C_D(z)$$

$$S_{n1} = \int_0^1 W_n \frac{U}{U_0} d\left(\frac{z}{L}\right)$$

$$S_{n2} = \int_0^1 W_n x_n d\left(\frac{z}{L}\right)$$

With the notation

$$\xi_n = \frac{a_n}{D_0}$$

$$\frac{\partial}{\partial t} = \frac{U_0}{D_0} \frac{\partial}{\partial s}$$

equation (B-2) becomes

$$\xi_n'' + (2\xi_n k_n + \kappa S_{n2}) \xi_n' + k_n^2 \xi_n = \kappa \left[\frac{1}{2} S_{n1} + \frac{\epsilon}{l} W(z_1) \frac{u(z_1, t)}{U_0} \right] \quad (B-5)$$

where $k_n = \frac{\omega_n D_0}{U_0}$

$$\kappa_n = \frac{\rho l D^2}{M_n}$$

and a prime denotes, $\frac{\partial}{\partial s}$.

If the gust at z_1 is assumed to vary sinusoidally with time in equation (B-5); that is, $u_n(z_1, t) = u_{n0} e^{iks}$, $\xi_n = \xi_{n0} e^{iks}$, then the frequency response function for dynamic deflections of a vehicle in the x direction associated with this gust input is

$$H_{\xi_n 1}(k) = \frac{\xi_{n0}}{\frac{u_{n0}}{U_0}} = \frac{\kappa \frac{\epsilon}{l} W_n(z_1)}{k_n^2 - k^2 + i(2\xi_n k_n + \kappa S_{n2})k} \quad (B-6)$$

Note that the static dragwise deflection has been subtracted from the total deflection in obtaining equation (B-6).

The response of the vehicle in the direction transverse to the wind can be similarly expressed in terms of natural modes

$$y(z,t) = b_1(t)y_1(z) + b_2(t)y_2(z) + \dots \quad (B-7)$$

where b_n is determined from the equation

$$\ddot{b}_n + 2\zeta_n \omega_n \dot{b}_n + \omega_n^2 b_n = \frac{Q_{y,n}}{M_n} \quad (B-8)$$

and $y_n(z) = x_n(z)$ by symmetry. The generalized force for transverse response is

$$Q_{y,n} = \int_0^L \frac{1}{2} \rho C_D D \left\{ U^2 + \left[-\dot{b}_n y_n + v(t) \delta(z, z_1) \right]^2 \right\} y_n \sin \beta dz \quad (B-9)$$

where

$$\sin \beta = \frac{-\dot{b}_n y_n + v \delta(z, z_1)}{\sqrt{U^2 + \left[-\dot{b}_n y_n + v \delta(z, z_1) \right]^2}}$$

In a manner similar to that followed in obtaining equation (B-6) the frequency response function for the transverse response becomes

$$H_{n,1}(k) = \frac{\eta_{n0}}{\frac{v_{n0}}{U_0}} = \frac{0.5 \kappa_n \frac{\epsilon}{L} W_n(z_1)}{k_n^2 - k^2 + i \left(2\zeta_n k_n + 0.5 \kappa_{n2} \right) k} \quad (B-10)$$

where $\eta_n = \frac{b_n}{D_0}$.

For cases wherein the gust input is assumed to be perfectly correlated along the length of a vehicle the frequency response functions may be obtained by

integrating equations (B-6) and (B-10) over the vehicle length. Thus for a uniformly distributed $u(t)$ gust the frequency response function for deflection in the x direction is from equation (B-6)

$$H_{\xi_n}(k) \Big|_{\text{uniform}} = \frac{\kappa_n S_{n3}}{k_n^2 - k^2 + i(2\zeta_n k_n + \kappa_n S_{n2})k} \quad (\text{B-11})$$

and similarly for a uniformly distributed $v(t)$ gust in equation (B-10)

$$H_{\eta_n}(k) \Big|_{\text{uniform}} = \frac{0.5\kappa_n S_{n3}}{k_n^2 - k^2 + i(2\zeta_n k_n + 0.5\kappa_n S_{n2})k} \quad (\text{B-12})$$

where $S_{n3} = \int_0^1 W_n(z) d(z/l)$.

Response Spectrum

With the turbulence spectra relationships in appendix A and the frequency response functions derived in the previous section, working equations for the structural response spectrum for the n th mode can be formulated as follows:

For a uniform one-dimensional gust input equations (3), (B-11), and (B-12) combine to yield

one-dimensional u gust

$$\Phi_{\xi}(k)_{n, \text{uniform}} = \frac{\kappa_n^2 S_{n3}^2}{(k_n^2 - k^2)^2 + (2\zeta_n k_n + \kappa_n S_{n2})^2 k^2} \Phi_{u/U_0}(k) \quad (\text{B-13a})$$

one-dimensional v gust

$$\phi_{\eta}(k)_{n, \text{ uniform}} = \frac{0.25\kappa_n^2 S_n^2}{(k_n^2 - k^2)^2 + (2\zeta_n k_n + 0.5\kappa_n S_n^2) k^2} \phi_{v/U_0}(k) \quad (\text{B-13b})$$

The turbulence spectra in these equations are expressed as a function of $k = \frac{\omega D_0}{U_0}$ and u and v are normalized with respect to U_0 . With these changes in variables the spectra given by equation (A-13) and equation (A-19) become, respectively

$$\phi_{u/U_0}(k) = \frac{2}{\pi} \frac{\overline{u^2}}{U_0^2} \frac{L/D_0}{1 + (L/D_0)^2 k^2} \quad (\text{B-14a})$$

$$\phi_{v/U_0}(k) = \frac{2}{\pi} \frac{\overline{v^2}}{U_0^2} \frac{L}{D_0} \frac{1 + 3(L/D_0)^2 k^2}{[1 + (L/D_0)^2 k^2]^2} \quad (\text{B-14b})$$

For two-dimensional gust inputs the following expressions can be derived
two-dimensional u gust

$$\phi_{\xi_n}(k) = T_{un}(k) \phi_{\xi}(k)_{n, \text{ uniform}} \quad (\text{B-15a})$$

two-dimensional v gust

$$\phi_{\eta_n}(k) = T_{vn}(k) \phi_{\eta}(k)_{n, \text{ uniform}} \quad (\text{B-15b})$$

where the functions $T_{un}(k)$ and $T_{vn}(k)$ are in the nature of "attenuation" factors which account for the two-dimensionality of the gust field. These "attenuation" factors can be expressed in matrix notation as follows:

$$T_n(k) = \frac{(\epsilon/l)^2}{S_{n1}^2} [W_n(j\epsilon)] [\gamma_{ij}(k)] \{W_n(j\epsilon)\} \quad (B-16)$$

where

$i = 1, 2, \dots, m$

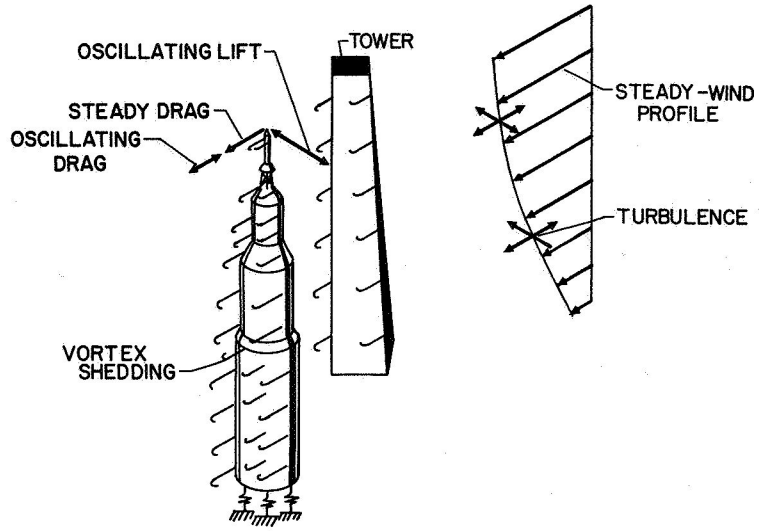
$j = 1, 2, \dots, m$

The elements $\gamma_{ij}(k)$, representing the real part of the normalized cross spectrum between points i and j , are given for the u and v components of turbulence by the approximate formulas in equation (A-22). This function depends on the properties of turbulence and is independent of structural parameters. The quantity $W(j\epsilon)$, on the other hand, depends on the diameter and mode shape of the structure as well as the shape of the mean wind profile. (See eq. (B-4).)

1. Pagon, W. Watters: Vibration Problem in Tall Stacks Solved by Aerodynamics. Engineering News Record, July 12, 1934.
2. Maher, F. J., Frederick, D., Estes, E. R., and Steinman, D. B.: Wind-Tunnel Tests of Suspension Bridge Section Models. Bull. Virginia Polytechnic Institute, Eng. Exp. Station, Series No. 69, Vol. 41, No. 6, 1948, pp. 1-50.
3. Den Hartog, J. P.: Recent Technical Manifestations of von Karman's Vortex Wake. Proc. Nat. Acad. Sci. of USA, Vol. 40, 1954, pp. 155-157.
4. Boorne, R. A.: The Aeroelastics of Tall Stacks. Inst. Aero. Sci., Preprint No. 851, Oct. 1958.
5. Goldman, R.: The Generation and Suppression of von Karman Vortex Forces. Martin Co. Eng. Report No. 8984, July 1957.
6. Buell, Donald A., and Kenyon, George C.: The Wind-Induced Loads on a Dynamically Scaled Model of a Large Missile in Launching Position. NASA TM X-109, December 1959.
7. Young, J. P.: Wind-Induced Oscillation Tests of 1/6-Scale Pershing Model. The Martin Company Engineering Report No. 11461, August 1960.
8. Killough, T. L.: Wind-Induced Loads on a Dynamic 1/5-Scale Unfueled SM-78 Jupiter in the Launch Position (U), U. S. Army Ordnance Missile Command, Report No. RG-TM-62-65, July 10, 1962.
9. Cincotta, J. J., and Lambert, W. H.: Investigation of Wind Induced Oscillations and Steady Ground Wind Forces on a 7 1/2% Dynamically Scaled Model of the 624A Vehicle (U). The Martin Company, May 1963. Contract No. ER 13022
10. Fung, Y. C.: Fluctuating Lift and Drag Acting on a Cylinder in a Flow at Supercritical Reynolds Numbers. Jour. Aerospace Sciences, Vol. 27, No. 11, pp. 801-804, Nov. 1960.
11. Humphreys, J. S.: On a Circular Cylinder in a Steady Wind. Jour. of Fluid Mechanics, Vol. 9, Pt. 4, Dec. 1960, p. 603.
12. Buell, Donald A., McCullough, George B., and Steinmetz, William J.: A Wind-Tunnel Investigation of Ground-Wind Loads on Axisymmetric Launch Vehicles. NASA TN D-1893, October 1963.
13. Roshko, Anatol: Experiments of the Flow Past Circular Cylinders at Very High Reynolds Number. Jour. of Fluid Mechanics, Vol. 10, 1961.
14. Regier, Arthur A.: The Use of Scaled Dynamic Models in Several Aerospace Vehicle Studies. Proceedings ASME Winter Annual Meeting, Philadelphia, Pa., November 1963, pp. 34-50.

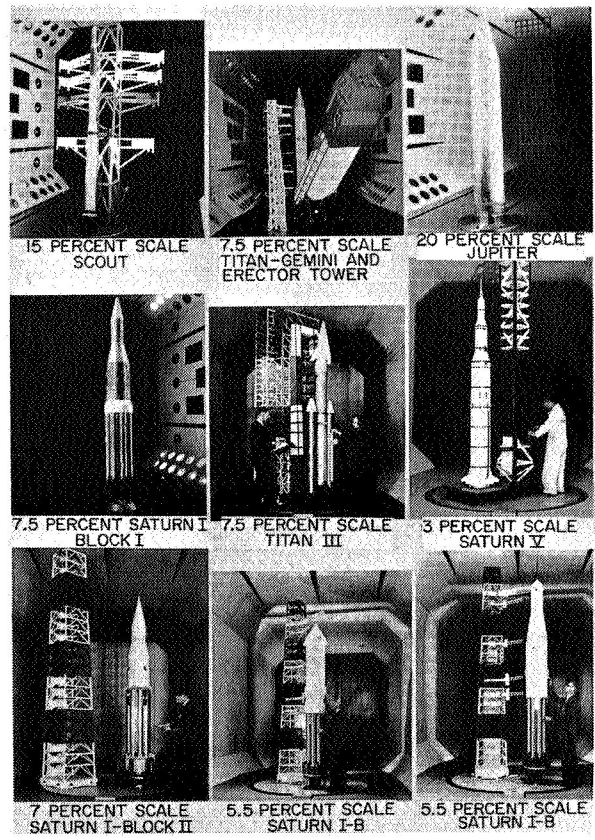
15. Hanson, Perry W., and Jones, George W., Jr.: On the Use of Dynamic Models for Studying Launch Vehicle Buffet and Ground-Wind Loads. Proceedings of Symposium on Aeroelastic and Dynamic Modeling Technology. RTD-TDR-63-4197, Part I, Dayton, Ohio, Sept. 23-25, 1963, pp. 333-387.
16. O'Neill, P. G. G.: Experiments to Simulate a Natural Wind Velocity Gradient in the Compressed Air Tunnel. NPL Aero Note 313, 1956.
17. Owen, P. R., and Zienkiewicz, H. K.: The Production of Uniform Shear Flow in A Wind Tunnel. Jour. of Fluid Mech., Vol. 2, Pt. 6, Aug. 1957, pp. 521-531.
18. Nemoto, S.: Similarity Between Natural Wind in the Atmosphere and Model Wind in a Wind Tunnel, Part III - Some Examples of Experiments. Meteorological Research Institute, Vol. 12, No. 2, 1961, Tokyo, pp. 129-154.
19. Den Hartog, J. P.: Mechanical Vibrations, 3rd Edition, McGraw-Hill, New York, 1947.
20. Woodgate, L.: Aerodynamic Stability Tests of a Model of a 250-Foot Steel Stack. NPL/Aero/408, National Physical Laboratory, Department of Scientific and Industrial Research, July 1960.
21. Ezra, A. A., and Birnbaum, S.: Design Criteria for Space Vehicles to Resist Wind-Induced Oscillations. American Rocket Soc. Paper 1081-60, Presented at the Struct. Design of Space Vehicles Conf., Santa Barbara, Calif., April 6-8, 1960.
22. Scruton, C.: On the Wind-Excited Oscillations of Stacks, Towers, and Masts. National Physical Laboratory, Paper 16, June 1963.
23. Houbolt, John C., Steiner, Roy, and Pratt, Kermit G.: Dynamic Response of Airplanes to Atmospheric Turbulence Including Flight Data on Input Response. NASA Technical Report R-199, 1964.
24. Houbolt, John C.: On the Response of Structures Having Multiple Random Inputs. Jahr. 1957 der WGL, Friedr. Vieweg and Sohn (Braunschweig), pp. 296-305.
25. Bohne, Q. R.: Power Spectral Considerations on the Launch Pad. USAF Geophysics Res. Dir. A. F. Surveys in Geophysics., No. 140, Proc. of National Symposium on Winds for Aerospace Vehicle Design, Vol. 1, AFCL-62-273(I), March 1962.
26. Henry, R. M., A Study of the Effects of Wind Speed Lapse Rate, and Altitude on the Spectrum of Atmospheric Turbulence at Low Altitude. IAS Preprint No. 59-43, Jan. 1959.
27. Davenport, A. G.: The Spectrum of Horizontal Gustiness Near the Ground in High Winds. Quarterly Jour. of Mat. Soc., Vol. 87, 1961.
28. Panofsky, H. A.: Surface Properties of Turbulence in the Boundary Layer. Unpublished report prepared for MSFC, Jan. 1964.

29. Davenport, Alan G.: The Response of Slender, Line-Like Structures to a Gusty Wind. Proc. Inst. Civil Engineers, 23: pp. 389-408.
30. Singer, Irving A.: A Study of the Wind Profile in the Lowest 400 Feet of the Atmosphere. Progress Reports No. 5 and 9, 1960-61, Brookhaven National Lab.
31. Daniels, Glenn E.: Terrestrial Environment (Climactic) Criteria Guidelines for Use in Space Vehicle Development, 1964 Revision. NASA TM X053023, Mar. 13, 1964, George C. Marshall Space Flight Center, Huntsville, Ala.
32. Reed, W. H., III, and Lynch, J. W.: A Simple Fast Response Anemometer. Jour. Applied Meteorology, Vol. 2, June 1963.
33. Dryden, H. L.: Turbulence Investigations at the National Bureau of Standards. Proc. Fifth International Congress of Applied Mechanics, Cambridge, 1938.
34. Liepmann, H. W., Laufer, J., and Liepmann, K.: On the Spectrum of Isotropic Turbulence. NACA TN No. 2473, 1951.



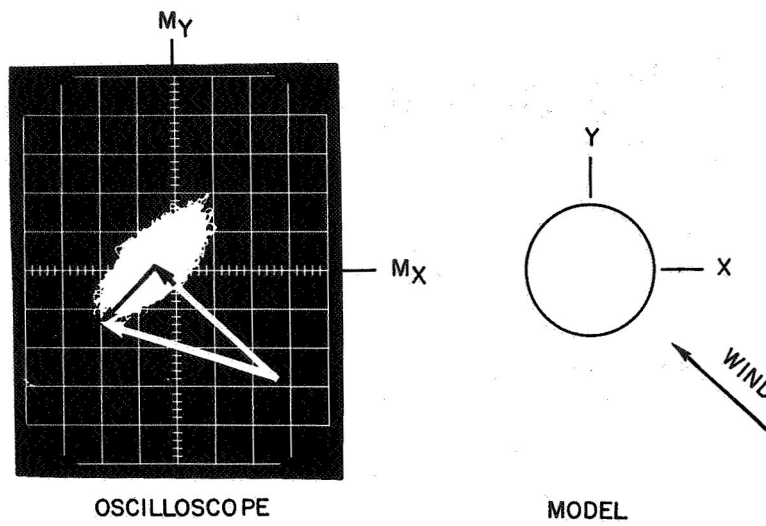
NASA

Figure 1.- Factors contributing to ground-wind loads.



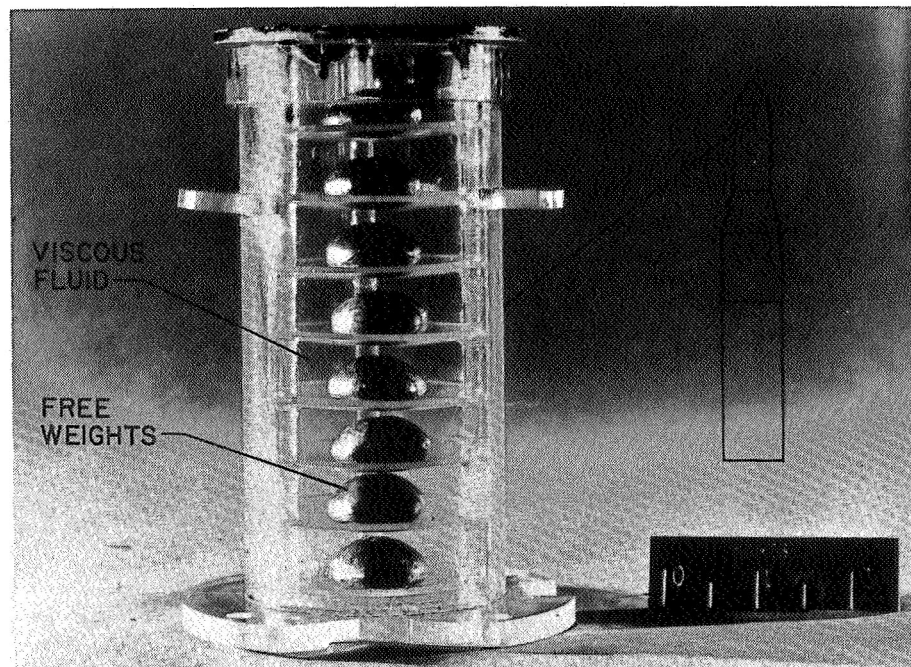
NASA

Figure 2.- Aeroelastic ground-wind-load models in the 16-foot Langley Transonic Dynamics tunnel.



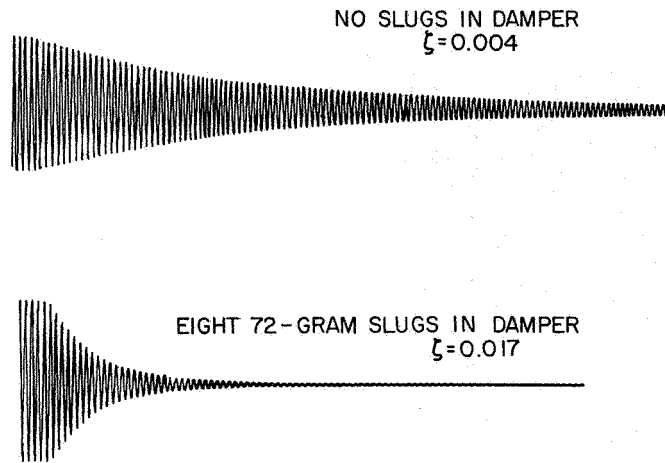
NASA

Figure 3.- Time exposure of bending moments on an oscilloscope screen.



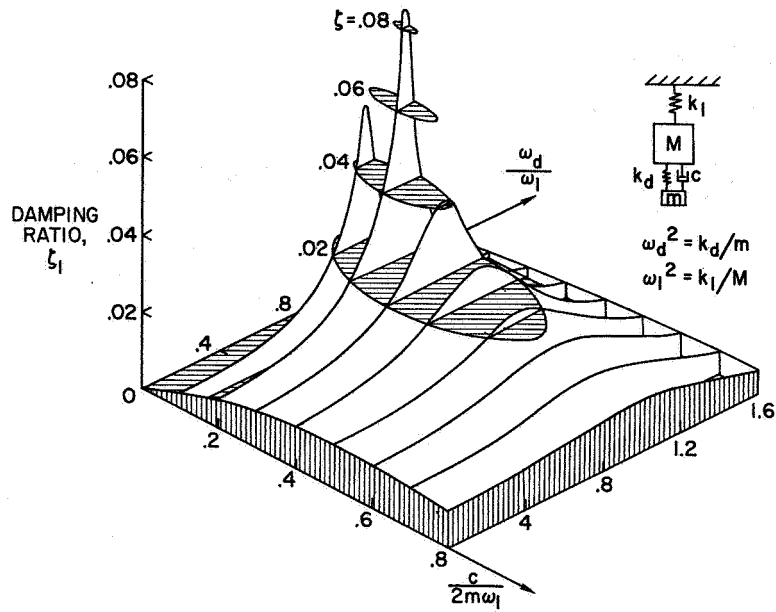
NASA

Figure 4.- Viscous damper used in ground-wind-load models.



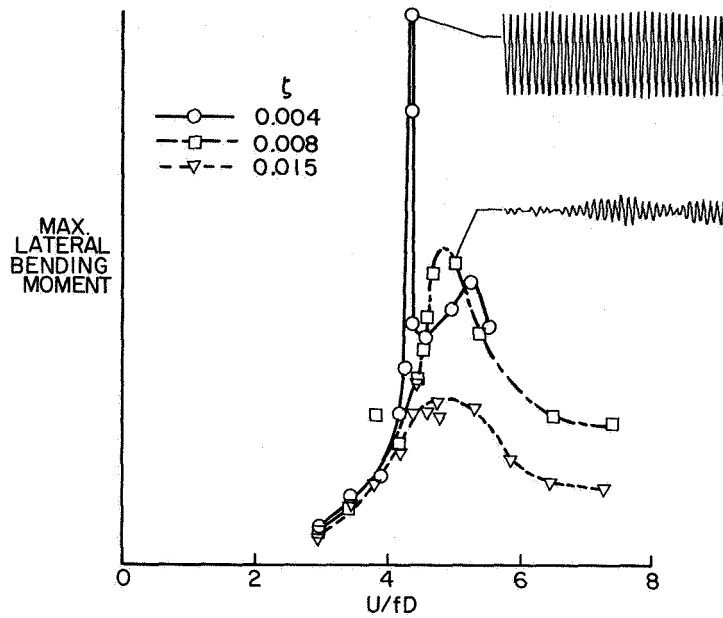
NASA

Figure 5.- Typical free-vibration records from 0.30-scale Saturn V model with and without slugs in damper.



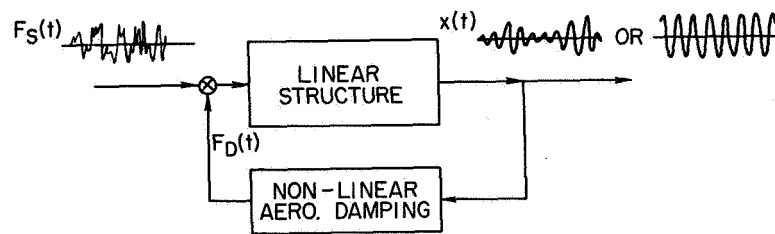
NASA

Figure 6.- Performance characteristics of an auxiliary mass damper. $m/M = 0.05$.



NASA

Figure 7.- Effect of damping on maximum dynamic bending moment response of 0.03-scale Saturn V model.



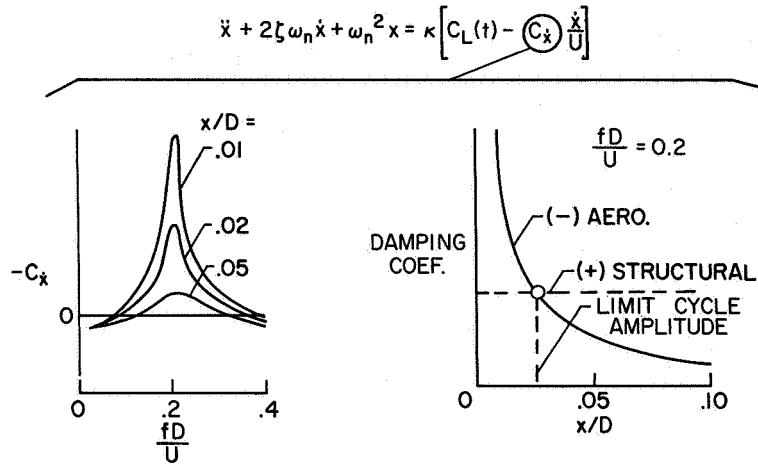
EQ. OF MOTION:

$$\ddot{x} + 2\zeta\omega_n\dot{x} + \omega_n^2x = \frac{1}{m} [F_S(t) + F_D(t)]$$

$$= \frac{\rho U^2 D}{2m} \left[C_L(t) - C_{\dot{x}} \frac{\dot{x}}{U} \right]$$

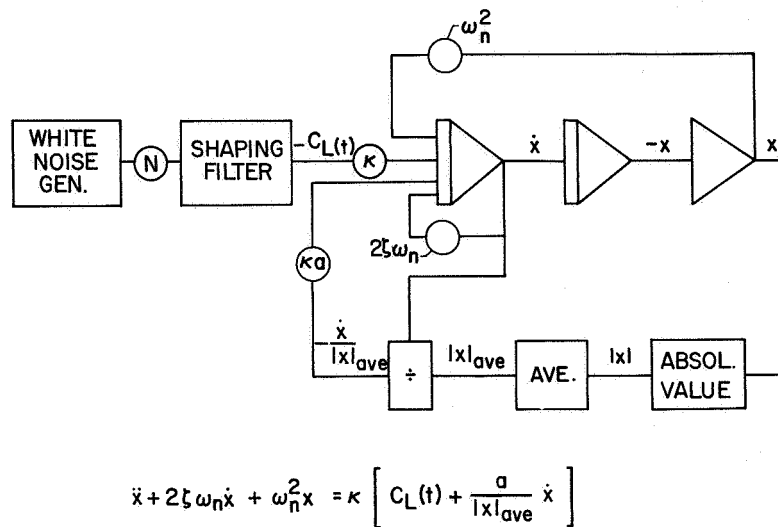
NASA

Figure 8.- A conceptual representation of dynamic response of structures to wind-induced loads.



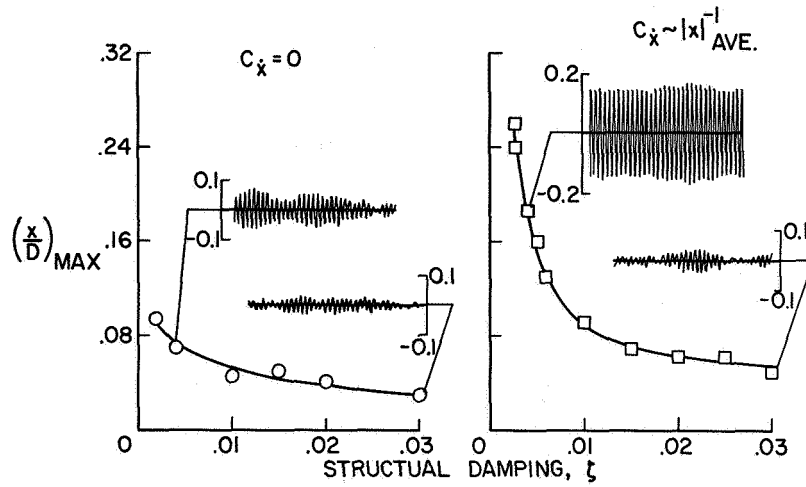
NASA

Figure 9.- Nonlinear aerodynamic characteristics associated with vortex shedding.



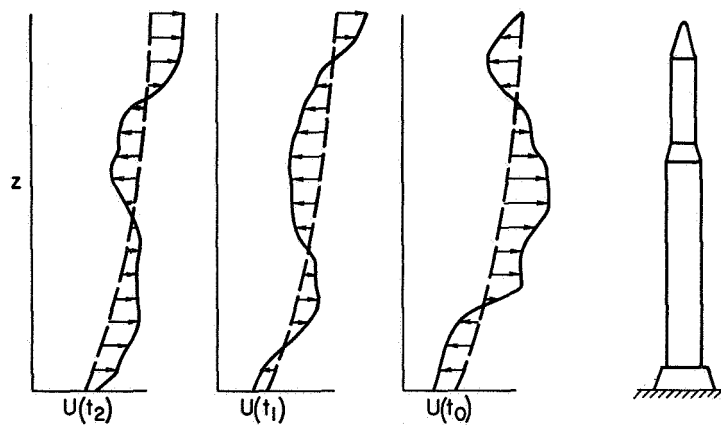
NASA

Figure 10.- Analog computer simulation of vortex-shedding phenomenon.



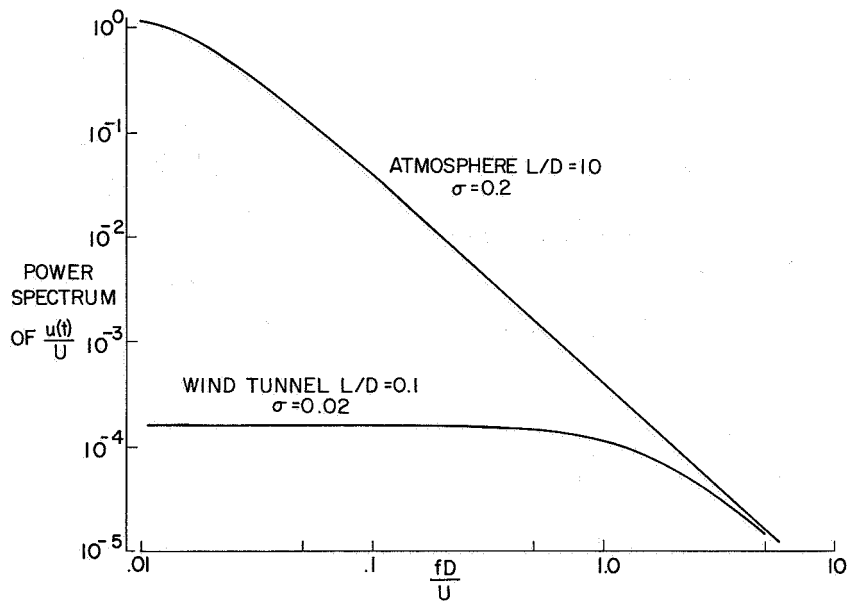
NASA

Figure 11.- Analog computer solutions showing effect of nonlinear aerodynamic damping on dynamic response.



NASA

Figure 12.- Typical variations of unsteady wind with height.

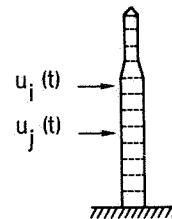


NASA

Figure 13.- Comparison of turbulence characteristics in wind tunnels and the atmosphere.

● ONE-DIMENSIONAL INPUT

$$\Phi_r(\omega) = |H(\omega)|^2 \Phi_u(\omega)$$

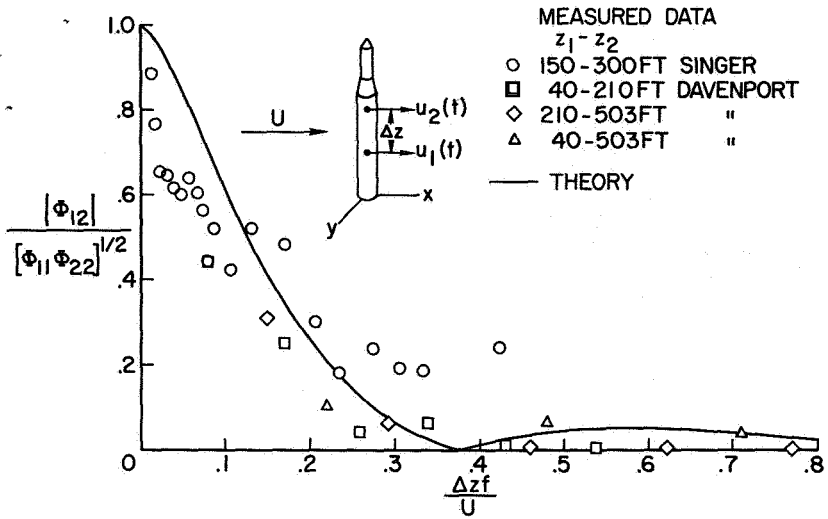


● TWO-DIMENSIONAL INPUT

$$\Phi_r(\omega) = \Phi_u(\omega) \left\{ H_1 H_1^* + H_2 H_2^* + \dots + 2R_e \left[\frac{\Phi_{12}}{\Phi_u} (H_1^* H_2 + H_2^* H_3 + \dots) \right. \right. \\ \left. \left. + \frac{\Phi_{13}}{\Phi_u} (H_1^* H_3 + H_2^* H_3 + \dots) + \dots + \frac{\Phi_{1n}}{\Phi_u} (H_1^* H_n + H_2^* H_{n+1} + \dots) \right] \right\}$$

NASA

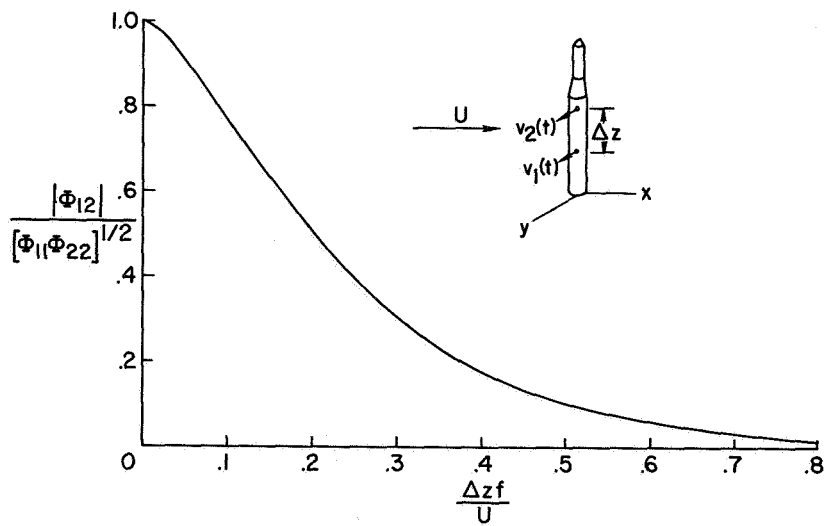
Figure 14.- Response equations for systems excited by multiple-random inputs.



(a) u component.

NASA

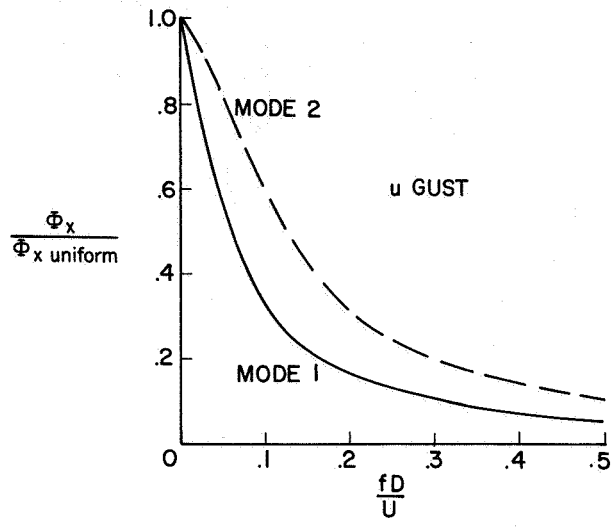
Figure 15.- Cross spectra of turbulence components as a function of vertical separation distance.



(b) v component.

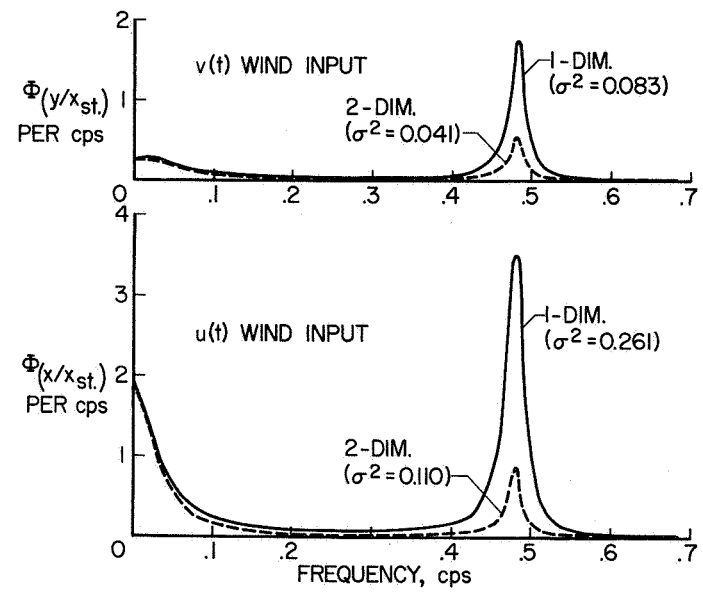
NASA

Figure 15.- Concluded.



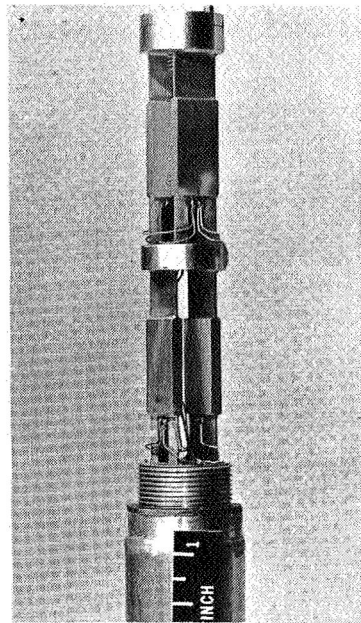
NASA

Figure 16.- Effect of gust correlation on modal response of a launch vehicle.

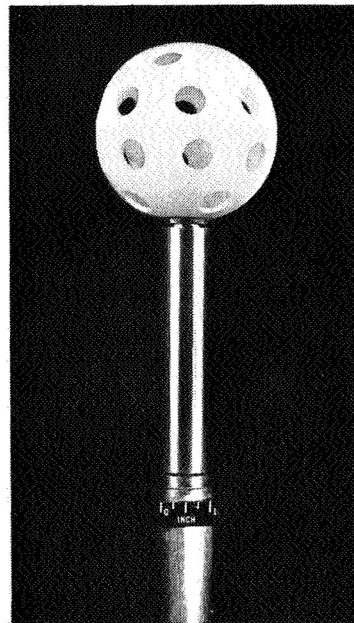


NASA

Figure 17.- Power spectrum of vehicle response to atmospheric turbulence.



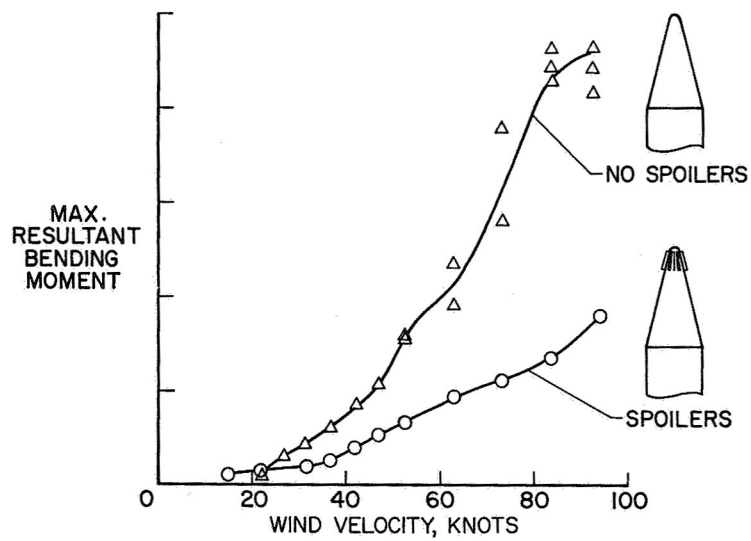
STRAIN GAGE BALANCE



ASSEMBLY

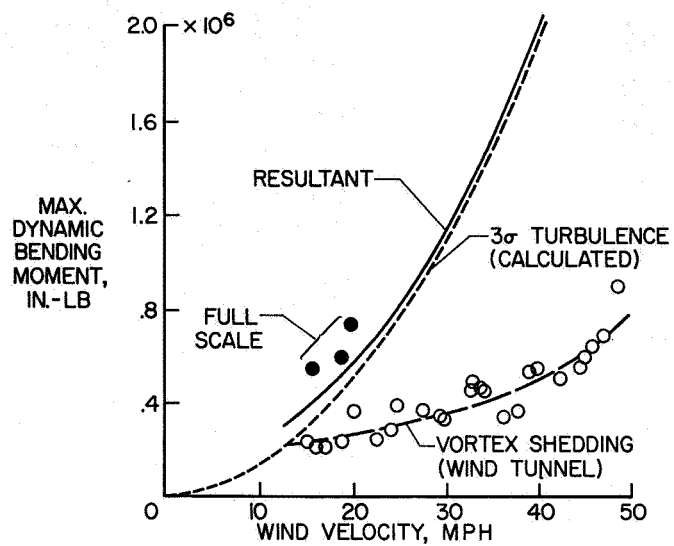
NASA

Figure 18.- Fast response anemometer.



NASA

Figure 19.- Effect of nose spoilers on bending moment response of 0.20-scale Jupiter model.



NASA

Figure 20.- Response of Titan-Gemini to ground-wind loads.

MSC-33619

SIMULATION OF STRUCTURAL DYNAMICS
OF SPACE VEHICLES DURING LAUNCH

by

H. L. Runyan

NASA Langley Research Center

The purpose of this presentation is to concentrate on simulation techniques which are of importance in the design and operation of launch vehicles. We shall concentrate on dynamic problems from the time of lift-off to the time at which the vehicles leaves the sensible atmosphere. This time interval is relatively short, being of the order of just several minutes and to paraphrase an old adage "the first hundred seconds are the hardest."

To give some idea of the stable of NASA launch vehicles, the first figure illustrates most of the launch vehicles now in use or soon to be operational. The payload capabilities for a 300 nautical mile orbit range from about 300 pounds for the Scout vehicle to 200,000 pounds for the Saturn V. The Scout is the smallest vehicle and is the only solid propellant vehicle which has injected payloads into orbit. It is interesting to note that the Scout and the three Saturn configurations are the only vehicles developed solely as space research vehicles, the first stages of the remaining vehicles were developed strictly as military vehicles by the Air Force and have been adapted for space use. The Saturn V, now in the design and manufacturing stage, is 360 feet high, has a first and second stage diameter of 33 feet, has a lift-off

weight of 6,000,000 pounds and has a total thrust of 7,500,000 pounds. Except for the Scout, all vehicles are liquid propelled, are very thin skinned, and present many interesting and sometimes baffling dynamic problems during their ascent through the rather hostile atmosphere. Thus, to solve many of these dynamic problems, dynamic modeling techniques are not only convenient, but in some cases, mandatory.

What are some of the problems which are of concern to the dynamicist in designing and operating a launch vehicle? A listing of these problem areas is given in figure 2. On the top of the figure is shown "input" loading, which is imposed on a "system" - the launch vehicle, and the "output" load, in terms of stresses and acceleration.

Buffet and acoustic loads are closely related as can be seen by the general similarity of the outputs. Winds, both ground and aloft, can induce bending moments which can involve such severe loads that certain portions of the vehicle must be designed to accommodate these loads.

Fuel slosh in general is a control problem, however, loads can be induced into the vehicle if the liquid oscillations are not kept to a minimum. Control loads during programmed maneuvers are sometimes severe and, in particular, we must insure that excessive loads during maneuvers are not applied during periods of high loading from other sources. Recently, we have become concerned about response and loads in the longitudinal direction. Since 90 percent of the weight of a typical liquid propellant vehicle may be liquid, the coupling of the liquid system with the structure and engine is possible. During

lift-off, when the hold-down clamps are released, a large dynamic response takes place and is the principal design consideration for the bottom of the tanks. Another phenomena which has recently occurred on two vehicles is the coupling of the engine, turbopump, structure, and fluid components into a system that can become unstable. This has been referred to as the POGO problem, since the vehicle responds in a longitudinal direction, in the manner of a boy who is bouncing on a pogo stick.

In addition to creation of loads due to all of these sources of excitation, pilot performance is an additional quantity of great significance. During his ride through the many faceted environment, this required performance capability is due to the necessity of retaining his ability to read small indicators, to judge whether his flight is satisfactory, and perhaps to operate his abort system in case of a malfunction. Of course, this leads into an entirely new field which we will not touch on, namely the dynamic response and resonances of the human body to various frequencies and acceleration levels.

One of the unfortunate aspects of this loading picture is the simultaneity of the occurrence of these loads. In figure 3, a plot for various loading sources against time of flights is shown, where the black area indicates the probable time at which the particular event will occur. The point here is that it appears rather black between the transonic region and the maximum dynamic pressure region for most of the loading conditions. We are still at the point of

tyring to understand each problem separately. These combined loads present a rather complex interaction problem, which, at the present time, is not entirely understood. Some of the interaction effects that one could visualize, for instance, involve the influence of the vehicle bending, either statically due to winds or dynamically during the bending response due to gusts, on the local vibrating characteristics of the thin plates and shells and the response of these shell structures to such random forces as buffet and acoustics pressures.

Now let us look at the loading picture in more detail in figure 4, in terms of a preliminary design. On the right is a sketch of a tank containing a fluid of height h , density ρ , in an acceleration field a , with an internal pressure p above the fluid surface. The sketch at the left depicts an elemental section of the tank wall skin and indicates the loading.

The hoop stress then is given for a particular time of flight by

$$\sigma_H(x) = \frac{\text{Internal Pressure } pr}{t} + \frac{\text{Hydrostatic Pressure } h(x)\rho ar}{t}$$

From this elementary formula, one can make a preliminary selection of the material and skin thickness required. The longitudinal stress is then given by

$$\sigma_L(x) = \frac{\text{Internal Pressure } pr}{2t} + \frac{\text{Bending Moment } M_c}{I} - \frac{\text{Acceleration Drag } m(x)a + D(x)}{2\pi rt}$$

where M is the applied external bending moment due to wind, control gusts, buffeting, etc., $m(x)$ is the mass above the longitudinal station x , $D(x)$ is the total drag down to station x . From preliminary trajectory studies, the acceleration a is known as well as the drag $D(x)$. Of course, σ_L will vary around the circumference from a tension load to a compressive load when the vehicle bends. For the most part, the critical loading occurs on the compression side and since 2000 papers have been written over the years on the subject of shell buckling, this area will not be touched on. However, for thin unstiffened shells, a conservative approach would be to set $\sigma_L(x) = 0$. With a value of σ_L decided upon, we can then calculate the bending moment M , which is the vehicle structural capability remaining for such loads as winds, gusts, control, etc. A typical bending moment capability curve plotted against vehicle station is shown in figure 5. Notches in the capability curve are due to joints, and unpressurized areas such as interstage structure.

Now we finally come down to the reason for presenting this rather detailed discussion of the preliminary design of a launch vehicle, namely the estimation of the loads from remaining loading sources. The summation of these estimated loads is shown in figure 6 for a particular time of flight. Estimation of most of these loads requires a knowledge of the vibrational characteristics of the structures, involving not only the complete vehicle response (lateral as well as longitudinal motion), but local or isolated vibration of shells, trusses, mounting brackets, etc. As a typical example, we plot the load due to (1) control, for instance a preprogrammed pitch-over of the launch vehicle,

(2) wind loads caused by wind velocities as high as 250 mph, (3) gusts, (4) low frequency buffeting, due mainly to bulbous payload shrouds, (5) fuel slosh. The summation of these loads may approach the vehicle capability curve, thus an accurate estimation of these sources is necessary and dynamic models are playing a very important role in estimating these loads. To illustrate the role of various simulation techniques, figure 7 has been prepared to give our estimation of the state (of-the-art) of the various simulation techniques for studying the various problem areas. The darker the box, the higher the state-of-the-art and usage. Also included is an estimation of the relative cost of the various approaches, mathematical analysis being the least expensive and full-scale being the most expensive. In general, you can see that modeling for all phases is rather dark, and is highly competitive with mathematical analysis or full-scale testing.

DYNAMIC MODELING

The remainder of the paper will be concerned with specific examples of dynamic model testing. First, the problem of the gross vehicle vibratory motion will be considered, followed by a section on buffeting, and finally a few comments on the acoustic problem.

Lateral Bending Vibration Models

For lateral bending vibration, the governing differential equation is the well known beam equation

$$\frac{d^2}{dx^2} EI \frac{dy^2}{dx^2} = m\omega^2 y$$

where y is the lateral deflection, x is the length coordinate, E is the modulus of elasticity, and I is the section moment of inertia. The scaling parameter may then be defined as

$$\frac{m\omega^2 L^4}{EI}$$

Note that the geometric shape is not involved, thus we could obtain proper simulation by simply duplicating EI by a bar with ballast weights added to provide mass simulation. Of four models which we shall discuss for the lateral bending studies, only one followed this simplified path, the other three models utilized the same geometric shape, same material, the same ratio of tank radius to skin thickness.

One-Fifth-Scale Vibration Model of Saturn

Description. The 1/5-scale Saturn model described in reference 1, was built for the study of lateral bending vibrations; therefore, the important parameters to be scaled were the mass-stiffness ratios. Such things as aerodynamic fairing and fuel piping were not scaled since they

did not contribute to stiffness; however, lead ballast weights were used to simulate their mass. Furthermore, the vibrations of principal interest were the overall vehicle modes, so local panel stiffnesses were not scaled. Such things as fuel sloshing and the suspension system were considered to have a secondary effect on the overall vehicle vibration and so were not scaled for the initial part of the test. The model is shown on the left of figure 8, and the full scale vehicle is shown on the right in a vibration test tower.

The type of scaling chosen for the Saturn model was a component-by-component uniform reduction of dimensions to one-fifth of the full-scale values, using the same materials as the full scale. This replica type of scaling was chosen because of the structural complexity of the Saturn booster with the resulting difficulty of determining accurate equivalent stiffness and mass properties for the multiple-beam truss-work assemblies incorporated in the vehicle. An example of model duplication of a full-scale multiple-beam structure is shown in figure 9. This figure is a close-up view of the base of the vehicle and shows that structural details such as skin corrugations, built-up riveted beams, tension rods, and longitudinal stiffeners in the outer tanks have been duplicated on the model; however, details such as the number of rivets, aerodynamic fairing supports, and piping supports are not true scale reproductions.

Two important structural simplifications were made on the model. First the engines were simplified as shown in figure 10. Only the total weight, center of gravity, and moment of inertia were scaled.

The simulated engines were firmly attached at the gimbal point without attempting to scale actuator stiffnesses. Second, some ring frames were omitted from the shell structure of the second stage. A view of the aft end of the second stage showing its internal construction is shown in figure 11. About 70 percent of the second-stage weight is contained in the ballast tank at the center, which is supported by the eight radial trusses attached to the outer shell. The outer shell is attached to the first stage only at the eight points at the ends of the radial trusses and thus forms the principal load structure of the second stage. Several ring frames on the full-scale vehicle were omitted from the outer-shell load carrying structure on the model, resulting in some distorted vibration results which will be discussed subsequently.

Scaling. The Saturn model was scaled by selecting a length scale factor L_m/L_p of 1/5 and using the same materials on the model as on the prototype. Therefore, the following relations are established:

$$\frac{E_m}{E_p} = \frac{\rho_m}{\rho_p} = 1$$

Then, in order to maintain the dimensionless ratios for lateral vibrations, the mass and time scale factors must be:

$$\frac{M_m}{M_p} = \frac{1}{(5)^3}$$

$$\frac{\tau_m}{\tau_p} = \frac{1}{5}$$

Other relationships between model and prototype parameters, resulting from the dimensionless ratios, are:

1. Mass moment of inertia: $\frac{I'_m}{I'_p} = \frac{1}{(5)^3}$

2. Bending stiffness: $\frac{(EI)_m}{(EI)_p} = \frac{1}{(5)^4}$

3. Bending frequency: $\frac{f_m}{f_p} = 5$

4. Sloshing frequency: $\frac{f_m}{f_p} = \sqrt{5}$

5. Shell frequency: $\frac{f_m}{f_p} = 5$

Comparison of the bending and sloshing frequency ratios shows that the full-scale bending-sloshing frequency relationship is not maintained on the model. Thus, the interaction of vehicle bending with sloshing on the model will not represent directly the full-scale situation. For the Saturn configuration, where the first sloshing frequency is lower than the first bending frequency, the reduction to model size separates the frequencies, thus tending to uncouple the sloshing from the bending modes. The shell frequency relationship is based on an unstiffened shell with the same material and internal pressure in both model and full scale. Comparison of the bending with the shell frequency ratio shows that interaction of

local shell vibration with vehicle bending vibration should be the same on the model as on the full scale in those cases where model construction and internal pressure are the same as the full scale.

Results. Some results of the model vibration test are shown in figures 12, 13, 14, and 15. In figure 12, the first vibration mode of the model and full-scale vehicles is shown with the vehicle ballasted to simulate the maximum dynamic-pressure weight condition. This figure shows almost exact agreement between model resonant frequency, when adjusted by the scale factor, and the full-scale resonant frequency. In order to obtain such good agreement, it was necessary to duplicate, on the model, the suspension system used to simulate free-free boundary conditions on the full-scale vehicle. The mode shapes of the full-scale and the model are in good agreement as can be seen from comparison of the circles with the square symbols. The booster outer tanks, which are free to deflect independently of the center tank except at their ends are shown in this figure to have the same deflection as the center tank, and this mode has the appearance of the more conventional bending modes obtained from non-clustered vehicles.

In contrast, the second vibration mode, shown in figure 13, shows one of the unusual vibration modes associated with the clustered arrangement of the Saturn booster. There is about a 10-percent difference in frequency between model and full scale in this mode, and comparison of the circles with the squares shows fairly good agreement of model with full-scale mode shape. The typical outer tank indicated by the flagged symbols is seen to deflect in the opposite direction as the center tank. Cross-section A-A at the

midsection of the booster shows that when the center tank deflects upward as indicated by the arrow, the outer tanks are deflecting independently in the downward direction. This unusual mode shape where the outer tanks deflect in the opposite direction from the center tank is associated with the clustered arrangement of the booster tanks and has been termed a cluster mode.

The effect of omission of the ring stiffeners from the outer shell of the second stage is illustrated by figure 14, which shows the fourth vibration mode of the 1/5-scale Saturn model. In the area of the second stage, two deflection curves are shown. The open circles indicate the deflection of the outer shell and the solid circles the deflection of the inner ballast tank. The data indicate that the outer shell and the ballast tank are deflecting in the opposite directions. This can be explained by examination of cross-section B-B. The solid lines in this sketch indicate the undisturbed position of the water-filled ballast tank, the eight radial trusses, and the outer shell; the data points indicate the experimentally determined vibration amplitude. This cross section shows that the outer shell is vibrating in a shell mode with seven waves, while the center tank is translating. The deflection measured at points A and B on the inner and outer tanks, respectively, are in opposite directions, as shown also in the sketch in the center. The shell mode in the second-stage outer shell shown here was observed on the model in the higher-frequency modes for most weight conditions; however, no shell modes in the second stage were observed on the full-scale Saturn vibration test vehicle.

The mode shapes and resonant frequencies which have been shown were measured at the weight condition which simulates flight near maximum dynamic pressure. An indication of how the resonant frequencies of model and full scale compare at other weight conditions is shown in figure 15. The ordinate is full-scale frequency, in cycles per second, and the abscissa is water level in the booster stage, in percent. Zero percent corresponds to first-stage burnout while 100 percent corresponds to lift-off. The previously shown data were measured at 48 percent full. Model frequencies, adjusted by the scale factor, are shown as circles while full-scale frequencies are shown as squares. The first bending mode frequency shows almost exact agreement except at lift-off, where the model frequency is about 7 percent high. The first cluster mode frequency is predicted by the model to within 10 percent. For higher modes, agreement between model and full scale is not as good.

The data presented in figure 15 were obtained using an eight-cable suspension system which duplicated a similar suspension system used for full-scale tests. Earlier model tests, using a two-cable free-free suspension system which gave much better separation between suspension frequency and bending frequency than the eight-cable system had given model first bending frequencies 5 to 10 percent lower than full-scale frequencies. This result indicated the importance of properly accounting for suspension system effects in comparing model and full-scale data and of properly interpreting ground test data when extrapolating to flight conditions.

Saturn V Dynamic Models

Figure 16 illustrates the present modeling project, which is a 1/10 scale replica model of the Saturn V. The model is 36 feet high, including the Apollo payload. The general type of construction of the full scale is shown including skin stringer, waffle pattern, integrally milled stringer, and corrugated skin. The model will duplicate all of these essential details up to the Apollo payload.

On the right of figure 16 is shown a scalloped or multicelled tank concept, which is also being constructed and will replace the cylindrical first stage for later tests. This concept has the advantage of higher fuel slosh frequencies, thus separating the control or pitch frequency from the fuel slosh frequency.

As an example of the construction detail adhered to in the model, figure 17 illustrates the interior of the first stage fuel tankage. Note in particular the detail in the fuel slosh baffles which are the thin, corrugated rings located on the circumference of the tank. The three corrugated pipes are three of the five tunnels which carry the fuel through the bottom tank to the five individual pumps for each engine. For the Apollo payload, beam simulation techniques are being used, whereby the structural and mass distributions are matched with no attempt being made to simulate the actual tankage construction.

In addition to the 1/10-scale model, a 1/40-scale model is being constructed which is shown in figure 18. An illustration of the details of the model construction is shown in figure 19. The modeling

concept for this case involved only the duplication of the mass and stiffnesses and does not follow the replica concept. On the lower left is shown the five-engine simulation. Next to the engine are two fuel slosh simulators, using a "bird-cage" spring-mass assembly. These simulators can be placed at various positions on the vehicle, and the spring constants as well as the mass can be changed in order to study the effect of fuel depletion. Thus, we will be able to study the coupling of fuel slosh with the elastic modes by spring constant and mass changes, in ranges of parameters not possible with liquids in a one "g" field.

Titan III

In addition to the NASA vehicle described, the Air Force has decided on scale model testing of the Titan III launch vehicle as shown in figure 20. This vehicle utilizes a modified Titan II as a center "core" on which two 100 inch diameter solid propellant boosters are strapped at two points. The length scaling factor selected here was 1/5, with the propellant tanks and interstage structure being rather faithfully reproduced by use of the same material as the prototype with the same ratio of tank radius to skin thickness.

This model was designed and constructed by the Martin-Marietta Co. of Denver, Colorado. It is not being tested in the Dynamics Research Laboratory at Langley Research Center by Martin Company personnel with the assistance of Langley engineers.

Fuel Slosh

One of the problem areas in testing liquid-fueled dynamic models is the effect of the coupling fuel slosh with other modes. In figure 21, several significant frequencies are plotted against flight time for the cylindrical tank as well as the scalloped tank for a vehicle in the Saturn V class. The first bending mode frequency variation is shown as a dashed line, flight fuel slosh frequency variation as a solid line, range of pitch frequency by the shaded area, a line depicting a 1/10-scale model fuel slosh frequency and a line illustrating fuel-scale ground test frequencies. A rather large separation in frequency exists between the first bending mode and the flight fuel slosh frequency. Thus, coupling of the fuel slosh mode with the elastic mode will be rather weak even in the flight case. A 1/10-scale model would have lower fuel slosh frequencies as indicated, but since the fuel slosh is already rather well uncoupled from the bending mode, the 1/10-scale model results should duplicate the full-scale flight results with very minor differences. As a matter of fact, even for full-scale ground tests, the proper fuel slosh frequency would not be exactly simulated as shown due to the 1 g field in which the vehicle must be tested.

On the right side of figure 21 is shown the effect of the system frequencies of a scalloped tank wherein only the first stage of the complete vehicle has been changed from the cylindrical tank to the scalloped tank. Note that the bending frequency has been reduced. This is due

to the basic design criteria of maintaining the same internal pressure and vertical load-carrying ability as in the cylindrical tank. This results in more material being used closer to the tank center thus reducing the moment of inertia and consequently the bending stiffness. On the other hand, the fuel slosh frequency has increased due to compartmentation. Thus, the two frequencies are approaching each other while moving the fuel slosh frequency away from the rigid body frequency, which, of course, is beneficial. However, a coupling between fuel slosh and the fundamental vibration modes now exists. In cases such as this, the adequacy of the structural duplication of the model may be checked against analytical representation for fuel slosh frequencies well removed from the coupling possibility. Then with confidence in the structural adequacy of the model, the effect of fuel slosh having frequencies in the neighborhood of the fundamental elastic frequencies may be estimated for control system design by calculating the effect by utilizing the spring-mass or pendulum fuel slosh analogies.

Buffeting

Now let us turn our attention to buffeting. The term "buffeting" is really not very well defined and precise. For the purposes of this paper, we shall consider the term "buffet" to refer to aerodynamic flows involving departure from potential flow with consequent flow breakdown and separation which can result in structural response of the vehicle. Obviously, this is a rather broad definition and is symptomatic of the wide spectra of buffet problems.

The occurrence of buffeting on launch vehicles has been a surprise to many people; the long cylindrical shape of typical launch vehicle did not appear at first to offer any substantial problem. However, certain vehicle failures in the early days of the space program were diagnosed to have been due to possible flow breakdown, inducing loads that could result in structural failure.

The following material and figures are taken from an excellent talk given by A. G. Rainey of Langley Research Center (reference 2) which was presented at the Fifth Annual AIAA Structures and Materials Conference in April, 1963 and covers the status of buffet research at that time.

Recognizing that there are many types of buffet, two general types of buffet are illustrated in figure 22. The power spectral density of the oscillating pressure is plotted against frequency. The ordinate indicates the relative "power" or pressure generated at a particular frequency. The integration of the area under the curve is the mean square of the pressure oscillation. The curve and figure on the left illustrate one type of buffeting that could be obtained on a nose or payload fairing shape in which the diameter is reduced in the direction of flow. Here the flow breaks down, alternately on the top and bottom of the fairing due to a rather shallow reverse angle on the rear part of the fairing during part of the transonic flight. As illustrated by the plot of the spectra, the predominant frequencies of the phenomena are rather low and, as a matter of fact, fall within the range of the fundamental bending vibration modes of the complete vehicle. A considerable

amount of research has been accomplished in this area, and there are some rough guides concerning the relationship of this reverse angle and the magnitude of the buffet pressures. Actually, if the angle were increased to 90° i.e. a step change from the larger diameter front section to the smaller diameter rear section, this low frequency buffet would be eliminated since the shock position and the turbulence would now be fixed at a given location and the possibility for it to oscillate from one side to the other is eliminated. However, this step could lead into another type of buffet which is of importance from the standpoint of local or small areas of the vehicle. An illustration of the type of buffet is shown rather dramatically in the sketch on the right of figure 22. Here we have buffeting due to attached shocks and boundary layer build up and collapse, due to flow through the open structure supporting the abort rocket motor and as well to a reverse angle due to the adapter. Note the spectra shape which contains nearly an equal amount of power throughout the frequency band from 0 to 220 cps, however, it is not as severe as for the bulbous nose shape, although the area under the curve, representing the mean square is about the same. Unfortunately, most of the panels and equipment as well as the astronaut can respond to some frequency in this range. Thus, consideration of this high frequency buffet must be taken into account in the design of the launch vehicle system.

Theoretical techniques for predicting these spectra do not exist, therefore, the dynamic model enters the picture. Dynamic models have been used to study both types of buffet. For the low frequency buffet,

the governing differential equation will be the usual beam equation, with the addition of a number of parameters which have been obtained mainly from our previous experience with aircraft buffet. The equation is

$$\frac{d^2}{dx^2} EI \frac{d^2 y}{dx^2} = m\omega^2 y + f \left[\frac{r}{L}, \frac{v}{a}, \frac{\rho v l}{\mu}, \frac{m}{\rho_f}, c/c_r, \frac{L\omega}{v} \right]$$

where r/L signifies geometric similitude, v/a is Mach number, $\rho v l / \mu$ is Reynolds number, m/ρ_f signifies the ratio of the mass of the model to the mass of the surrounding fluid, $L\omega/v$ is the familiar reduced frequency parameter and c/c_r is the structural damping ratio. All of these parameters can be faithfully reproduced in our present tunnels by the use of dynamic models, with the possible exception of Reynolds number and damping. However, we believe that as long as the full scale vehicle has Reynolds numbers in the turbulence boundary layer range and our models reproduce Reynolds numbers well into this same range, the effect of Reynolds numbers is of secondary importance. The structural damping usually turns out to be within the range found in the full scale vehicle.

With a scaled model-wind tunnel combination satisfying the above criteria, the measured quantities of interest will be buffet pressures and bending moment power spectral densities. The relation between model and full scale power spectral density pressure is

$$\frac{P(\omega)V}{q^2 L}$$

while for the bending moment, the power spectral density is

$$\frac{P(\omega)V}{q^2 L^7}$$

One of the unfortunate aspects of modeling technology is the lack of adequate full scale results for correlation, consequently, the proof of scaling laws is, in many instances, substantiated by utilizing models having different scale factors. An example of this aspect of modeling is shown in figure 23, for the Apollo-Saturn I space vehicle. The measured random pressure was obtained on the service module which is just below the Apollo spacecraft. The top curve represents the power spectra density of pressure divided by the square of the model dynamic pressure plotted against model frequency. Two models are shown, a 1.6 percent model and an eight percent model. Note the large differences between the curves. When the similarity parameter for the power spectral density is applied, the curves are brought rather closely together, thus indicating that we are not violating or neglecting large scaling parameters.

An example of the buffet model utilizing these scaling laws is shown in figure 24, which is an eight percent dynamic simulation for the Apollo-Saturn I space vehicle. The basic structural stiffness is duplicated by a hollow cylindrical tube of varying diameter to approximate the stiffness; mass was simulated by the addition of weights, and the whole structure covered by rings of styrofoam to provide the proper aerodynamic shape. These tests were very successful, results being utilized to predict the buffet bending moment for the full scale

vehicle. An example of the results is shown in figure 25, where the bending moment is plotted against vehicle station. The solid curve represent the RMS of the buffet bending moment, the dashed lines represent the contribution from each of the first three vibration modes. Of major significance is the very large contribution due to the second bending mode. Apparently the input was of such a nature as to have frequencies and phases as to cause a large response in this mode.

The previous discussion has been concerned with the low frequency buffet problem. We feel that, in general, the technology has advanced sufficiently so that rather reliable results may be obtained. The picture for higher frequency buffet, of importance for panel response, equipment environment, and astronaut performance, is rather foggy at the present time. The main reason for this difficulty is the introduction of the thin, elastic shell into the problem. Even the governing differential equations appear in many ramifications, depending on the approximations used to obtain the equations. When the vibration amplitude is greater than the skin thickness, nonlinear effects may take over; plate characteristics are sensitive to small changes in the boundary conditions (temperature differences as well can cause large changes in the panel response). In the face of these difficulties, efforts are underway to search for means for solving the problem. Based on examination of the governing differential equation, on previous buffet experience, the following list of parameters are thought to be the more significant:

- | | |
|-------|--|
| r/L | Geometric ratio (radius to length) |
| r/t | Ratio of tank radius to skin thickness |

r/h	Ratio of tank radius to fluid height (in cases of tanks containing a propellant)
$\frac{\rho_l}{\rho_a}$	Ratio of fluid density to air density
μ	Poisons ratio
P/E	Ratio of internal pressure to modulus of elasticity
$\frac{\rho \omega^2 L^2}{E}$	Ratio of dynamic to elastic forces
$L\omega/V$	Reduced frequency

The technique now being followed to perfect a technique for studying this high frequency buffet problem, is to resort to replica (or very detailed) dynamic modeling. In order to provide a model that can be used for basic research as well as provide information of immediate use in NASA's largest and most significant program, the service module of the Apollo-Saturn configuration was chosen as a sample case. The model is being constructed of the same material as the prototype, all rings and stringers are being duplicated, and even the rivet size and spacing is a very close approximation of the actual structure. Figure 26 shows a photograph of the parts of the 1/10 scale model now under construction. The three sections of the service module are shown before the installation of the skin. This reproduction has gone to the extent of attempting to scale the rivets, where were made by hand from a aluminum wire. Tests will be made on this model in the near future. This concludes the discussion of buffeting, but let us turn our attention now to a closely related topic, acoustics.

Acoustics

The subject of acoustics is in some instances closely related to buffet, in other cases the relationship is not clear. In the first instance, noise can be generated by flow breakdown and separation just as in the case for buffet, during transonic and low supersonic flights. In the other case, the noise source is the engine, important during lift-off phase and early flight and its effect is in the more classical since the source of the noise is some distance from the point of interest. For this case, we are not only interested in the noise effect on the vehicle itself, but also on the buildings, equipment, and personnel in the vicinity of the launch site. As a matter of fact, a large amount of property has been purchased by the NASA at Cape Kennedy in order to insure that sufficient distance between the new launch sites and populated areas will be maintained in order to reduce the community noise problem.

In testing for vehicle acoustic response, noise will usually be focused on relatively small areas, and thus testing of full scale components is becoming the accepted practice. Langley Research Center has gradually built up a number of specialized facilities ranging from anechoic chambers, heated noise jets, to a new ultra low frequency testing chamber. As a matter of fact, the first specimen to be tested in the new low frequency facility is full scale and involves the response of humans to high intensity noise in the range of 0 to 50 cps. This sub-audible and near sub-audible range is of extreme importance

since most of the power in the characteristic engine noise spectra of the new larger launch vehicle will be concentrated in this low frequency range. This new facility consists of a tank 24 feet in diameter and will handle a full scale Apollo spacecraft. Tests on the spacecraft will be made at a later time. This concept has already been used in the case of the Mercury spacecraft. The 9 x 6 foot thermal structures tunnel is a blow-down tunnel and intense noise fields are generated at its exit. This noise field has been rather extensively surveyed and it has been found that the intensity (db's) and spectra shape rather closely approximate that which has been measured during early unmanned flights of the Atlas. Thus, a full-scale capsule including a full-scale human was placed in the appropriate position near the exit of the 9 x 6 foot tunnel and exposed to the noise field. Problems of astronaut communication and equipment functioning were then studied.

Many specimens are under test in the various facilities, with a good deal of attention being paid to the fatigue problem. A general discussion of work in the acoustic field is given in reference 3. As an illustration of a current research study, we are studying the response of a typical launch vehicle tank to sinusoidal inputs due to both a point source of excitation as well as sinusoidal acoustic inputs. Ultimately, we hope to impose random noise on the tank, and, utilizing the information obtained from the sinusoidal tests, predict the random response of the tank. The tank being used in these tests is one of the cluster tanks from the first stage of the 1/5 scale model of Saturn I,

which has been previously discussed. The tank is 11 feet long, 14 inches in diameter.

The tank has been installed in the Langley Research Center Anechoic Chamber and figure 27 illustrates the test set-up. The tank may be oscillated by means of the shaker or by a siren having discrete input frequency, or by an air jet located near the model. In a theory of response of structures to noise, reference 4, it is shown that the response is proportional to the radiation resistance, i.e., its noise radiation properties when vibrated. Since the tests are being performed in an anechoic chamber, the sound radiation from the tank may be measured by means of surrounding microphones during tank mechanical vibrations.

In figure 28, the acceleration response of a point midway on the tank, due to a 1 pound slowly varying sinusoidal force applied by a shaker at one end of the tank, is shown. The figure illustrates the acceleration response for an empty tank and a tank full of water. The surprising result that the numerous responses for both cases were relatively the same, where the large response peak for the lowest frequency for the full case was simply shifted to a lower frequency.

Concluding Remarks

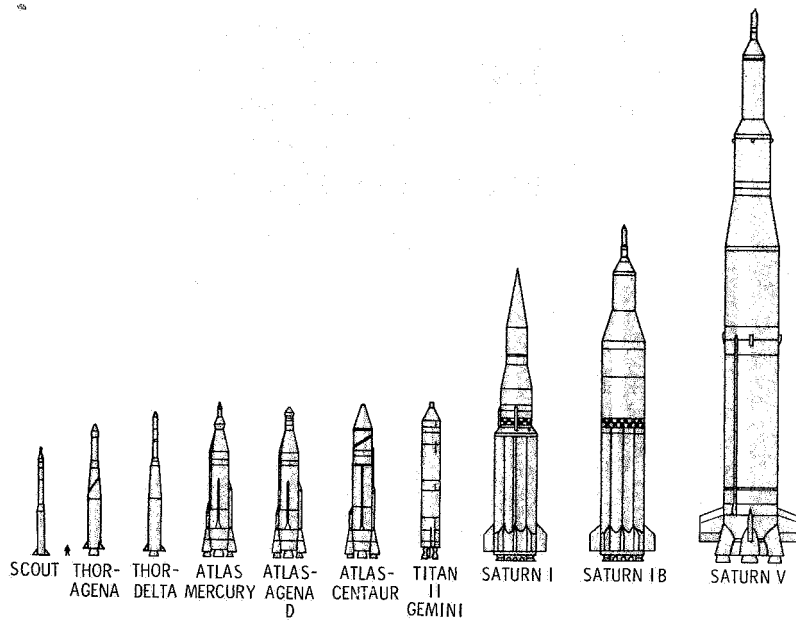
The use of reduced scale physical models and the areas requiring full scale tests for the solution of dynamic problems have been pointed out. In general, modeling technology for the solution of dynamic

problems of launch vehicles has been recently updated through a rather broad and vigorous research program, and a good foundation now exists for the solution of many of these perplexing problems.

The areas requiring additional work are usually associated with small sections of the vehicle and involve the difficult problem of estimation of response of a shell type structure to random buffet and/or acoustic sources. The combined loads problem involving the correlation of the various loading sources is still not settled and much research is required in this area.

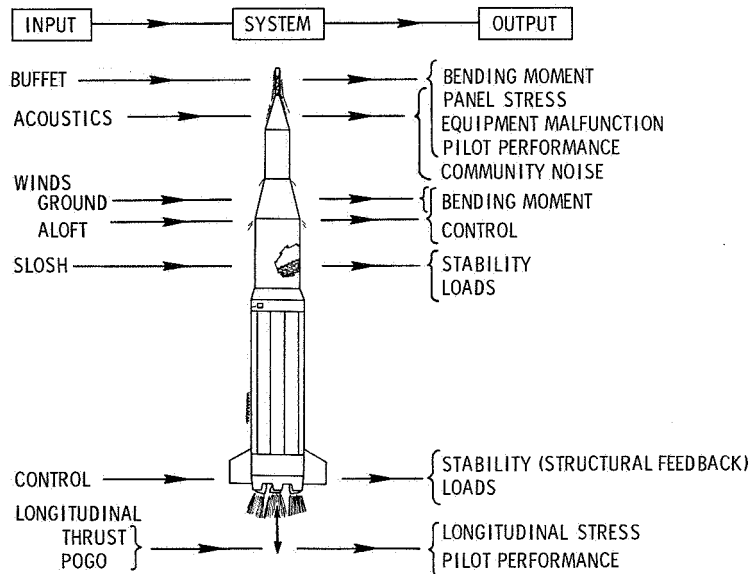
REFERENCES

1. Mixson, J. S., Catherine, J. J., and Arman, Ali: Investigation of the Lateral Vibration Characteristics of a 1/5-Scale Model of Saturn SA-1. NASA TN D-1593, 1963.
2. Rainey, A. Gerald: Progress on the Launch-Vehicle Buffeting Problem. Presented at the Fifth Annual AIAA Structures and Materials Conference, April 1-3, 1964, Palm Springs, California.
3. Edge, Phillip, M., Jr., and Rucker, Carl E.: Response-To-Noise Studies of Some Aircraft and Spacecraft Structures. Presented at the Second International Conference on Acoustical Fatigue, April 29 - May 1, 1964, Dayton, Ohio
4. Crandal, Stephen, ed. Random Vibration, Volume 2. MIT Press. Chapter 7.



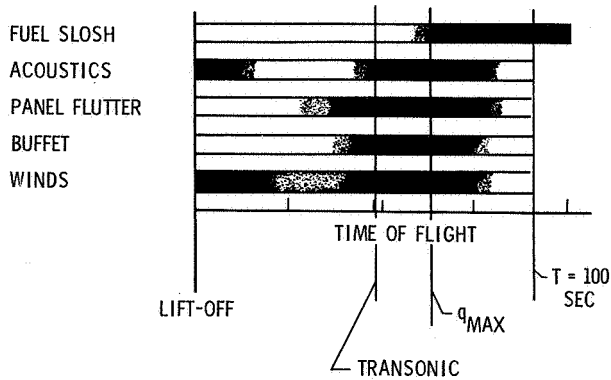
NASA

Figure 1.- NASA launch vehicles.



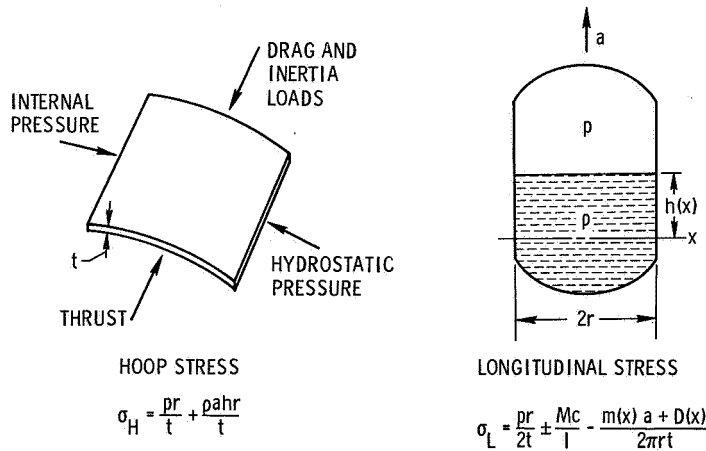
NASA

Figure 2.- Structural dynamic loading.



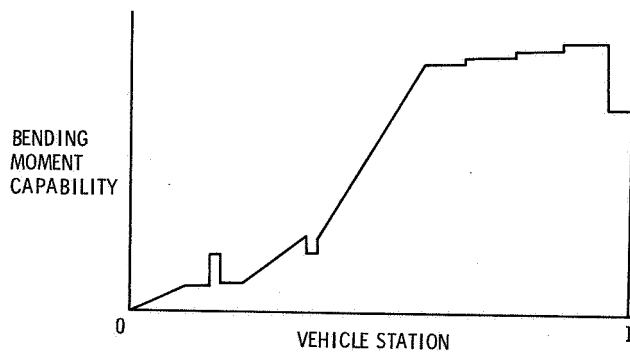
NASA

Figure 3.- Loading conditions versus time of flight.



NASA

Figure 4.- Preliminary design considerations.



NASA

Figure 5.- Bending-moment-capability curve for a launch vehicle.

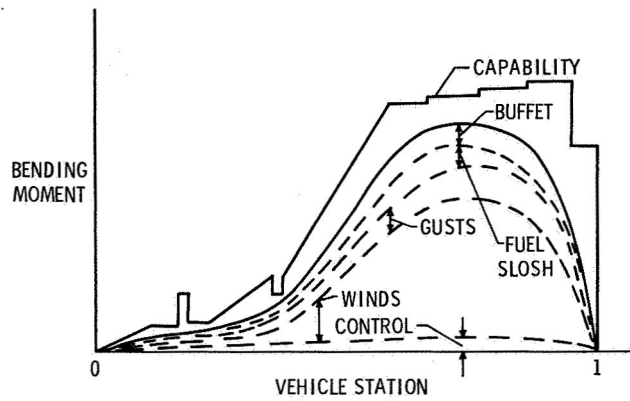


Figure 6.- Bending-moment capability and applied loads.

NASA

(MORE ADVANCE TECHNOLOGY HAS THE GREATER NUMBER OF LINES)

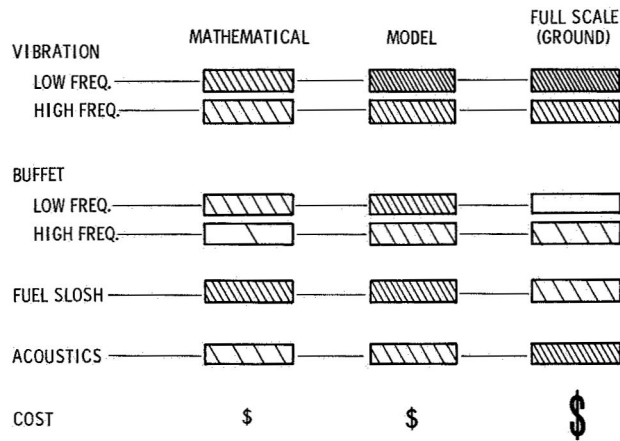


Figure 7.- Estimation of status of simulation techniques for launch vehicles.

NASA

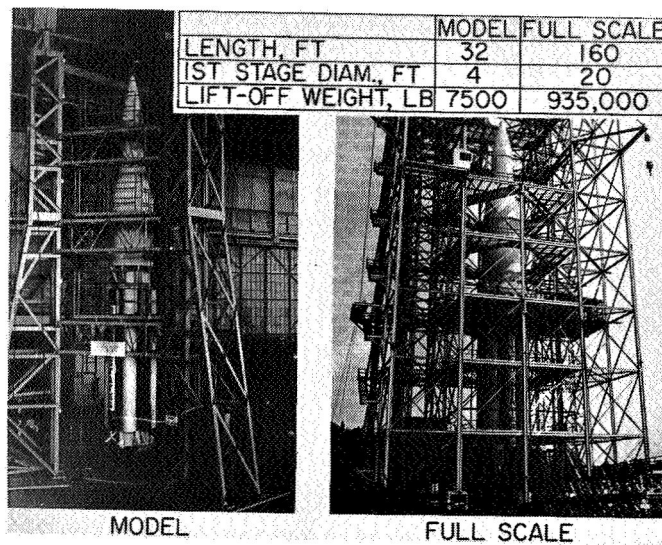
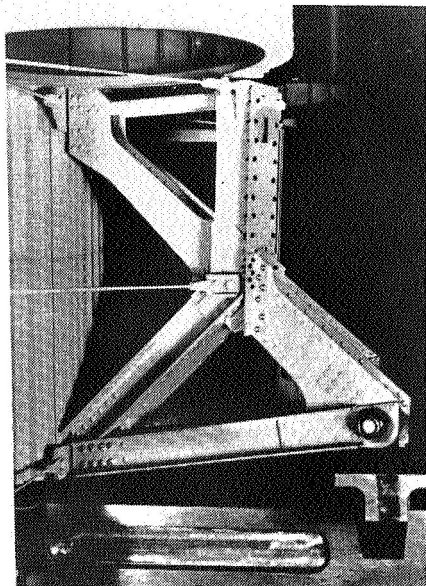
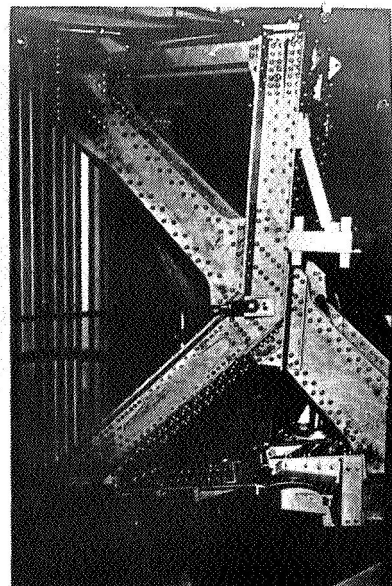


Figure 8.- Saturn vibration-test vehicles.

NASA



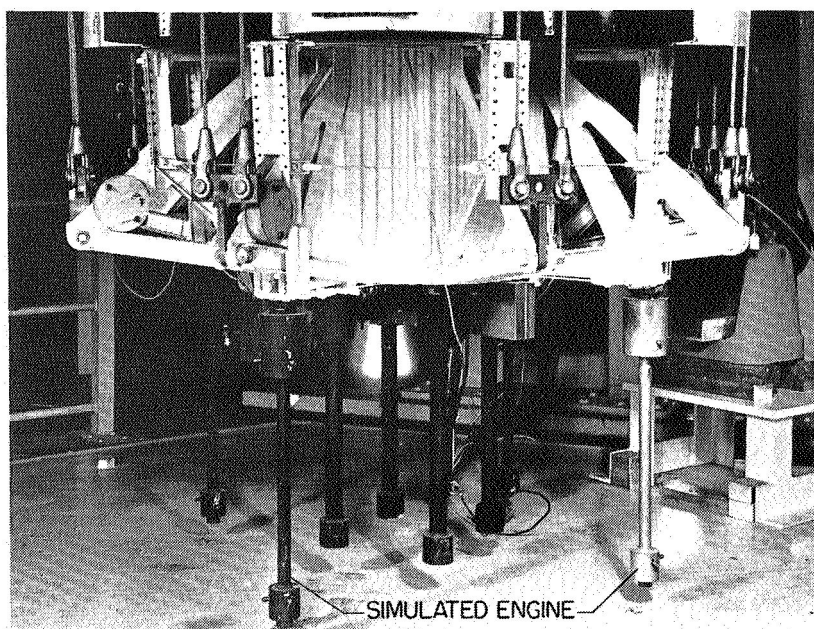
MODEL



FULL SCALE

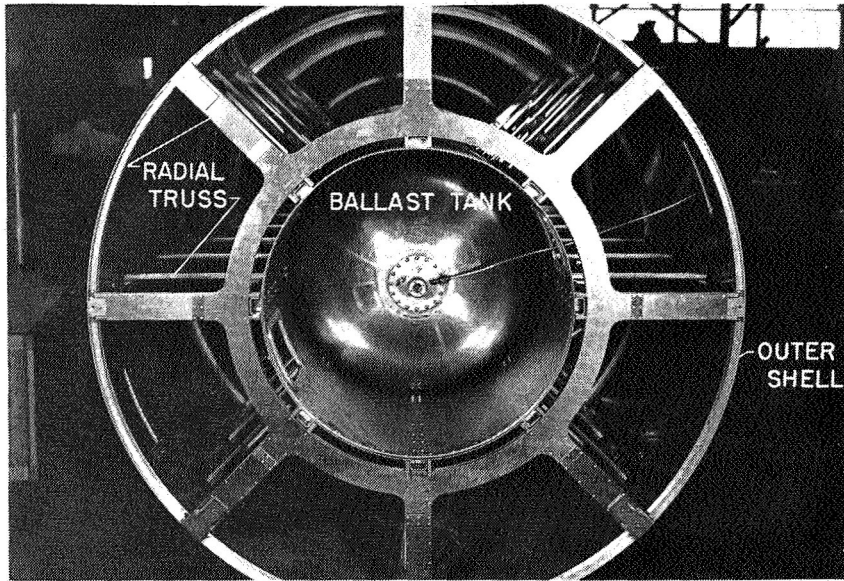
NASA

Figure 9.- Saturn structural details.



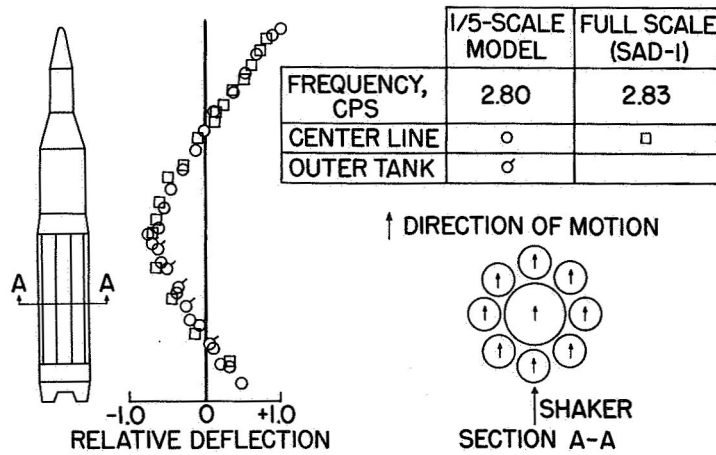
NASA

Figure 10.- Photograph showing 1/5-scale Saturn engines.



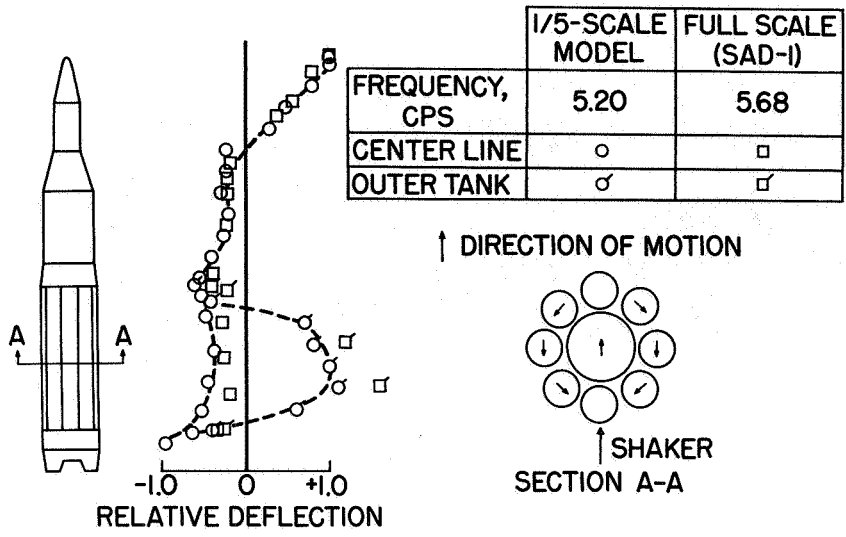
NASA

Figure 11.- End view of 1/5-scale Saturn second stage.



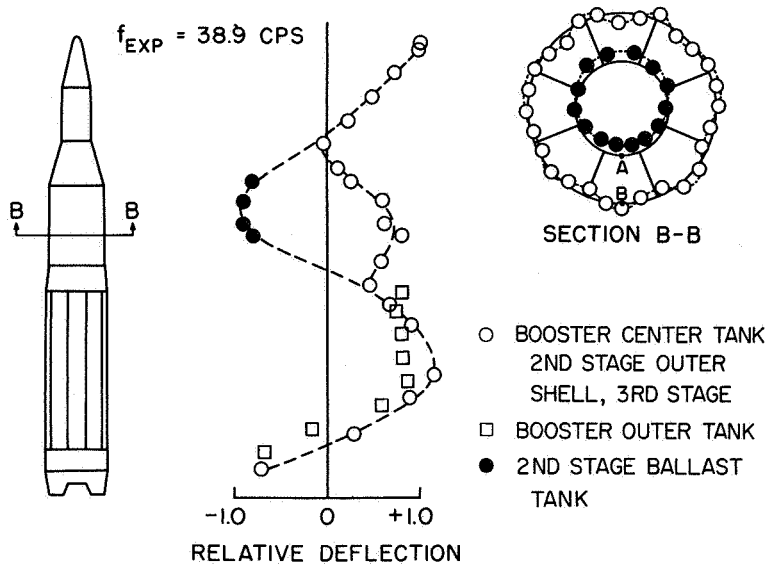
NASA

Figure 12.- First bending mode of Saturn, maximum dynamic pressure weight.



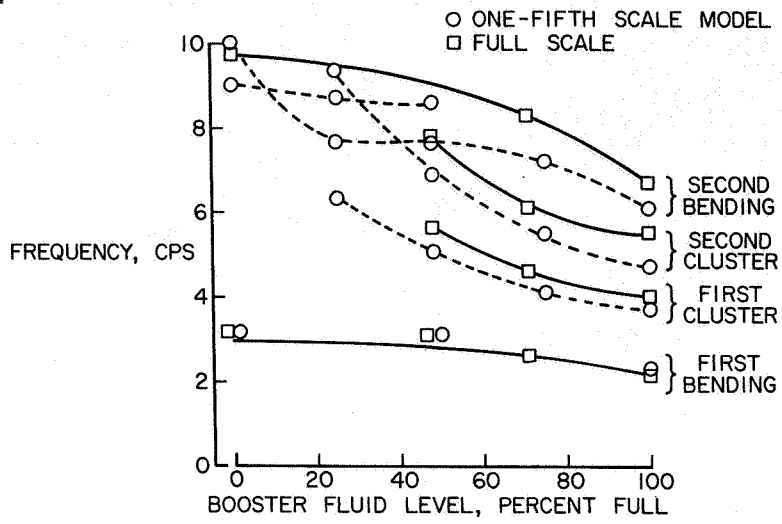
NASA

Figure 13.- First cluster mode of Saturn, maximum dynamic pressure weight.



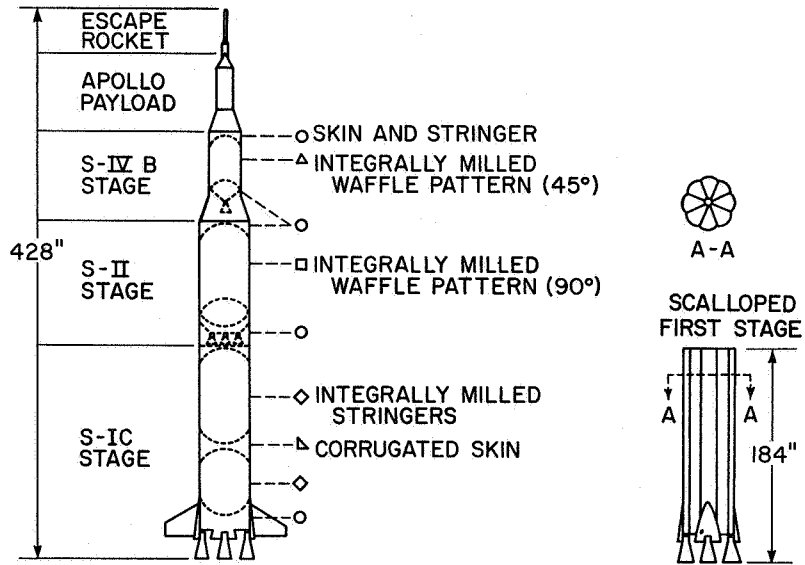
NASA

Figure 14.- Fourth vibration mode of 1/5-scale Saturn.



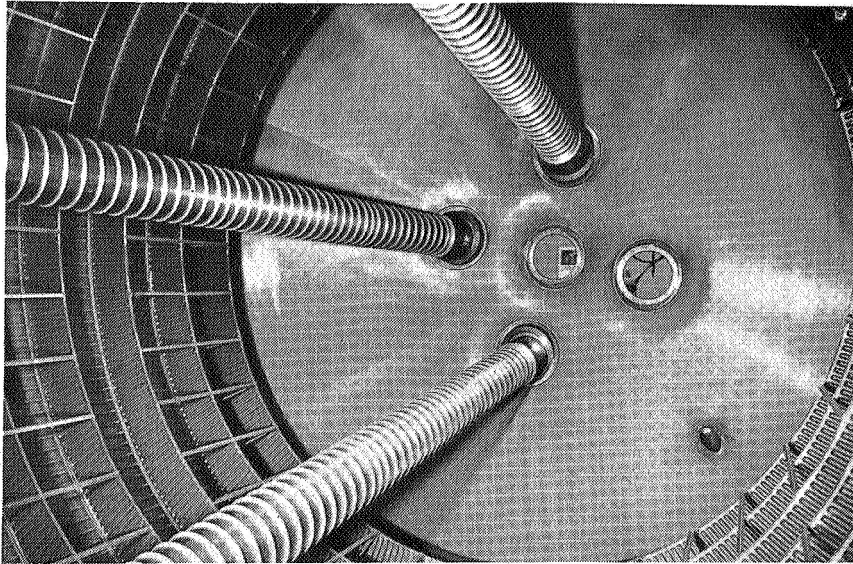
NASA

Figure 15.- Fundamental vibration frequencies of Saturn I.



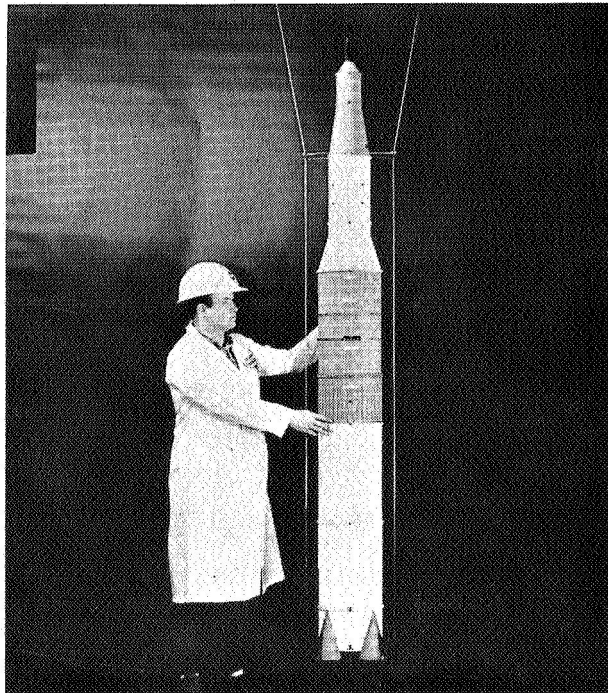
NASA

Figure 16.- 1/10-scale model of Saturn V and scalloped first stage.



NASA

Figure 17.- Internal view of Saturn V model fuel tank.



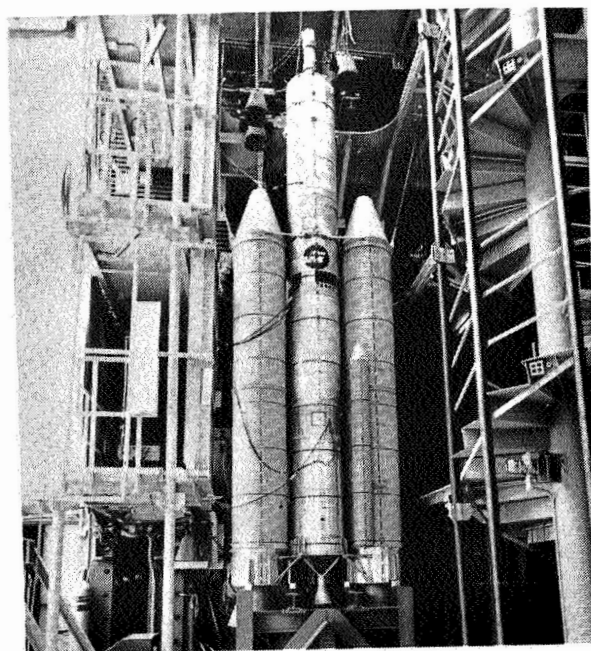
NASA

Figure 18.- 1/40-scale model of Saturn V.



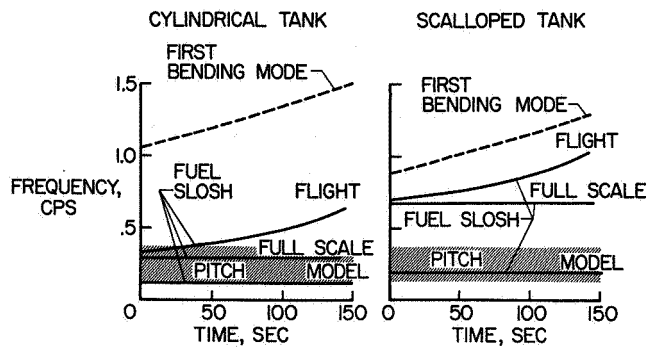
NASA

Figure 19.- 1/40-scale model details of Saturn V.



NASA

Figure 20.- 1/5-scale model of Titan III in dynamic test tower.



NASA

Figure 21.- Fundamental frequencies calculated for large launch vehicle for cylindrical and scalloped first stage.

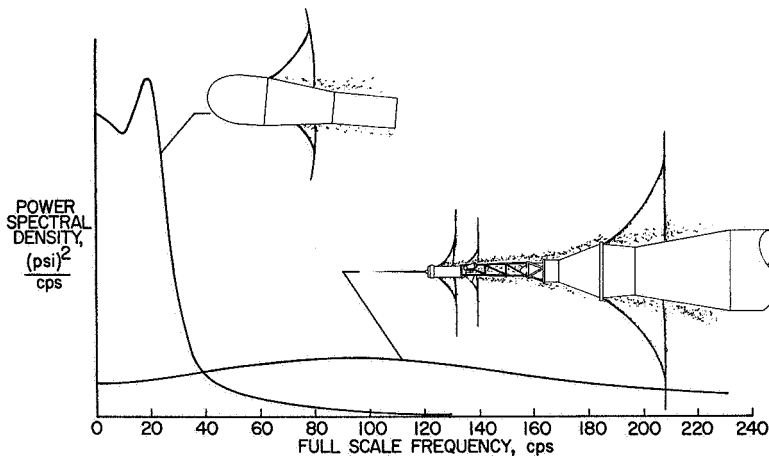


Figure 22.- Two types of buffet pressure spectra.

NASA

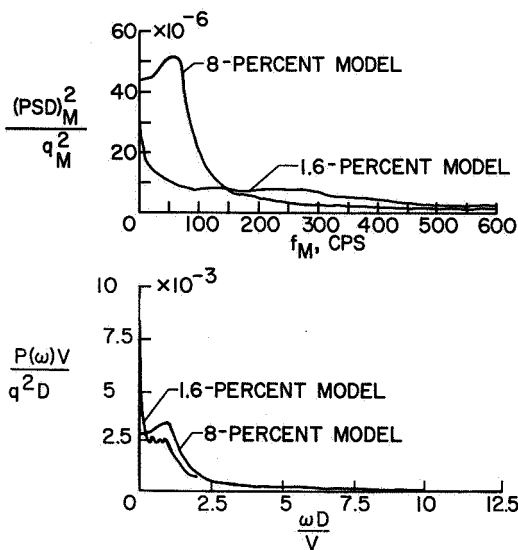
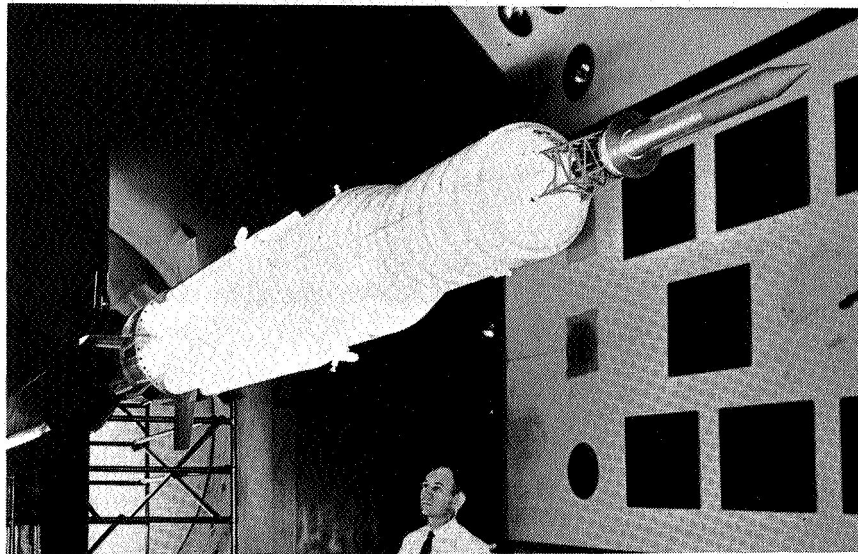


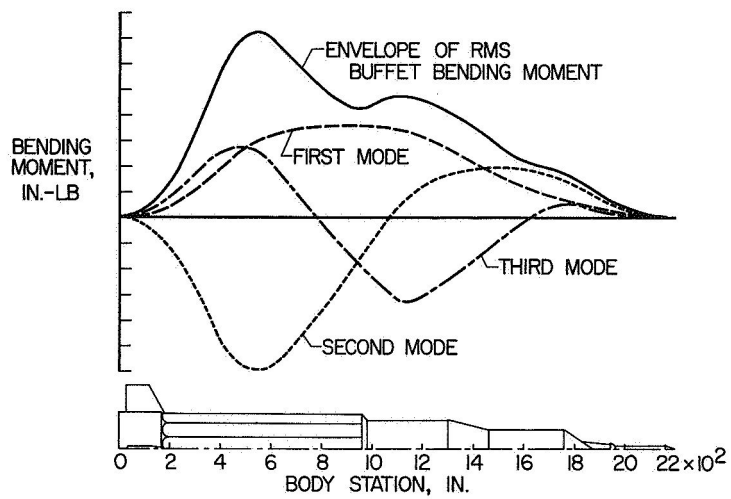
Figure 23.- Scaling of buffet pressure spectra.

NASA



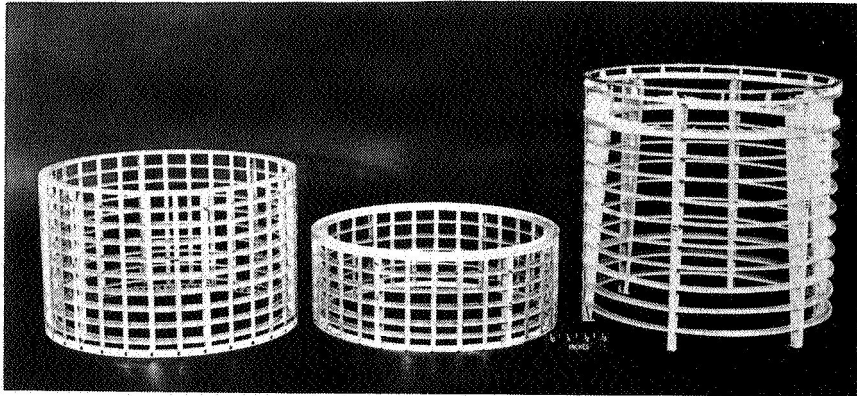
NASA

Figure 24.- 8-percent buffet model mounted in tunnel.



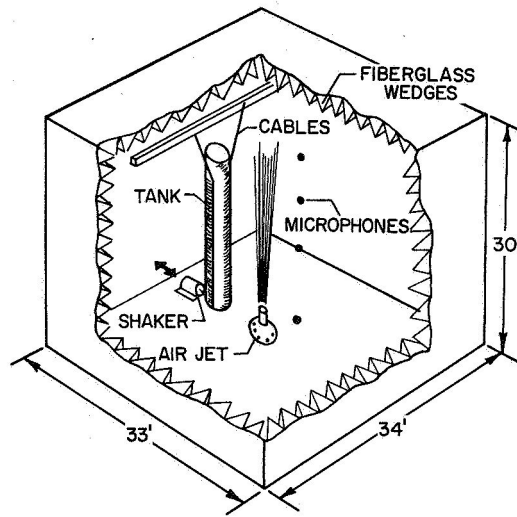
NASA

Figure 25.- Modal contribution to buffet bending moment predicted from Saturn-Apollo model results.



NASA

Figure 26.- Parts for 1/10-scale replica model of Apollo service module.



NASA

Figure 27.- Tank response.

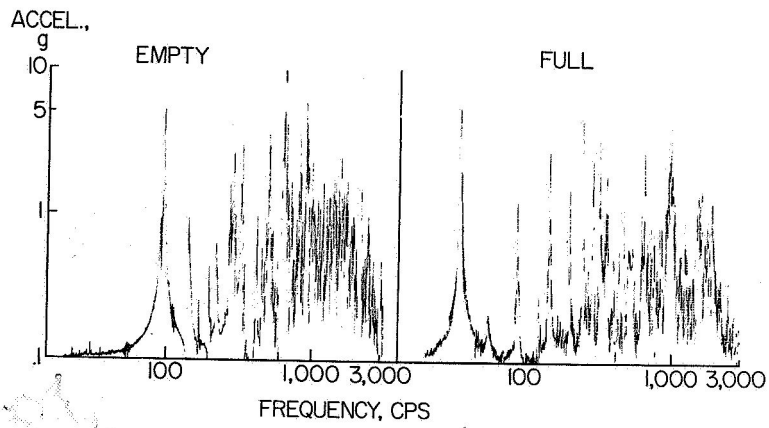
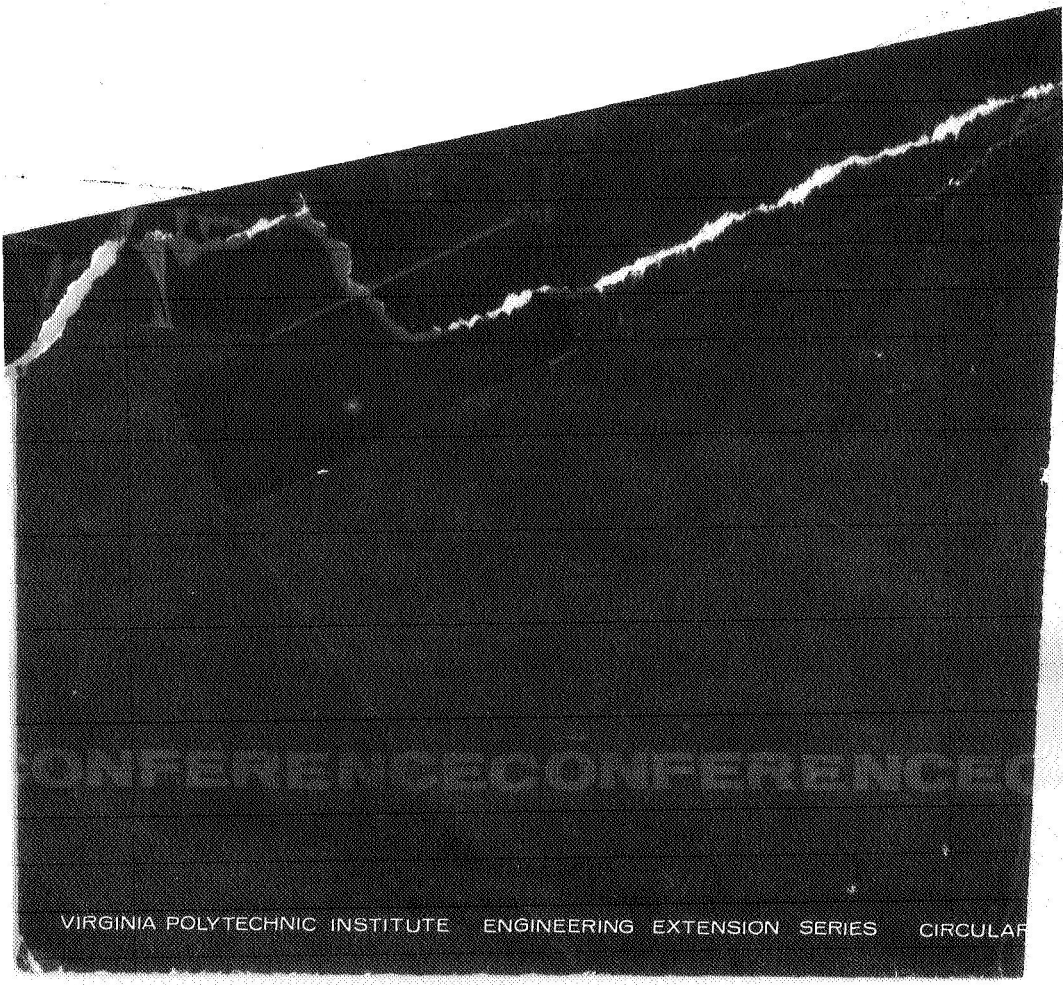


Figure 28.- Response of 1/5-scale Saturn with and without fuel.

NASA

VIRGINIA ENGINEERING EXPERIMENT
STATION

DIRECTOR	583
Aerospace Engineering	255
Architecture (School)	243
Business (School)	440
Ceramic Engineering	548
Chemical Engineering	248
Chemistry	258
Civil Engineering	281
Electrical Engineering	409
Engineering Mechanics	245
Geological Sciences	279
Industrial Engineering	285
Mathematics	252
Mechanical Engineering	206
Metallurgical Engineering	382
Mining Engineering	380
Physics	295
Wood Construction	488



CONFERENCE CONFERENCE

VIRGINIA POLYTECHNIC INSTITUTE ENGINEERING EXTENSION SERIES CIRCULAR